

Tensor product state algorithms for characterizing entanglement and excitations of correlated quantum matter

Dissertation

Elisabeth A. A. Wybo

Tensor product state algorithms for characterizing entanglement and excitations of correlated quantum matter

Elisabeth A. A. Wybo

Vollständiger Abdruck der von der Fakultät für Physik der Technischen Universität München zur Erlangung des akademischen Grades einer Doktorin der Naturwissenschaften (Dr. rer. nat.) genehmigten Dissertation.

Vorsitzender: Prof. Dr. Wilhelm Auwärter

Prüfer der Dissertation:

1. Prof. Dr. Michael Knap
2. Prof. Dr. Johannes Knolle

Die Dissertation wurde am 27.07.2022 bei der Technischen Universität München eingereicht und durch die Fakultät für Physik am 24.08.2022 angenommen.

Abstract

Quantum many-body systems exhibit a wealth of phenomena, but are challenging to simulate numerically due to the exponential growth of the Hilbert space with system size. In this thesis, we study various one-dimensional systems with tensor-network techniques to overcome these limitations. First we investigate the entanglement dynamics of many-body localized systems coupled to a bath. Second, we describe entanglement properties of low-energy excitations in equilibrium. Third we study the quasiparticles in a spin ladder, and show the emergence of the sine-Gordon field theory.

Kurzfassung

Quantenvielteilchensysteme weisen eine Fülle von Phänomenen auf, sind jedoch aufgrund des exponentiellen Wachstums des Hilbertraums mit der Systemgröße schwierig numerisch zu simulieren. In dieser Arbeit untersuchen wir verschiedene eindimensionale Systeme mit Tensor-Netzwerk-Techniken, um diese Einschränkungen zu überwinden. Zuerst untersuchen wir die Verschränkungsdynamik von lokalisierten Vielteilchensystemen, die an ein Bad gekoppelt sind. Zweitens beschreiben wir die Verschränkungseigenschaften von niederenergetischen Anregungen im Gleichgewicht. Drittens untersuchen wir die Quasiteilchen in einer Spinleiter und zeigen die Emergenz der Sine-Gordon-Feldtheorie.

Contents

Abstract	iii
Kurzfassung	v
List of Publications	1
1 Introduction	3
2 Isolated quantum systems	7
2.1 Quantum states and entanglement	7
2.1.1 Quantum many-body systems	7
2.1.2 The Schmidt decomposition and von Neumann entanglement entropy	8
2.1.3 Other entanglement measures	8
2.2 Quantum thermalization	9
2.2.1 The eigenstate thermalization hypothesis	10
2.3 Thermalization breaking mechanisms	11
2.3.1 Integrability	12
2.3.2 Many-body localization	13
3 Open quantum systems: dynamics and entanglement	19
3.1 Properties of density matrices and quantum channels	19
3.2 The Lindblad master equation	22
3.3 Entanglement of mixed states	24
3.3.1 The Peres–Horodecki criterion and the negativity	25
3.3.2 The Rényi negativity	27
3.3.3 R_3 is not an entanglement monotone	29
3.3.4 Entanglement witnesses	30
4 Matrix-product states	33
4.1 Matrix-product state decomposition and canonical forms	33
4.2 Area versus volume law entanglement scaling	36
4.3 Matrix-product state algorithms	37
4.3.1 Density-matrix renormalization group algorithm	37
4.3.2 Time-evolving block decimation	39
4.3.3 Time-evolving block decimation for density matrices	41
4.4 Rényi negativity as contraction of a tensor network	42
5 Entanglement dynamics of a many-body localized system coupled to a bath	45
5.1 Model and setup	46
5.2 Results of the computation of Rényi negativities	47
5.2.1 Closed system	48

5.2.2	Open system	49
5.3	Convergence of the time-evolving block decimation algorithm for density matrices	54
5.4	Comparison of the negativity and R_3 by exact diagonalization	55
5.5	Sudden death dynamics of the negativity	55
5.6	Quantum Fisher information as an entanglement witness	57
5.7	Conclusion and outlook	58
6	Wannier-Stark localized systems coupled to an environment	61
6.1	Model and setup	62
6.2	Results	63
6.2.1	Isolated system	64
6.2.2	Open System	67
6.3	Understanding the late-time dynamics by exact diagonalization	69
6.4	Conclusion and outlook	69
7	Entanglement of quasiparticles	75
7.1	Correlation matrix approach for quasiparticle entanglement	76
7.2	Degeneracy theorem for the quasiparticle entanglement spectrum	80
7.2.1	Quasiparticles with Z_2 charge and reflection symmetry	80
7.2.2	Quasiparticles with Z_2 charge and translation symmetry	82
7.2.3	Non-local quasiparticles without Z_2 charge	82
7.2.4	Quasiparticles with U(1) charge and reflection symmetry	83
7.3	Entanglement fragmentation, a feature of SPT quasiparticles	84
7.3.1	Quasiparticles of the topological SSH chain	84
7.3.2	Quasiparticles of the topological SSH model with periodic boundary conditions	86
7.4	Conditional mutual information for quasi-particles in SPT chains	88
7.4.1	Ground state properties	88
7.4.2	Quasiparticle properties	90
7.5	Conclusion and outlook	95
8	Quantum sine-Gordon dynamics in coupled spin chains	97
8.1	Model and setup	98
8.1.1	The sine-Gordon field theory on a spin ladder	99
8.1.2	Luttinger parameter in the symmetric sector	101
8.2	The quantum sine-Gordon model	101
8.3	Spectral analysis of the low energy sector	103
8.3.1	The spectral function	105
8.3.2	Breather spectroscopy from periodic modulations of the interchain coupling	109
8.3.3	Form factor suppression of B_1	111
8.3.4	The contribution of the interchain zz coupling	114
8.3.5	Technical details on the calculation of spectral functions	115
8.4	Real-time scattering of sine-Gordon excitations	116
8.4.1	$B_1 - B_1$ scattering	117
8.4.2	$B_1 - B_2$ scattering	118
8.4.3	Technical details on the creation of wave packets	119

8.5 Conclusion and outlook	121
9 Conclusion	123
Acknowledgments	127
List of Figures	129
Acronyms	139
Bibliography	141

List of publications

Parts of this thesis have been previously published or uploaded to a preprint server.

- The content of Chapter 5 is based on Ref. [1].
- The content of Chapter 6 is based on Ref. [2].
- Chapter 7 is mostly based on Ref. [3]. In addition some illustrative numerical results obtained by the author of this thesis that are contained in the preprint [4], are added and discussed.
- Most of the content of Chapter 8 has appeared in Ref. [5].

- [1] E. Wybo, M. Knap, and F. Pollmann. “Entanglement dynamics of a many-body localized system coupled to a bath.” *Phys. Rev. B* **102**, p. 064304, 2020. doi:[10.1103/PhysRevB.102.064304](https://doi.org/10.1103/PhysRevB.102.064304).
- [2] E. Wybo, M. Knap, and F. Pollmann. “Dynamics of negativity of a wannier–stark many-body localized system coupled to a bath.” *physica status solidi (b)* p. 2100161, 2021. doi:<https://doi.org/10.1002/pssb.202100161>.
- [3] E. Wybo, F. Pollmann, S. L. Sondhi, and Y. You. “Visualizing quasiparticles from quantum entanglement for general one-dimensional phases.” *Phys. Rev. B* **103**, p. 115120, 2021. doi:[10.1103/PhysRevB.103.115120](https://doi.org/10.1103/PhysRevB.103.115120).
- [4] Y. You, E. Wybo, F. Pollmann, and S. L. Sondhi. “Observing quasiparticles through the entanglement lens.” 2020. arXiv:[2007.04318](https://arxiv.org/abs/2007.04318).
- [5] E. Wybo, M. Knap, and A. Bastianello. “Quantum sine-gordon dynamics in coupled spin chains.” *Phys. Rev. B* **106**, p. 075102, 2022. doi:[10.1103/PhysRevB.106.075102](https://doi.org/10.1103/PhysRevB.106.075102).

The author of this thesis has made significant and substantial contributions to the publications [1–3, 5], ranging from literature research, development of ideas, design and implementation of numerical codes, analytic calculations, to the interpretation of results, and writing of the papers. For the preprint [4] the author of this thesis wrote a numerical code to obtain the results presented in the figures.

1 Introduction

Many-body quantum systems exhibit a wide range of fascinating phenomena, both in *equilibrium* and *non-equilibrium* scenarios. In equilibrium, the existence of various *quantum phases* at zero temperature illustrates how seemingly simple variations of short range potentials and dimensionality can lead to extremely rich physics [6].

For instance, Hubbard models [7–9] are known for possessing complex quantum phase diagrams [10,11]. In particular, in the bosonic model there is a well-studied phase transition between a critical superfluid and a Mott insulating phase [12,13]. The transition takes place as a function of interaction strength. When the interactions are strong and for integer fillings, the system is in an insulating phase characterized by an energy gap. While if the interactions are weak the system is in the superfluid phase.

A prominent class of quantum phases, that has sparked a lot of interest over the recent years, are *topological* quantum phases [14]. These phases feature special types of non-local orders that go beyond Landau’s theory of symmetry-breaking [15], and in 2016 a Nobel prize was awarded for theoretical advances in characterizing these phases and their transitions [16,17]. Of particular interest are the more recently discovered *symmetry-protected topological* (SPT) phases which have been subject to intense classification efforts over the last years [18,19]. The most famous model that features an SPT phase in the ground state (the *Haldane phase*), is the spin-1 Heisenberg chain [16].

Yet another class of models that have become the subject of intense investigations over the recent years are *many-body localized* (MBL) systems. These systems are characterized by strong disorder and interactions, and are believed to form a robust phase of matter at finite temperature with very non-conventional properties [20–23].

In general it is very difficult to detect these exotic quantum phases of matter. However it has been demonstrated that crucial signatures can be deduced from studying *quantum entanglement* [24–28].

In 1935, quantum entanglement was first investigated by A. Einstein, B. Podolsky, and N. Rosen [29], and referred to by Einstein as a *spooky action at a distance*. Afterwards, the concept mostly rooted in quantum information theory [30]. It is only quite recently, since the establishment of the *density matrix renormalization group* (DMRG) algorithm in 1992 [31], that entanglement has become a very important concept in condensed-matter physics as well. In 1992, S. White first applied the DMRG algorithm on the aforementioned spin-1 Heisenberg chain [31,32]. Since then, it became one of the standard methods to investigate ground states of strongly-correlated systems. In short, DMRG employs a class of variational states, known as *matrix-product states* (MPS) [33,34], to accurately and efficiently represent ground states of low-dimensional models, by renormalizing the state based on the amount of entanglement. Like this, the amount of parameters needed to represent a state in an exponentially large Hilbert space can be dramatically reduced. Thanks to the DMRG algorithm, tremendous progress has been made in the understanding of quantum phases. For instance, not surprisingly, there is a large amount of literature aiming at a better understanding of the properties of the Hubbard model using DMRG. Of course, properties of many other models have also

been investigated with **DMRG**, and later also with **MPS** techniques, for review articles, see Refs. [33, 34]. Within the language of **MPS**, entanglement captures indeed very naturally physically relevant information, such as long-range orders that are present in topologically non-trivial ground states [24, 25].

In this thesis, entanglement plays a central role as well: first because it provides crucial fingerprints of various phases, and secondly because it forms the foundation of tensor-network methods. Although equilibrium physics remains extremely interesting and challenging, we will also consider some non-equilibrium scenarios. However, *out-of-equilibrium* scenarios are among the hardest to theoretically describe in the field of many-body quantum systems, due to the complexity of the quantum states they involve. Indeed, in these setups, we necessarily need to dive into the study of *quantum dynamics*. There however exist several straightforward algorithms to perform time-evolution using **MPS**. In particular, in context of this thesis we have made extensively use of the **time-evolving block decimation (TEBD)** algorithm [35]. A review of state-of-the-art algorithms for time-evolution based on **MPS** can be found in Ref. [36]. However, even with these algorithms the study of quantum dynamics remains notoriously hard on classical computers [34, 36]. The problem is that the dimension of the matrices of the **MPS** which are needed to faithfully represent the state, can grow very quickly (exponentially) with simulation time. In practice this might be limiting us to either short systems, or short times. Not surprisingly, out-of-equilibrium dynamics spans a huge range of possible scenarios, so we necessarily need to confine ourselves to some tiny subset, in this thesis chosen to be *couplings to an environment* [37, 38] and *quantum quenches* [39–41].

Perhaps the most intuitive way of driving a system out of equilibrium, is to couple it with another system or *environment* to then see how it equilibrates [37]. The joint system remains pure at all times as the dynamics is unitary. However, in realistic setups we only have access to the degrees of freedom of the bare system. This implies that the dynamics of the system itself will *not* be unitary, and that the system will be described by a *mixed state* or density matrix. This terminology refers to the fact that quantum correlations are mixed together with classical ones. If the environment immediately forgets all acquired information about the system, it is said to be *Markovian* [37, 42]. For this type of environment, the dynamics of system can be described by a closed evolution equation, the *Lindblad* equation [37, 38, 43], which also has been widely applied in setups relevant for this thesis [44–51]. Lindbladian dynamics consists of a unitary part, governed by a Hamiltonian, and a dissipative part, governed by Lindblad jump operators. It turns out that when the jump operators are Hermitian, the system is destined to heat up to an infinite temperature state, irrespective of the Hamiltonian. This is not the case in general for non-hermitian jump operators.

Another well-studied non-equilibrium scenario, where the state remains *pure* at all times, is a *quantum quench* [39–41]. Here, the system is prepared in a certain initial state (usually the ground state of a local Hamiltonian), and then a sudden change of parameters of the Hamiltonian is made. This will result in unitary dynamics (unless the initial state remains an eigenstate). For most systems, the dynamics under such a sudden quench is characterized by a rapid (linear) growth of entanglement [52]. However, this is not generically true for all interacting many-body systems. In **MBL** systems [20–23], this behavior is slowed down drastically to only a logarithmic growth [26–28]. However, these **MBL** systems have other very surprising properties: most importantly it is believed that

they do *not thermalize*. With this, we mean that at late times, the expectation values of *local* operators are *not* set by statistical ensembles that only take into account globally known quantities about the state (such as energy, particle number, etc.) [53–56].

A simple and experimentally relevant protocol by which thermalization can be probed, is to make a quench starting from a state with a strong density modulation [57]. Such state has a well-defined initial pattern that will be completely lost after evolution with a thermalizing Hamiltonian [23]. However with an MBL Hamiltonian, parts of this pattern can still be recognized at late times. This protocol has been implemented experimentally in a cold atom setup in Ref. [57], that is well isolated from the environment.

Yet another class of (one-dimensional) models, apart from MBL systems, that do not thermalize are *integrable* models [55, 56]. In contrast to MBL systems they can exhibit fast growth of entanglement [58], but they however do not thermalize in the conventional way because of the existence of extensively many *local* conservation laws. This class of models is also very interesting. First, because they allow for exact results even in complicated non-equilibrium scenarios. Second, because they can show very distinct behavior as has been experimentally demonstrated in Ref. [59]. Here Bose gases in different dimensionalities were investigated. Initially the gases were driven out of equilibrium. While the two and three dimensional gases quickly relaxed to an equilibrium ensemble, the one-dimensional (nearly integrable) gas relaxed to a distinctly non-equilibrium state.

In this thesis, we will combine various aspects of these equilibrium and non-equilibrium scenarios, with the goal to better understand a selection of emergent phenomena in one-dimensional strongly-correlated systems. We will study the dynamics of quantum entanglement in an MBL system that is coupled to an environment. Then we will study the entanglement content of quasiparticles in various equilibrium quantum phases, including SPT. Finally we will study, the emergence of the sine-Gordon field theory in a system of coupled spin chains. In all of these projects, we have made extensive use of MPS techniques, even for simulating density matrices or critical systems.

The next three chapters of this thesis should be read as an extended introduction to some of the concepts mentioned in this general introduction. The later chapters then contain the results.

In Chapter 2 we briefly review the basic concepts about many-body pure quantum states and their dynamics. We discuss the most commonly used entanglement measures, and introduce the concept of quantum thermalization. Finally we discuss two classes of systems that break this paradigm: integrable systems and MBL systems.

In Chapter 3 we turn to open quantum systems and discuss their dynamics by deriving the Lindblad master equation under the Markovian approximation. We also discuss entanglement measures for mixed states. However measuring the amount of quantum entanglement is much harder in an open quantum system than in a closed quantum system. Indeed, in the open system one must find a way to ‘filter out’ the classical superpositions. Moreover we also would like that the amount of entanglement is computable in a many-body context. Therefore the computation should not rely on the diagonalization of the density matrix, as this is prohibitively expensive.

In Chapter 4 we will summarize the main ideas behind representing quantum states as MPS in a concise way. Afterwards we will shortly introduce the main algorithms that we have used, and particularly focus on their extension to density matrices.

In Chapter 5 we start presenting our main work. Here we describe time evolution according to the Lindblad equation, where the Hamiltonian is [MBL](#) and the dissipation terms represent dephasing noise. This will result in a competition between entanglement growth driven by the unitary Hamiltonian dynamics, and entanglement loss by the dephasing process. However at intermediate time scales, when the dephasing is not too strong, the logarithmic growth of entanglement which forms a key dynamical feature of [MBL](#), remains intact.

In Chapter 6 we consider the same problem but for a Wannier-Stark localized system [[60,61](#)]. When a linear potential is applied to the system, it turns out that some of the features of disorder induced [MBL](#) are preserved, including the logarithmic growth of entanglement under a quench from a product state. This could allow for a disorder-free implementation that is slowing down the growth of entanglement. We indeed find that most of the features we observed for the disordered system carry over to the Wannier-Stark system. The differences are discussed.

In Chapter 7 we discuss signatures in the entanglement content of quasiparticle excitations that allow us to distinguish between various phases, for instance topologically trivial and non-trivial phases. We performed large-scale numerical simulations of the transverse-field cluster model, and showed that the transition between the [SPT](#) and trivial phase can be detected via the quasiparticles.

In Chapter 8 we investigate the emergence of the sine-Gordon field theory in a ladder system of two tunnel-coupled XXZ spin chains. The anti-symmetric sector of this setup naturally realizes the integrable sine-Gordon model in its quantum regime. We show good compatibility with the exact theory, and investigate quasiparticle scattering events. This setup could potentially be realized in existing quantum gas microscopes, which then would implement a quantum simulator of the sine-Gordon model.

In Chapter 9 we end with a brief summary of our results and give a short outlook.

2 Isolated quantum systems

In this chapter we describe properties of quantum systems that are completely isolated from their surrounding environment. Therefore these systems are also called *pure* quantum systems. In Sec. 2.1 we will briefly summarize some properties of pure quantum states and define bipartite entanglement measures. In Sec. 2.2, we will then consider the dynamics of these systems and introduce the concept of quantum thermalization. While most physically relevant systems obey the framework quantum thermalization, not *all* relevant systems are thermalizing. In fact, there are two interesting and well-studied classes of systems do not thermalize in the conventional way: integrable systems and MBL systems. We will discuss these in Sec. 2.3.

2.1 Quantum states and entanglement

In this section we summarize some generic properties of static pure states. We will focus on the many-body case, and discuss entanglement measures that capture the amount of entanglement between two subsystems.

2.1.1 Quantum many-body systems

A pure quantum-many body system consisting of particles on an L -site lattice, is fully represented by a vector $|\psi\rangle$ in the Hilbert space \mathcal{H} . This Hilbert space has a tensor-product structure

$$\mathcal{H} = \mathcal{H}_1 \otimes \mathcal{H}_2 \otimes \dots \mathcal{H}_L, \quad (2.1)$$

where \mathcal{H}_i is the Hilbert space associated with the particle on the i th lattice site. We will assume that our system consists of particles that are each described by the same local Hilbert space with dimension $\dim\mathcal{H}_i = d$. Therefore the total Hilbert space dimension is given by $\dim\mathcal{H} = d^L$. Hence, it scales exponentially with the size of the system.

The Hilbert space \mathcal{H} has the usual properties of a vector space, with in particular the existence of an inner product $\langle\phi|\psi\rangle$ which satisfies

- (i) positivity $\langle\psi|\psi\rangle > 0$ (when $|\psi\rangle \neq 0$);
- (ii) linearity if $|\psi\rangle = a|\psi_1\rangle + b|\psi_2\rangle$ then $\langle\phi|\psi\rangle = a\langle\phi|\psi_1\rangle + b\langle\phi|\psi_2\rangle$;
- (iii) conjugation symmetry $\langle\phi|\psi\rangle = \langle\psi|\phi\rangle^*$.

Each vector in the Hilbert space can be expanded in a basis (that carries over the tensor-product structure)

$$|\psi\rangle = \sum_{s_1, s_2, \dots, s_L} \psi_{s_1, s_2, \dots, s_L} |s_1, s_2, \dots, s_L\rangle, \quad (2.2)$$

where $|s_1, s_2, \dots, s_L\rangle$ is the shorthand notation for $|s_1\rangle \otimes |s_2\rangle \otimes \dots \otimes |s_L\rangle$, and $\{|s_i\rangle\}$ forms a basis of \mathcal{H}_i .

2.1.2 The Schmidt decomposition and von Neumann entanglement entropy

The degrees of freedom of a pure quantum many-body state that lives in the Hilbert space, see Eq. (2.2), can be straightforwardly regrouped into a bipartite quantum state. We decompose $\mathcal{H} = \mathcal{H}_A \otimes \mathcal{H}_B$, with respective basis $\{|s_A\rangle\}$ and $\{|s_B\rangle\}$. Then,

$$|\psi_{AB}\rangle = \sum_{s_A, s_B} \psi_{s_A, s_B} |s_A\rangle \otimes |s_B\rangle, \quad (2.3)$$

where the coefficients can now be viewed as a matrix. Thus we can apply a (compact) [singular-value decomposition \(SVD\)](#) to this matrix which means it can be decomposed as $\psi_{s_A, s_B} = \sum_i U_{s_A, i} \lambda_i V_{i, s_B}$ where the Schmidt coefficients $\lambda_i \geq 0$ (and are hence also real numbers), and where both U, V are semi-unitary matrices $U^\dagger U = V V^\dagger = \mathbb{1}$. Hence they can be used for a basis transformation, such that

$$|\psi_{AB}\rangle = \sum_i \lambda_i |i_A\rangle \otimes |i_B\rangle. \quad (2.4)$$

This is the so-called Schmidt decomposition of a quantum state. It follows that $\sum_i \lambda_i^2 = 1$, if $|\psi\rangle$ was originally normalized. Furthermore the λ_i^2 are eigenvalues of the reduced density matrices $\rho_{A/B}$. Indeed, the reduced density matrix is defined as $\rho_{A/B} = \text{Tr}_{A/B}(|\psi\rangle\langle\psi|)$. Therefore, the Schmidt values are directly related to the amount of entanglement between part A and B as can be quantified with the von Neumann entanglement entropy

$$S_{\text{vN}}(|\psi_{AB}\rangle) = -\text{Tr}(\rho_{A/B} \log \rho_{A/B}) = -\sum_i \lambda_i^2 \log \lambda_i^2. \quad (2.5)$$

Notice that for a bipartite pure state, it does not matter which reduced-density matrix ρ_A or ρ_B we consider for the computation of S_{vN} . This is logic as for a pure state these quantum correlations between part A and B , are the *only* correlations. We will see in the next chapter that this is not true for mixed states.

For a bipartite product state, there is only one $\lambda_i = 1$, the others are zero. Therefore $S_{\text{vN}}(|\psi_{AB}\rangle) = 0$ as expected.

The von Neumann entanglement entropy is a proper entanglement measure or so-called *entanglement monotone*, meaning that it satisfies all required properties a good entanglement measure should have (these properties are listed in the review article Ref. [62]). A necessary requirement is invariance to actions that fall into the class of [local operations and classical communication \(LOCC\)](#), which particularly implies that it must be constant under all local unitary rotations

$$S_{\text{vN}}(|\psi_{AB}\rangle) = S_{\text{vN}}(U_1 \otimes U_2 \otimes \cdots \otimes U_L |\psi_{AB}\rangle). \quad (2.6)$$

2.1.3 Other entanglement measures

Apart from the von Neumann entanglement entropy we have discussed in the previous section, there are other entanglement measures that could be used to quantify the amount of entanglement in pure states. The most widely used alternative quantities are the Rényi entanglement entropies that are defined on powers of the reduced density matrices

$$S_n(|\psi_{AB}\rangle) = \frac{1}{n-1} \text{Tr} \log(\rho_{A/B}^n). \quad (2.7)$$

For all powers $n > 0$, the Rényi entropies are entanglement monotones. One can find back the von Neumann entanglement entropy by taking the limit $n \rightarrow 1$.

Another widely used quantity that is directly based on the von Neumann entropy, but however is not an entanglement monotone, is the [mutual information \(MI\)](#). It is defined with respect to two non-complementary subsystems A_1 and A_2 of $|\psi\rangle$, we will denote the rest of the system as B

$$I(A_1 : A_2) = S(A_1) + S(A_2) - S(A_1 \cup A_2). \quad (2.8)$$

Here we used the shorthand notation $S(A_1) = S_{\text{vN}}(|\psi_{A_1, A_2 \cup B}\rangle)$. Intuitively, it forms a measure to quantify the amount of correlations between A_1 and A_2 by first summing over their separate correlations with the full system and then subtracting their joint correlations with the rest of the system. There are also Rényi versions of the [MI](#), but no power n will correspond to an entanglement monotone.

We further note that if we want to ask for the amount of quantum correlations between the non-complementary subsystems A_1 and A_2 of $|\psi\rangle$, we actually want to quantify correlations in the bipartite density matrix

$$\rho_{A_1 A_2} = \text{Tr}_B(|\psi\rangle\langle\psi|). \quad (2.9)$$

However as this will be generically a *mixed* state, referring to the fact that there are also classical correlations present, we must find a way to filter out the quantum correlations. It is however not an easy task to define a proper entanglement monotone in this case. We will delay the discussion of entanglement measures that are applicable to bipartite density matrices to the next Chapter [3](#) where we will discuss open quantum systems.

In Chapter [7](#), we will use the discussed pure state quantities to investigate the entanglement content of fundamental excitations.

2.2 Quantum thermalization

In this section we will introduce the concept of quantum thermalization [[23](#), [55](#), [63](#)]. In a closed quantum system time-evolution is unitary. Indeed, the time-dependent Schrödinger equation is given by

$$\frac{d|\psi(t)\rangle}{dt} = -iH(t)|\psi(t)\rangle, \quad (2.10)$$

and the Hamiltonian is a hermitian operator. For a time-independent Hamiltonian, we can expand the time-evolution operator in its eigenbasis

$$|\psi(t)\rangle = e^{-iHt}|\psi(0)\rangle = \sum_n c_n e^{-iE_n t} |n\rangle, \quad (2.11)$$

with c_n the basis-expansion coefficients of the initial state $|\psi(0)\rangle = \sum_n c_n |n\rangle$. So, under time evolution each coefficient acquires a phase that is set by the corresponding energy eigenvalue. Therefore the probability of measuring the system in an eigenstate $|n\rangle$, $p_n = |c_n|^2$, remains constant over time. So at first sight it might seem that thermalization can simply not occur, as everything is fixed by the arbitrary choice of initial coefficients c_n .

However, the crucial point here is that thermalization is not something that is ‘visible’ on the state as a whole. Rather, one should look at how *physical observables* behave in the long-time limit under evolution with a *physical* Hamiltonian, when starting from a *physical* initial state. Then, we say that a system is thermalizing when the observables reach expectation values set by the *micro-canonical statistical ensemble*

$$\langle O \rangle_\infty = \lim_{T \rightarrow \infty} \frac{1}{T} \int_0^T dt \langle \psi(t) | O | \psi(t) \rangle \simeq O^{\text{mc}}(E), \quad (2.12)$$

where E is the energy of the state. In the thermodynamic limit, an equivalent statement would be that the steady state of the system is *locally* equal to a Gibbs ensemble

$$\rho^{[\text{st.st.}]} = \lim_{L \rightarrow \infty} \rho^{[\text{sys}]}(t \rightarrow \infty) \stackrel{\text{loc.}}{=} \rho^{[\text{Gibbs}]} = \frac{e^{-H/T_{\text{eff}}}}{\text{Tr}(e^{-H/T_{\text{eff}}})}. \quad (2.13)$$

Here we call two density matrices locally equivalent if the reduced density matrices for all finite size subsystems A are equal, i.e.

$$\text{Tr}_{|B| \rightarrow \infty}(\rho^{[\text{st.st.}]}) = \text{Tr}_{|B| \rightarrow \infty}(\rho^{[\text{Gibbs}]}) \Rightarrow \rho^{[\text{st.st.}]} \stackrel{\text{loc.}}{=} \rho^{[\text{Gibbs}]}, \quad (2.14)$$

with B the complement of A . Here the density matrix of the system is given by

$$\rho^{[\text{sys}]}(t) = |\psi(t)\rangle \langle \psi(t)| = \sum_{m,n} c_m c_n^* e^{-i(E_m - E_n)t} |m\rangle \langle n|, \quad (2.15)$$

and the effective temperature in Eq. (2.13) is set by the energy of the system

$$\lim_{L \rightarrow \infty} \frac{1}{L} \text{Tr}(\rho^{[\text{Gibbs}]} H) = \lim_{L \rightarrow \infty} \frac{1}{L} \text{Tr}(\rho^{[\text{sys}]}(0) H). \quad (2.16)$$

As mentioned in the introduction, we are mostly interested in quench setups. In this context, a physical initial state would usually mean a product state, as they can be easily prepared in experiments and (generically) have overlaps with an extensive number of eigenstates. On the other hand highly excited eigenstates contain mostly large amounts of entanglement. Therefore they are considered as unphysical initial states, because they would require inaccessibly long preparation times. Physical observables and Hamiltonians mean in this context that they are local. More precisely this means that the observables, and the operators that are contained the Hamiltonian, only act on a finite number of lattice sites around a certain lattice site i .

The notion of quantum thermalization (2.12) is further refined by the eigenstate thermalization hypothesis, which we discuss below.

2.2.1 The eigenstate thermalization hypothesis

As the name suggests the [eigenstate-thermalization hypothesis \(ETH\)](#) makes assumptions about the matrix elements of local observables in the eigenbasis of the system’s Hamiltonian H at sufficiently long times. If O is a physical observable (in this context physical again means local), the time average also used in Eq. (2.12) is also given by

$$\langle O \rangle_\infty = \lim_{T \rightarrow \infty} \frac{1}{T} \int_0^T dt \langle \psi(t) | O | \psi(t) \rangle = \sum_n p_n \langle n | O | n \rangle. \quad (2.17)$$

Notice that the terms containing off-diagonal matrix elements $\langle m|O|n\rangle$ are not contained in the final expression because they carry a phase and hence average out.

However, as the $p_n = |c_n|^2$ are fixed, a way to ensure thermalization of the system according to Eq. (2.12) is to *assume* that the expectation values of physical observables in an *individual eigenstate* $\langle n|O|n\rangle$ obey the micro-canonical ensemble, i.e.

$$\langle n|O|n\rangle \simeq O^{\text{mc}}(E_n). \quad (2.18)$$

This assumption has been proposed in Refs. [53, 54] and is known as the **ETH**.

In practice, we are mostly interested in quench setups where we want to know that late-time expectation value $\langle O\rangle_\infty$ when we start from a physical initial state. However, for these states the probabilities p_n will be highly likely centred around a certain energy \bar{E} , such that effectively $\langle O\rangle_\infty \simeq O^{\text{mc}}(\bar{E})$. Of course, this is just the final step: one could also be very interested in describing the approach towards these equilibrium values, as well as making sure that the temporal fluctuations are bound. For this we do need further information about the off-diagonal matrix elements of O in the eigenbasis. In 1999, M. Srednicki introduced the following ansatz in Ref. [64], which ensures thermalization of local observables as well as bounded fluctuations

$$\langle m|O|n\rangle \simeq O^{\text{mc}}(\bar{E})\delta_{mn} + e^{-S_{\text{th}}(\bar{E})/2}R_{mn}f(\omega, \bar{E}). \quad (2.19)$$

The average energy is here simply given by $\bar{E} = \frac{E_m + E_n}{2}$, while the frequency is given by the energy difference $\omega = E_m - E_n$. $S_{\text{th}}(\bar{E})$ is the microcanonical ‘thermodynamic’ entropy and R_{mn} is a random number drawn from a Gaussian distribution. Finally, $f(\omega, \bar{E})$ is just a smooth function that is dependent on O . So the **ETH** in the form of Eq. (2.19) contains (2.18), as the off-diagonal matrix elements vanish exponentially fast with the average-energy entropy (up to a random prefactor and an observable dependent function).

We end this section by discussing some direct consequences of the **ETH** on the entanglement properties of thermalizing eigenstates. As Eq. (2.19) illustrates, all observables acting within a sufficiently small subsystem A of the eigenstate $|n\rangle$ (that is obeying the **ETH**), will have thermal expectation values. As we have seen, this also implies that the reduced density matrix of the subsystem ρ_A will be a *thermal* density matrix, with the temperature set by eigenenergy. Therefore the we also have that

$$S_{\text{vN}}(A) = S_{\text{th}}(A; E). \quad (2.20)$$

As the thermodynamic entropy is extensive this implies that eigenstates obeying the **ETH** (highly excited eigenstates) obey a *volume-law* entanglement scaling, meaning that the entropy scales with the volume of the subsystem A .

In the next section, we will discuss many-body localized systems for which the **ETH** is believed to be broken. For those systems the entanglement entropy of the eigenstates scales very differently.

2.3 Thermalization breaking mechanisms

In this section we discuss two classes of systems that break the framework of eigenstate thermalization. The first class are integrable systems which are characterized by the existence of extensively many local conserved charges. The second class are **many-body localized** (**MBL**) systems, in which due to the presence of strong disorder so-called **local integrals of motion** (**LIOMs**) emerge.

2.3.1 Integrability

Integrable models are characterized by the presence of extensively many *locally* conserved charges [56]. Although they exist both on the lattice and in the continuum, non-trivial ones exist only in *one dimension*. On the lattice, paradigmatic examples include the [transverse-field Ising \(TFI\)](#) and XY chains which can be mapped to free fermions, and the XXZ and (one-dimensional) Fermi-Hubbard model [65, 66]. In the continuum the most famous integrable theories include the Lieb-Liniger model, free relativistic field theories like Luttinger and Klein-Gordon, and massive relativistic field theories like sine-Gordon. In Chapter 8, we will investigate an emergent lattice realization of the latter.

It is very important to stress the locality property of the conservation laws in integrable models. Indeed, one can easily realize that in fact *every* Hamiltonian has many *non-local* conserved charges. For example the expectation values of the projectors on the eigenstates of the Hamiltonian are conserved

$$H|n\rangle = E_n|n\rangle, P_n = |n\rangle\langle n| \quad \text{then} \quad [H, P_n] = 0, \text{ and } [P_m, P_n] = 0, \quad (2.21)$$

but these are clearly non-local operators. Similarly, expectation values of arbitrary powers of the Hamiltonian are conserved as well, but these contain however sums over highly non-local operators.

We consider a system described by a Hamiltonian H that is having an extensive number of local conservation laws $I^{(n)}$. We note that in practice we also mean with this that the operators $I^{(n)}$ can contain extensive *sums of local operators*. In any case, we need to have that

$$[H, I^{(n)}] = 0. \quad (2.22)$$

It is usually assumed that these operators are mutually commuting $[I^{(m)}, I^{(n)}] = 0$, there are however integrable exceptions known, but these are not relevant for this discussion. Just the bare fact of the existence of an extensive number of these conservation laws in integrable systems, versus $\mathcal{O}(1)$ in non-integrable systems, implies that eigenstate thermalization does not happen. So Eq. (2.18) does not hold for integrable systems. However, this does not mean that the long-time average (2.12) cannot not be described by an ensemble average. It will just need to be a type of *generalized* ensemble that takes into account all those non-trivial conserved quantities. The principle of maximal entropy [67] implies that the steady-state is given by a [generalized Gibbs ensemble \(GGE\)](#) [68]

$$\rho^{[\text{GGE}]} = \frac{e^{-\sum_n \lambda_n I^{(n)}}}{\text{Tr}\left(e^{-\sum_n \lambda_n I^{(n)}}\right)}, \quad (2.23)$$

here λ_n are Lagrange multipliers that should be determined by the initial conditions, i.e. such that $\text{Tr}\left(I^{(n)}\rho^{[\text{GGE}]}\right)$ is equal to the expectation value of $I^{(n)}$ in the initial state.

The presence of an extensive number of locally conserved charges in integrable models has also profound consequences on the structure of the Hilbert space, and hence on all types of dynamics occurring in these models. In particular, elementary excitations can not be created nor annihilated during scattering events, as this would create or destroy charges. Even more drastically, the momenta of the quasiparticles can not

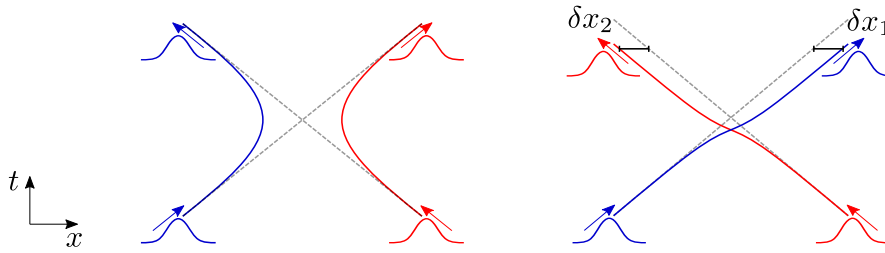


Figure 2.1 Wave-packet scattering in integrable models is subjected to strong constraints. On the left, we show a forbidden event where the particles are reflected, and hence change momentum. On the right, we show an allowed event. Here the momenta of the particles do not change. However, interactions between the particles result in spatial scattering displacements.

be transferred either. In a non-integrable model we just need to satisfy energy and momentum conservation

$$\begin{cases} k_1 + k_2 = k'_1 + k'_2 \\ E_1(k_1) + E_2(k_2) = E_1(k'_1) + E_2(k'_2) \end{cases} \quad (2.24)$$

where k'_i denotes the outgoing momentum, and E_i the dispersion relation of the i th particle. If the dispersion relation of the two particles are *different*, there is generically a momentum transfer expected. However, for integrable models this set of equations needs to be extended with *all* conserved charges. As the $I^{(n)}$ contain an extensive sum of local operators they must act additively on two distant wave packets, hence like the energy we have that,

$$I_1^{(n)}(k_1) + I_2^{(n)}(k_2) = I_1^{(n)}(k'_1) + I_2^{(n)}(k'_2), \quad \forall n. \quad (2.25)$$

Here $I_i^{(n)}$ denotes the action of the conserved charge on the i th particle. It is clear that (2.24) combined with an extensive number of (2.25) can not have solutions other than the trivial one $k'_i = k_i$, unless some extremely rare constraints are imposed. This holds also true for scattering events that involve more than two particles, as they can always be decomposed into two-body events.

Hence, the momenta of two quasi-particles in an integrable scattering process can not change. Therefore an event as sketched in Fig. 2.1 (left) that would be kinematically allowed in a non-integrable model, is forbidden. However integrable theories can still be *interacting*, and during a scattering event these interactions can only result in spatial scattering displacements as illustrated in Fig. 2.1 (right). These displacements are governed by the S -matrix of the theory that describes how two fundamental quasiparticles interact.

In Sec. 8.4 we will discuss integrable scattering events in the context of an emergent lattice realization of the sine-Gordon model. We will numerically extract scattering displacements and compare them to the analytic results of the exact theory.

2.3.2 Many-body localization

Many-body localization is believed to also form a robust mechanism to avoid quantum thermalization. It is achieved by adding *strong disorder* to an *interacting* quantum system. Here, we will only consider one-dimensional systems. The existence of an [MBL](#)

regime in higher dimensional systems is an active field of research. Review articles can be found in Refs. [23, 69, 70]. The paradigmatic model of a system that exhibits an MBL phase is the disordered XXZ spin chain

$$H = J \sum_{i=1}^{L-1} \left(S_i^x S_{i+1}^x + S_i^y S_{i+1}^y + \Delta S_i^z S_{i+1}^z \right) + \sum_{i=1}^L h_i S_i^z, \quad (2.26)$$

where $S_i^{x,y,z}$ are the spin-1/2 operators, and the h_i 's are local disorder potentials randomly and uniformly drawn from the interval $[-W, W]$. As a function of disorder strength W , there is a *dynamical* phase transition between a thermalizing and an MBL phase. This phase transition is called dynamical because *all* eigenstates are subjected to it, and because it does not possess any signatures in thermodynamic quantities. We also note that the model (2.26) can be transformed by the Jordan-Wigner transformation

$$\begin{cases} S_i^+ = e^{-i\pi \sum_{k=0}^{i-1} n_k} c_k^\dagger \\ S_i^- = e^{i\pi \sum_{k=0}^{i-1} n_k} c_k \\ S_i^z = n_i - 1/2 \end{cases} \quad (2.27)$$

into the following model for spinless fermions (up to constants)

$$H = t \sum_{i=1}^{L-1} \left(c_i^\dagger c_{i+1} + \text{h.c.} \right) + V \sum_{i=1}^{L-1} n_i n_{i+1} + \sum_{i=1}^L h_i n_i, \quad (2.28)$$

where c_i^\dagger, c_i are the fermionic creation and annihilation operators, thus obeying anti-commutation relations $\{c_i^\dagger, c_j\} = \delta_{ij}$, and $n_i = c_i^\dagger c_i$. Hence the nearest-neighbor zz coupling transforms into a nearest neighbor interaction $\Delta J = V$. Therefore, if $\Delta = 0$ the model is non-interacting: in that case a *finite* amount of disorder is sufficient to make the model *single-particle* or *Anderson* localized [71, 72].

In the interacting case, there is numerical evidence that the MBL transition occurs around a critical W_c [22]. However, estimating W_c from small-scale numerics is challenging. The MBL phase is characterized by the absence of transport and by Poissonian level-spacing statistics [22].

In what follows, we will further summarize some properties of many-body localized systems. We will also introduce the concept of **local integrals of motion (LIOMs)** which allows one to construct a phenomenological model of MBL which captures the main features. The existence of these LIOMs suggests an emergent integrability of MBL systems, and it is indeed this emergent integrability that explains the lack of thermalization in MBL systems.

However there are some crucial differences with respect to the integrability discussed in the previous section. First, we will see that the integrals of motion of MBL systems are *quasi-local* operators. While in integrable systems, as we have seen, the integrals of motion are extensive sums of *local* operators. Second, the MBL phase is robust under perturbations. Therefore a slightly different set of LIOMs can still be defined after the perturbation has been applied. On the contrary, integrable models are less robust under perturbations, and they usually should be seen as isolated points in the parameter space of the Hamiltonian. For example, the XXZ spin chain (2.26) without disorder, is integrable. However, the addition of a small amount of disorder breaks its integrability,

and the model appears to thermalize in the conventional way unless the disorder is sufficiently large to enter the [MBL](#) regime.

Local integrals of motion and logarithmic entanglement growth

Now we will turn towards the dynamical properties of isolated [MBL](#) systems. Here it is most important to understand what is happening in a quench protocol, that usually starts from a simple product state such as a Néel state. The key dynamical feature here is a slow, logarithmic, growth of entanglement [26–28], that should be contrasted to a fast ballistic growth under a thermalizing Hamiltonian [52]. Such dynamics originates from the fact that the eigenstates of a many-body localized Hamiltonian do not carry a high amounts of entanglement [73, 74]. Indeed, as localization is usually defined from exponentially decaying tails of the single-particle wave functions, there can be a *localization length* ξ associated with the state. The existence of such a localization length, implies that correlations will also decay very quickly over distances larger than ξ , implying so-called *area-law* entanglement in the eigenstates.

Due to these quickly decaying correlations, the eigenstates of an [MBL](#) Hamiltonian can be associated with product states in a different basis obtained by *quasi-local* unitary transformations [23]. We say that a unitary transformation is quasi-local when it can be decomposed into a network with layers of 2-site, 3-site, 4-site, \dots and n -site unitary gates, and the higher n , the exponentially closer the n th gates are to the identity,

$$U = \prod_i \dots U_{i,i+1,i+2}^{(3)} U_{i,i+1}^{(2)} \quad \text{with} \quad \left\| \mathbb{1} - U_{i,i+1,\dots,i+n}^{(n)} \right\| < e^{-n/\xi}. \quad (2.29)$$

For eigenstates of a thermalizing Hamiltonian, the transformation which diagonalizes the Hamiltonian is highly non-local and cannot be decomposed in such way.

For [MBL](#) systems, a transformation of the form of Eq. (2.29) takes the physical spin operators into related spin operators $\tau_i = U^\dagger \sigma_i^z U$, and therefore these τ -spin operators can be expanded as

$$\tau_i^z = a \sigma_i^z + \sum_n b_i^n O_i^{\{n\}}, \quad (2.30)$$

where the coefficient a characterises the overlap with the physical spin operators. The operators $O_i^{\{n\}}$ contain a sum of operators that act on a distance n from site i , but the coefficients b_i^n in front decay exponentially with distance set by the localization length $b_i^n < e^{-n/\xi}$. The τ -operators are called [LIOMs](#) [75–77], first because of their clearly localized nature, and second, and more importantly, because the Hamiltonian of an [MBL](#) system can be effectively transformed into the universal form

$$H_{\text{MBL}} = \sum_i h_i \tau_i^z + \sum_{i>j} J_{ij} \tau_i^z \tau_j^z + \sum_{i>j>k} J_{ijk} \tau_i^z \tau_j^z \tau_k^z \dots, \quad (2.31)$$

where the couplings decay exponentially with distance, i.e. $J_{ij} \simeq J_0 e^{-|i-j|/\xi'}$, $J_{ijk} \simeq J_0 e^{-|i-k|/\xi'}$. This Hamiltonian is thus diagonal in the τ basis and therefore all the τ 's are indeed integrals of motion $[H, \tau_i^z] = 0$, and their products as well. The picture behind this Hamiltonian is that the τ -spins dephase in a magnetic field that is set by all other spins, but the farther the other spins are the exponentially fewer they influence. This seemingly simple picture directly helps to understand some key dynamical features of

MBL systems and we will also use it explicitly in Sec. 5.2.1. As mentioned before, one of those key dynamical features is a logarithmic growth of entanglement, and Eq. (2.31) can explain this non-trivial dynamics if the initial state is in a superposition of eigenstates.

If we start by only considering two spins in the τ -spin basis initialized as $|\psi_0\rangle = |++\rangle$ with $|+\rangle = (|\uparrow\rangle + |\downarrow\rangle)/\sqrt{2}$, and consider their evolution with the lowest-order coupling term of the Hamiltonian (2.31), we obtain that

$$|\psi(t)\rangle = e^{-iJ_{01}t}(|\uparrow\uparrow\rangle + |\downarrow\downarrow\rangle)/2 + e^{iJ_{01}t}(|\uparrow\downarrow\rangle + |\downarrow\uparrow\rangle)/2. \quad (2.32)$$

The reduced density matrix of a single qubit is therefore given by

$$\rho_{1/2} = (|\uparrow\rangle\langle\uparrow| + |\downarrow\rangle\langle\downarrow|)/2 + \cos(2J_{01}t)(|\uparrow\rangle\langle\downarrow| + |\downarrow\rangle\langle\uparrow|)/2, \quad (2.33)$$

with eigenvalues $\lambda_{\pm} = \frac{1}{2} \pm \frac{\cos(2J_{01}t)}{4}$. Hence at times $J_{01}t = \pi/4$ we build up a maximal entanglement of $\log 2$.

While in Sec. 5.2.1 we will generalize another entanglement quantity to the many-body case by summing over the two-particle contributions and averaging over the distribution of couplings J_{01} , there is a simpler argument to see the logarithmic growth in the many-body system directly from Eq. (2.31) [23, 78]. Under time-evolution, a τ -spin τ_i acquires a phase that is dependent on the state of another τ -spin τ_{i+d} that is a distance d away from the given spin. This phase is given by the operator

$$\varphi(t, d) = t \underbrace{\left(J_{i, i+d} + \sum_{j \in [i, i+d]} J_{i, j, i+d} \tau_j + \dots \right)}_{\tilde{h}_{i, i+d}}. \quad (2.34)$$

Notice here that the value of this phase also depends on all the other τ -spins located between i and $i+d$. Notice as well that this phase does not depend on the static fields, they indeed do not generate any entanglement between the spins. However, we can say that the spins have become entangled if the phase becomes of order one. This happens at time

$$t(d) \simeq 1 / \langle \tilde{h}_{i, i+d} \rangle. \quad (2.35)$$

All the couplings appearing in appearing in Eqs. (2.31) and (2.34) decay exponentially with distance. Therefore, it can be shown that the prefactor of the total effective magnetic field $\tilde{h}_{i, i+d}$ will also decay exponentially with distance $\langle \tilde{h}_{i, i+d} \rangle \propto J_0 e^{-d/\kappa}$, however with a slightly different exponent κ . Therefore the time it takes to entangle the two spins at a distance d is given by $tJ_0 = e^{d/\kappa}$, and the light cone of entanglement only grows logarithmically in time

$$d = \kappa \log(J_0 t). \quad (2.36)$$

The entanglement entropy can maximally grow with the volume of this light cone, directly implying that it also grows logarithmically in time.

In Chapter 5, we will consider the entanglement dynamics of an MBL system that is coupled to an environment that causes the system to dephase. In the next Chapter 3, we will summarize the relevant dynamics of mixed states and their entanglement measures.

Wannier-Stark many-body localization

Recently it has been observed that a tilted potential, instead of strong disorder, can also lead to non-thermalizing dynamics [60, 61, 79, 80]. This phenomenon which we will refer to as Wannier-Stark MBL, in the literature sometimes also shortly called Stark MBL, is the extension of non-interacting Wannier-Stark localization [81] to interacting systems.

If the tilt is purely linear, the dynamics starting from an initial separable state, is quite special: initially the entanglement entropy shows a very strong growth which is followed by a slower growth [61]. This type of dynamics can be traced back to the fact that there are many exact degeneracies in the non-interacting case [61]. However, these degeneracies can be lifted by the addition of a quadratic perturbation to the linear tilt, then the on-site potentials in Eq. (2.26) are given by

$$h_i = -\gamma i + \alpha i^2 / (L - 1)^2. \quad (2.37)$$

In that case a long-time logarithmic growth of the entanglement can be observed [2] [61, 80]. In this respect see also Chapter 6, where we will investigate the entanglement dynamics of such a Wannier-Stark MBL system and couple it to a dephasing environment. Instead of adding a quadratic perturbation to a linear tilt, Ref. [60] also reports clear features in the level spacing statistics when there is a small amount of disorder present, in addition to the linear tilting potential.

3 Open quantum systems: dynamics and entanglement

In this chapter, we will discuss properties of systems that are coupled to an environment. These *open* quantum systems are fully described by a density matrix or *mixed* quantum state.

This chapter is organized as follows. In Sec. 3.1 we describe basic properties of density matrices and the most generic evolution they can undergo via quantum channels. In Sec. 3.2, we describe dynamics governed by interactions of the system with a *Markovian* environment, in addition to the usual unitary dynamics set by the Hamiltonian of the system. We derive the evolution equation describing this type of dynamics, the *Lindblad master equation*, which can be seen as an analogue to the Schrödinger equation for mixed states. However, in contrast to the Schrödinger equation, the Lindblad equation is describing non-unitary dynamics. In Sec. 3.3 we discuss bipartite entanglement measures for mixed states. Unlike the entanglement entropy for pure states, there is no such ‘perfect’ measure for quantum entanglement in this case. Rather there exist several imperfect criteria, and depending on the specific problem one has to choose the one that is the most suited. We will also introduce the Rényi negativity as a bipartite entanglement proxy, which we will use intensively in the next Chapters 5 and 6.

3.1 Properties of density matrices and quantum channels

An open quantum system can always be described as a subsystem (i.e. a reduced density matrix) of a larger, *pure* quantum system. If we only have access to the degrees of freedom of the subsystem, the other degrees of freedom are simply ‘traced’ away. Therefore, the subsystem is indeed described by a reduced density matrix, i.e. an operator living in the operator Hilbert space of the subsystem. Dynamics within this operator space is generically not unitary, and also measurements are no longer orthogonal projections.

In Chapter 2 we have already introduced the reduced density matrix in the context of bipartite pure quantum systems. There the goal was to quantify the amount of entanglement between the two partitions. In this context, we will assume that partition A corresponds to the system, while partition B corresponds to the environment, and $|\psi\rangle_{AB}$ is the joint system. However, here we only have access to the degrees of freedom of part A . Therefore, the accessible observables will have the form $O_A \otimes \mathbb{1}_B$, and we have that

$$\begin{aligned}
\langle O_A \rangle &= \langle \psi_{AB} | O_A \otimes \mathbb{1}_B | \psi_{AB} \rangle \\
&= \sum_{\substack{s_A, s_B \\ s'_A, s'_B}} \psi_{s'_A, s'_B}^* \psi_{s_A, s_B} (\langle s_A | \otimes \langle s_B |) (O_A \otimes \mathbb{1}_B) (|s'_A\rangle \otimes |s'_B\rangle) \\
&= \sum_{s_A, s'_A, s_B} \psi_{s'_A, s_B}^* \psi_{s_A, s_B} \langle s_A | O_A | s'_A \rangle \\
&= \text{Tr}(O_A \rho_A),
\end{aligned} \tag{3.1}$$

where we have used the basis expansion Eq. (2.3). Here, we called ρ_A the (reduced) density matrix of the system A

$$\rho_A = \sum_{s_A, s'_A, s_B} \psi_{s'_A, s_B}^* \psi_{s_A, s_B} |s'_A\rangle \langle s_A| \equiv \text{Tr}_B(|\psi_{AB}\rangle \langle \psi_{AB}|). \tag{3.2}$$

Notice that if we had used the decomposition in the Schmidt basis, see Eq. (2.4), we would have directly ended up with a diagonal density matrix

$$\rho_A = \sum_i \lambda_i^2 |i_A\rangle \langle i_A|. \tag{3.3}$$

From the definitions Eqs. (3.2) and (3.3) we can directly read-off the following properties of density matrices:

- (i) ρ_A is hermitian $\rho_A^\dagger = \rho_A$;
- (ii) ρ_A is positive $\langle \phi | \rho_A | \phi \rangle \geq 0 \forall |\phi\rangle$;
- (iii) ρ_A is normalized $\text{Tr}(\rho_A) = \sum_{s_A, s_B} |\psi_{s_A, s_B}|^2 = 1$ as $|\psi_{AB}\rangle$ was originally normalized to $\langle \psi_{AB} | \psi_{AB} \rangle = 1$.

The next step would be describing dynamics: if the evolution of the complete system AB is unitary, how is part A then evolving? If we assume that the environment B is initialized in the state $|0_B\rangle$, irrespective of the state of the system (so they are not entangled), then the effect of any unitary acting on the whole system can be described as [37]

$$U(|\psi_A\rangle \otimes |0_B\rangle) = \sum_\alpha M_\alpha |\psi_A\rangle \otimes |\alpha_B\rangle. \tag{3.4}$$

The conservation of the norm of the input state translates into the condition

$$\sum_\alpha M_\alpha^\dagger M_\alpha = \mathbb{1}. \tag{3.5}$$

If we then want to ask the question of how ρ_A evolves, all we in principle need to do is tracing out the degrees of freedom of the B part in Eq. (3.4). This results in a linear mapping acting on $\rho_A = |\psi_A\rangle \langle \psi_A|$

$$\mathcal{E}(\rho_A) = \sum_\alpha M_\alpha \rho_A M_\alpha^\dagger. \tag{3.6}$$

This linear mapping is called a *quantum channel* and it is the most generic evolution a density matrix can undergo. This terminology comes originally from quantum communication theory: the idea is that one party sends the state ρ_A through a communication

channel \mathcal{E} to another party, who receives $\mathcal{E}(\rho_A)$. In our context, we will mostly refer to \mathcal{E} as a type of *superoperator*, i.e. a mapping which maps operators to operators. The operators M_α in Eq. (3.6) are called Kraus operators, and they are not unique in representing a specific channel [37, 82]. Indeed, the trace over the environment B in Eq. (3.4) can be performed in any basis of B , it does not need to be the basis where A and B are initially not entangled. If we make a unitary basis transformation

$$\sum_{\alpha,\gamma} M_\alpha |\psi_A\rangle \otimes |\gamma_B\rangle V_{\gamma\alpha} = \sum_{\gamma} N_\gamma |\psi_A\rangle \otimes |\gamma_B\rangle, \quad (3.7)$$

the Kraus operators undergo the same transformation $N_\gamma = \sum_{\alpha} V_{\gamma\alpha} M_\alpha$.

Of course, in addition to being linear, a quantum channel must also map density matrices into density matrices. Therefore it must be a *trace-preserving completely positive* map [37, 82], meaning that it must preserve the positivity, hermiticity and the trace of the density matrix. However the channel has a stronger requirement than positivity, it must be *completely positive*.

Complete positivity means that the channel must remain positive even when it is only acting on a partition of a larger system. More precisely, if \mathcal{E} is a quantum channel acting on a density matrix living in the (operator) Hilbert space \mathcal{H}_A , then any extension of the mapping acting on an enlarged Hilbert space $\mathcal{H}_A \otimes \mathcal{H}_B$ of the form $\mathcal{E} \otimes \mathbb{1}_B$ must also be positive.

In this context, it is important to note that not all relevant positive maps are completely positive. A very important example of a positive, but not completely positive, mapping is *transposition*. It will arise in the context of the Peres-Horodecki criterion later on (see Sec. 3.3). The transposition operator T simply acts as

$$T(|m\rangle \langle n|) = |n\rangle \langle m|, \quad (3.8)$$

and is clearly a positive mapping as indeed

$$\langle \psi_A | \rho_A^T | \psi_A \rangle = \langle \psi_A^* | \rho_A | \psi_A^* \rangle = \sum_i \lambda_i^2 |\langle \psi_A^* | i_A \rangle|^2 \geq 0 \quad (3.9)$$

where we have used the diagonal form of Eq. (3.3), and $|\psi_A\rangle \in \mathcal{H}_A$. However this mapping is not completely positive. Indeed, if we consider the two-qubit Bell pair,

$$|\psi\rangle = \frac{1}{\sqrt{2}} (|01\rangle + |10\rangle), \quad (3.10)$$

for which the density matrix is given by

$$|\psi\rangle \langle \psi| = \frac{1}{2} (|01\rangle \langle 01| + |10\rangle \langle 01| + |01\rangle \langle 10| + |10\rangle \langle 10|), \quad (3.11)$$

and as this density matrix obviously belongs to a pure state, it has just one non-zero eigenvalue $\lambda = 1$, while the other three eigenvalues are zero. However, if we now act with the operator $T \otimes \mathbb{1}$

$$(T \otimes \mathbb{1}) |\psi\rangle \langle \psi| = \frac{1}{2} (|01\rangle \langle 01| + |00\rangle \langle 11| + |11\rangle \langle 00| + |10\rangle \langle 10|), \quad (3.12)$$

we immediately note that the off-diagonal elements have been mapped away into different magnetization sectors. Diagonalizing this matrix now yields four non-zero eigenvalues

$$3 \times \frac{1}{2} \text{ and } 1 \times \left(-\frac{1}{2}\right), \quad (3.13)$$

of which one eigenvalue is negative. So we conclude that although the transposition is a positive mapping, see Eq. (3.9), it is not completely positive.

3.2 The Lindblad master equation

We have discussed before that pure-state evolution is unitary, while as discussed in the last section, mixed-state evolution is generically described by a quantum channel. However, it also would be practical to be able to describe the evolution of an open quantum system in an infinitesimally small time interval. We thus ask the question whether there exist an analogue for the Hamiltonian, and for the Schrödinger equation to describe the decoherent evolution of mixed states.

This turns out to be only possible if the evolution of the system is *local in time*. [37] This means that the density matrix $\rho_A(t+dt)$ must be fully determined by $\rho_A(t)$. Equivalently, this means that information cannot be transferred back from the environment to the system. Indeed, if that would be the case, $\rho_A(t+dt)$ cannot be solely dependent on $\rho_A(t)$, but will also depend on earlier times. Such an evolution is called *Markovian* but poses however some important questions: it does not seem physical that information is not allowed to go back to the system. Indeed when there is *dissipation* of the system, there are generically also *fluctuations* in the system, as characterised by the fluctuation-dissipation relations [83]. However it turns out to be all a matter of time scales: if the typical time scale of the dissipation is much larger than the typical time scale in which the environment scrambles the information

$$(\Delta t)_{\text{dissipation}} \gg (\Delta t)_{\text{environment}}, \quad (3.14)$$

a Markovian evolution is a good approximation. From now on we will call $\rho \equiv \rho_A$ as we do not have any explicit information about the environment and follow the derivation of Ref. [37]. Then we have that

$$\rho(t+dt) = \mathcal{E}_{dt}(\rho(t)), \quad (3.15)$$

where \mathcal{E}_{dt} is the quantum channel describing the infinitesimal time evolution. We can expand this up to first order

$$\mathcal{E}_{dt} = \mathbb{1} + dt \mathcal{L} \quad \Rightarrow \quad \frac{d\rho}{dt} = \mathcal{L}(\rho). \quad (3.16)$$

The linear mapping \mathcal{L} that describes the time evolution is known as the *Lindbladian* or *Liouvillian*. This Liouvillian must of course have the structure of a superoperator and take physical operators or density matrices to other physical operators or density matrices. The equation has the following (formal) solution if \mathcal{L} is time independent

$$\rho(t) = \lim_{m \rightarrow \infty} \left(1 + \frac{\mathcal{L}t}{m}\right)^m \rho(0) = e^{\mathcal{L}t} \rho(0). \quad (3.17)$$

The channel must have a Kraus representation

$$\rho(t+dt) = \mathcal{E}_{dt}(\rho(t)) = \sum_{\alpha} M_{\alpha} \rho(t) M_{\alpha}^{\dagger} = \rho(t) + O(dt). \quad (3.18)$$

If this depends only on linear terms in dt , we can assume that M_0 contains all the terms of order dt , while all other M_{α} ($\alpha > 0$) are of the order \sqrt{dt} . Then the Kraus operators M_{α} $\alpha > 0$ describe so-called *quantum jumps*, corresponding to incoherent evolution the

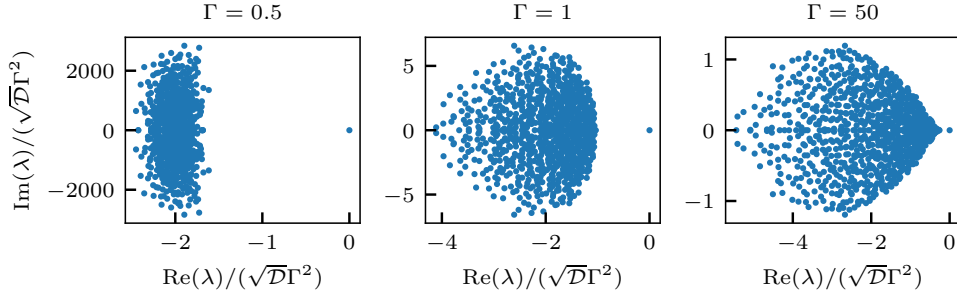


Figure 3.1 The eigenvalues of a random Lindbladian in the complex plane for various dissipation strengths. These plots illustrate the general properties of the eigenvalue spectrum of Lindbladians, i.e. that all eigenvalues come in complex pairs, have a negative real part and there is at least one eigenvalue that is exactly zero. For stronger dissipation strength, the spectrum becomes shaped like a lemon, a finding that stems from Refs. [84, 85].

system might undergo during the time interval dt . So the Kraus operators have the following form (the inclusion of the Hamiltonian H is anticipated)

$$M_0 = \mathbb{1} + (-iH + N) dt, \quad \text{and} \quad M_\alpha = L_\alpha \sqrt{dt}, \quad \alpha > 0, \quad (3.19)$$

where both H and N are both hermitian operators. We can solve for N by using the completeness of the Kraus operators given by Eq. (3.5)

$$\mathbb{1} = \sum_\alpha M_\alpha^\dagger M_\alpha = \mathbb{1} + dt \left(2N + \sum_{\alpha>0} L_\alpha^\dagger L_\alpha \right), \quad (3.20)$$

and therefore

$$N = -\frac{1}{2} \sum_{\alpha>0} L_\alpha^\dagger L_\alpha. \quad (3.21)$$

When we substitute now the Kraus operators of back into the channel (3.18) we get

$$\frac{d\rho}{dt} = \mathcal{L}(\rho) = -i[H, \rho] + \sum_{\alpha>0} \left(L_\alpha^\dagger \rho L_\alpha - \frac{1}{2} \{ L_\alpha^\dagger L_\alpha, \rho \} \right). \quad (3.22)$$

This equation is known as the *Lindblad master equation*: it is the generic evolution equation for density matrices under the condition of Markovianity, and under the condition that time evolution is a trace-preserving completely positive mapping. For a different derivation see Ref. [38].

We end this section with some generic comments about the spectrum of the Lindbladian, when we look at the Lindblad equation as an eigenvalue problem $\mathcal{L}\rho = \lambda\rho$. First if there were no dissipation, all eigenvalues would lie symmetrically on the imaginary axis as the Hamiltonian is hermitian, and correspond to eigenenergy differences of the form $i(E_m - E_n)$. When there is dissipation the eigenvalues acquire a non-zero negative real part $\text{Re} \lambda \leq 0$. Furthermore there is always at least one eigenvalue at the origin $\lambda_0 = 0$, corresponding to the steady state. The requirement that the density matrix must remain Hermitian under the action of the Liouvillian translates into the fact that its eigenvalues are always complex conjugate pairs. The typical time for the system

to reach the steady state is set by the gap $\Delta = \min_{i>0} \text{Re}(-\lambda_i)$, which is set by the eigenvalue with the smallest real part (in absolute value).

Recently, some literature appeared on the characterization of spectral properties of *random* Lindbladian operators [84–86]. The main result here is that the spectrum has the shape of a *lemon* if the dissipation is strong [84, 85]. In Fig. 3.1 we also diagonalized random Lindbladians to highlight this result, together with the general facts stated above. If we work in a Hilbert space of dimension \mathcal{D} , each Lindblad operator can be expanded as [85]

$$L_\alpha = \Gamma \sum_{k=1}^{\mathcal{D}^2-1} G_k v_{k\alpha} \quad (3.23)$$

where the matrices $\{G_k\}$ form an orthogonal and complete basis for the operator space associated with the Hilbert space, where $G_0 \sim \mathbf{1}$ and all the other $G_k, k > 0$ are traceless matrices, so called Gell-Mann matrices, satisfying $\text{Tr}(G_k^\dagger G_l) = \delta_{kl}$. For the data shown, we considered $\mathcal{D} = 30$ and only 2 jump operators, $\alpha = 0, 1$. The Hamiltonian is drawn from a Gaussian unitary ensemble $\sim e^{-\frac{1}{2} \text{Tr}(H^2)}$, and the rectangular matrix v from a Ginibre ensemble $\sim e^{-\frac{1}{2} \text{Tr}(v^\dagger v)}$ as in Ref. [85]. In Fig. 3.1 we show the resulting spectra of the Lindbladian in the complex plane for a couple of different values for Γ . These spectra are similar to the ones shown in Ref. [85].

Importantly, in the special case where the Lindblad operators are all hermitian operators, the identity operator is always an eigenvector corresponding to eigenvalue zero. Hence the infinite temperature state is always a steady state. This can be straightforwardly checked by realizing that $\mathcal{L}(\mathbf{1}) = 0$ with $L_\alpha = L_\alpha^\dagger$. For non-hermitian Lindblad operators, the steady state can however be highly non-trivial, and it is referred to as [non-equilibrium steady state \(NESS\)](#).

3.3 Entanglement of mixed states

If the quantum state is described by a density matrix ρ , we do not know exactly in which state it is. Indeed, in Eq. (3.3) we can interpret the λ_i^2 's as probabilities. So all we know is that the state with probability $p_i = \lambda_i^2 \geq 0$ is in the state $|i\rangle$, where we dropped the subscript A . Now we want to investigate the quantum entanglement of the density matrix. For this we want to consider, similarly as for the pure case, bipartite entanglement, between parts A and B of the density matrix

$$\rho_{AB} = \sum_{\substack{s_A, s_B \\ s'_A, s'_B}} \rho_{s_A s'_A, s_B s'_B} |s_A\rangle \langle s'_A| \otimes |s_B\rangle \langle s'_B|, \quad (3.24)$$

and again we want to ask how much part A is entangled with part B .

If the density matrix can be decomposed as

$$\rho_{AB} = \rho_A \otimes \rho_B, \quad (3.25)$$

this would correspond to applying a basis transformation in Eq. (3.24) resulting in only one non-zero coefficient, then this state would be nothing more than a product state with respect to the cut. Indeed, part A and B of the system are completely uncorrelated.

On the other hand, if a unitary transformation of Eq. (3.24) would result in a diagonal coefficient matrix, we have that

$$\rho_{AB} = \sum_i p_i \rho_A^{(i)} \otimes \rho_B^{(i)}. \quad (3.26)$$

Such a state is called *separable*, meaning that there are correlations present but they are of a classical nature. Indeed such a state can be created by LOCC [37]. By classical communication, A and B can share the outcomes of a random number generator which generates outcomes i with probabilities p_i . For each i , they can then decide to prepare the state $\rho_A^i \otimes \rho_B^i$ locally, hence creating the joint density matrix (3.26). This procedure is very generic and does not create any quantum entanglement between A and B .

In this context, we also note that the set of separable states is convex, as the convex combination of two separable states ρ'_{AB} and $\tilde{\rho}_{AB}$

$$\rho_{AB} = \alpha \rho'_{AB} + (1 - \alpha) \tilde{\rho}_{AB}^{(2)} \quad \text{with } \alpha \in [0, 1] \quad (3.27)$$

is again a separable state.

If a state can not be written in the form of Eq. (3.26), it is not separable. Hence it carries also quantum correlations. A question which naturally arises here is if a certain density matrix is entangled or separable. It turns out that this *separability problem* is actually very complicated, it has been shown to fall into the class of NP hard problems (non-deterministic polynomial-time hardness) [87], and it has not been generally solved. There are however various criteria known that either detect separability or entanglement [62]. In the remainder of this section, we will discuss the most famous of these criteria: the Peres–Horodecki criterion, and the entanglement monotone that follows from this criterion, the negativity. Then we will consider Rényi versions of this quantity, we will see that these are no entanglement monotones but they are more easily computable than the negativity. We will end this section by briefly discussing yet another type of separability criteria, so-called *entanglement witnesses*. They have the property, which can be seen as an advantage or disadvantage, to be dependent on observables.

As a side remark, we mention that naive extensions of pure state entanglement measures to mixed states, such as the von Neumann entropy, are very sensitive to classical correlations. Indeed, the reduced density matrix of part A or B of Eq. (3.26), would give rise to a non-zero von Neumann entropy (except if (3.26) would reduce to (3.25)). However, we have seen that this state is not even entangled over the bipartition, so the von Neumann entropy is clearly not a good measure for mixed-state entanglement.

3.3.1 The Peres–Horodecki criterion and the negativity

Most separability criteria that are known are based either on positive maps or on entanglement witnesses. Here we will start by discussing a very famous separability criterion that is based on a positive map, namely transposition. As we have demonstrated in Sec. 3.1, the transposition map is positive, but not completely positive.

The *Peres–Horodecki criterion* or **PPT** criterion [88] considers a bipartite density matrix and states that

$$\text{if } \rho_{AB} \text{ is separable then } \rho_{AB} \text{ has a positive partial transpose.} \quad (3.28)$$

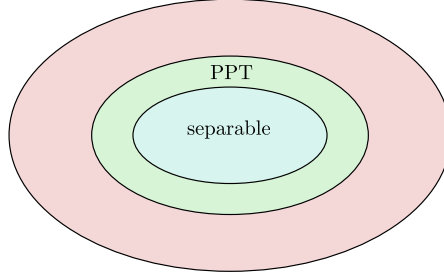


Figure 3.2 In the set of all states, separable states are a convex subset. These are embedded in the larger subset of states that are characterized by a **positive partial transpose (PPT)**. States that are only contained in the red region do not have a **PPT**, and by the negation of (3.28), their entanglement can be detected.

This is illustrated in Fig. 3.2. We say that ρ_{AB} has a **PPT** if

$$\rho_{AB}^{T_A} \geq 0 \Leftrightarrow \rho_{AB}^{T_B} \geq 0, \quad (3.29)$$

where the partial transposition with respect to subsystem B is acting as

$$\rho_{AB}^{T_B} = \sum_{\substack{s_A, s_B \\ s'_A, s'_B}} \rho_{s_A s'_A, s_B s'_B} |s_A\rangle \langle s'_A| \otimes |s'_B\rangle \langle s_B|, \quad (3.30)$$

starting from Eq. (3.24). The proof of (3.28) directly relies on the definition of separability in Eq. (3.26) and is therefore straightforward: the state is separable, so it can be written in the form of Eq. (3.26), therefore

$$\rho_{AB}^{T_B} = \sum_i p_i [\rho_A^{(i)}]^T \otimes \rho_B^{(i)} = \sum_i p_i \tilde{\rho}_A^{(i)} \otimes \rho_B^{(i)} \geq 0. \quad (3.31)$$

The negation of this criterion detects entanglement. For a given density matrix, the computation of the eigenvalues after partial transposition is a well defined procedure. And if this yields any negative eigenvalues, we can conclude that the density matrix carries quantum entanglement. The magnitude of these negative eigenvalues can be used to quantify the amount of entanglement in the density matrix, via an entanglement monotone that is known as the *negativity* [89]

$$\mathcal{N}(\rho_{AB}) = \frac{\|\rho_{AB}^{T_B}\|_1 - 1}{2}. \quad (3.32)$$

Here the trace norm is defined as $\|O\|_1 = \text{Tr} \sqrt{OO^\dagger}$, and is nothing more than a summation over the absolute values of the eigenvalues of the partially transposed density matrix. We note that trace is invariant under partial transposition, which implies that

$$1 = \text{Tr} \rho_{AB} = \text{Tr} \rho_{AB}^{T_B} = \sum_i \lambda_i, \quad (3.33)$$

with λ_i the eigenvalues of the partially transposed density matrix. Therefore the negativity can be rewritten as

$$\mathcal{N}(\rho_{AB}) = \sum_{\lambda_i < 0} |\lambda_i|, \quad (3.34)$$

thus as a summation over negative eigenvalues that arise under partial transposition. We can also define the logarithmic negativity¹ $\mathcal{E}(\rho_{AB}) = \log \|\rho_{AB}^{T_B}\|_1$. The negativity is known as a *computable* measure [89], as it relies on a fixed procedure that is formally defined for any density matrix.

We end this subsection with some remarks. First notice that the negativity is, by definition, not able to detect entanglement in PPT states. Indeed, the observation that a state has a PPT is not sufficient to conclude that a state is not entangled. In general the set of separable states does not fully overlap with the set of PPT states, as illustrated in Fig. 3.2. However, it has been shown that for the special case of 2×2 or 2×3 systems, having a PPT is a sufficient condition for separability [90].

We will compute the negativity in some sections of Chapters 5 and 6 using exact diagonalization for MBL systems. In closed MBL systems the negativity has been studied before in Ref. [91, 92] and has been experimentally measured between two qubits in Ref. [93]. We also note that the dynamics of negativity can be very special. For instance it is known that under some circumstances it can be non-asymptotic, meaning that it can become exactly zero at a finite time. In Sec. 5.5 we will briefly discuss this type of dynamics.

As we have seen above, the negativity relies on the knowledge of the negative eigenvalues of the bipartite density matrix under partial transposition. However, full exact diagonalization of density matrices becomes already prohibitively expensive for systems of ~ 10 qubits. Therefore, it is not such a useful measure in a many-body context. We will now introduce the Rényi negativity as an alternative quantity for larger systems.

3.3.2 The Rényi negativity

Much in the spirit of the Rényi entropies for pure states which have been introduced in Sec. 2.1.3, we can define the Rényi negativities,

$$\mathcal{E}_q(\rho_{AB}) = \log \text{Tr} \left(\rho_{AB}^{T_B} \right)^q. \quad (3.35)$$

These rely on powers of the partially-transposed density matrix, and thus on q copies of this matrix. This so-called replica construction for entanglement negativities has been originally proposed in the context of field theories in Refs. [94–96].

It is very important to notice that unlike the Rényi entropies for pure states, the Rényi negativities for mixed states are not entanglement monotones. For this we will explicitly consider an example in the next subsection 3.3.3. However the moments of the partially transposed density matrix can be used to estimate the negativity as shown in Ref. [97]. It is also easy to see that the analytic continuations of (3.35) are different for even (q_e) and odd (q_o) powers [95]. We have that

$$\lim_{q_e \rightarrow 1} \mathcal{E}_{q_e}(\rho_{AB}) = \mathcal{E}(\rho_{AB}), \quad (3.36)$$

while

$$\lim_{q_o \rightarrow 1} \mathcal{E}_{q_o}(\rho_{AB}) = \log \left(\text{Tr} \rho_{AB}^{T_B} \right) = 0, \quad (3.37)$$

¹Both the logarithmic negativity and quantum channels are denoted by \mathcal{E} in the literature. However confusion should not arise in the context of this thesis.

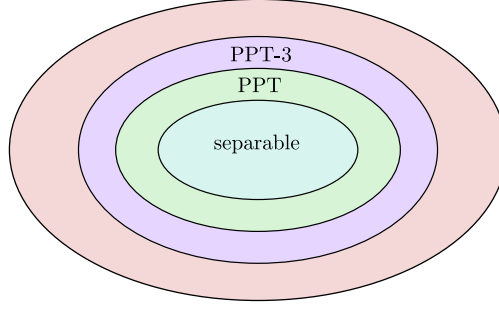


Figure 3.3 The set of **PPT** states is contained in the set of states that satisfy the PPT-3 condition. The set of entangled states that violate the PPT-3 condition is smaller than the set of states that violate the **PPT** condition (3.28) (red part vs. red and purple part).

due to the the normalization of the density matrix.

For pure states, we can work out the powers of the partially transposed density matrix in terms of the reduced density matrix [95]

$$\mathrm{Tr}(\rho_{AB}^{T_B})^q = \begin{cases} \mathrm{Tr} \rho_B^{q_o}, & q_o \text{ odd,} \\ (\mathrm{Tr} \rho_B^{q_e/2})^2, & q_e \text{ even.} \end{cases} \quad (3.38)$$

By taking the limit $q_e \rightarrow 1$, we see that the logarithmic negativity can be linked to the Rényi entropy of order 1/2 for a pure state [95]

$$\mathcal{E}(|\psi\rangle) = 2 \log(\mathrm{Tr} \rho_B^{1/2}) = S_{1/2}. \quad (3.39)$$

As entanglement proxy we will consider

$$R_q(\rho_{AB}) = -\log\left(\frac{\mathrm{Tr}(\rho_{AB}^{T_B})^q}{\mathrm{Tr} \rho_{AB}^q}\right) = \log(\mathrm{Tr} \rho_{AB}^q) - \mathcal{E}_q(\rho_{AB}), \quad (3.40)$$

as this quantity remains zero for diagonal density matrices. For $q = 1, 2$, R_q vanishes, such that the first non-trivial quantity is R_3 . We will also refer to these quantities as Rényi negativities, they always give zero for product states, but are not necessarily zero for all separable (classically correlated) states, and hence are no entanglement monotones. We work out R_3 for the 2-qubit Werner state as an example in Sec. 3.3.3. It is however a computable, and potentially measurable, entanglement probe. Note that for a pure state $|\psi\rangle$

$$R_3(|\psi\rangle) = -\log(\rho^{T_B})^3 = -\log \mathrm{Tr}(\rho_B^3) = 2S_3. \quad (3.41)$$

R_3 has been previously studied in Ref. [98] in the context of finite-temperature phase transitions.

In Ref. [99], there is a test demonstrated for bipartite entanglement of the density matrix, that solely relies on the second and third moments of the partially-transposed density matrix. It states that,

$$\text{if } \rho_{AB} \text{ has a positive partial transpose then } \mathrm{Tr}(\rho_{AB}^{T_B})^3 \geq [\mathrm{Tr}(\rho_{AB})^2]^2. \quad (3.42)$$

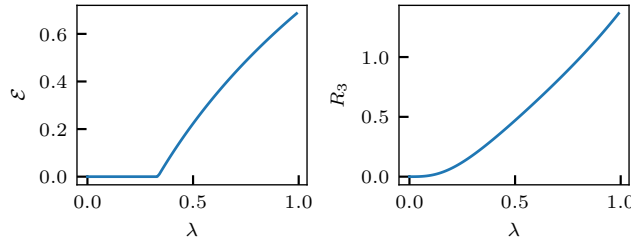


Figure 3.4 The logarithmic negativity \mathcal{E} and the third Rényi negativity R_3 for the two-qubit Werner state (3.43) defined by λ . R_3 is not an entanglement monotone as it takes a non-zero value in the separable regime $\lambda < 1/3$.

The statement on the right is referred to as the PPT-3 condition. And if this condition is violated, we know that ρ_{AB} does not have a PPT and is thus entangled. Two comments are in order here. First the PPT-3 condition is weaker than the Peres-Horodecki criterion (3.28), so it detects entanglement in fewer cases. This is illustrated in Fig. 3.3. On the other hand it does not rely on a full diagonalization of the partially transposed density matrix. Second, unlike the negativity for the PPT condition, there does not seem an entanglement monotone related to the violation of the PPT-3 condition.

In Ref. [100] the PPT-3 criterion is further refined in two directions. On one hand a sequence of conditions on higher order moments is found, and if all those moments can be estimated, the sequence forms a necessary and sufficient condition for the bipartition to have a PPT. On the other hand the conditions are further optimized, and applied on different symmetry sectors, see also Ref. [101].

3.3.3 R_3 is not an entanglement monotone

Part of this section was originally included as an appendix in the publication [1] of the author. The content is directly relevant for this chapter.

By the partial transposition criterion of Peres-Horodecki, it follows that each separable state has a positive partial transpose. Therefore each separable state has negativity $\mathcal{E}(\rho^{\text{sep}}) = 0$, however this is not true for the Rényi negativity. Consider for instance the two-qubit Werner state

$$\rho(\lambda) = \lambda |\phi\rangle \langle \phi| + \frac{1}{4}(1 - \lambda)\mathbb{1} \quad (3.43)$$

with $\lambda \in [0, 1]$ and $|\phi\rangle$ a Bell pair. In the PPT regime $\lambda < 1/3$. In this regime ρ^{T_B} has only positive eigenvalues, and as the PPT criterion is a sufficient for separability in the two qubit case, $\rho(\lambda < 1/3)$ is separable. However the eigenvalues of ρ^{T_B} and ρ are not the same, which implies a non-trivial value of R_3 . Explicitly the eigenvalues of $\rho(\lambda)$ are

$$3 \times \frac{1}{4}(1 - \lambda), 1 \times \frac{1}{4}(3\lambda + 1), \quad (3.44)$$

while the eigenvalues of $\rho^{T_B}(\lambda)$ are

$$3 \times \frac{1}{4}(1 + \lambda), 1 \times \frac{1}{4}(1 - 3\lambda). \quad (3.45)$$

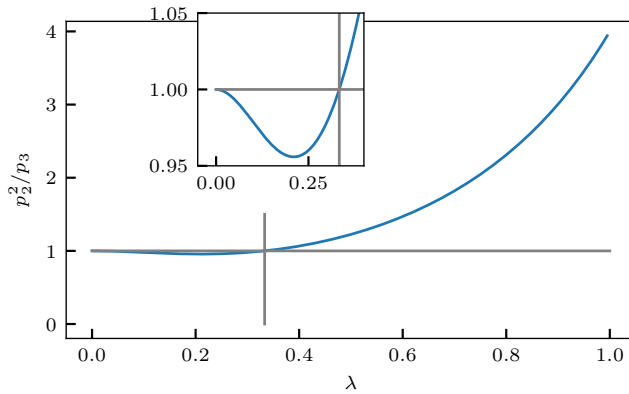


Figure 3.5 The ratio p_2^2/p_3 for the two-qubit Werner state defined by λ , see Eq. (3.43). For the Werner state the PPT-3 condition (3.42) is sufficient, so when $p_2^2/p_3 > 1$ the state is entangled. The inset shows a zoom for the smallest values of λ . The vertical grey line corresponds to $\lambda = 1/3$, and when $\lambda < 1/3$, the state is separable.

So in this case R_3 takes a non-trivial value, while $\mathcal{E} = 0$. This is illustrated in Fig. 3.4. Entanglement monotones satisfy invariance under LOCC. However a separable state is transformable into any other separable by means of LOCC. Indeed, notice that local unitary transformations fall into the class of LOCC transformations. Therefore an entanglement monotone must remain constant over the set of separable states, which is clearly not the case for the Rényi negativity in our example.

In Fig. 3.5, we additionally show the PPT-3 condition (3.42) in action for the Werner state, which is known to be sufficient as well in this specific case [99]. Here the abbreviations are $p_2 = \text{Tr}(\rho_{AB}^{T_B})^2 = \text{Tr}(\rho_{AB})^2$ and $p_3 = \text{Tr}(\rho_{AB}^{T_B})^3$, and the PPT-3 test states that the density matrix is entangled when

$$p_2^2/p_3 > 1. \quad (3.46)$$

Hence this is consistent with the fact that the completely mixed state $\lambda = 0$, where $p_2^2/p_3 = 1$, does not carry any entanglement.

3.3.4 Entanglement witnesses

The PPT criterion we discussed above, assumed full access to the density matrix of a state to determine whether it is entangled. Sometimes, there is no such access, and we can only directly measure observables. There however exist criteria, that are called *entanglement witnesses*, that only rely on observables [62]. Generically an observable (or a function of observables) is said to be an entanglement witness if

$$\begin{aligned} \text{Tr}(\rho\mathcal{W}) &< 0 \text{ for at least one } \rho \text{ that is not separable;} \\ \text{Tr}(\rho\mathcal{W}) &\geq 0 \text{ for all separable } \rho. \end{aligned} \quad (3.47)$$

Therefore if $\text{Tr}(\rho\mathcal{W}) < 0$ is measured, one can be certain that the state is entangled. The fact that they can be directly measured makes them useful tools for experiments. If a witness acts linearly, the set of states where $\text{Tr}(\rho\mathcal{W}) = 0$ can be geometrically interpreted as a hyperplane that divides the Hilbert space in two parts. In one part,

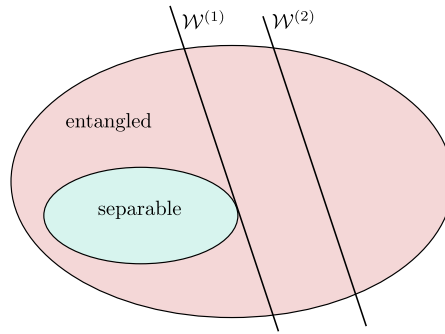


Figure 3.6 The set of all states in which the separable states are a subset. Entanglement witnesses divide the set in two parts: one in which they do not witness entanglement (here the left part), and one where they witness entanglement (here the right part). Therefore the witness $\mathcal{W}^{(1)}$ is better than $\mathcal{W}^{(2)}$ as it is able to detect more entangled states.

where $\text{Tr}(\rho\mathcal{W}) < 0$, entanglement is witnessed while in the other part it is not. This is illustrated in Fig. 3.6. From this picture it is also intuitive that in principle each entangled state can be detected by a witness. The proof of this theorem *completeness of entanglement witnesses* can be found in Ref. [90], and goes back to the already mentioned fact that the set of separable states is convex (and closed).

The disadvantage of entanglement witnesses is that they are strongly dependent on the choice of operator, and that sometimes an optimization over the whole Hilbert space is needed. In the next Chapters 5 and 6, we will therefore mostly focus on quantities that are based on the PPT criterion. In Sec. 5.6, we will however briefly consider an entanglement witness, the quantum Fisher information [102–105]. This specific witness is however quite hard to compute for general mixed states, therefore we will only study it using exact diagonalization.

4 Matrix-product states

In this chapter, we will briefly introduce the **MPS** formalism. We have extensively used this framework to perform numerical simulations for most of the systems that will be discussed in the following Chapters 5, 6, 7, and 8. **MPS** techniques are a subset in the very-broad class of tensor-network techniques and are mostly used to simulate one-dimensional systems. Extensive reviews about the topic can be found in Refs. [33, 34, 36, 106].

Shortly speaking, there are two main reasons why **MPS** algorithms have been so successful over the last three decades, since S. White established the **DMRG** algorithm in 1992 [31]. First a technical reason: there exist a *canonical form* that allows for efficient calculations, and manipulations of the network. In Sec. 4.1 we will decompose a state vector as an **MPS** by making use of the **SVD** decomposition, this procedure naturally brings the **MPS** into its canonical form. Secondly, a physical reason: some states (including the ground states of local and gapped Hamiltonians) are easy to represent because they only contain a *limited amount of entanglement*. In Sec. 4.2, we will discuss this so-called *area-law* scaling of entanglement.

Afterwards in Sec. 4.3, we give a brief overview of the two most important algorithms that we have used, **DMRG** and **TEBD**. We will also discuss the extension of **TEBD** algorithm to simulate the Lindblad dynamics of open quantum systems. The Lindblad equation has been discussed before in Sec. 3.2. Lastly in Sec. 4.4, we end this chapter with a brief sketch on how to compute the third Rényi negativity (see Sec. 3.3.2) as a contraction of the tensor network.

4.1 Matrix-product state decomposition and canonical forms

As discussed in Sec. 2.1.1 a pure quantum state is a vector in the Hilbert space, see Eq. (2.2). This vector can be represented graphically as an L -leg tensor

$$|\Psi\rangle = \left[\begin{array}{c} \psi \\ \hline s_1 \quad s_2 \quad s_3 \quad \dots \quad s_{L-2} \quad s_{L-1} \quad s_L \end{array} \right]. \quad (4.1)$$

From now on we will not write down the spin indices explicitly. We can regroup the legs, and successively apply the compact **SVD** decomposition which has been introduced in

Sec. 2.1.2. We note that in the graphical notations connected lines represent a sum over the corresponding indices, i.e. a matrix multiplication.

$$\begin{aligned}
|\Psi\rangle &= \begin{array}{c} \boxed{\psi} \\ | \\ \boxed{A^{[1]}} \end{array} \\
&= \begin{array}{c} \boxed{A^{[1]}} \text{---} \bigcirc{\lambda^{[1]}} \text{---} \boxed{\psi^{[2,\dots,L]}} \\ | \qquad \qquad \qquad | \\ \boxed{A^{[1]}} \end{array} = \begin{array}{c} \boxed{A^{[1]}} \text{---} \boxed{\tilde{\psi}^{[2,\dots,L]}} \\ | \qquad \qquad \qquad | \\ \boxed{A^{[1]}} \end{array} \\
&= \begin{array}{c} \boxed{A^{[1]}} \text{---} \boxed{A^{[2]}} \text{---} \bigcirc{\lambda^{[2]}} \text{---} \boxed{\psi^{[3,\dots,L]}} \\ | \qquad \qquad \qquad | \qquad \qquad \qquad | \\ \boxed{A^{[1]}} \text{---} \boxed{A^{[2]}} \end{array} = \begin{array}{c} \boxed{A^{[1]}} \text{---} \boxed{A^{[2]}} \text{---} \boxed{\tilde{\psi}^{[3,\dots,L]}} \\ | \qquad \qquad \qquad | \qquad \qquad \qquad | \\ \boxed{A^{[1]}} \text{---} \boxed{A^{[2]}} \end{array} \quad (4.2) \\
&= \dots \\
&= \begin{array}{c} \boxed{A^{[1]}} \text{---} \boxed{A^{[2]}} \text{---} \dots \text{---} \boxed{A^{[L]}} \text{---} \bigcirc{\lambda^{[L]}} \\ | \qquad \qquad \qquad | \qquad \qquad \qquad | \\ \boxed{A^{[1]}} \end{array} .
\end{aligned}$$

Here, as a first step, we start by regrouping the indices into a rectangular matrix $\psi_{s_1, s_2, \dots, s_L}^{[1, \dots, L]}$. This is followed by an **SVD** decomposition. This results in a product of a $(d \times d)$ -dimensional left unitary matrix or *isometry* $A^{[1]}$, a $(d \times d)$ -dimensional diagonal matrix $\lambda^{[1]}$, and a $(d \times d^{L-1})$ -dimensional right unitary matrix $\psi_{\eta_1, s_2, \dots, s_L}^{[2, \dots, L]}$. Then we multiply the singular values with the right unitary. This completes the first iteration (first line).

For the next iteration, we again start by a regrouping of the indices: we reshape the $(d \times d^{L-1})$ -dimensional matrix $\psi_{\eta_1, s_2, \dots, s_L}^{[2, \dots, L]}$ into a $(d^2 \times d^{L-2})$ -dimensional one, and then perform an **SVD**. Now the left unitary is $(d^2 \times d^2)$ -dimensional, which we however have to reshape into a $(d \times d \times d^2)$ -dimensional tensor to fit with the matrix multiplication of $A^{[1]}$ from the left.

Like this we can continue the iteration. Note that the horizontal dimension or *bond dimension* of the multiplication grows exponentially with system size: the maximal bond dimension is reached in the middle of the chain and is therefore $d^{\lfloor L/2 \rfloor}$. Finally, we have that $\lambda^{[L]} = [1]$ because of normalization, and can therefore be discarded.

The **MPS** obtained in the last line of (4.2), is written in formula form as

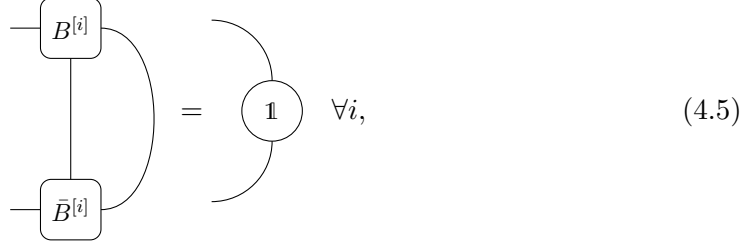
$$|\psi\rangle = \sum_{\{s_i\}} \sum_{\{\eta_i\}} A_{\eta_0, \eta_1}^{[1]s_1} A_{\eta_1, \eta_2}^{[2]s_2} \dots A_{\eta_{L-1}, \eta_L}^{[L]s_L} |s_1, s_2, \dots, s_L\rangle. \quad (4.3)$$

The left-unitary condition valid on the $A^{[i]}$ tensors originating from the **SVD** means that

$$\begin{array}{c} \boxed{A^{[i]}} \\ | \\ \boxed{\bar{A}^{[i]}} \end{array} = \bigcirc{\mathbf{1}} \quad \forall i, \quad (4.4)$$

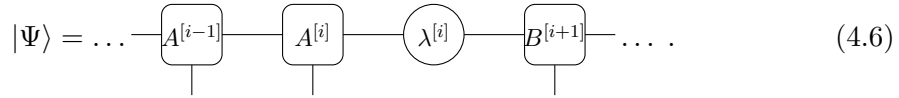
This condition is also called the *left-canonical* form. In these diagrams, the bar denotes complex conjugation.

In the decomposition (4.2), we could have equally well started from the right, i.e. from the rectangular matrix $\psi_{s_1, \dots, s_{L-1}, s_L}^{[1, \dots, L]}$, then we would have kept the right-unitary matrices from the SVD decomposition. This would then mean that

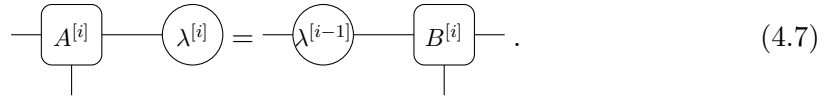


which is referred to as *right-canonical* form. To denote tensors in the right (left) canonical form, we will use ‘ B ’ (‘ A ’).

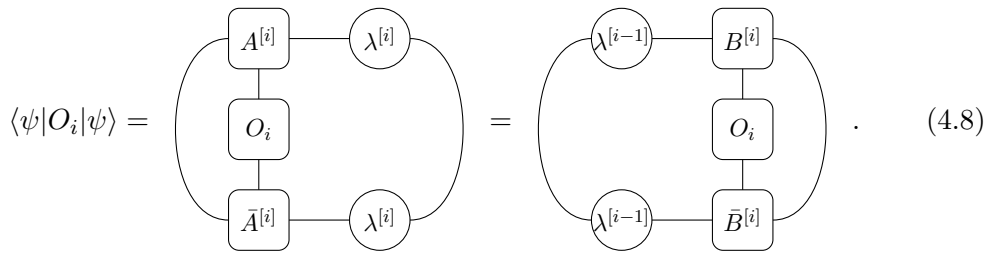
When we combine both forms, the MPS can be written in *mixed-canonical* form



Here the matrix containing the Schmidt coefficients is also referred to as the *orthogonality center*. The orthogonality center can be moved around freely by insertion of the Schmidt coefficients of the neighboring bounds. This allows to conveniently change the canonical form of the tensors.



The mixed-canonical form results in the very convenient property that *local* operations can be performed *locally*. For instance, the evaluation of a local expectation value simply becomes



We end this section by remarking that the MPS representation of a quantum state is not unique. This is already manifested by the fact that we can freely move around the orthogonality center. However, there are much more gauge degrees of freedom than this. Indeed the insertion of *any* invertible matrix of the correct dimensionality as $\mathbf{1} = X X^{-1}$ on the bonds, followed by an absorption of X and X^{-1} in the neighbouring tensors, already gives rise to a different MPS. This MPS will however not be in canonical form any longer, but still represents the same quantum state. The canonical form is arising very naturally from the SVD decompositions and turns out to be extremely convenient, but is strictly speaking not necessarily for representing a quantum state as an MPS.

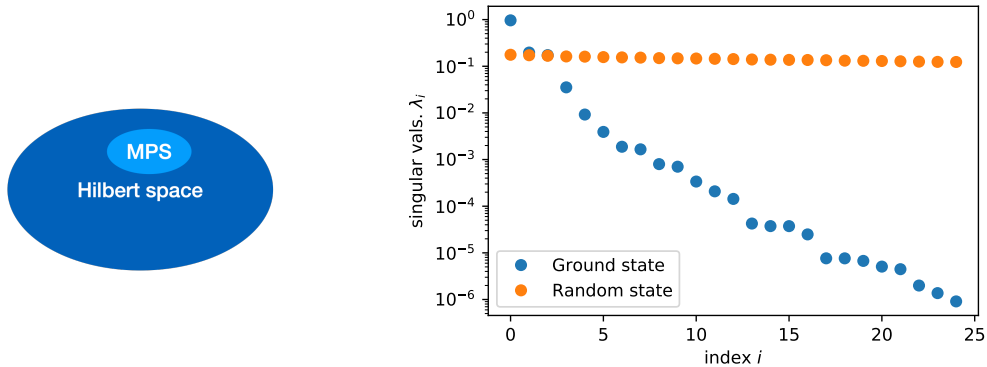


Figure 4.1 States that can be efficiently represented by an MPS form only a small subset of the Hilbert space. This subset is characterised by area-law scaling of the entanglement entropy. For instance, ground states of local gapped Hamiltonians fall into this class of area-law states. In the graph we plot the 25 largest singular values of the ground state of the paramagnetic TFI chain for a spin-1/2 system of $L = 10$ sites. These should be contrasted with the singular values of a state that is randomly drawn from the 2^{10} dimensional Hilbert space according to the Haar measure, which satisfies a volume law.

4.2 Area versus volume law entanglement scaling

In the previous Section, we have discussed the generic MPS decomposition of a quantum many-body state. However, we saw that the maximally reached bond dimension is growing exponentially as a function of system size. For some physical systems, however, such an exponential growth is not needed to faithfully represent the state as an MPS. Most prominently this is true for the ground states of local and gapped Hamiltonians. More specifically, these ground states satisfy the *area law*, which means that for any subsystem A the entanglement entropy scales at most as the *area of the boundary of A* [107]

$$S(\rho_A) = \mathcal{O}(\text{boundary area}(A)). \quad (4.9)$$

Rigorous derivations that this is true for the ground state of local gapped Hamiltonians can be found in Ref. [107]. Specifically in one dimension, the area of the boundary is constant, implying a constant amount of ground-state entanglement irrespective of the system size.

To illustrate, we show in Fig. 4.1 the 25 largest singular values in the middle of an $L = 10$ site MPS that represents the ground state of the TFI model in the paramagnetic phase. We see that these singular values quickly (exponentially) decay in magnitude. This implies that we can indeed just truncate the size of these matrices, while maintaining an almost full overlap with the exact ground state $|\langle \psi_0^{\text{MPS}} | \psi_0^{\text{exact}} \rangle| \simeq 1$.

However, this truncation is certainly not something we can do for generic states in the Hilbert space: indeed, when we simply pick a random vector in the Hilbert space according to the Gaussian unitary ensemble, we definitely do not observe such a decay as can also be seen in Fig. 4.1. In fact, an analytical formula has been obtained by D. Page in 1993 which quantifies the average amount of entanglement over *all* pure

quantum states as a function of system (V) and subsystem (V_A) volume [108]. In the thermodynamic limit, and for a fixed ratio $V_A/V \leq 1/2$, the result for $d = 2$ is

$$\overline{S(\rho_A)} = V_A \log(2) - 2^{-|1-2V_A/V|V-1} + \mathcal{O}(2^{-V}). \quad (4.10)$$

Here, the first term clearly indicates a *volume-law* scaling of the entanglement entropy [109]. The second term is an exponential correction if $V_A/V \neq 1/2$. From this we can deduce that *almost all* states in the Hilbert space satisfy such a volume-law scaling of the entanglement entropy. Hence, we conclude that states that can be most efficiently represented by an MPS which satisfy an area law, form actually only a tiny subset of the Hilbert space.

We end this section by noting that these results are true in arbitrary dimensionality for systems of spins, fermions and hard-core bosons. However, they are not valid for soft-core bosons as the average entanglement in this case might just diverge due to the infinite dimension of the local Hilbert space.

4.3 Matrix-product state algorithms

In this section we will review two widely used MPS algorithms. First we start with discussing the DMRG algorithm which is used for variationally finding an MPS representation of the ground state [31, 34]. Then we will discuss the TEBD algorithm [35], which is widely used for performing the time evolution of an MPS [34, 36].

4.3.1 Density-matrix renormalization group algorithm

The DMRG algorithm is a variational algorithm that is widely used to find ground states. It has been established by S. White in 1992 [31], and later on it has been understood as a variational optimization over the class of MPS [34, 110]. The variational principle guarantees that for any state $|\psi\rangle$

$$\frac{\langle\psi|H|\psi\rangle}{\langle\psi|\psi\rangle} \geq \langle 0|H|0\rangle, \quad (4.11)$$

where $|0\rangle$ is the (normalized) exact ground state of H . The goal is thus to bring a state $|\psi\rangle$ represented by an MPS with maximal bond dimension χ as close as possible to the target state $|0\rangle$ by minimizing the energy.

Before discussing the DMRG algorithm, we first need to introduce a convenient representation for the Hamiltonian. In Sec. 4.1 we have seen that every state can in principle be decomposed in an MPS. Therefore it is not surprising that a similar decomposition is also possible for operators. Hence, any operator can be expanded as a **matrix-product operator (MPO)**

$$O^{s_1, \dots, s_L} = \sum_{\{s_i\}, \{s'_i\}} \sum_{\{\eta_i\}} W_{\eta_0, \eta_1}^{[1]s_1, s'_1} W_{\eta_1, \eta_2}^{[2]s_2, s'_2} \dots W_{\eta_{L-1}, \eta_L}^{[L]s_L, s'_L} |s_1, s_2, \dots, s_L\rangle \langle s'_1, s'_2, \dots, s'_L| \quad (4.12)$$

$$= \dots \text{---} \begin{array}{c} s'_{i-1} \\ | \\ \boxed{W^{[i-1]}} \\ | \\ s_{i-1} \end{array} \text{---} \begin{array}{c} s'_i \\ | \\ \boxed{W^{[i]}} \\ | \\ s_i \end{array} \text{---} \begin{array}{c} s'_{i+1} \\ | \\ \boxed{W^{[i+1]}} \\ | \\ s_{i+1} \end{array} \text{---} \begin{array}{c} s'_{i+2} \\ | \\ \boxed{W^{[i+2]}} \\ | \\ s_{i+2} \end{array} \text{---} \dots \quad (4.13)$$

$$(4.14)$$

For the **DMRG** algorithm the Hamiltonian should be written as an **MPO** first. For the most common Hamiltonians the bond dimension of the **MPO** is small compared to the bond dimension of a typical **MPS**. Below we will briefly sketch the **DMRG** algorithm with a two-site update. There is also a scheme with a single-site update, but this does not allow to expand the initial bond dimension of the **MPS**.

We start from an **MPS** fully in its left canonical form – of course, we could equally well start from an **MPS** in right-canonical form. Then we start from the right with updating the rightmost two tensors. For this we solve the effective eigenvalue problem

$$H_{L-1, L}^{\text{eff}} \Phi^{[L-1, L]} = \lambda \Phi^{[L-1, L]}, \quad (4.15)$$

for the ground state of the two-site effective Hamiltonian using the Lanczos algorithm [111]. The effective Hamiltonian for updating the tensors on positions i and $i+1$, connected by the bond labelled by η_i , is given by

$$H_{i, i+1}^{\text{eff}} = \begin{array}{c} \begin{array}{c} \boxed{A^{[1]}} \text{---} \dots \text{---} \boxed{A^{[i-1]}} \xrightarrow{\eta_{i-1}} \begin{array}{c} s_i \\ | \\ \boxed{W^{[i]}} \\ | \\ s_{i+1} \end{array} \xrightarrow{\eta_{i+1}} \boxed{B^{[i+2]}} \text{---} \dots \text{---} \boxed{B^{[L]}} \\ | \\ \boxed{W^{[1]}} \text{---} \dots \text{---} \boxed{W^{[i-1]}} \text{---} \boxed{W^{[i+1]}} \text{---} \boxed{W^{[i+2]}} \text{---} \dots \text{---} \boxed{W^{[L]}} \\ | \\ \boxed{\bar{A}^{[1]}} \text{---} \dots \text{---} \boxed{\bar{A}^{[i-1]}} \text{---} \boxed{\bar{B}^{[i+2]}} \text{---} \dots \text{---} \boxed{\bar{B}^{[L]}} \end{array} \end{array} \quad (4.16)$$

The new two-site wave function that comes out of this procedure will be a vector $\Phi^{[L-1, L]}$ that should be reshaped into a matrix. Then we take an **SVD** of this matrix and from this we can immediately identify the updated tensors

$$\Phi_{\eta_{i-1} s_i s_{i+1} \eta_{i+1}}^{[L-1, L]} = \begin{array}{c} \boxed{\Phi} \\ | \\ \eta_{i-1} s_i s_{i+1} \eta_{i+1} \end{array} = \begin{array}{c} \eta_{i-1} \\ | \\ \boxed{\tilde{A}^{[i]} \text{---} \tilde{\lambda}^{[i]} \text{---} \tilde{B}^{[i+1]}} \\ | \\ \eta_{i+1} \\ | \\ s_{i+1} \end{array} \quad (4.17)$$

Notice that the bond dimension after the update step has grown, $\dim(\tilde{\eta}_i) = \dim(\eta_i) \times d$. If $\dim(\tilde{\eta}_i) > \chi$ we truncate the dimension of the matrices in the multiplication shown by the thicker lines such that $\dim(\tilde{\eta}_i) = \chi$. This completes the update of the tensors on position i and $i + 1$, around the i th bond. In a sweep from right to left, the next step would be updating the tensors on position $i - 1$ and i , around the $i - 1$ th bond. For this we would first need to move the orthogonality center according to Eq. (4.7). If the sweep from right to left is completed all tensors are in the right-canonical form. If we then sweep again from left to right, all tensors would be back into the left-canonical form. After each sweep the energy of the MPS should be calculated and compared to the energy of the previous iteration, until the desired convergence is reached.

4.3.2 Time-evolving block decimation

The TEBD algorithm is used to perform time evolution according to Hamiltonians that only contain *nearest-neighbor* couplings [35]. It relies on the Suzuki-Trotter decomposition of the exponential of two non-commuting operators V and W . The first and second order decompositions are given by [34]

$$e^{(V+W)dt} = e^{Vdt}e^{Wdt} + \mathcal{O}(dt^2) \quad (4.18)$$

$$e^{(V+W)dt} = e^{Vdt/2}e^{Wdt}e^{Vdt/2} + \mathcal{O}(dt^3). \quad (4.19)$$

Higher order decompositions are widely used as well, but are however quite cumbersome expressions. The decompositions for the fourth order can be found in Ref. [34]. The error that is made by this decomposition is referred to as *Trotter error*. In the Hamiltonian $H = \sum_n H^{[n,n+1]}$ under consideration, we regroup the terms acting on even and odd bonds in separate sums, i.e. $V = \sum_{n \text{ odd}} H^{[n,n+1]}$ and $W = \sum_{n \text{ even}} H^{[n,n+1]}$. Within these sums all terms obviously commute as they act on different sites, but V is not commuting with W . Using this we can expand the time-evolution operator $U(dt)$ that evolves the state by dt , $|\psi(t + dt)\rangle = U(dt)|\psi(t)\rangle$ as

$$\begin{aligned} U(dt) &\equiv e^{-iHdt} = \exp\left(-i\left(\sum_{n \text{ odd}} H^{[n,n+1]} + \sum_{n \text{ even}} H^{[n,n+1]}\right)dt\right) \\ &\approx \exp\left(-i\sum_{n \text{ odd}} H^{[n,n+1]}\frac{dt}{2}\right)\exp\left(-i\sum_{n \text{ even}} H^{[n,n+1]}dt\right)\exp\left(-i\sum_{n \text{ odd}} H^{[n,n+1]}\frac{dt}{2}\right) \\ &= \prod_{n \text{ odd}} \exp\left(-iH^{[n,n+1]}\frac{dt}{2}\right) \prod_{n \text{ even}} \exp\left(-iH^{[n,n+1]}dt\right) \prod_{n \text{ odd}} \exp\left(-iH^{[n,n+1]}\frac{dt}{2}\right) \\ &= \prod_{n \text{ odd}} U^{[n,n+1]}\left(\frac{dt}{2}\right) \prod_{n \text{ even}} U^{[n,n+1]}(dt) \prod_{n \text{ odd}} U^{[n,n+1]}\left(\frac{dt}{2}\right), \end{aligned} \quad (4.20)$$

for the widely used second order decomposition. Graphically this is represented as

$$|\psi(t + dt)\rangle = \begin{array}{c} A^{[1]} \text{---} A^{[2]} \text{---} A^{[3]} \text{---} A^{[4]} \text{---} A^{[5]} \text{---} \dots \\ | \\ U^{[1,2]}(dt/2) \quad U^{[3,4]}(dt/2) \quad U^{[5,6]}(dt/2) \\ | \\ U^{[2,3]}(dt) \quad U^{[4,5]}(dt) \\ | \\ U^{[1,2]}(dt/2) \quad U^{[3,4]}(dt/2) \quad U^{[5,6]}(dt/2) \\ | \\ \text{---} \end{array} \quad (4.21)$$

Note here that if we would apply N time-evolution operators $U(dt)$, the network would only be of depth $2N + 1$ and not $3N$ as the odd layers can be recombined.

Now we will turn towards the technicalities about the gate application procedure. Usually a finite-size MPS is stored by (i) its tensors on each site either in left or right canonical form, and (ii) the corresponding Schmidt coefficients on each site that allow to switch the canonical form. This also means that after each update step, it needs to be brought back in this form.

As the gates are unitary, they do not destroy the canonical form. Therefore, gates in each layer can be applied independently. For a gate application we start by making the contracting between the two-site effective wave function and the gate

$$\Phi_{\eta_{i-1}, \eta_{i+1}}^{s_i, s_{i+1}} = \begin{array}{c} \eta_{i-1} \text{---} A^{[i]} \text{---} \lambda^{[i]} \text{---} B^{[i+1]} \text{---} \eta_{i+1} \\ | \\ U(dt) \\ | \\ s_i \quad s_{i+1} \end{array} \quad (4.22)$$

This gate application comes with a cost of $\chi^2 d^4$ where $\dim(\eta_j) \leq \chi$. Then we regroup the legs into a matrix

$$\Phi_{\eta_{i-1} s_i, \eta_{i+1} s_{i+1}} = \begin{array}{c} \eta_{i-1} \text{---} A^{[i]} \text{---} \lambda^{[i]} \text{---} B^{[i+1]} \text{---} \eta_{i+1} \\ | \\ U(dt) \\ | \\ s_i \quad s_{i+1} \end{array}, \quad (4.23)$$

and of this matrix we take an SVD decomposition, resulting in

$$\Phi_{\eta_{i-1} s_i, \eta_{i+1} s_{i+1}} = \begin{array}{c} \eta_{i-1} \text{---} \tilde{A}^{[i]} \text{---} \tilde{\lambda}^{[i]} \text{---} \tilde{B}^{[i+1]} \text{---} \eta_{i+1} \\ | \\ \tilde{U}(dt) \\ | \\ s_i \quad s_{i+1} \end{array}, \quad (4.24)$$

This SVD comes with a cost of $\chi^3 d^3$, and is the most expensive step in the update procedure, because χ is usually the largest dimension. The thicker horizontal lines

indicate that during the decomposition the dimension of these tensor is multiplied by d . Then we simply need to ungroup the legs of the updated tensors

$$\Phi_{\eta_{i-1}, \eta_{i+1}}^{s_i, s_{i+1}} = \begin{array}{c} \eta_{i-1} \\ \text{---} \end{array} \boxed{\tilde{A}^{[i]}} \text{---} \bigcirc \tilde{\lambda}^{[i]} \text{---} \boxed{\tilde{B}^{[i+1]}} \begin{array}{c} \eta_{i+1} \\ \text{---} \end{array} . \quad (4.25)$$

s_i s_{i+1}

If the gates are applied without any truncation, the bond dimension is multiplied by d after the application of each gate. Thus it increases exponentially with number of time steps. However it quickly becomes unfeasible to represent such a large matrices. Therefore, we require that $\dim(\eta_i) \leq \chi$ after all updates. If the dimension turns out larger, we truncate it back to χ . This corresponds to discarding the Schmidt coefficients with the lowest weight. The summed-up weight of the discarded coefficients is referred to as the *truncation error*. A normalization step is required after truncation. While the trotter error is controlled and can be *chosen* smaller by decreasing the time step, the truncation error is less controlled as we can not indefinitely increase the bond dimension. This will necessarily lead to some discrepancy between the [MPS](#) and target state for larger systems evolved to later times, and convergence checks are required.

4.3.3 Time-evolving block decimation for density matrices

The density matrix ρ is nothing more than an operator, so can be represented by an [MPO](#), exactly as in Eq. (4.26),

$$\rho = \sum_{\{s_i\}, \{s'_i\}} \sum_{\{\eta_i\}} M_{\eta_0, \eta_1}^{[1]s_1, s'_1} M_{\eta_1, \eta_2}^{[2]s_2, s'_2} \dots M_{\eta_{L-1}, \eta_L}^{[L]s_L, s'_L} |s_1, s_2, \dots, s_L\rangle \langle s'_1, s'_2, \dots, s'_L| \quad (4.26)$$

$$= \dots \text{---} \boxed{M^{[i-1]}} \text{---} \boxed{M^{[i]}} \text{---} \boxed{M^{[i+1]}} \text{---} \boxed{M^{[i+2]}} \text{---} \dots \quad (4.27)$$

s'_{i-1} s'_i s'_{i+1} s'_{i+2}
 s_{i-1} s_i s_{i+1} s_{i+2}

Here, the matrix $M_{\eta_l, \eta_{l'}}^{[l]s_l, s'_l}$ has dimension $\chi_{l-1} \times \chi_l$ with $\max(\chi_{l-1}, \chi_l) \leq \chi$, where χ is the maximally allowed bond dimension. If we now group the physical indices of the [MPO](#) together, we can effectively view the [MPO](#) as an [MPS](#).

$$|\rho\rangle = \dots \text{---} \boxed{M^{[i-1]}} \text{---} \boxed{M^{[i]}} \text{---} \boxed{M^{[i+1]}} \text{---} \boxed{M^{[i+2]}} \text{---} \dots \quad (4.28)$$

s'_{i-1} s'_i s'_{i+1} s'_{i+2}
 s_{i-1} s_i s_{i+1} s_{i+2}

Therefore, in exactly the same way as for the [MPS](#), we can impose a canonical form. Now the goal is to apply the [TEBD](#) algorithm on this density matrix, with a Lindbladian superoperator governing the time evolution [89, 112–114]. We will use the Lindblad Eq. (3.22) with single-site Lindblad operators L_i with prefactor $\sqrt{\Gamma_i}$. The time-evolution superoperator $\exp(\mathcal{L}dt)$ in terms of the two-site time-evolution superoperators reads

$U_{i,i+1}(\delta t) = \exp(\mathcal{L}_{i,i+1}\delta t)$, note however that $U_{i,i+1}(\delta t)$ does not need to be unitary in this case, with

$$\begin{aligned} \mathcal{L}_{i,i+1} = & -iH_{i,i+1} \otimes \mathbb{1} + i\mathbb{1} \otimes H_{i,i+1} \\ & + \Gamma_i \left(\frac{1}{2}(L_i^\dagger \otimes L_i) - \frac{1}{4}(L_i^\dagger L_i \otimes \mathbb{1}) - \frac{1}{4}(\mathbb{1} \otimes L_i^\dagger L_i) \right) \\ & + \Gamma_{i+1} \left(\frac{1}{2}(L_{i+1}^\dagger \otimes L_{i+1}) - \frac{1}{4}(L_{i+1}^\dagger L_{i+1} \otimes \mathbb{1}) - \frac{1}{4}(\mathbb{1} \otimes L_{i+1}^\dagger L_{i+1}) \right). \end{aligned} \quad (4.29)$$

Here we took into account a factor $1/2$ in the dissipative part because, unless at the edges, each i is counted twice. Now, we need to make a Suzuki-Trotter decomposition of this operator. In our simulations in Chapters 5 and 6, we used the usual fourth order decomposition scheme, which does in principle destroy the canonical form while performing the updates on all even or odd bonds, because dissipation makes the time-evolution operator (4.29) non-unitary. However, this effect is small for $\Gamma \lesssim J$, with J the energy scale of the model. Therefore we found that we could still use this scheme with good accuracies in our setup discussed in Chapters 5 and 6. Alternatively, we could perform sweeps like in DMRG. Such a scheme is also often used for imaginary time evolution, where the evolution operator is manifestly non-unitary. It has as advantage that the canonical form is restored after each gate application.

Dissipation does not always result in states with a higher complexity. For instance, in case of dephasing noise, as we will study in Chapters 5 and 6, the complexity of the state can be reduced. Indeed, note that the infinite temperature state $\sim \mathbb{1}$ can be represented by an MPO with bond dimension $\chi = 1$.

We truncate the singular values after acting with $U_{i,i+1}(\delta t)$ on a bond by only keeping the χ largest ones, or by only keeping the ones that are larger than a certain ϵ_{trunc} . Note that, unlike for the pure state case, this does not fully correspond to truncating in the entanglement of the density matrix, but rather in its complexity, or so-called operator-space entropy [115]. Therefore the operator entropy of $|\rho\rangle$ will be limited to $\log \chi$ during the evolution towards the steady state. Strictly speaking, in this procedure we do not end up with a state that satisfies all properties of a density matrix listed in Sec. 3.1. While hermiticity and normalization can always be restored, the positivity is a global property that will be lost via truncation. However, for small system this effect can be quantified by comparing to exact results in specific setups. And for the setups we will discuss in Chapters 5 and 6, we found that it is indeed small even for very small bond dimensions. From this we concluded that the effect will also be small for the moderate system sizes we will discuss.

4.4 Rényi negativity as contraction of a tensor network

We will now very briefly sketch how the third Rényi negativity, R_3 , is computed using tensor-network techniques. This is not very complicated, we just need to jointly contract three copies of the network. In Fig. 4.2, we sketch how to compute the quantity $\text{Tr}\left((\rho_{AB}^{T_B})^3\right)$.

Note that three half contractions of the three layer network are sufficient to calculate R_3 , because the partial contraction over subsystem A is used in the same way for $\text{Tr}(\rho_{AB}^3)$ and $\text{Tr}\left((\rho_{AB}^{T_B})^3\right)$.

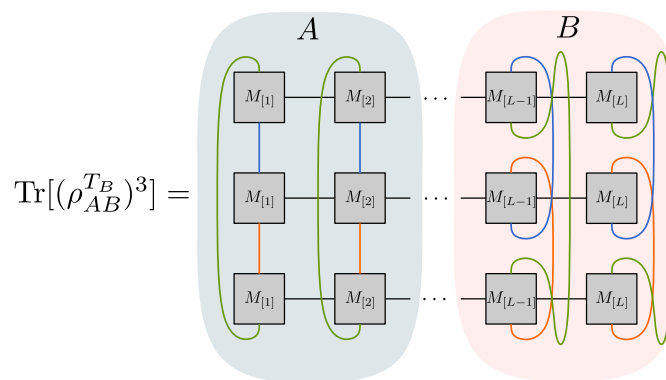


Figure 4.2 A sketch of the contraction of the three layer tensor network to compute $\text{Tr}[(\rho_{AB}^{T_B})^3]$. We take a bipartition of the system into two equal subsystems A and B , and take the transpose of the degrees of freedom of partition B , simultaneously with the trace of the system (green lines).

5 Entanglement dynamics of a many-body localized system coupled to a bath

Most of the content of this chapter can also be found in the previous publication of the author [1]. Text and figures have been adjusted to fit into the context of the thesis.

Interacting quantum systems subjected to strong disorder can realize an exotic **MBL** phase of matter [20, 23, 69, 116]. Similarly to a non-interacting Anderson insulator [71], the **MBL** phase is characterized by the absence of conventional transport and by spatial correlations that decay exponentially with distance. However, there are also important differences for example in the frequency-dependent response [117, 118] and in the entanglement dynamics [26, 27, 78]. Most prominently, the entanglement entropy grows logarithmically in time [26, 27, 78], due to effective interactions between the localized orbitals (**LIOMs**) [74, 75]. Evidence for an **MBL** phase has also been found experimentally in systems of ultracold atoms, trapped ions or superconducting qubits by the observation of a non-thermal saturation value of local densities [57, 105, 119, 120] and by entanglement dynamics [28, 93, 121, 122].

An important question is on which time scales signatures of **MBL** are observable in real systems, which are never truly isolated. In general, we expect that a coupling of the system to a bath leads to delocalization as transport is restored [45–50]. However it has also been shown that a coupling to a certain non-equilibrium bath can activate the **LIOMs** and allows to observe signatures of localization [123, 124]. When considering Markovian dephasing noise described by the Lindblad equation, the interference between the **LIOMs** is destroyed and the **MBL** state is driven into a featureless infinite temperature state [46–48]. It has been argued that local densities (e.g. the imbalance [57]) show a universal slower than exponential (specifically, a stretched exponential) decay that can be explained in terms of the **LIOMs** [46, 47]. The stretched exponential decay has also been observed experimentally in a cold atom setup [119]. These works explain the dynamics of the imbalance in dephasing **MBL** systems by means of purely classical rate equations, that thus only consider the hopping of diagonal states in the density matrix. Given the recent experimental focus on entanglement dynamics in **MBL** systems, it is an open question of how Markovian noise affects pure quantum correlations.

In this chapter, we investigate how the **MBL** phase is dynamically destroyed by a dephasing coupling to a bath, and focus on the decay of quantities that are sensitive to quantum correlations over bipartitions of the system. This is motivated by the fact that one of the most striking dynamical signatures of **MBL** is a generic logarithmic growth of entanglement under a quench which is completely absent in case of Anderson localization. Our goal is to investigate a recently introduced entanglement proxy for open quantum systems based on the negativity, the *third Rényi negativity* [94, 95, 97, 98], that can dynamically capture the difference between Anderson localization and **MBL**

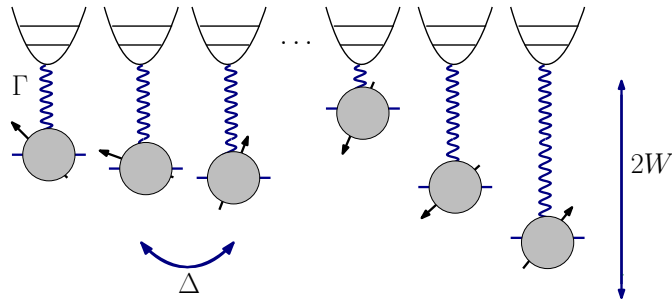


Figure 5.1 A sketch of our setup: a spin chain with disordered z-directed fields $h_i \in [-W, W]$, spin exchange Δ and coupling Γ to a bath.

provided the dissipation is sufficiently weak. We motivate our choice of this quantity, investigate how it scales, and discuss its experimental relevance.

The remainder of this chapter is organized as follows. We start by introducing our model and setup in Sec. 5.1. In Sec. 5.2 we present our main result: the MPS calculations for the third Rényi negativity. In a previous chapter, in Sec. 3.3.2, we motivated the use of this quantity, while in Sec. 4.4 we showed how to calculate it using MPS techniques. In Sec. 5.3 we provide a quick check of the performance of the TEBD algorithm for the calculation of the third Rényi negativity for various TEBD parameters.

In Sec. 5.4 we compare the negativity with the third Rényi negativity by means of exact diagonalization. In Sec. 5.5 we show, also by exact diagonalization, that the negativity can behave non-asymptotically in case the magnetization conservation of our model is broken.

Another possibility to quantify entanglement in open quantum systems is given by entanglement witnesses. They have the advantage that they can be experimentally relevant, because often they rely on simple expectation values. In Sec. 5.6, we show some results for the quantum Fisher information (QFI) by exact diagonalization.

We conclude in Sec. 5.7.

5.1 Model and setup

The random-field XXZ Hamiltonian on a chain with open boundary conditions is given by

$$H = J \left[\sum_{i=1}^{L-1} \left(S_i^x S_{i+1}^x + S_i^y S_{i+1}^y + \Delta S_i^z S_{i+1}^z \right) \right] + \sum_{i=1}^L h_i S_i^z, \quad (5.1)$$

where $S_i^{x,y,z}$ are the spin- $\frac{1}{2}$ operators, and the h_i 's are randomly and uniformly distributed in the interval $[-W, W]$. Here, we will fix the disorder to $W = 5J$ such that our systems are in the MBL phase [22].

The time dependence of the density matrix is given by the Lindblad master equation [38]

$$\dot{\rho} = -i[H, \rho(t)] + \sum_i \left(L_i^\dagger \rho(t) L_i - \frac{1}{2} \{ L_i L_i^\dagger, \rho(t) \} \right) \equiv \mathcal{L}\rho, \quad (5.2)$$

which models the coupling of the system to a Markovian, i.e. memoryless, bath. We consider the Lindblad operators for dephasing noise $L_i = \sqrt{\Gamma} S_i^z$, with this choice the

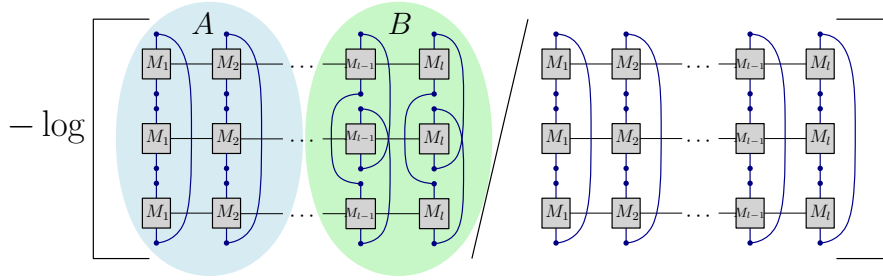


Figure 5.2 A sketch of the R_3 entanglement probe, see Eq. (3.40), that we compute using tensor-network techniques. We make a bipartition of the system into two subsystems A and B , and partially transpose the degrees of freedom of subsystem B before taking the trace.

decoherent part of the Lindblad equation also conserves the total magnetization $\sum_i S_i^z$ in the system. The Lindblad equation then takes the simplified form

$$\dot{\rho} = -i[H, \rho(t)] + \Gamma \sum_i \left(S_i^z \rho(t) S_i^z - \frac{1}{4} \rho(t) \right). \quad (5.3)$$

We sketch our system in Fig. 5.1. In the limit of a purely dephasing coupling $H = 0$ the off-diagonal matrix elements of the density matrix just decay exponentially. So this specific choice of Lindblad operators removes entanglement over time.

To simulate the time evolution according to the Lindblad equation, we use exact diagonalization and the **TEBD** algorithm on density matrices [112, 113], see also Sec. 4.3.3, where the time-evolution operator is given by $U(t) = \exp(\mathcal{L}t)$ with the superoperator

$$\mathcal{L} = -iH \otimes \mathbf{1} + i\mathbf{1} \otimes H + \Gamma \sum_i \left(S_i^z \otimes S_i^z - \frac{1}{4} \mathbf{1} \otimes \mathbf{1} \right). \quad (5.4)$$

As initial state of the quench we use the Néel product state $\rho_0 = |\psi_0\rangle\langle\psi_0|$ with $|\psi_0\rangle = |0101\dots\rangle$, so we work in the sector with total magnetization $M = \sum_i \langle S_i^z \rangle = 0$.

The time-evolution operator acts on a vectorized version of the density matrix in which the spin indices are combined as $|\rho(t+dt)\rangle = \exp(\mathcal{L}dt)|\rho(t)\rangle$. We note that the efficiency of our **TEBD** simulation of the density matrix critically depends on the entropy of $|\rho(t)\rangle$ viewed as a pure state in operator space. This operator-space entropy cannot be easily related to the quantum entanglement of the density matrix as it also contains classical correlations [115]. In our setup, it has been shown that this quantity grows logarithmically which allows for a simulation over long times [26, 48]. At late times the operator-space entropy converges to a value set by the steady state, which in our case is the identity restricted to the $M = 0$ sector, and scales as $\log L$ [48].

5.2 Results of the computation of Rényi negativities

Here we present our **MPS** results for the computation of the Rényi negativity R_3 , which is a probe for the quantum entanglement of the density matrix. This quantity has been extensively introduced in Sec. 3.3.2 and is sketched once more in Fig. 5.2. We recall that the extension of the **TEBD** algorithm to perform Lindblad time evolution was discussed in Sec. 4.3.3, while in Sec. 4.4 we illustrated how to contract the tensor network to obtain $\text{Tr}(\rho_{AB}^{T_B})^3$ for an **MPO** representing the density matrix.

First, we will consider the closed system, and observe the logarithmic growth of entanglement between the two halves of the system A and B . Second we will turn to the open quantum system. Here, the Néel state at $t = 0$ and the maximally mixed state at $t = +\infty$ have a value of $R_3 = 0$ as their density matrices obviously do not have any negative eigenvalues. At intermediate times, when there is some entanglement, the trace of the partially transposed bipartite density matrix is reduced meaning that

$$\frac{\text{Tr}(\rho_{AB}^{T_B})^3}{\text{Tr} \rho_{AB}^3} < 1, \quad (5.5)$$

and thus $R_3 \equiv R_3(\rho_{AB}) > 0$.

5.2.1 Closed system

As we have shown in Sec. 3.3.2, R_3 reduces to the third Rényi entropy in the closed quantum system. To check that it indeed shows the same characteristic features as the von Neumann entropy in the thermodynamic limit, we have plotted its behavior in Fig. 5.3. We observe the typical logarithmic growth in R_3 for MBL systems, and a fast saturation for Anderson localized systems.

As a next step we analyze the distributions of R_3 . Therefore we start from a simplified Hamiltonian in terms of the LIOMs neglecting couplings between three or more τ -spins

$$H = \sum_i h_i \tau_i^z + \sum_{i>j} J_{ij} \tau_i^z \tau_j^z \quad (5.6)$$

in which the J_{ij} 's decay exponentially with the distance between the spins $J_{ij} = J_0 e^{-r/\xi}$ with $r = i - j$.

Assuming an initial product state of two spins $|\psi(0)\rangle = \frac{1}{\sqrt{2}}(|0\rangle + |1\rangle) \otimes \frac{1}{\sqrt{2}}(|0\rangle + |1\rangle)$, which are generated for the LIOMs because our initial state is prepared in a product state for the physical spins. We obtain for the entanglement generated under time-evolution with Hamiltonian (5.6), that

$$R_3(t; J_r) = -\log\left(\frac{5 + 3 \cos(tJ_r)}{8}\right), \quad (5.7)$$

hence the maximum R_3 that can be generated between the spins is $2 \log 2$ as expected.

The couplings J_r have been shown to be distributed according to a log-normal distribution [125]

$$P_J(J; r, \xi_1, \xi_2) = \sqrt{\frac{\xi_2}{8\pi r}} \frac{1}{J} \exp\left(-\frac{(\log J + 2r/\xi_1)^2}{8r/\xi_2}\right). \quad (5.8)$$

The parameters ξ_1 and ξ_2 characterize respectively the growth of the mean and variance with distance between the spins. Then we can estimate the distribution of R_3 for a bipartition of size L by summing over L values of R_3 that are calculated by sampling the J 's from L distribution functions (5.8)

$$R_3(t) = \sum_{r=1}^L R_3(t; J_r). \quad (5.9)$$

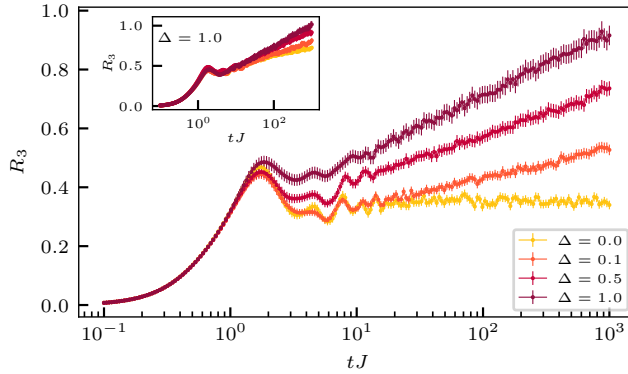


Figure 5.3 Quench dynamics of $R_3 = 2S_3$ in the closed quantum system at fixed system size $L = 14$ for various interaction strengths. In the inset we show the finite size scaling of R_3 at fixed interaction strength $\Delta = 1$, from bottom to top $L = 10, 12, 14, 16$. The errorbars show the standard error of the mean.

The average and some histograms given by this model are compared to the numerics in Fig. 5.4 for $L = 16$ and $\Delta = 1$. We have taken the parameters ξ_1 and ξ_2 of the distribution such that the growth of our model has the same slope ($\xi \log t$) as our data, and such that $\xi_1/\xi_2 \approx 2$ as reported in Ref. [125], see Fig. 5.4(a). We compare the distributions obtained by the model and by the numerics in Fig. 5.4(b)-(c) at various times. First we note a resonance at $R_3 = 2 \log 2$ both in the model as in the numerics corresponding to a singlet bound over the bipartition [126]. Secondly we note that there are two simplifications in our model (i) the difference between τ -spins and physical spins and (ii) the fact that we only took into account 2-spin couplings. The first simplification is reflected in the short-time dynamics. The second simplification induces too long tails in the model towards low entanglement, as we did not take into account multi-spin couplings which can also provide significant contributions to the entanglement.

The distribution of R_3 for Anderson localized systems would decay quickly for values higher than the singlet bond $R_3 = 2 \log 2$ as entanglement cannot propagate through the system, in contrast to what we observe for the MBL system.

5.2.2 Open system

Many-body localization at intermediate time scales

We now turn to finite dephasing strength and study the entanglement dynamics under the Lindblad Eq. (6.3). As we have argued in Sec. 3.3, R_3 stays a good probe for quantum correlations when we switch on the dephasing, unlike the von Neumann or Rényi entropies. This implies that the entanglement probe R_3 is able to distinguish MBL from Anderson localization by capturing signatures of the characteristic logarithmic growth in the MBL phase. Whether this is possible depends on the interaction strength and on the dephasing strength. The timescale on which the logarithmic growth starts, depends on the interactions $t_{\text{int}} \sim (\Delta J)^{-1}$, while the timescale on which the dephasing becomes dominant is directly related to the coupling strength $t_{\text{deph}} \sim 1/\Gamma$. Hence at short timescales neither interactions nor dephasing influence the entanglement dynamics. This implies that we need to have that $t_{\text{int}} \lesssim t \lesssim t_{\text{deph}}$ if we want to observe an effect of the

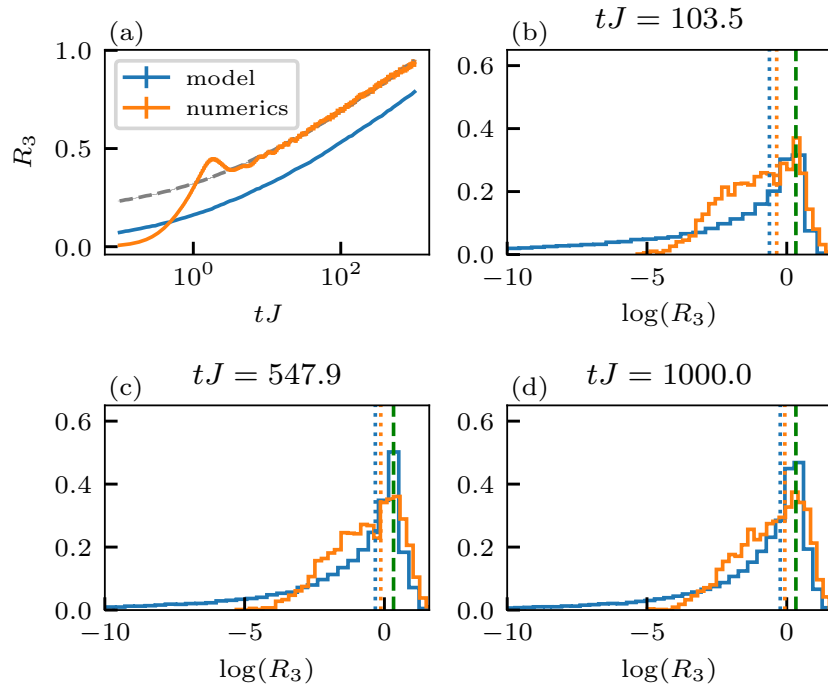


Figure 5.4 (a) Comparison of the average of R_3 obtained by the numerics over 2500 disorder realizations with system size $L = 16$ and $\Delta = 1$ and by the model described in the text with $\xi_1 = 0.40$ and $\xi_2 = 0.195$. The dashed grey line shows the curve of the model shifted by a constant. (b)-(d) Normalized histograms of the model and numerics at several times. The dotted vertical lines indicate the mean, while the dashed green line indicates the resonance at $2 \log 2$. The tails in the distributions of the model are more pronounced, as it does not take into account multi-spin couplings.

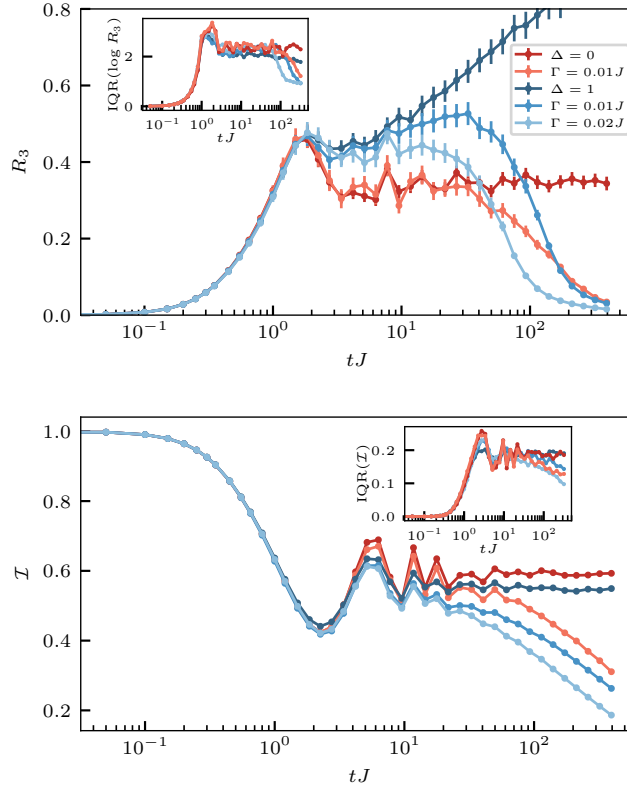


Figure 5.5 Dynamics of the Rényi negativity (top) and the imbalance (bottom) under a quench in the open or closed system ($L = 20$). The disorder is fixed to $W = 5J$ and the interaction strength is $\Delta = 1$ for the MBL system, and $\Delta = 0$ for the non-interacting Anderson localized system. The two darkest colors (red and blue) show the closed system for comparison. At intermediate time scales and for sufficiently weak dephasing strength, R_3 distinguishes MBL from single particle localization. A feature that is absent in the imbalance. In the insets we show the interquartile range (IQR) which forms a measure for the spread of the distribution.

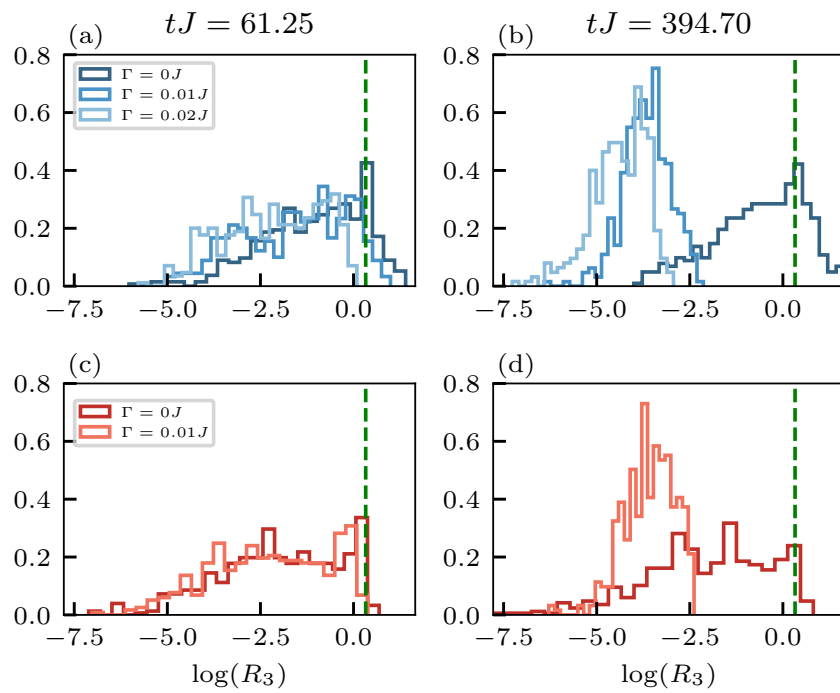


Figure 5.6 Histograms at two different times (columns) corresponding to the averages shown in Fig. 5.5. (a)-(b) Interacting system with $\Delta = 1$. (c)-(d) Non-interacting system $\Delta = 0$. The green line indicates $R_3 = 2 \log 2$ which corresponds to the maximal entanglement between 2-spins.

interactions, and in that way make the distinction between MBL and Anderson localization. For this regime to be existent we need to have that $\Gamma/J \lesssim \Delta$ meaning that the dephasing strength needs to be sufficiently weak compared to the interaction strength. We show our computations for the dephasing MBL and Anderson systems in Fig. 5.5, and compare them to the closed case. From this we indeed conclude that R_3 can distinguish MBL from Anderson localization on intermediate time scales by its maximally reached value. At this point, we stress again that quantities like the operator-space entropy would simply grow logarithmic until saturation [48] both for MBL and Anderson because of their sensitivity to classical correlations, and thus are no good probes to track the quantum correlations. We compare the entanglement dynamics to the relaxation dynamics of the imprinted density pattern, as measured by the imbalance, $\mathcal{I} = \frac{\langle S_e^z - S_o^z \rangle}{\langle S_e^z + S_o^z \rangle}$, where S_e^z/S_o^z sums S_i^z over even/odd sites, see Fig. 5.5.

We also compute the interquartile range (IQR) of our data, shown in the insets of Fig. 5.5, which is a measure for the spread of a distribution that is less sensitive to the tails than the variance. We choose this measure because of the limited number of disorder realizations that are numerically feasible for open quantum systems, which implies that we only have limited access to the tails. The dephasing is driving the state into a trivial steady state which implies that the distribution of R_3 will converge to a δ -peak at zero entanglement. We indeed see a clear dip in the spread of the distribution as the dephasing sets in. The full distributions of R_3 , shown in Fig. 5.6, possess strong tails even in the presence of dephasing noise, however, their width is decreasing over time.

The fact that R_3 carries only traces from MBL at intermediate times, when the dephasing is not yet completely dominating the dynamics can also be seen from the distributions: if we want to detect traces of MBL, we need to have some larger entanglement clusters remaining over the bipartition in some disorder realizations. Thus the distribution of R_3 must contain some part that has an entanglement that is higher than the singlet entanglement $R_3 = 2 \log 2$, for MBL to be detectable. This criterion is more sensitive than just looking at the mean of R_3 , since it focuses on the upper part of its full distribution.

Stretched exponential decay of R_3

At timescales $t \gtrsim t_{\text{deph}}$ there is no distinction possible between Anderson and MBL, but we can still determine the functional form of the decay. In the open system, R_3 undergoes a characteristic stretched exponential decay starting at time scales t_{deph} as shown in Fig. 5.7. Such a decay can be understood as a superposition of local exponential decays, and has also been observed in the imbalance in Refs. [46, 47, 49] and is also experimentally confirmed [119]. We observed such a decay as well in our exact simulations for the negativity as we show in Sec. 5.4 and the Fisher information in Sec. 5.6.

Next, we quantitatively extract the stretching exponent b of $R_3 \sim e^{-(\Gamma t/a)^b}$ by considering different system sizes for the rather large coupling strength $\Gamma = 0.1J$. From Fig. 5.7 we see that the exponent is around $b \approx 0.25$, and our data shows that interactions in the Hamiltonian do not influence this exponent, confirming that the dephasing is indeed dominating this dynamics. This is expected to hold true as long as interactions are small compared to the disorder in the system $\Delta \lesssim W$ [49]. Ref. [46, 47] respectively reported a stretching exponent $b \approx 0.38$ and $b \approx 0.42$ for the imbalance. We observe an

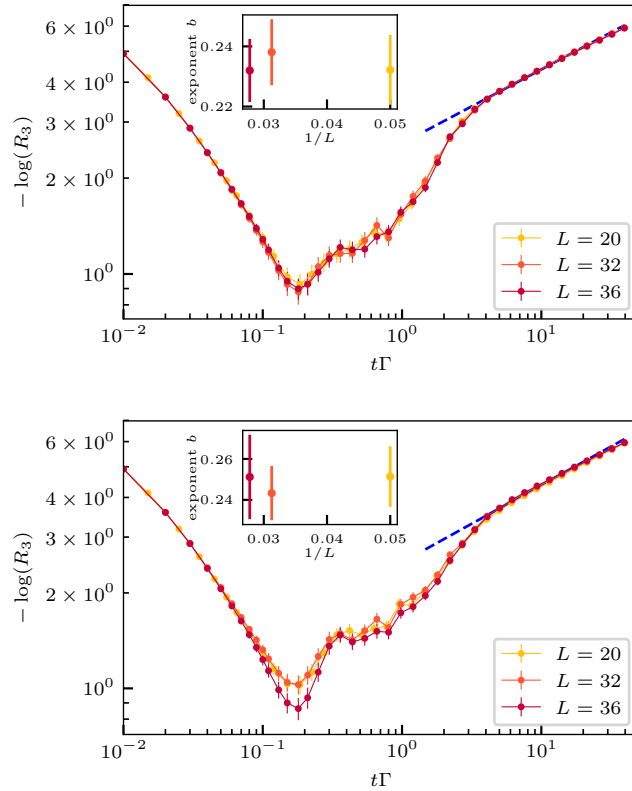


Figure 5.7 Quench dynamics of the Rényi negativity R_3 in a system with disorder $W = 5J$ and coupling $\Gamma = 0.1J$. Top: MBL with interaction strength $\Delta = 1$. Bottom: Non-interacting system $\Delta = 0$. In the inset we show the best fitting parameter for the stretching exponent b with 3σ errorbars obtained by the least-square method. These exponents do not depend on the interactions up to leading order. The blue line shows one of the fitting functions with $b \approx 0.25$.

exponent in R_3 that is significantly smaller indicating that entanglement is more robust than transport under dephasing.

5.3 Convergence of the time-evolving block decimation algorithm for density matrices

In this section, we show a comparison between various parameters of the **TEBD** on **MPO** algorithm. We show results for one particular disorder realization such that we can compare the errors caused by the algorithm, without the statistical errors from the averaging. In Fig. 5.8 we compare the fourth order **TEBD** algorithm with the exact results, by showing the relative error in the Rényi negativity. As expected this error increases in time and with decreasing bond dimension. The main source of error that declares the small deviations from the exact result at maximal bond dimension is the Trotter error because of the splitting of the time-evolution operator. However this error can be controlled by choosing a small enough time step, as can be deduced from Fig. 5.8 where we also plotted the performance of the **TEBD** scheme at various time steps at the exact bond dimension.

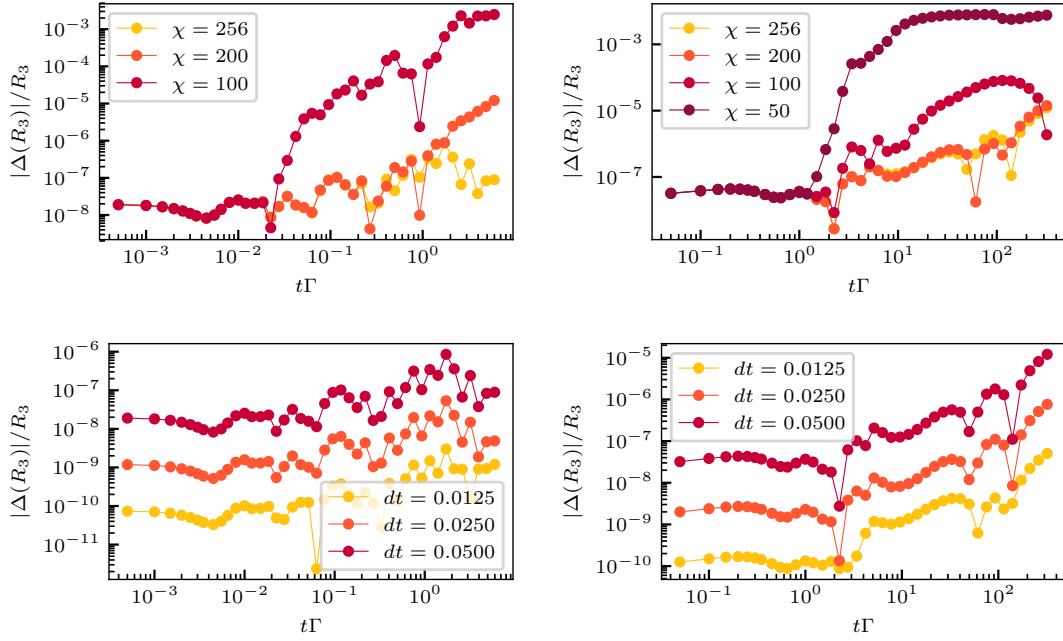


Figure 5.8 Relative error of the fourth order TEBD scheme for various simulation parameters for a small system of $L = 8$ spins. In the left column the coupling is $\Gamma = 0.01J$, in the right one $\Gamma = 1J$. In the top line we vary the maximal bond dimension. In the bottom line we vary the time step (in units of J^{-1}) at maximal bond dimension $\chi = 256$.

In Fig. 5.9 we show the relative error with respect to the largest bond dimension that was easily computable for a system size of $L = 40$, as well as a comparison between different time steps. From this we conclude that we maximally need a bond dimension around $\chi = 400$, and time step $dt = 0.05$.

5.4 Comparison of the negativity and R_3 by exact diagonalization

In this section we show some exact diagonalization results for a small chain of $L = 8$ spins for which we could still diagonalize the full density matrix, allowing us to compute the negativity. In Fig. 5.10 we compare the negativity with the third Rényi negativity, and see that the stretching exponents of the negativity and R_3 are indeed equal. This indicates that R_3 captures the main dynamic behavior of the entanglement seen by the negativity, and thus that it stays rather blind to the growing classical correlations between part A and B of the system.

5.5 Sudden death dynamics of the negativity

Entanglement quantities in open quantum systems may decay non-asymptotically, unlike transport quantities. This so-called sudden death dynamics is a known phenomenon, that imposes challenges on the stability of quantum memories [127, 128]. In our setup this specific dynamics only occurs in the negativity when we explicitly break the spin-

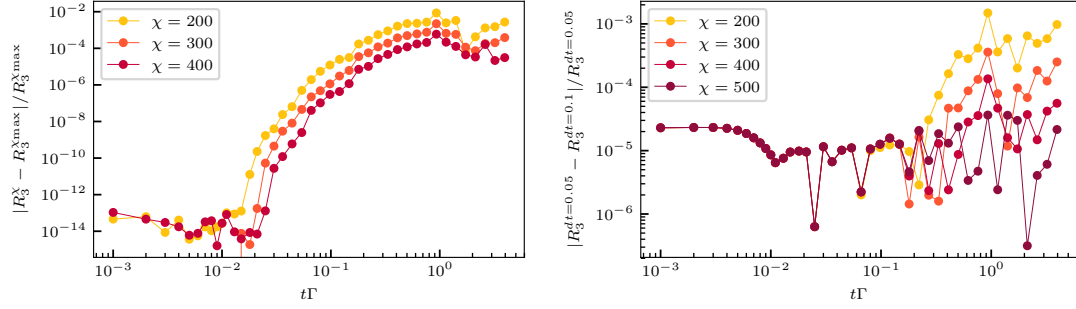


Figure 5.9 Relative error of the fourth order TEBD scheme for $L = 40$ spins with a coupling strength of $\Gamma = 0.01J$. On the left we show the relative difference between simulations with bond dimension χ and bond dimension $\chi_{\max} = 500$ with a time step of $dt = 0.05$. On the right we show the difference between simulation with time step is $dt = 0.1$ and $dt = 0.05$ at bond dimension χ .

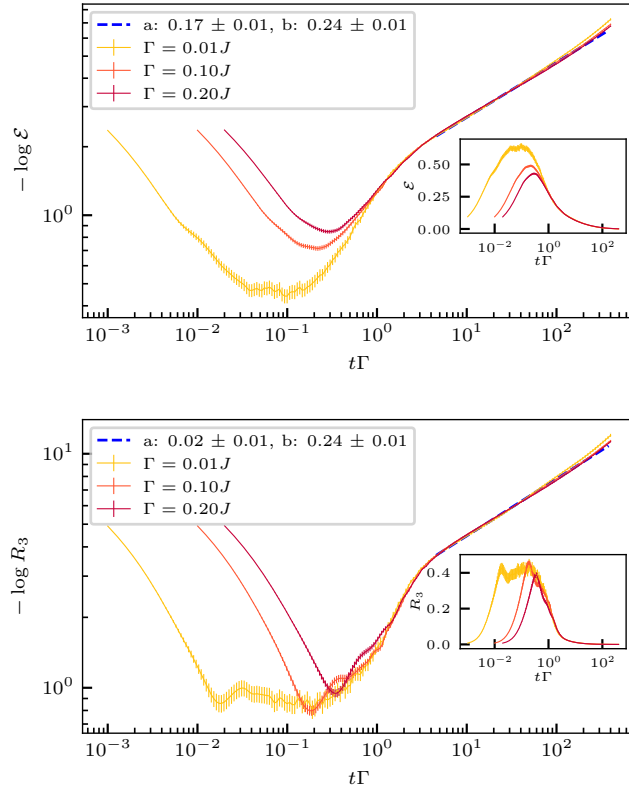


Figure 5.10 Comparison of the negativity (top) and the third Rényi negativity (bottom) in the Lindblad quench dynamics in the XXZ model at disorder $W = 5J$, interaction strength $\Delta = 1$ and small system size $L = 8$. The dashed blue line shows the stretched exponential fits $e^{-(\frac{\Gamma t}{a})^b}$ for the decay. The stretching exponents are equal for both quantities. The insets show the same data in a different scale. The errorbars show the standard error of the mean and the averages are taken over 1000 disorder realizations.

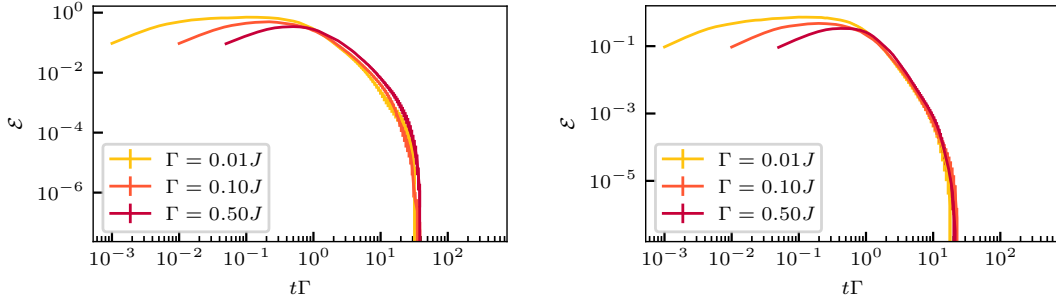


Figure 5.11 Negativity dynamics in a small system of $L = 8$ spins. When spin-conservation is broken by adding a term $g \sum_i S_i^x$ to the Hamiltonian, the negativity dynamics stops abruptly at a finite time. In the left plot $g = 0.2J$, and in the right one $g = 0.4J$.

conservation symmetry as illustrated in Fig. 5.11. In this section we investigate why the negativity decay is always asymptotic when the evolution conserves the total spin. The $U(1)$ -symmetry leads to entries of the density matrix that are always zero, only one sub-block of the density matrix that corresponds to the considered spin-sector is occupied. In the $M = \sum_i \langle S_i^z \rangle = 0$ sector, for a chain with an even number of spins, the dimension is $m = C_{L/2}^L$. Partial transposition maps at least part of the off-diagonal elements of the occupied sub-block to other spin sectors. Consider for instance the two qubit matrix element in the $M = 0$ sector $c|01\rangle\langle 10|$, after partially transposing the second qubit index this becomes $c|00\rangle\langle 11|$, which is a matrix element outside the $M = 0$ sector. Clearly under spin-conserving dynamics this matrix element would have remained zero.

As the diagonal elements remain of course invariant under partial transposition, we can split ρ^{TB} into two blocks B^{in} and B^{out} , corresponding to occupied elements inside or outside the original spin sector, with the blocks of the generic form

$$B^{\text{out}} = \begin{pmatrix} & A \\ A^\dagger & \end{pmatrix} \in \mathbb{C}^{2n,2n} \quad \text{and} \quad B^{\text{in}} = (B^{\text{in}})^\dagger \in \mathbb{C}^{m,m} \quad (5.10)$$

with $m + 2n = \dim(\mathcal{H})$, because of the Hermiticity of the original density matrix. From this simple argument we can make no a priori assumptions about the structure of the eigenvalues of B^{in} . However, it is easy to see that for a density matrix of the form B^{out} the eigenvalues come in pairs with opposite signs $\pm\lambda_1, \pm\lambda_2, \dots, \pm\lambda_n$. The fact that there are always negative eigenvalues present due to inherent structure of the partially transposed density matrix of a system with spin conservation, prevents sudden death dynamics in the negativity.

5.6 Quantum Fisher information as an entanglement witness

Here we discuss the **QFI** which quantifies the sensitivity of a state to a unitary transformation $e^{i\theta O}$ generated by a linear Hermitean operator of the form $O = \sum_i \mathbf{n}_i \cdot \mathbf{S}_i$, where \mathbf{n}_i is a unit vector and \mathbf{S}_i is the vector of spin matrices (S_i^x, S_i^y, S_i^z) . Therefore it measures the spread of quantum correlations via the operator O [62, 129]. The **QFI** witnesses entanglement in a state if its value is larger than the system size $F_Q > L$, and

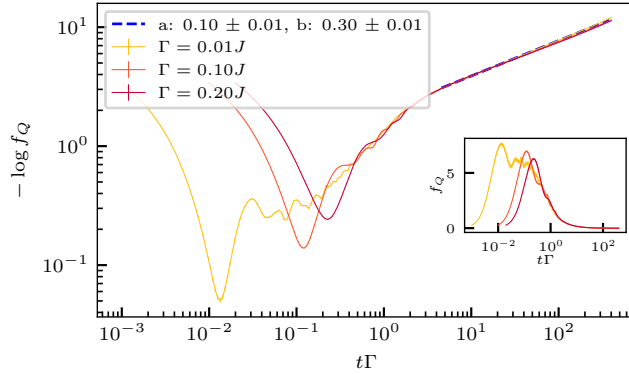


Figure 5.12 The quench dynamics of the Fisher information density $f_Q = F_Q/L$ at disorder $W = 5J$, interaction strength $\Delta = 1$ and system size $L = 8$. We show stretched exponential fits $e^{-(\frac{t}{a})^b}$ for the decay that start approximately at time $\sim \frac{1}{\Gamma}$. The inset shows the same data in a different scale. The errorbars show the standard error of the mean and the averages are taken over 1000 disorder realizations.

by other conditions it can also witness multipartite entanglement [103, 104]. For pure states, the QFI is given by the variance of O

$$F_Q(|\psi\rangle, O) = 4 \left(\langle \psi | O O | \psi \rangle - |\langle \psi | O | \psi \rangle|^2 \right). \quad (5.11)$$

For mixed states the QFI cannot be related to simple expectation values, instead the full spectral decomposition of the density matrix $\rho = \sum_i p_i |s_i\rangle \langle s_i|$ is necessary [102]

$$F_Q(\rho, O) = 2 \sum_{\substack{i,j \\ p_i + p_j > 0}} \frac{(p_i - p_j)^2}{p_i + p_j} |\langle s_j | O | s_i \rangle|^2, \quad (5.12)$$

and can only be computed using exact diagonalization, unless ρ takes the form of a thermal state [130]. The QFI relies on the choice of generator O , and for simplicity we will choose the staggered magnetization $O = \sum_i (-1)^i S_i^z$ which seems a natural choice to consider the quench dynamics from an initial Néel state. Note that the choice $O = \sum_i S_i^z$ would imply a vanishing Fisher information due to spin conservation, while $O = \sum_i S_i^x$ would imply that the Fisher information is equal to the system size for the Néel state $F_Q^{(t=0)} = L$ and under dephasing dynamics again converges to the system size $F_Q^{(t \rightarrow +\infty)} = L$. The QFI has been experimentally measured in the context of MBL in Ref. [105].

In Fig. 5.12 we have computed the QFI by exact diagonalization. From this we see that the QFI also decays according to a stretched exponential.

5.7 Conclusion and outlook

We have discussed a novel entanglement probe for open quantum systems in the context of many-body localization. We have seen that the third Rényi negativity forms a promising probe to study the entanglement dynamics of an MBL system that is slightly coupled to a dephasing environment. R_3 can distinguish MBL from Anderson up to intermediate

time scales as it reproduces the logarithmic growth of entanglement in the clean MBL system. In addition, we conclude that all quantities, entanglement and transport, decay according to a stretched exponential. However the stretching exponents are found to be smaller for the entanglement quantities, meaning that the late time entanglement dynamics is slower than for instance the dynamics of the imbalance under dephasing.

The quantities $\text{Tr} \rho_{AB}^3$ and $\text{Tr}(\rho_{AB}^{T_B})^3$ are measurable without the need of full state tomography by performing joint measurements on $n = 3$ copies of the state [97, 131–134]. Alternatively, one could link $\text{Tr} \rho_{AB}^n$ and $\text{Tr}(\rho_{AB}^{T_B})^n$ to the statistical correlations of random measurements on a single copy of the state [135], by further developing the measurement protocols proposed for the Rényi entanglement entropies [121, 136–140].

For future work it would be interesting to investigate whether these novel protocols to measure entanglement in open quantum systems could be potentially experimentally as relevant as the protocols to measure Rényi entropies in closed quantum systems. From the theoretical perspective it would be interesting to investigate how R_3 behaves under different forms of dissipation. In particular for non-hermitean types of Lindblad operators it would be interesting to investigate which signatures the entanglement structure of a non-trivial steady state contains.

6 Wannier-Stark localized systems coupled to an environment

Most of the content of this chapter can also be found in the previous publication of the author [2]. Text and figures have been adjusted to fit into the context of the thesis.

Over the past decade there has been a huge research interest in disordered interacting many-body systems. It was realized that these systems could host an MBL phase provided that the disorder is strong enough [20, 23, 69, 116]. This MBL phase is robustly non-thermalizing, and should be contrasted to a single-particle Anderson localized phase occurring in non-interacting systems [71]. While both phases are characterized by the absence of transport, there are also notable differences, most prominently in the entanglement dynamics under a quench. In the Anderson localized system, quantum correlations cannot propagate through the system. Hence the entanglement saturates after a fast ballistic initial growth resulting from local rearrangements of particles. In the interacting MBL system, on the contrary, quantum correlations can propagate in the system but that happens only logarithmically in time [26, 27, 78]. This slow growth can be understood in terms of effective exponentially decaying interactions between so-called LIOMs that form a phenomenological picture to understand MBL [74, 75].

The existence of MBL has been experimentally confirmed [57, 105, 119, 120], and the logarithmic spread of quantum correlations has been observed as well [28, 93, 121, 122]. Recently, there have been many proposals to establish *disorder-free* types of localization [60, 61, 141–149], including for instance lattice gauge theories [148], or mixtures of two types of particles where the light ones are localized on the heavy ones [143–145, 150, 151]. In particular, it has been realized recently that many features of MBL are also inherited by interacting systems subjected to a strong linear potential [60, 61, 79, 80, 152, 153], yet also differences have been identified and understood in terms on Hilbert-space fragmentation [154, 155]. In the non-interacting case this phenomenon is referred to as Wannier-Stark localization [81, 156]; in the interacting case it is referenced to as Wannier-Stark MBL (or shortly Stark MBL in the literature). This type of localization has the advantage that it can potentially be induced solely by the tuning of an external electric field, without the need of engineering internal properties in the system. Experimental signatures of non-ergodic dynamics in systems subjected to a tilted field have been observed in Refs. [157–159], while Ref. [160] was the first experiment that investigated the effect of a tilted potential on the approach to equilibrium.

Typical experiments are never fully isolated from the surrounding environment. This implies that it is hard to distinguish interacting types of localization from non-interacting types of localization. The most prominent difference between the two types is the logarithmic spreading of quantum correlations in the interacting (and isolated) case after a quench. In this work we therefore focus on the entanglement dynamics of interacting and non-interacting Wannier-Stark systems that are coupled to a dephasing Markovian environment. This extends our previous work [1], or previous Chapter 5 where we

considered a similar setup for disorder-induced MBL. Related setups have also been considered to mostly investigate transport properties in Refs. [45–50] (and [1]) in the context of disorder-induced MBL, and in Ref. [51] in the context of Wannier-Stark MBL coupled to a dephasing environment.

Measuring quantum correlations in open systems is challenging both theoretically as well as experimentally. From the theoretical side, it is hard to find generically computable measures that do not rely on a full diagonalization of the (partially transposed) density matrix. We circumvent this problem by considering moments of the partially transposed density matrix and calculate the third Rényi negativity R_3 [94, 95, 97–99] [1], which is not an exact entanglement monotone but which captures the relevant dynamics as it behaves quantitatively similar as the negativity [97] [1]. From the experimental side, it is challenging to measure non-local correlations as full-state tomography is exponentially expensive in the system size, and as joint measurements on multiple copies of the state are also hard to engineer [97, 131–134]. Recently there has been a lot of progress in measuring Rényi entropies in synthetic quantum matter by random unitary measurements [121, 136–140], and this toolbox naturally includes the measurement of mixed state entanglement via Rényi negativities [99].

The remaining of this chapter is organized as follows. In Sec. 6.1, we will introduce the model and setup, as this is closely related to the previous chapter, we will be brief here. In Sec. 6.2 we present our main results, i.e. the MPS calculations of the Rényi negativity. A difference with respect to the previous chapter is that we here investigate other initial states than solely the Néel state. In Sec. 6.3 we show exact diagonalization results, to better understand the late-time decay of the entanglement. In Sec. 6.4 we conclude this chapter.

6.1 Model and setup

Like in the previous Chapter 5, we will consider the XXZ Hamiltonian with an on-site potential

$$H = J \left[\sum_{i=0}^{L-2} \left(S_i^x S_{i+1}^x + S_i^y S_{i+1}^y + \Delta S_i^z S_{i+1}^z \right) \right] + \sum_{i=0}^{L-1} h_i S_i^z, \quad (6.1)$$

where $S_i^{x,y,z}$ are the spin- $\frac{1}{2}$ operators. However now, as on-site potential we take a linear potential with small quadratic corrections of the form

$$h_i = -\gamma i + \alpha i^2 / (L-1)^2 \quad (6.2)$$

to induce Wannier-Stark localization. Here γ gives the slope of the linear potential, and α describes small quadratic corrections to it.

The parameter Δ describes the strength of the nearest-neighbor interactions which can be seen by writing the Hamiltonian (6.1) in terms of spinless fermions by means of the Jordan-Wigner transformation. When there are no interactions present, $\Delta = 0$, the system is ‘single-particle’ Wannier-Stark localized. In the presence of interactions, it is Wannier-Stark many-body localized. We will focus on the weakly interacting regime where $\Delta J < \gamma$ as to avoid resonance effects where e.g. a particle could move up the linear potential without energy cost.

As we have seen in Sec. 2.3.2, localization also occurs in the same model (6.1) for randomly disordered on-site potentials. In the interacting case, there is an MBL phase

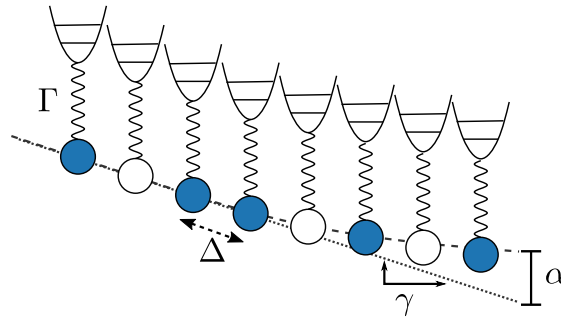


Figure 6.1 A sketch of our setup: A chain of spins (or, equivalently spinless fermions) is subjected to a linear potential with small quadratic corrections, and is uniformly coupled to an environment.

if the disorder is strong enough, i.e. higher than a critical disorder strength under which the system is thermalizing.

The Wannier-Stark model exhibits many similar properties as the model with disorder, e.g. most importantly a slow logarithmic growth of entanglement under a quench, if the linear field γ is sufficiently strong, and if there is some non-uniformity to this linearity [60, 61, 79, 80]. When only a linear field is applied, the (non-interacting) system contains a lot of degeneracies, and therefore properties like the level spacing statistics, can deviate from the ones of the disorder-induced localized systems. By adding a quadratic gradient most of these degeneracies are resolved, and the level-spacing statistics of the two cases are very similar [61].

For these different on-site potentials, we wish to study the exact same setup as in the previous Chapter 5. Hence, we couple the system to a simple, yet realistic [119], Markovian dephasing environment which is modelled by the jump operators $L_i = \sqrt{\Gamma} S_i^z$, such that the time-evolution of the state is again described by the following Lindblad master equation [38]

$$\dot{\rho} = -i[H, \rho(t)] + \Gamma \sum_i \left(S_i^z \rho(t) S_i^z - \frac{1}{4} \rho(t) \right). \quad (6.3)$$

A sketch of our setup is shown in Fig. 6.1. In this setup the goal is again to calculate the third Rényi negativity. This quantity has been introduced in Sec. 3.3.2. In Sec. 4.4 we showed how to calculate it using MPS techniques. We refer to these sections, or to Ref. [1] for further details. Our goal here is to study a global quench by starting from an initial (pure) product state $\rho_0 = |\psi_0\rangle\langle\psi_0|$ where $|\psi_0\rangle$ is a product state in the zero magnetization sector.

6.2 Results

In this section, we discuss our results. In the closed case, we first look at the entanglement dynamics by making a quench from a Néel state, and secondly at the dynamics by making a quench from a random product state in the zero magnetization sector and average over the results. Afterwards, we discuss the results in the open case $\Gamma > 0$.

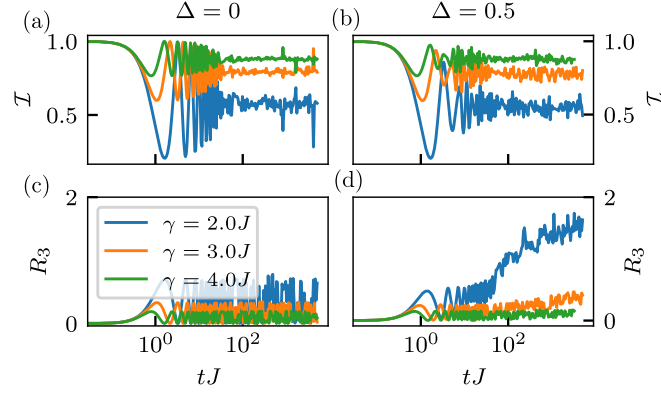


Figure 6.2 The evolution of the imbalance [(a)-(b)] and third Rényi negativity [(c)-(d)] in closed Wannier-Stark localized systems of $L = 24$ sites. The slope of the linear potential γ is given in the legend and the quadratic corrections have a strength of $\alpha = 2J$. The most striking difference between the non-interacting localized case (c) and the interacting localized case (d) is that entanglement can propagate through the system in the interacting case, most notably when the slope of the linear potential is not too strong.

6.2.1 Isolated system

We start by investigating the dynamics of R_3 in the isolated system $\Gamma = 0$. In this case we have that R_3 is directly related to the third Rényi entropy as discussed in the previous section.

Quench from a Néel state

When we start initially from a Néel state $|\downarrow\uparrow\downarrow\uparrow \dots\rangle$, we can track how fast the Wannier-Stark MBL system ‘loses’ information about this initial state pattern. This can be realized by considering a quantity like the imbalance

$$\mathcal{I} = \frac{\langle N_e^z - N_o^z \rangle}{\langle N_e^z + N_o^z \rangle} \quad (6.4)$$

where N_e^z/N_o^z is summing over the occupation numbers $N_i^z = S_i^z + 1/2$ for even/odd sites. For localized systems \mathcal{I} decays to a highly non-thermal (i.e. non-zero) value, and this forms a simple and accessible experimental probe for localization [57]. However, a priori the imbalance decay does not directly allow one to distinguish interacting types of localization from non-interacting types of localization. This is shown in Fig. 6.2, where we show both the imbalance and entanglement dynamics in the interacting ($\Delta = 0.5$) and non-interacting ($\Delta = 0$) cases for various slopes of the linear potential. From this it is clear that only the entanglement dynamics provides a striking difference between the two cases.

Quench from a random initial state

We now consider a random product state in the zero magnetization sector and average the results over the different realizations. This can be seen in Fig. 6.3(a), where we show the logarithmic growth of R_3 for different interaction strengths at field parameters $\alpha = \gamma = 2J$. Without interactions $\Delta = 0$ the system is single-particle Wannier-Stark

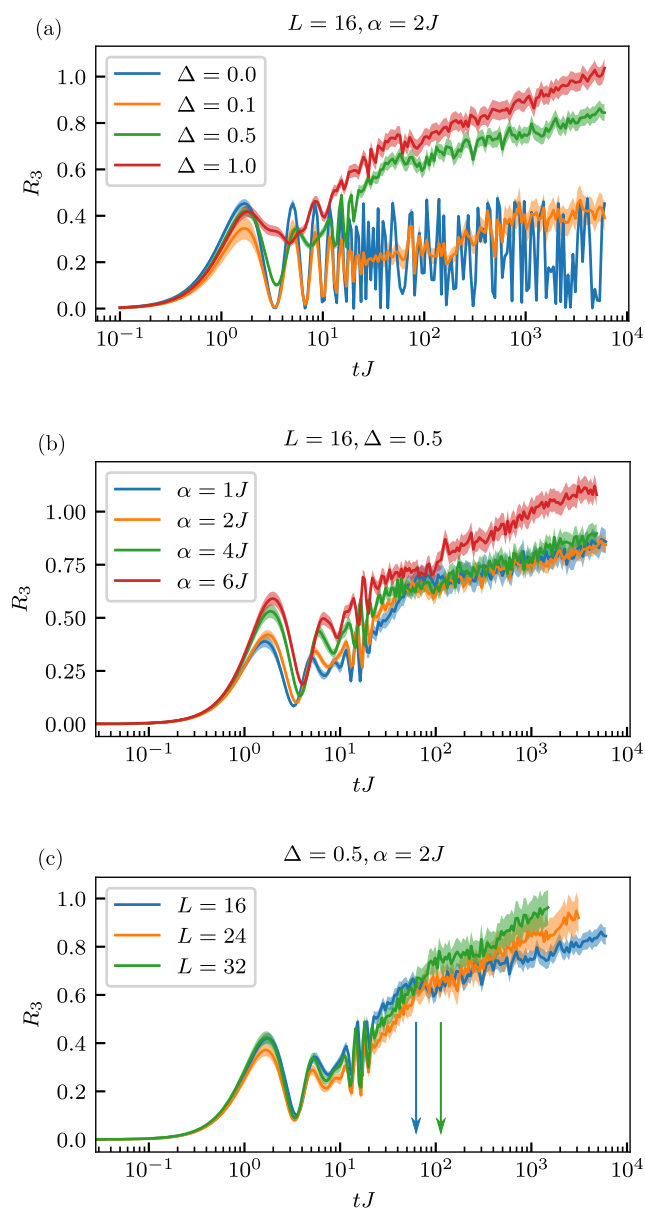


Figure 6.3 The growth of entanglement quantified by the third Rényi negativity (entropy) R_3 in the isolated system. (a) When the system size is fixed, the interactions determine the onset of logarithmic growth. (b) When the potential parameter α is decreased the finite-time cross-over becomes more pronounced. (c) If only the system size is varied, t_{cross} is doubled with system sizes as indicated by the arrows.

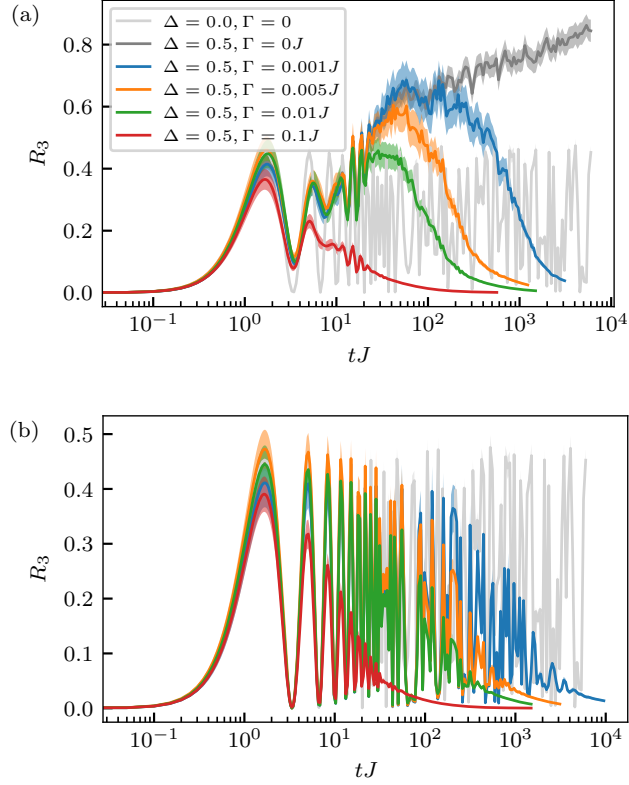


Figure 6.4 The dynamics of R_3 in a Wannier-Stark system of length $L = 16$ with $\alpha = 2J$, $\gamma = 2J$ coupled to a dephasing environment. (a) Interacting case $\Delta = 0.5$, where we show the data for the closed non-interacting case for comparison (light grey line). R_3 reproduces the onset of entanglement growth for sufficiently weak dephasing. (b) Non-interacting case $\Delta = 0$. The coupling strengths are given in the legend. We averaged over about 100 initial states in the $M = 0$ sector for $\Gamma > 0$, and over about 300 states for $\Gamma = 0$ (exact diagonalization was used in this case).

localized and entanglement cannot propagate through the system. Fluctuations are stronger in the non-interacting limit, as the level spacing is only inversely proportional to the system size. The time scale at which the effect of the interactions becomes dominant is set by $t_{\text{int}} \sim (\Delta J)^{-1}$. In the data obtained for finite interactions, a cross-over time-scale t_{cross} becomes apparent, which is absent in the case of disorder-induced MBL, where there is a faster logarithmic growth, after the initial ballistic growth up to times $tJ \sim 1$. Beyond this cross-over regime, there is then a slower, logarithmic growth. We attribute the existence of this cross-over regime to the quadratic contribution of the potential of strength α in (6.2). When increasing the quadratic deviations, the cross-over regime becomes less pronounced, as we show in Fig. 6.3(b).

In Fig. 6.3(c) we show the logarithmic growth at one particular interaction strength $\Delta = 0.5$ for various system sizes. Also, t_{cross} is doubled when the system size is doubled which confirms that the parameter α of our local potential (6.2) is indeed governing t_{cross} . When increasing system size, α thus has to be rescaled accordingly when considering the in the literature commonly used form of the local potential [61].

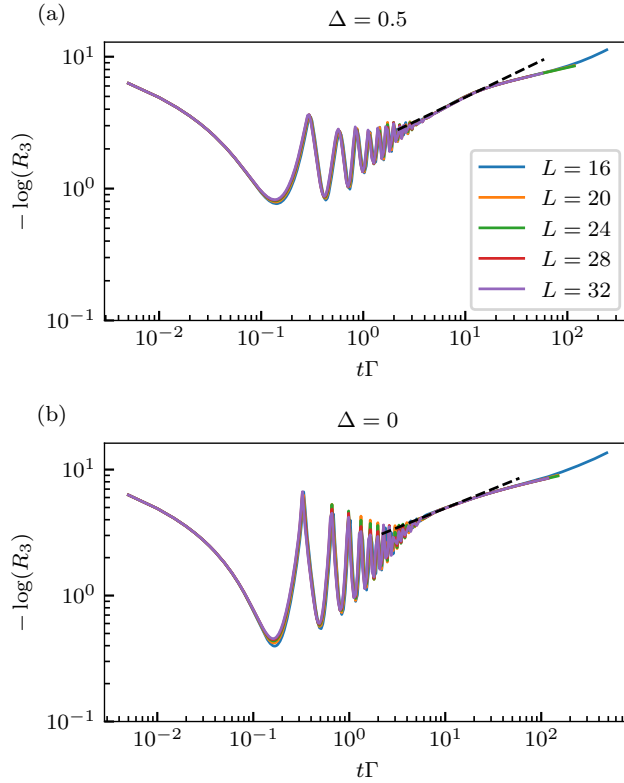


Figure 6.5 The dynamics of R_3 in a Wannier-Stark system with $\alpha = 2J$, $\gamma = 2J$ coupled to a dephasing environment under a quench from the Néel state. The black dashed lines are stretched-exponential fits to intermediate-time regime of $L = 16$. (a) Interacting case $\Delta = 0.5$, the slope of the fit shown is $b \approx 0.37$. (b) Non-interacting case $\Delta = 0$, the slope of the fit shown is $b \approx 0.31$. In both cases the late-time dynamics deviates from stretched exponential decay.

6.2.2 Open System

We now turn to the investigation of the dynamics of R_3 in the open system $\Gamma > 0$. When the system is coupled to a dephasing environment, all entanglement structure will be eventually lost as the system heats up to the infinite temperature state. The time scale on which the dephasing starts to dominate the dynamics is set by the coupling strength $t_{\text{deph}} \sim 1/\Gamma$. In order to allow that the interactions can still dominate the dynamics at intermediate times, we need to have that $t_{\text{int}} \ll t \ll t_{\text{deph}}$ which implies that we must have that $\Gamma/J \ll \Delta$. Hence, the dephasing strength must be sufficiently weak compared to the interaction strength to be able to still observe signatures of the logarithmic entanglement growth. In Fig. 6.4 we show the entanglement dynamics for various coupling strengths. One of the main advantages of looking at the Rényi negativity R_3 is that we can capture the logarithmic growth of quantum correlations even if the system becomes slightly mixed. This onset of logarithmic growth can indeed be still observed for sufficiently weak dephasing strengths in Fig. 6.4(a). In principle, for characterizing interacting dynamics it is sufficient that the entanglement reaches a value that is higher than the maximal value of the oscillations in the non-interacting case. The decay of R_3 in the non-interacting case is shown in Fig. 6.4(b) for comparison.

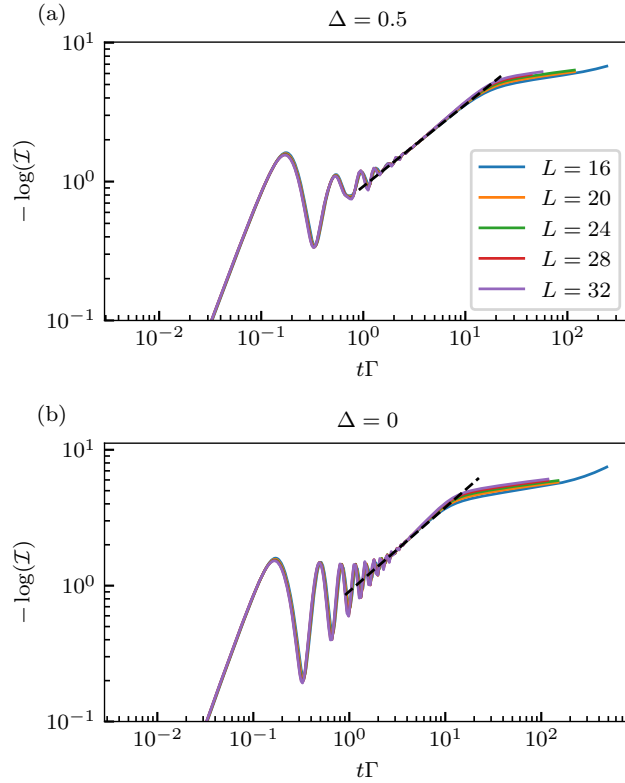


Figure 6.6 The dynamics of the imbalance in a Wannier-Stark system with $\alpha = 2J$, $\gamma = 2J$ coupled to a dephasing environment under a quench from the Néel state. The black dashed lines are stretched-exponential fits for $L = 16$. (a) Interacting case $\Delta = 0.5$, the slope of the fit shown is $b \approx 0.59$. (b) Non-interacting case $\Delta = 0$, the slope of the fit shown is $b \approx 0.62$. Again, in both cases the late-time dynamics is incompatible with stretched exponential decay.

From disordered MBL it is known that the tails of the decay of the imbalance [46, 47] and the negativity or R_3 [1] are stretched exponentials $\sim e^{-(\Gamma t/a)^b}$ with $b < 1$. These stretched exponentials are in that case understood as a superposition of many local exponential decays [46], originating from very broad distributions of exponentially decaying couplings in the phenomenological LIOMs picture of MBL [74, 75, 125]. However, the Wannier-Stark case is disorder free, which could therefore lead to a different behavior of the tails of the decay. In the non-interacting case, such a difference has been reported in the decay of the imbalance in Ref. [51].

In Fig. 6.5 and Fig. 6.6, we show the decay of respectively R_3 and the imbalance under a quench from the Néel state with $\Gamma = 0.1$. These figures have a double logarithmic scale on the y -axis and single logarithmic scale on the x -axis, such that a stretched exponential $\sim e^{-(\Gamma t/a)^b}$ would appear as a straight line with b the slope, and a related to the offset. We have fitted stretched exponentials to the data in the intermediate-time regime. However, in the late-time regime, the functional form of the decay changes. For small system sizes, exponential decay can be observed at late times as we illustrate in Sec. 6.3. Here, we also demonstrate that averaging over initial states does not lead to a quantitatively different behavior in the decay of R_3 .

In Ref. [51] they report that the decay of the imbalance happens according to an exponential in the non-interacting case, while in the interacting case it happens according to a stretched exponential. They however consider much stronger tilts and interactions. As we focus here on a more moderate regime of weaker tilts and weak interactions as relevant for experiments [79], we can not distinguish qualitative differences between both cases in the late-time dynamics.

6.3 Understanding the late-time dynamics by exact diagonalization

In this Section, we present some exact diagonalization data, obtained by numerically integrating the Lindblad Equation (6.3) for a small system of $L = 8$ sites. In Fig. 6.7 we show the collapse of the tails for various coupling strengths Γ for a quench starting from the Néel state. We have fitted stretched exponentials $\sim e^{-(\Gamma t/a)^b}$ in the intermediate-time regime, and exponentials $\sim \alpha e^{-\Gamma t/\beta}$ in the late-time regime. In Fig. 6.9 we show the same data in a different scale that makes the exponential form of the late-time tails clearly visible. In Fig. 6.8 and Fig. 6.10, we show the data when we average over different initial states. From this, it is clear that the averaging does not alter the behavior of the tails quantitatively, e.g. the best-fit stretching exponents in the intermediate-time regime stay very similar as can be seen by comparing Fig. 6.7 and Fig. 6.8.

6.4 Conclusion and outlook

We have investigated the dynamics of entanglement in a non-interacting Wannier-Stark localized and in an interacting Wannier-Stark MBL system. In the closed case, we have observed a cross-over regime that is absent in the case of disordered MBL and that is related to the quadratic corrections from linearity of the field. In the open system with dephasing noise, it is possible to still observe parts of the characteristic logarithmic growth for sufficiently weak dephasing strengths.

Our results confirm that the Wannier-Stark MBL system indeed inherits many properties from the disordered MBL system in particular when considering the entanglement dynamics coupled to an environment. However, we do not observe a robust stretched-exponential functional form of the entanglement decay in the Wannier-Stark case.

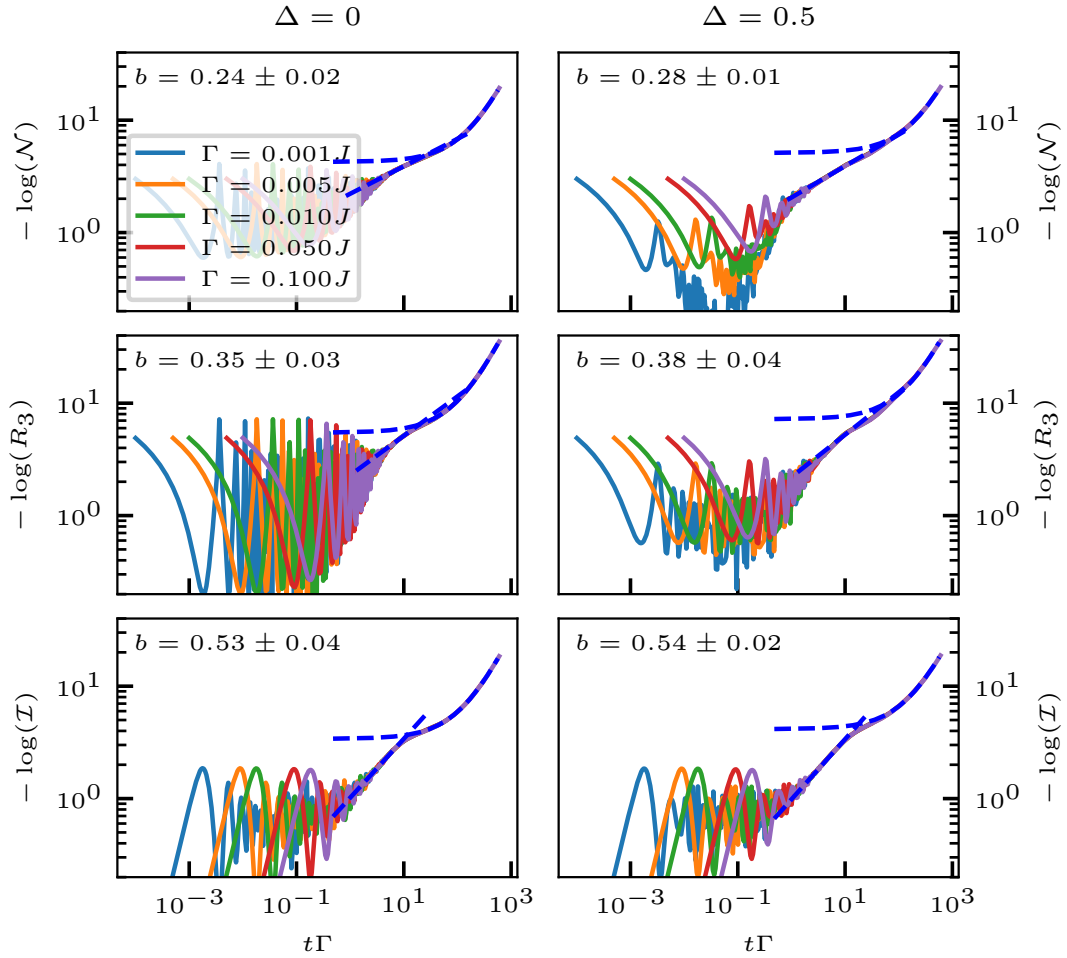


Figure 6.7 The dynamics of the negativity, R_3 , and the imbalance for a system of $L = 8$ sites under a quench starting from the Néel state. The tilted potential is characterized by $\alpha = \gamma = 2J$. The non-interacting ($\Delta = 0$) and interacting ($\Delta = 0.5$) cases are shown. The blue dashed lines show a stretched-exponential fit $\sim e^{-(\Gamma t/a)^b}$ for the intermediate-time regime and an exponential fit for the late-time regime. The stretching exponent b is written inside the panels with 3σ confidence level.

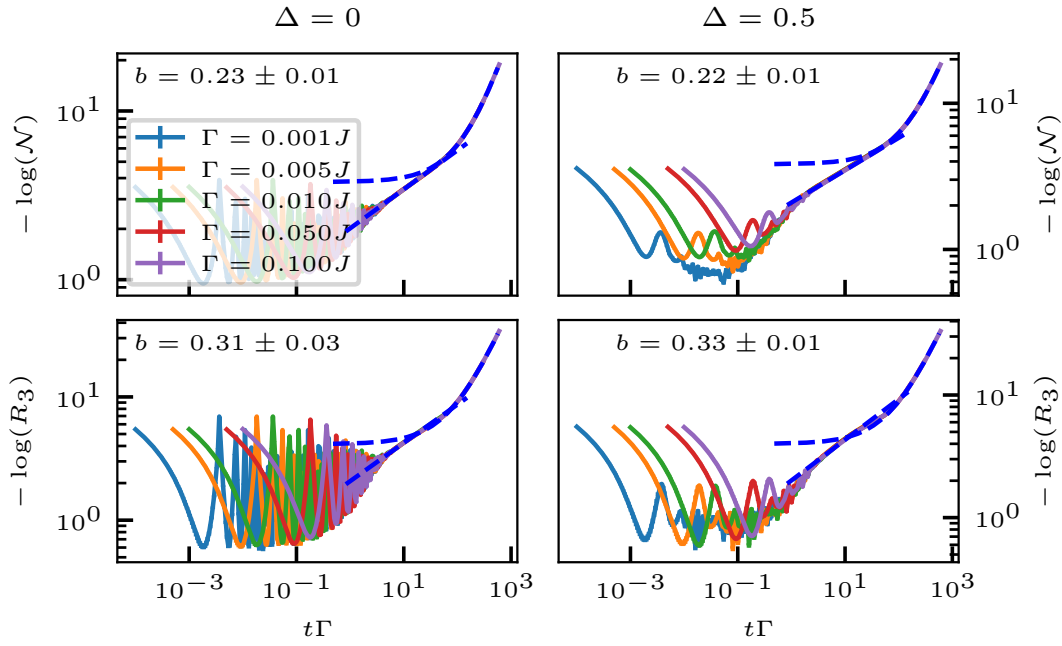


Figure 6.8 The dynamics of the negativity and R_3 for a system of $L = 8$ sites under a quench starting from a random initial state. Averages are taken over initial product states in the $M = 0$ sector. The tilted potential is characterized by $\alpha = \gamma = 2J$. The non-interacting ($\Delta = 0$) and interacting ($\Delta = 0.5$) cases are shown. The blue dashed lines show a stretched-exponential fit $\sim e^{-(\Gamma t/a)^b}$ for the intermediate-time regime and an exponential fit for the late-time regime. The stretching exponent b is written inside the panels with 3σ confidence level.

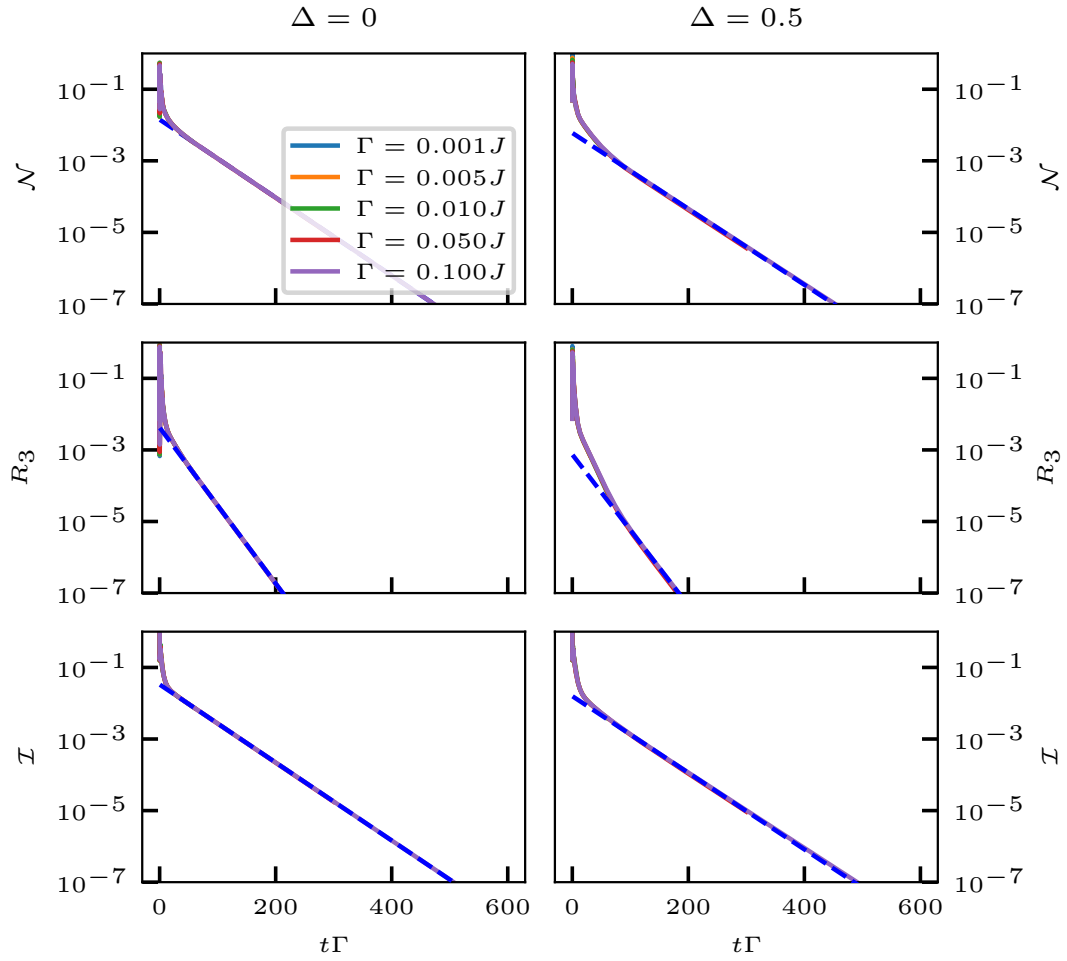


Figure 6.9 The same data as in Fig. 6.7 but in a different scale to make the exponential form of the tails visible.

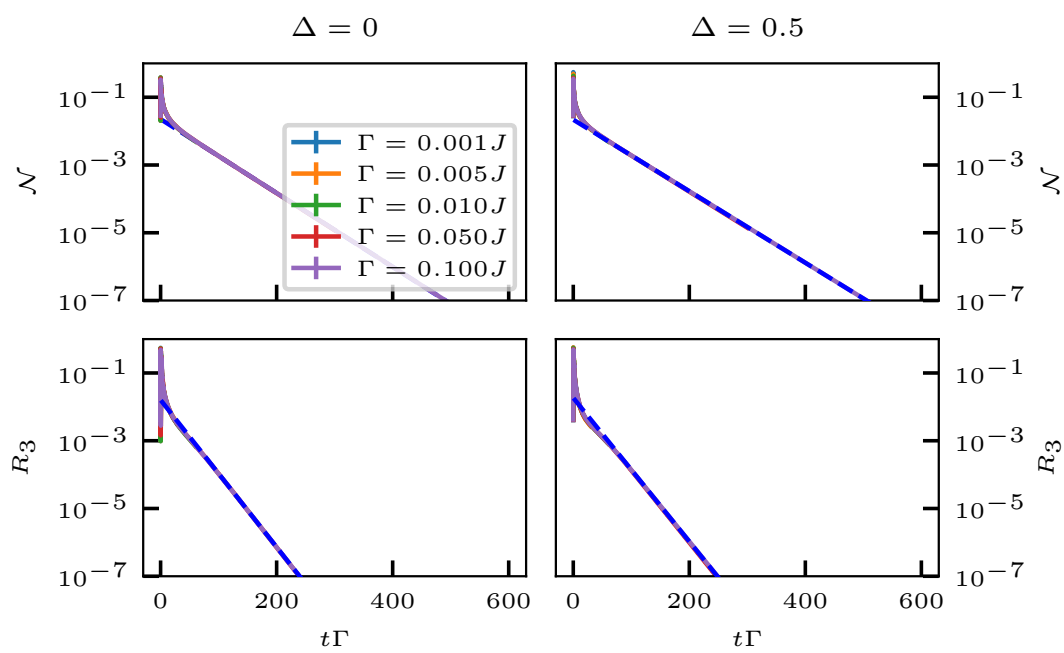


Figure 6.10 The same data as Fig. 6.8 but in a different scale to make the exponential form of the tails visible.

7 Entanglement of quasiparticles

Most of the content of this chapter can also be found in a previous publication of the author [3]. Text and figures have been adjusted to fit into the context of the thesis. Additionally, some results of Ref. [4] have been incorporated in Sec. 7.2.

Considerable progress has been made over the past decades in understanding the nature of the entanglement behavior in many-body systems from a quantum information perspective [33, 34, 161–172]. An example is the topological entanglement entropy whose scaling exhibits a correction to the area law as a manifestation of topological order [173, 174]. Following this identification, it was proposed that SPT phases can be characterized by the presence of fractionalized modes in the entanglement spectrum. These transform differently under the symmetry group from the constituent microscopic degrees of freedom of the system [18, 24, 164, 165, 167–171, 175–179]. The relation between the topological structure and the entanglement spectrum has been widely explored since then [164, 165, 167–171, 179]. Remarkably, most topological properties, including quasiparticle statistics, edge excitations, central charge and topological Berry phase can be reached by scrutinizing the entanglement spectrum [172, 179–182]. Such correspondences provide a powerful tool to explore quantum phases or critical points from a quantum information perspective, and have been successful in describing a wide variety of exotic states or phase transition phenomena [162, 172, 183].

While the entanglement structure for the quantum many-body ground state has been widely explored, much less is known about the entanglement structure of the quasiparticles at low energy [184–191]. In particular, the universal entanglement features of low-energy quasiparticle states in diverse phases remain unclear and leave important open questions. It is widely accepted that the ground state encodes essential topological features of the phase. In this respect, does the quasiparticle inherit similar features? Can we distinguish two phases via their low-energy quasiparticles instead of the ground state? How to reveal the symmetry and internal structure of quasiparticles from their entanglement spectrum?

In this chapter, we present an entanglement protocol to detect various quasiparticles in one-dimensional systems with short-range correlations. In accordance with the results for the entanglement of the ground state in topological phases [24, 25], we anticipate that the entanglement spectrum of the low-energy quasiparticle can also differentiate and distinguish topological from trivial phases. In particular, we propose an *entanglement fragmentation* feature for quasiparticle states in free-fermion SPT phases with weak interactions, as a consequence of the hybridization between edge zero mode and bulk zero modes in the quasiparticle entanglement Hamiltonian.

Afterwards, we study the quasiparticles in strongly-interacting SPT chains, and develop a conditional MI protocol to characterize those quasiparticles. In particular, we show that the non-vanishing conditional mutual information indicates the emergence of non-local quantum orders, either in the ground state or in a low-energy quasiparticle state. While a non-local order parameter is operator dependent, and hence hard to iden-

tify for a general state, the conditional mutual information is directly accessible from the reduced density matrix, and easy to measure in numerical simulations. In addition, we also propose a protocol based on the measurement induced long-range entanglement to identify distinct **SPT** quasiparticles with potential experimental accessibility in cold atom setups [121, 134, 138, 192–194].

The structure of this chapter is as follows. In Sect. 7.1 we start by discussing the correlation matrix spectra of quasiparticle states in *non-interacting* systems based on Peschel’s approach [164], and illustrate the ideas by studying the paradigmatic *trivial* SSH model. In Sect. 7.2 we extend the discussion to *interacting* systems, and develop criteria for the degeneracy of the many-body quasiparticle entanglement spectrum based on the presence of reflection symmetry in combination with specific (e.g. Z_2) charges. In the scope of this section, we also briefly reiterate the results of Ref. [4] and show some of the numerical data. In this section we will study the **TFI** with an integrability breaking perturbation (which also makes the model interacting), and the *trivial interacting* SSH model.

Next we will focus on *topologically non-trivial models*. In Sect. 7.3 we discuss the universal *fragmentation feature* in the entanglement spectrum of quasiparticle states in topological free-fermion systems. We will illustrate this for the *topological* SSH model. In Sect. 7.4 we study the conditional **MI** and measurement-induced **MI** for the ground state and quasiparticle states of (interacting) **SPT** phases. In particular, we show that both quantities provide feasible ways to probe **SPT** phases, not only via ground states but also via quasiparticle states. In this section, we will study the cluster model.

7.1 Correlation matrix approach for quasiparticle entanglement

In this section, we present a general framework to bridge the connection between the correlation matrix and the single-particle entanglement spectra for quasiparticle states in *non-interacting systems*, under a spatially symmetric bipartition, and study the *trivial* SSH chain as a concrete example.

Previous work on the correspondence of the correlation matrix and entanglement Hamiltonian for free theory was carried out in Ref. [164, 169, 195]. It was shown that the entanglement Hamiltonian for a gapped insulator is like a Hamiltonian matrix (with open boundary at the cut) where the states above/below the gap are flattened to energies ∞ and $-\infty$ respectively. Besides, if the insulator displays a topological band structure, its single-particle entanglement Hamiltonian contains an in-gap mode at zero energy related to the edge mode in the physical Hamiltonian. This implies that, even without access to the full band structure, the entanglement spectrum can determine the band topology by analyzing the reduced density matrix of the ground state.

We begin our discussion by reviewing Peschel’s approach [164] for calculating the entanglement spectrum of a free-fermion system with trivial band topology by means of the correlation-matrix method. For a non-interacting system where the Hamiltonian can be expressed in terms of fermion bi-linears, the reduced density matrix with respect to region A can be written as

$$\rho_A = e^{-H_A}/Z, \quad (7.1)$$

where the constant Z is chosen such that $\text{Tr} \rho_A = 1$. Here H_A is the so-called *entanglement Hamiltonian*. In this way the properties of the reduced density matrix can be

reformulated in terms of thermodynamic properties of the entanglement Hamiltonian. Then the correlation matrix for subsystem A can be obtained as,

$$C_{ij}^A = \langle c_i^\dagger c_j \rangle_{i,j \in A} = \text{Tr} [c_i^\dagger c_j \rho_A] = \text{Tr} [c_i^\dagger c_j e^{-H_A}] / Z. \quad (7.2)$$

The entanglement Hamiltonian can be diagonalized in terms of new fermion operators $(\tilde{c}_\alpha, \tilde{c}_\alpha^\dagger)$ which relate to the old ones by a canonical transformation

$$H_A = \sum_{\alpha} e_{\alpha} \tilde{c}_{\alpha}^{\dagger} \tilde{c}_{\alpha}, \quad (7.3)$$

where e_{α} is the single-particle energy level of the entanglement Hamiltonian.

Since the entanglement Hamiltonian represents a free-fermion theory, the expectation values of charge operators obey Fermi-Dirac statistics. We can then diagonalize the correlation matrix in terms of the new basis

$$\langle \tilde{c}_{\alpha}^{\dagger} \tilde{c}_{\alpha} \rangle_{GS} = \text{Tr} [\tilde{c}_{\alpha}^{\dagger} \tilde{c}_{\alpha} e^{-H_A}] / Z = \frac{1}{1 + e^{e_{\alpha}}}, \quad (7.4)$$

from which it follows that the eigenvalues of the correlation matrix p_{α} are related to the single-particle spectrum of H_A as

$$e_{\alpha} = \log [(1 - p_{\alpha}) / p_{\alpha}]. \quad (7.5)$$

The many-body entanglement spectrum is the union of the quasienergies of all possible filled states, $E = \sum_{\alpha} n_{\alpha} e_{\alpha}$. If the energy level of H_A resembles a gapped insulator, the many-body entanglement spectrum also exhibits a gap.

As the correlation matrix has eigenvalues $p_{\alpha} = 0, 1$ for an insulating ground state, the entanglement Hamiltonian H_A has a finite gap for the bulk orbitals. For now, we focus solely on a trivial band insulator whose ground state entanglement Hamiltonian H_A does not carry any in-gap state. We will return to the cases of topological insulators with in-gap states in Sect. 7.3.

Now we add a quasiparticle from the conducting band to the ground state and make a center symmetric cut to obtain the subsystem A . We calculate the correlation matrix based on the quasiparticle state with momentum k ,

$$\begin{aligned} C_{ij}^{QP} &= \langle QP | c_i^\dagger c_j | QP \rangle_{i,j \in A} \\ &= \langle GS | \frac{1}{\sqrt{2}} (a_A^k + a_B^k) c_i^\dagger c_j \frac{1}{\sqrt{2}} (a_A^{k\dagger} + a_B^{k\dagger}) | GS \rangle_{i,j \in A} \end{aligned} \quad (7.6)$$

where $a_A^{k\dagger} = \frac{1}{\sqrt{L/2}} \sum_{i \in A} e^{ikr_i} a_i^\dagger$ is the operator which creates an excited state with momentum k in the A region. a_i^\dagger represents the Wannier orbital in the upper-band, as this orbital might involve a linear combination of the degrees of freedom among several sites, there are some a_i^\dagger operators near the cut sitting in both the A and B region. However, these operators can be ignored in the thermodynamic limit as they only carry a weight proportional to $\frac{1}{\sqrt{L}}$. Therefore,

$$\begin{aligned} C_{ij}^{QP} &= \langle QP | c_i^\dagger c_j | QP \rangle_{i,j \in A} \\ &= \frac{1}{2} [\langle GS | c_i^\dagger c_j (1 - a_B^{k\dagger} a_B^k) | GS \rangle_{i,j \in A} + \langle GS | a_A^k c_i^\dagger c_j a_A^{k\dagger} | GS \rangle_{i,j \in A}] \\ &= \frac{1}{2} [\langle GS | c_i^\dagger c_j | GS \rangle_{i,j \in A} + \langle GS | a_A^k c_i^\dagger c_j a_A^{k\dagger} | GS \rangle_{i,j \in A}], \end{aligned} \quad (7.7)$$

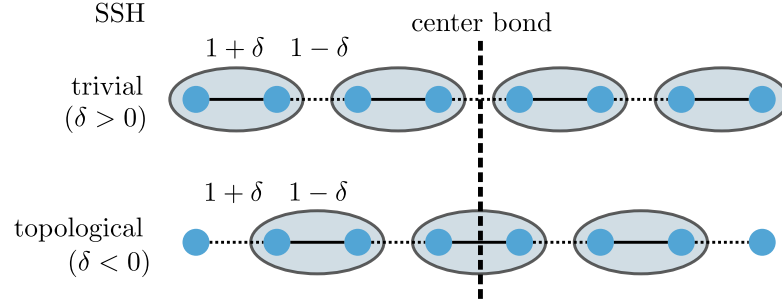


Figure 7.1 A sketch of the SSH model in our setup: we consider chains of length $L = 4m$ (with m integer), such that we have an even number of unit cells in the trivial phase and an odd number in the topological phase. In the trivial phase the center bond is weak, while in the topological phase it is strong.

and if we diagonalize the correlation matrix in terms of the basis \tilde{c}_α , we obtain the eigenvalues p_α of the correlation matrix

$$p_\alpha = \frac{1}{2} \left[\langle GS | \tilde{c}_\alpha^\dagger \tilde{c}_\alpha | GS \rangle_{i,j \in A} + \langle GS | a_A^k \tilde{c}_\alpha^\dagger \tilde{c}_\alpha a_A^{k\dagger} | GS \rangle_{i,j \in A} \right] \quad (7.8)$$

$$= \begin{cases} 1, & \alpha \in \text{filled orbitals} \\ 0, & \alpha \in \text{empty orbitals} \\ 1/2, & \alpha \in \text{QP orbitals.} \end{cases}$$

The eigenvalues of the correlation matrix with respect to the quasiparticle state have three types of eigenstates. For filled (or empty) orbitals, it remains 1 (or 0) like the correlation matrix of the ground state. The additional quasiparticle orbital generates an eigenvalue $p_\alpha = 1/2$ independent of the momentum of the quasiparticle. This $p_\alpha = 1/2$ mode can be understood as the position uncertainty of the quasiparticle: with a probability 1/2 the quasiparticle is in region A/B and this thus creates an additional contribution to the entropy. Based on the correspondence in Eq. (7.5), this additional $p_\alpha = 1/2$ mode is equivalent to the statement that the entanglement Hamiltonian H_A^{QP} contains an exact zero mode $e_\alpha = 0$ inside the gap for the quasiparticle in a trivial system (this is illustrated in Fig. 7.2(b) for the trivial SSH chain, see below). As the $p_\alpha = 1/2$ mode signals that the quasiparticle is extended in region A , the in-gap mode in the entanglement Hamiltonian denotes an extended bulk state in H_A^{QP} so the entanglement Hamiltonian for the quasiparticle resembles a metallic system with one conducting state in the bulk. In the presence of such in-gap zero mode, the many-body entanglement spectrum $\{E = \sum_\alpha n_\alpha e_\alpha\}$ exhibits a two-fold degeneracy for all energy levels as a consequence of the empty/filled in-gap state (see also Fig. 7.3).

We illustrate the theorem by simulating the one-dimensional SSH model (Su-Schrieffer-Heeger [196])

$$H = \sum_{i=0}^{L-1} \left((1 + \delta) c_{2i}^\dagger c_{2i+1} + (1 - \delta) c_{2i+1}^\dagger c_{2i+2} + \text{h.c.} \right) + V(n_0 + n_{L-1}), \quad (7.9)$$

with $V > 0$. For $\delta < 0$ this model has weak bonds on the edges and is topological, while for $\delta > 0$ it is trivial and resembles an atomic insulator. We will always simulate chains

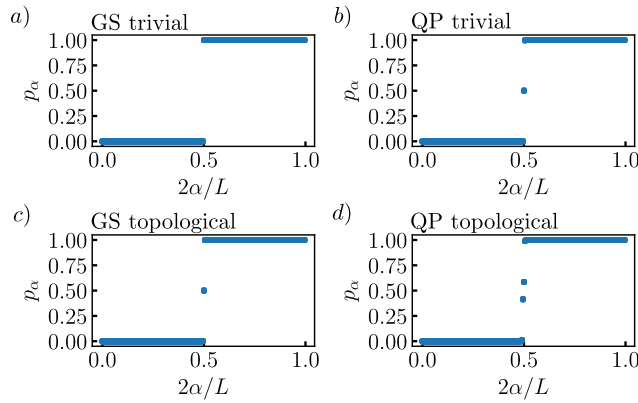


Figure 7.2 The correlation matrix spectra of the ground state and quasiparticle in the SSH chain. The simulations are performed on chains of $L = 400$ sites, but we rescaled the number of states with the system size as the results are universal. a) For the ground state in the trivial phase no in-gap states are present, half of the orbitals are filled and half are empty. b) There is an in-gap state for the quasiparticle in the trivial phase which is an extended bulk state reflecting the position uncertainty of the quasiparticle. c) There is also an in-gap state for the ground state in the topological phase but this one is due to the protected boundary modes. d) For the quasiparticle in the topological phase there are two in-gap states, one reflecting the bulk mode and one the boundary mode. Note that when δ approaches zero (from the negative side, as we are in the topological phase) the two in-gap states move further apart, which represents further mixing of the bulk/boundary modes. They can only disappear into the empty or filled orbitals by crossing the phase transition point at $\delta = 0$.

of length $L = 4m$ (with m integer) such that the center bond is always weak (strong) in the trivial (topological) phase, and such that there is an even number ($2m$) of two-site unit cells in the trivial phase. These properties are summarized in Fig. 7.1. We additionally choose to add a boundary field V in order to lift the four-fold degeneracy of the ground state in the topological regime. This does not change the physics.

Here, we will demonstrate the above statements for the *trivial* SSH case, and delay the discussion of the topological phase to Sect. 7.3. In the trivial phase the ground state is located at half filling such that the correlation matrix spectrum will just consists of zeros and ones, as shown in Fig. 7.2(a). We then create a quasiparticle state by adding an additional orbital with zero-momentum from the empty band. The resultant correlation matrix spectrum is shown in Fig. 7.2(b). The in-gap metallic state is clearly visible, and indicates the quasiparticle position uncertainty as outlined above. For that reason the many-body entanglement spectrum is also two-fold degenerate for all levels as shown in Fig. 7.3(a).

Our current argument relies on the fact that the system is non-interacting, and that the quasiparticle originates from a band with trivial topology. For quasiparticle states in topological insulators or superconductors, the band topology adds more variation to their entanglement structure. In particular, here the entanglement Hamiltonian of the ground state already contains an in-gap state which resembles the gapless edge mode (see Fig. 7.2(c)). In the forthcoming discussion in Sec. 7.3, we will discuss a universal fragmentation structure of the quasiparticle entanglement spectrum in topological band theory as a consequence of the level mixing between the edge mode and the quasiparticle.

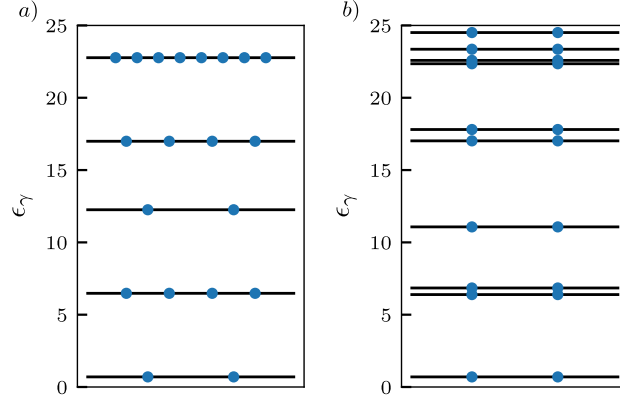


Figure 7.3 The entanglement spectrum of the first excited state in the trivial SSH model on a chain with $L = 20$ sites with $\delta = 0.5$. a) The non-interacting case with $U = 0$. b) The interacting case with $U = 0.2$. Both entanglement spectra exhibit two-fold degeneracy in all energy levels.

7.2 Degeneracy theorem for the quasiparticle entanglement spectrum

In the previous section, we saw for a free-fermion system with trivial topology, that the double degeneracy of the entanglement spectrum is manifested by exact zero modes in the single-particle entanglement Hamiltonian. When it comes to the *interacting* system, it remains unclear whether the degeneracy of the quasiparticle entanglement spectrum would persist as the entanglement Hamiltonian cannot be reduced to a single particle operator.

In this section, we develop a universal criterion for the degeneracy of the quasiparticle entanglement spectrum based on a Kramers theorem. The basic idea can be traced back to our previous work, Ref. [4], where we examined the symmetry representation of the quasiparticle reduced density matrix. For instance, if the reduced density matrix has a projective representation under a symmetry G , the entanglement spectrum must display a degeneracy for all energy levels. We will study some concrete cases in the remainder of this section.

7.2.1 Quasiparticles with Z_2 charge and reflection symmetry

To set the stage, we reiterate the quasiparticle entanglement spectrum degeneracy theorem in the paramagnetic phase of the one-dimensional perturbed TFI of Ref. [4]. There we considered the TFI model with an integrability breaking perturbation

$$H = \sum_i (J_z \sigma_i^z \sigma_{i+1}^z + h_x \sigma_i^x + J_x \sigma_i^x \sigma_{i+1}^x), \quad (7.10)$$

and consider the regime where $h_x > J_z \gg J_x$ such that the ground state is polarized in the x direction and the quasiparticle, which we will refer to as a Z_2 magnon, is generated by a local spin flip operator $Q_i = \sigma_i^z$. This operator creates a Z_2 charge measured by the parity operator $P = \prod_i \sigma_i^x$. Away from the extreme paramagnetic limit Q_i remains an odd operator under Z_2 but now spreads out over a correlation length ξ . With periodic

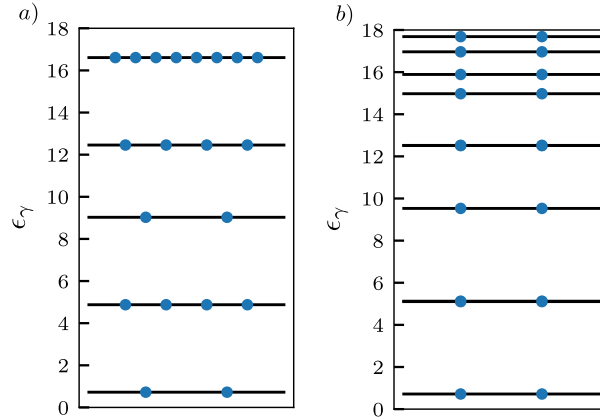


Figure 7.4 The entanglement spectrum of the first excited state in the PM Ising model (18 sites, $h_x = 1.5$). a) The non-interacting case with $J_x = 0$. b) The interacting case with $J_x = 0.2$. Both entanglement spectrum exhibit two-fold degeneracy in all energy levels.

boundary conditions, the system is translationally invariant and the low-energy magnon states are momentum eigenstates of the form [185],

$$|\psi^{1M}\rangle_k = \sum_i e^{ikr_i} Q_i |\text{GS}\rangle \quad (7.11)$$

where we have ignored the subleading k dependence of the operator Q_i itself.

We now consider the entanglement spectrum of the magnon at $k = 0$, defined as $\epsilon_\gamma = -\log \lambda_\gamma^2$, which is obtained from a Schmidt decomposition

$$|\psi^{1M}\rangle = \sum_\gamma \lambda_\gamma |\gamma_A\rangle |\gamma_B\rangle. \quad (7.12)$$

Here λ_γ^2 are the eigenvalues of the reduced density matrices $\rho_{A/B}$ of two subsystems. For a reflection symmetric cut, the entanglement spectrum exhibits an *exact* two-fold degeneracy. As is pointed out in Ref. [4], this exact degeneracy of the Schmidt values arises from a combination of the reflection symmetry $R|\psi^{1M}\rangle = |\psi^{1M}\rangle$ and the non-trivial Z_2 charge of the magnon $P|\psi^{1M}\rangle = -|\psi^{1M}\rangle$.

Indeed, assume that the entanglement spectrum contains a non-degenerate eigenvalue λ_γ . Then the fact that the state $|\psi^{1M}\rangle$ is symmetric under R implies $|\gamma_A\rangle = R|\gamma_B\rangle$ up to a $U(1)$ phase. However, as the quasiparticle state carries an odd charge parity we have that $P|\psi^{1M}\rangle = -|\psi^{1M}\rangle$, hence $|\gamma_A\rangle$ and $|\gamma_B\rangle$ must have opposite parity eigenvalues. This leads to a contradiction with the requirement $|\gamma_A\rangle = R|\gamma_B\rangle$ as R does not change this charge. Consequently, all Schmidt values have to be degenerate. This is illustrated in Fig. 7.4 for both the non-interacting ($J_x = 0$) and interacting ($J_x \neq 0$) case.

We now consider a bipartition of the system (with periodic boundary conditions) into two equal regions. Due to the position uncertainty of the magnon, the entanglement excess of the quasiparticle with respect to the ground state is given by

$$S^{1M} = S^{\text{GS}} + \log(2) + \mathcal{O}(1/L), \quad (7.13)$$

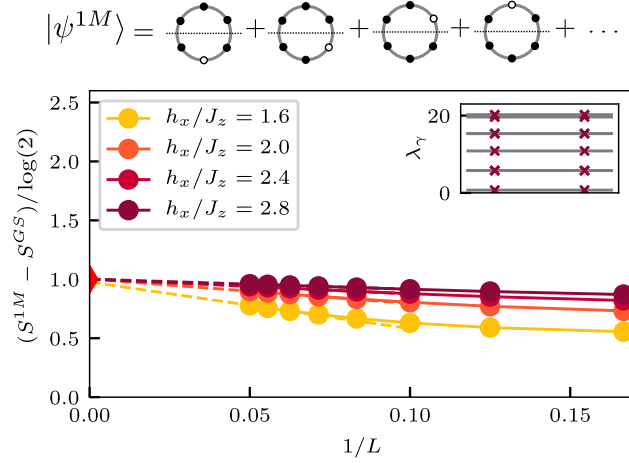


Figure 7.5 Entanglement excess of the single magnon state with respect to the ground state in the paramagnetic phase of the TFI with $J_x/J_z = 0.1$ for a reflection symmetric bipartition. The red marker on the y-axis shows the expected $\log(2)$ excess. Inset: The two-fold degeneracy of the entanglement spectrum is protected by the reflection symmetry.

irrespective of k and irrespective of the exact ratio h_x/J_z of the Hamiltonian parameters. For a finite correlation length, there is a finite probability of the magnon reaching across the cut, yielding the $\mathcal{O}(1/L)$ corrections. However, in the thermodynamic limit, the additional entanglement entropy created by the magnon is $\log(2)$, corresponding to one bit, as illustrated in Fig. 7.5.

7.2.2 Quasiparticles with Z_2 charge and translation symmetry

The arguments in our previous section can be generalized to magnon quasiparticle states with $k \neq 0$ where instead of reflection we can use translations over half the system size $T_x = e^{ikL/2}$ and impose periodic boundary conditions. We now consider the magnon entanglement spectrum of the quasiparticle at k , defined as $\epsilon_\gamma = -\log \lambda_\gamma^2$, which is obtained from a Schmidt decomposition,

$$|\psi^{1M}\rangle_k = \sum_\gamma \lambda_\gamma |\gamma_A\rangle |\gamma_B\rangle. \quad (7.14)$$

Again, we begin by assuming that the entanglement spectrum contains a non-degenerate eigenvalue $\lambda_{\gamma'}$. The state $|\psi^{1M}\rangle$ being symmetric under T_x implies $|\gamma'_A\rangle = R|\gamma'_B\rangle$ up to a phase factor. So the pattern $\lambda_{\gamma'} |\gamma'_A\rangle |\gamma'_B\rangle$ carries even charge parity. This leads to a contradiction with the fact that the quasiparticle $|\psi^{1M}\rangle_k$ carries odd charge parity. Consequently, all Schmidt values have to be degenerate.

7.2.3 Non-local quasiparticles without Z_2 charge

Now we turn to the ferromagnetic phase of the TFI model, see Eq. (7.10). In this phase, the Z_2 symmetry is broken and the ground state is double degenerate in the thermodynamic limit. The fundamental excitations are now domain walls, which do *not* carry a Z_2 charge and which are non-local defects between $|0\dots 0\rangle$ and $|1\dots 1\rangle$ states. Clearly, creating a domain wall is a non-local operation. As we would like to study

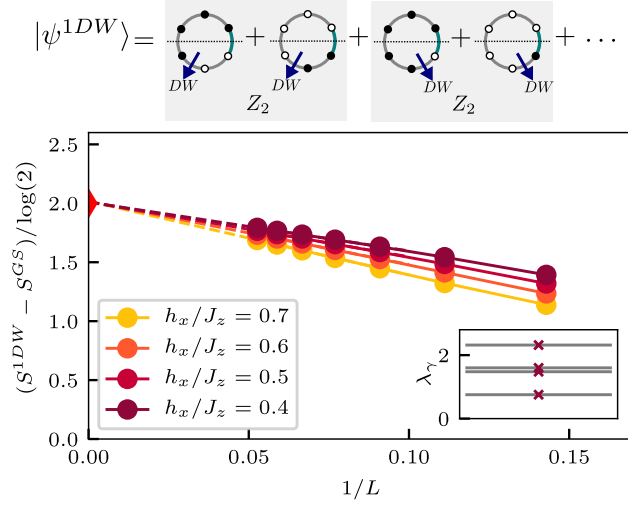


Figure 7.6 Entanglement excess of a single domain wall with respect to the symmetry-broken ground state in the ferromagnetic phase of the TFI model with $J_x/J_z = 0.1$. The red marker on the y-axis shows the expected $2\log(2)$ excess. Inset: There are no symmetry-protected degeneracies in the entanglement spectrum.

finite-size systems and a single domain wall excitation, we will additionally study the model with *anti-periodic* boundary conditions. In this setup a *single* domain wall is present in the ground state.

For each domain wall position, there are two macroscopically different patterns that are related by Z_2 symmetry, as the spectrum itself is still Z_2 symmetric. This is illustrated on top of Fig. 7.6. Therefore, the entanglement excess with respect to the ground state when considering a spatially symmetric cut, is given by

$$S^{1DW} = S^{GS} + 2\log(2) + \mathcal{O}(1/L). \quad (7.15)$$

This is shown in Fig. 7.6. So again, an excess of one bit arises from the position uncertainty of the quasiparticle. In addition, another excess bit $\log(2)$ stems from the superposition of the macroscopically different domain-wall patterns.

Notice also that in this case the entanglement spectrum does *not* exhibit a two-fold degeneracy, see also the inset in Fig. 7.6. The absence of degeneracy is directly related to the fact that there is no Z_2 charge associated with the domain wall.

7.2.4 Quasiparticles with $U(1)$ charge and reflection symmetry

The treatment of quasiparticles carrying a $U(1)$ charge is similar to the Z_2 case, as Z_2 is a subgroup of $U(1)$, so the argument in Sec. 7.2.1 applies. Based on this argument, we begin with a zero momentum quasiparticle state in a trivial SSH chain and obtain its entanglement spectrum with respect to the center cut. As the zero momentum quasiparticle state carries an odd charge and is reflection symmetric, we expect a robust two-fold degeneracy in the entanglement spectrum. We verify this conjecture by adding

interactions (that do not break the $U(1)$ symmetry) to the SSH chain (7.9), such that the model becomes

$$H = \sum_{i=0}^{L-1} \left((1 + \delta) c_{2i}^\dagger c_{2i+1} + (1 - \delta) c_{2i+1}^\dagger c_{2i+2} + \text{h.c.} \right) + U n_i n_{i+1} + V (n_0 + n_{L-1}) \quad (7.16)$$

where n is the onsite charge density away from half-filling, and $V > 0$. We construct the quasiparticle state in the trivial phase for a chain of 20 sites with $U = 0.2$, and obtain the entanglement spectrum from a center cut. As long as the reflection symmetry and $U(1)$ symmetry are preserved in the quasiparticle state, the Kramers theorem still applies regardless of the interaction strength and the two-fold degeneracy remains robust as shown in Fig. 7.3(b).

7.3 Entanglement fragmentation, a feature of SPT quasiparticles

The relation between one-dimensional SPT phases and their entanglement properties has been widely explored in Refs. [24, 164, 165, 167–171, 178, 179, 197]. In particular, it has been shown that one-dimensional SPT phases can be characterized by their ground state entanglement spectrum [24, 165, 178]. More precisely, it was shown that the irreducible representation of the projective symmetry in the MPS determines the degeneracy of the ground state entanglement spectrum, and hence can be treated as a fingerprint of SPT states. Similar ideas have been applied to a wide variety of SPT phases in higher dimensions with higher-order topology [198].

The universal entanglement behavior of quasiparticle states in SPT phases remains unclear. In particular, despite the fact that the SPT ground state captures salient features of the underlying topology, it is unclear whether and how these features are inherited by the quasiparticles at low energy. In this section, we try to answer this question by proposing a universal *entanglement fragmentation* feature for SPT quasiparticles. Such a feature indicates that the low-energy quasiparticle states in non-interacting SPT phases still retain some of the topological features of the ground state. Based on this observation, one can identify different phases via the entanglement content of the quasiparticle states.

7.3.1 Quasiparticles of the topological SSH chain

Let us continue with the example of the SSH chain, now we consider the topological regime protected by $U(1)$ and reflection symmetry (R). Assume the ground state has the Schmidt decomposition,

$$|GS\rangle = \sum_{\gamma} \lambda_{\gamma} |\gamma_A\rangle |\gamma_B\rangle. \quad (7.17)$$

Due to the strong dimer bond between the cut, the charge difference $q_A - q_B$ between left and right half of the wave function is always an odd number, as the total number of unit cells in the ground state is odd, see also Fig. 7.1. Therefore, following the discussion in the previous section, the ground state entanglement spectrum $\epsilon_{\gamma} = -\log \lambda_{\gamma}^2$ must now exhibit a two-fold degeneracy. This degeneracy also has a simple explanation in terms

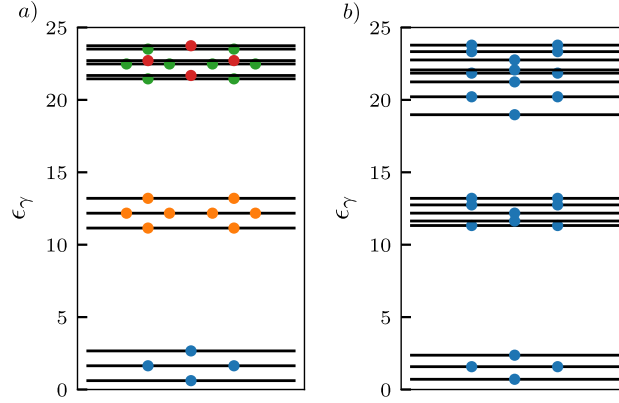


Figure 7.7 The entanglement spectrum of the first excited state in the topological SSH model on a chain with $L = 20$ sites and $\delta = -0.5$. a) The non-interacting case with $U = 0$. The entanglement spectrum exhibit a clear fragmentation pattern with each fragment being particle-hole symmetric. The colors are added to make the fragmentation pattern clearly visible. b) The interacting case with $U = 0.2$. The fragmentation pattern is clear for the low-energy patterns but not for the higher ones. The particle-hole symmetry within each fragment is broken.

of the single-particle entanglement Hamiltonian introduced in Sec. 7.1: the existence of the entanglement in-gap mode, shown in Fig. 7.2(c), reflects the character of the topologically-protected mode at the boundary of the system [169, 178, 195].

Now we add a quasiparticle with zero momentum to the filled topological band. Its position uncertainty is giving rise to another in-gap zero mode, as we have showed in Sec. 7.1, which is an extended bulk state. Subsequently, the quasiparticle's entanglement Hamiltonian H_A^{QP} , in the zero-correlation length limit (i.e. the fully dimerized limit on the topological side), contains two zero modes $p_\alpha = 1/2$ labeled by f and c which corresponds to the bulk and edge in-gap mode. The entanglement Hamiltonian can be viewed as a metallic system with one conducting state in bulk, in addition to one edge mode.

Now we consider the case with finite correlations. This is like turning on a symmetry allowed coupling $f^\dagger c + h.c.$ which hybridizes these bulk and edge zero modes, and thus lifts the degeneracy and delocalizes the edge zero mode. In particular, terms like $f^\dagger f, c^\dagger c$ are still absent from the entanglement Hamiltonian as they would break the reflection symmetry. Consequently, the degeneracy lifting between two zero modes is particle-hole symmetric with energy levels $\pm\epsilon$ as shown in Fig. 7.2(d). In the many-body entanglement spectrum, these splitting modes imply an entanglement fragmentation pattern, where each fragment contains four eigenvalues $E_a + \epsilon, E_a - \epsilon, E_a, E_a$ as shown in Fig. 7.7. The states $E_a \pm \epsilon$ come from the situation where either the ϵ or $-\epsilon$ mode is filled. The two degenerate E_a states originate from the situation where the two modes are either completely filled or completely empty.

For the non-interacting theory, this entanglement fragmentation feature has some universal properties that are independent of the microscopic Hamiltonian: (i) each layer in the fragmented entanglement spectrum has three energy levels ($E_a, E_a \pm \epsilon$), with the middle one (E_a) being $2n$ -fold degenerate, and (ii) the top and bottom energy level are n -fold degenerate, and are related to the middle one via particle-hole symmetry. Based on this argument, we found an immediate distinction between quasiparticles from distinct

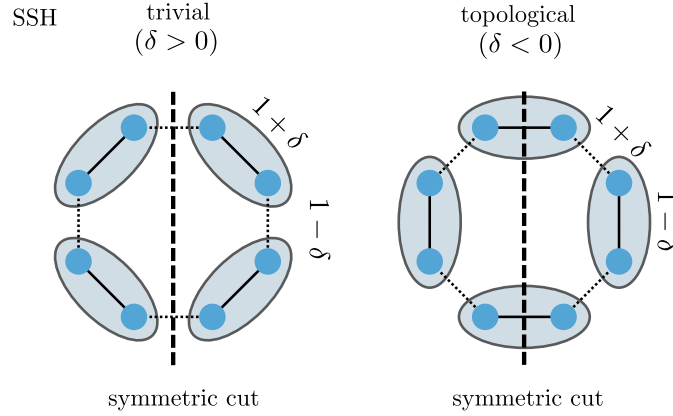


Figure 7.8 Sketch of the SSH model with periodic boundary conditions in our setup, we choose $L = 4m$ sites (with m integer) such that the trivial (topological) phase is characterized by the cutting of weak (strong) bonds.

phases in the SSH chain: in the topological phase the quasiparticle carries a universal entanglement fragmentation pattern, while in the trivial phase the quasiparticle exhibits a 2-fold degeneracy due to the degeneracy theorem. Because of its inherent robustness, such a unique quasiparticle entanglement fragmentation pattern is expected for most non-interacting SPT systems.

Our current analysis was based on the non-interacting SSH chain. In the free-fermion limit, the coupling between two in-gap modes is always particle-hole symmetric so their level mixing also inherits a particle-hole symmetric fragmentation pattern.

However, the situation is very different in the interacting case. We can turn on a symmetry-invariant interaction

$$H_{int} = U(f^\dagger f - 1/2)(c^\dagger c - 1/2), \quad (7.18)$$

which creates a gap between different charge parity sectors such that all filled or all empty states $n_f = n_e$ have larger energy. This would break the particle-hole symmetric pattern in the entanglement fragmentation and thus mix different fragments in the entanglement spectrum. As a result, for each fragment, the middle energy level with two-fold degeneracy is no longer symmetric with respect to the top and bottom energy level with odd charge parity. Thus, the particle-hole symmetric fragmentation pattern is lost in the presence of interactions as shown in Fig. 7.7(b).

7.3.2 Quasiparticles of the topological SSH model with periodic boundary conditions

Now we consider the SSH model (7.9) with periodic boundary conditions and $V = 0$ in the topological regime. As sketched in Fig. 7.8, this means that two strong bonds are cut in a symmetric bipartition of the system. For the ground state, we will encounter an entanglement spectrum with four-fold degeneracy due to the two zero modes c^\dagger, d^\dagger in the entanglement Hamiltonian localized near each cut, see Fig. 7.9(a). The quasiparticle state adds an additional extended zero mode f^\dagger to the entanglement Hamiltonian and makes the entanglement Hamiltonian like that of a metallic system with one conducting

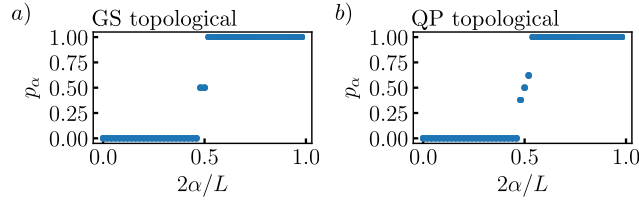


Figure 7.9 The correlation matrix spectra for the topological SSH model with periodic boundary conditions. a) The spectrum of the ground state is characterized by two states $p_\alpha = 1/2$ because of the two boundary modes – one near each cut. b) For the quasiparticle in the topological phase, two in-gap edge states are hybridized via the zero energy bulk state in a particle-hole symmetric way.

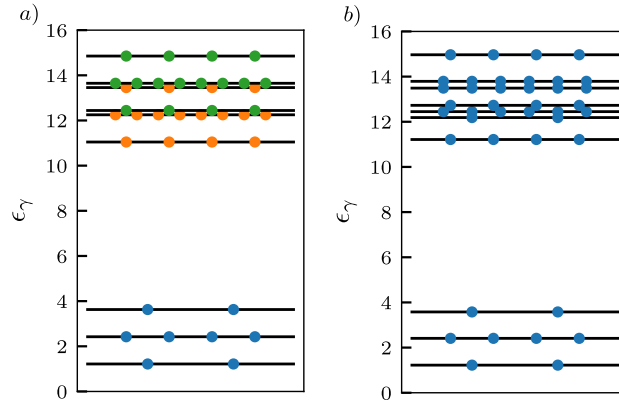


Figure 7.10 Many-body entanglement spectra for the topological SSH model with periodic boundary conditions for a ring with $L = 20$ sites and $\delta = -0.5$. a) Non-interacting case $U = 0$. All quasienergy levels are two-fold degenerate due to one in-gap zero mode. The entire entanglement spectrum exhibits a clear fragmentation pattern with each fragment being particle-hole symmetric. b) Interacting case $U = 0.1$. The fragmentation pattern is destroyed for all but the lowest levels, but the two-fold degeneracy remains robust.

state in the bulk in addition to two edge modes. We expect these two edge modes to hybridize via the bulk conducting state and thus lift the degeneracy away from the zero correlation length limit, as shown in Fig. 7.9(b).

We can turn on the reflection invariant coupling $f^\dagger c + f^\dagger d + h.c$ to hybridize the three zero modes into energies 0 and $\pm\epsilon$ which is still a particle-hole symmetric spectrum. The zero energy mode again implies that the entanglement spectrum should have a two-fold degeneracy, so that the fragmentation structure is doubled compared to the single cut with open boundary. This doubling is shown in Fig. 7.10. The degeneracy theorem still applies as the quasiparticle state has odd charge parity. So this two-fold degeneracy is robust against any $U(1)$ preserving interaction, as depicted in Fig. 7.10 for the model (7.16) with $U = 0.1$ and $V = 0$, but the fragmentation patterns are mostly lost.

7.4 Conditional mutual information for quasi-particles in SPT chains

Despite the lack of local order or long-range correlations, the ground states of one-dimensional SPT phases bear a hidden non-local order furnished by local entanglement patterns. Such hidden non-local order can be quantitatively defined and detected by measuring string-order parameters in the ground state. While string-order parameters do exist for all SPT phases, these can be rather involved to measure for more complex phases [25, 199]. In this section, we will provide a quantum information perspective to leverage the relation between string order and conditional mutual information. In particular, we demonstrate that the non-local string order can be understood as the conditional long-range mutual information [200] of the wave function where a measurement of qubits at the two ends of a string reduces the information entropy of the total qubits on the string. When it comes to the quasiparticle of the SPT phase, despite its vanishing string order, the conditional mutual information is still nonzero and hence provides a feasible way to detect the SPT phase via quasiparticle entanglement.

7.4.1 Ground state properties

Mutual information and conditional mutual information

We start our discussion by considering a simple model of an SPT phase in one dimension, namely the transverse-field cluster model [201–203]

$$H = K \sum_i \sigma_{i-1}^z \sigma_i^x \sigma_{i+1}^z + h \sum_i \sigma_i^x. \quad (7.19)$$

The SPT phase is protected by a $Z_2 \times Z_2$ symmetry generated by $Z_2^a = \prod_i \sigma_{2i+1}^x$ and $Z_2^b = \prod_i \sigma_{2i}^x$, and the system undergoes a phase transition from SPT to trivial at $h = 1$. In the presence of an open boundary, each edge gives rise to a two-fold degeneracy due to the projective symmetry generated by the two Ising (Z_2) symmetries at the boundary. It is noteworthy to mention that the ground state contains a non-vanishing string order [204],

$$\sigma_{2i}^z \left(\prod_{j=0}^{m-1} \sigma_{2i+2j+1}^x \right) \sigma_{2i+2m}^z = 1. \quad (7.20)$$

This non-vanishing string order is a direct consequence of the decorated domain wall condensate because the total Z_2^a charge living on the odd sites of the string is locked to the two spin configuration at the edge of the string (on the even sites). When the spins at the $2i, 2i + 2m$ sites are in the $|00\rangle, |11\rangle$ pattern, the total Z_2^a charge between them is even. Such non-vanishing hidden order can be detected via the mutual information between the two spins (A) at positions $2i$ and $2i + 2m$ living at the ends of the string, and the odd site spins (B) living inside the string as shown in Fig. 7.11

$$I(A : B) = S(B) + S(A) - S(A \cup B) \neq 0. \quad (7.21)$$

Due to the decorated domain wall condensate structure, the spin pattern in the ground state is strongly fluctuating. Hence, the entanglement entropy of region A converges to $S(A) = 2 \log(2)$ for large m . Likewise, for the m spins living on the odd sites of the

string, referred to as region B , $S(B) = m \log(2)$ as each spin can have two configurations. However, if we compute the entropy $S(A \cup B)$ of the $m + 2$ spins, it is $\log(2)$ smaller than the entropy addition $S(A) + S(B)$. The reason is obvious: by fixing the pattern of the spin at the end of the string, the total Z_2^g charge on the odd sites is fixed and the entropy is reduced.

We performed DMRG [31] simulations to calculate the MI for the model (7.19) with PBC, such that the ground state is non-degenerate. In our simulations we choose the (even) sites as $A_1 = \frac{L}{4}$, $A_2 = \frac{3L}{4}$ and use system sizes L divisible by eight. The results are shown in Fig. 7.11, where we indeed observe a non-vanishing MI in the topological phase that approaches $\log(2)$ for the fixpoint $h = 0$. Note that we need to construct the reduced density matrix of the subsystem $A \cup B$, and are therefore limited to rather small subsystems of the order of 12 sites.

Alternatively, we could consider Rényi versions of the entropies in the MIs

$$S^\alpha = \frac{1}{1 - \alpha} \log \text{Tr}(\rho_A^\alpha) \quad (7.22)$$

and use, e.g., the replica trick to compute those. In that way larger system sizes can be accessed when using MPS. In addition, there exist efficient experimental protocols based on randomized measurements to obtain S^2 [121, 134, 138, 192–194].

Although one expects that a non-vanishing string order creates a non-vanishing MI $I(A : B)$ between the ‘edge’ and the ‘bulk’ of the string, a non-vanishing MI itself cannot be treated as a solid manifestation of the string order. Since some of the sites in B region are adjacent to A , the local entanglement between adjacent sites can add some trivial contribution to the mutual information. In order to exclude such trivial contributions, we divide B into two regions: the center region B_1 far from the string end, and the two parts B_2 within the correlation length of the string boundary.

We then define the conditional MI [205],

$$I(A : B_1 | B_2) = I(A : B_1 \cup B_2) - I(A : B_2). \quad (7.23)$$

This conditional MI computes the ‘hidden correlation’ between the bulk and boundary of the string while excluding the ‘trivial’ MI induced by local entanglement. This is also shown in Fig. 7.11 by the dots, where we took the region B_2 to be the spins directly neighboring the A spins at positions $\frac{L}{4} + 1$ and $\frac{3L}{4} - 1$. Only near the phase transition there is an offset between the data, illustrating that the non-vanishing mutual information is indeed due to the string order.

Measurement induced non-local entanglement

An alternative understanding of the MI in the ground state can be obtained by introducing the concept of measurement induced non-local entanglement, where a charge measurement of the B region $P_B | GS \rangle$, with

$$P_B = 1 + \prod_{i \in B} \sigma_i^x, \quad (7.24)$$

triggers a dramatic non-local entanglement among the two spins in the A region. A measurement of the spins living at the odd sites of the string reduces the entanglement entropy of the two spins living on the edge of the string. Such an entropy reduction after

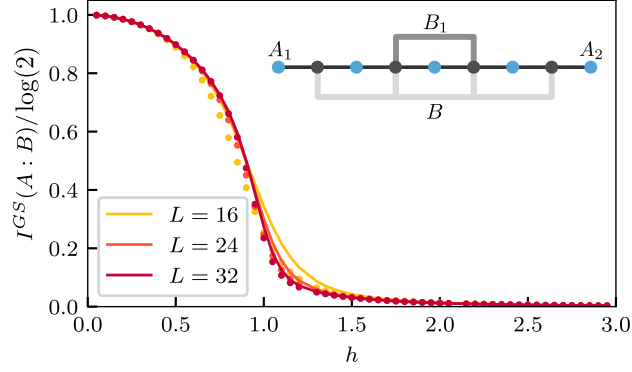


Figure 7.11 The MI in the ground state of the cluster model between the grey spins in the middle (B area) and the blue spins ($A = A_1 \cup A_2$) at the boundaries of the string. In the SPT phase $h_x < 1$ it is non-vanishing for the ground state. The dotted data points are the conditional MIs (7.23), where we subdivided the region B such that $B_2 = B \setminus B_1$ is the region the closest to the A spins. There is only a small difference between the MI and conditional MI near the transition as the correlations are still dominantly local.

measurement is accompanied by the emergence of long-range entanglement between two distant spins. This is illustrated in Fig. 7.12, the inset shows the MI between the A spins before the measurement which is just zero as these spins are not correlated. Note that we can compute the measurement induced MI for much larger system sizes than we could for the MI $I(A : B)$ of the previous paragraph, because we only need construct the reduced density matrix explicitly for two spins. Hence this approach is easily scalable and also accessible in experiments.

7.4.2 Quasiparticle properties

Mutual information and conditional mutual information

Now we focus on the quasiparticle state and use a slightly different model

$$H = \sum_i (K \sigma_{2i}^z \sigma_{2i+1}^x \sigma_{2i+2}^z + K' \sigma_{2i-1}^z \sigma_{2i}^x \sigma_{2i+1}^z + J \sigma_{2i-1}^z \sigma_{2i+1}^z + h \sigma_i^x), \quad (7.25)$$

such that when $J \ll K < K'$ and $h = 0$, the (non-degenerate) low-energy excitation is the energy flipping of the stabilizer term $K \sigma_{2i}^z \sigma_{2i+1}^x \sigma_{2i+2}^z$ which removes the Z_2^a charge on site $2i + 1$ from the domain wall between sites $2i, 2i + 2$ ¹. This can be accomplished by the quasiparticle operator σ_{2i+1}^z which flips the charge at site $(2i + 1)$. Due to the $J \sigma_{2i-1}^z \sigma_{2i+1}^z$ term, the quasiparticle acquires dynamics and can hop among odd sites as $\sum_i e^{ikR_{2i+1}} \sigma_{2i+1}^z$. Such quasiparticle unbinds the Z_2^a charge with the domain wall for odd-site clusters. Consequently, the string order could vanish as the quasiparticle being inside/outside the string exactly reverse the value of string order. Nevertheless, the quasiparticle still carries non-vanishing MI between the three distant sites (living on the even lattice) labelled as $A = A_1 \cup A_2 \cup A_3$ and the odd sites between them labelled as $B = B_L \cup B_R$ as in Fig. 7.13(a).

¹Or it adds a Z_2^a charge on site $2i + 1$ provided there is no domain wall between sites $2i, 2i + 2$

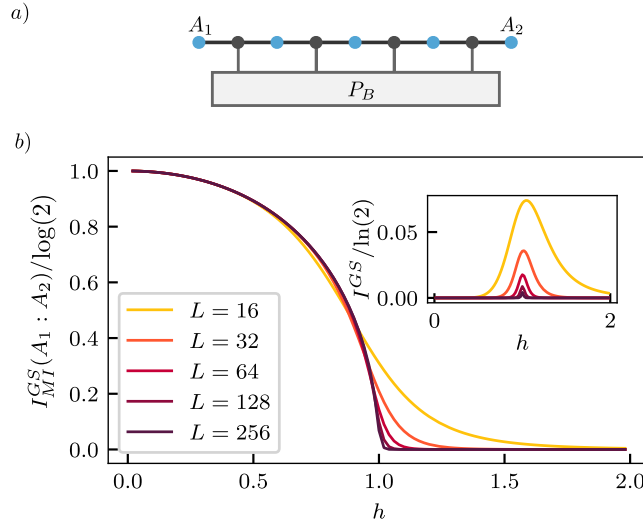


Figure 7.12 a) Sketch of the projection of the odd sites in between A_1 and A_2 to a sector with definite (e.g. even) parity. b) The measurement induced MI in the ground state of the cluster model $P_B|GS$. The inset shows the data without the projection of the region B to the even sector. In this case the distant spins in the A region do not carry any mutual information in the thermodynamic limit, as expected.

If we do not make any measurement and barely look at the quasiparticle state, region B has entropy $S(B) = m \log(2)$ with m being the number of odd site spins in B region. However, once we make a measurement of the spins in the A region, say they are in the $(0, 0, 0)$ state, then B_L and B_R could have all-even charge, or an even-odd/odd-even charge pattern depending on the position of the quasiparticle. However, it is impossible to get a configuration of B with odd charges on both sides based on the measurement outcome. The reason is obvious: if the quasiparticle is outside the B region, then both B_L and B_R have even charges, but if the quasiparticle is inside the $B = B_L \cup B_R$ region, one of them has even charge and the other one odd charge. This result implies that the entanglement entropy of region B can be reduced after measuring region A , hence their mutual information is nonzero

$$I(A : B) \neq 0. \quad (7.26)$$

This is shown in Fig. 7.13(b) for some points in the phase diagram. To numerically investigate the quasiparticle state, we have constructed the first excited state of our model with standard DMRG techniques [34] that involve projecting away the lower lying states. In our case, we would only need to orthogonalize with respect to the non-degenerate ground state. In the simulations we take $A_1 = \frac{L}{4}$, $A_2 = \frac{L}{2}$ and $A_3 = \frac{3L}{4}$ and use system sizes L divisible by eight. In addition, to exclude the contribution to the MI by local correlation, we can choose a small region near A and again define the conditional MI,

$$I(A : B_1|B_2) = I(A : B_1 \cup B_2) - I(A : B_2). \quad (7.27)$$

We show some data points for the conditional MI in Fig. 7.13(b), where we choose the region B_2 to be the four odd spins directly neighboring the A spins. If we use the von

Neumann entropies to compute the MIs, we are limited to small subsystems. In order to obtain data for somewhat larger systems sizes, we also computed the MIs by using the second order Rényi entropies as shown in Fig. 7.13(c).

Measurement induced non-local entanglement

Also for the quasiparticle state, we can extend our understanding of the MI by measurement induced long-range entanglement between distant spins. Of course, if we obtain the reduced density matrix of the three distant sites A_1, A_2, A_3 of the quasiparticle state, the reduced density matrix can be approximated as the product of the reduced density matrices of the three spins provided their distances are much larger than the correlation length. This also implies that there is no non-local entanglement among these three spins and that their mutual information vanishes, see the inset in Fig. 7.14.

However, if we make a measurement of the quasiparticle state by projecting the spins in the B region such that both B_L and B_R carry an even number of charges, the projected quasiparticle state $P_{B_L} P_{B_R} |QP\rangle$ contains non-vanishing MI (see Fig. 7.14) as,

$$\begin{aligned} I(A_1 \cup A_3 : A_2) &= S(A_1 \cup A_3) + S(A_2) - S(A_1 \cup A_3 \cup A_2) \\ &= 3 \log(2) - S(A_1 \cup A_3 \cup A_2). \end{aligned} \quad (7.28)$$

Following a similar argument from the previous paragraph, it is not hard to conclude that provided both B_L and B_R carry even number of charges, the possible patterns for (A_1, A_2, A_3) are

$$(0, 0, 0), (1, 1, 1) \quad (7.29)$$

for quasiparticle outside, and

$$(1, 0, 0), (0, 0, 1), (0, 1, 1), (1, 1, 0) \quad (7.30)$$

for quasiparticle inside, so the total entropy of (A_1, A_2, A_3) is smaller than the sum of each individual entropy $S(A_1 \cup A_3) + S(A_2) = 3 \log(2)$. This indicates that the three distant spins in $P_{B_L} P_{B_R} |QP\rangle$ contain non-vanishing long-range MI $I(A_1 \cup A_3 : A_2)$ as shown in Fig. 7.14. Such ‘emergent long-range mutual information’ and non-local entanglement is absent for the quasiparticle wave function due to its short-range correlations. However, the charge projection of the B region entangles the three distant spins and creates non-vanishing long-range MI $I(A_1 \cup A_3 : A_2)$ due to the hidden correlation between the total Z_2^a charges living on the odd sites of the B region and the spin coherence patterns of A_1, A_2, A_3 .

To explicitly illustrate that the measurement induced MI can also probe phase transitions in the quasiparticle state, we consider the case where we vary the J parameter in the cluster model (7.25) and fix $K = K' = 1$ and $h = 0$. This drives the system from an SPT phase ($J < 2$) to a symmetry broken phase ($J > 2$), we illustrate this in Fig. 7.15 via the quasiparticle measurement induced MI. This measurement induced long-range MI is easy to implement in cold atom experimental setups [121, 134, 138, 192–194] and hence provides insight into visualizing the low-energy excitation and suggests an experiment-feasible protocol to probe quasiparticles in SPT phases.

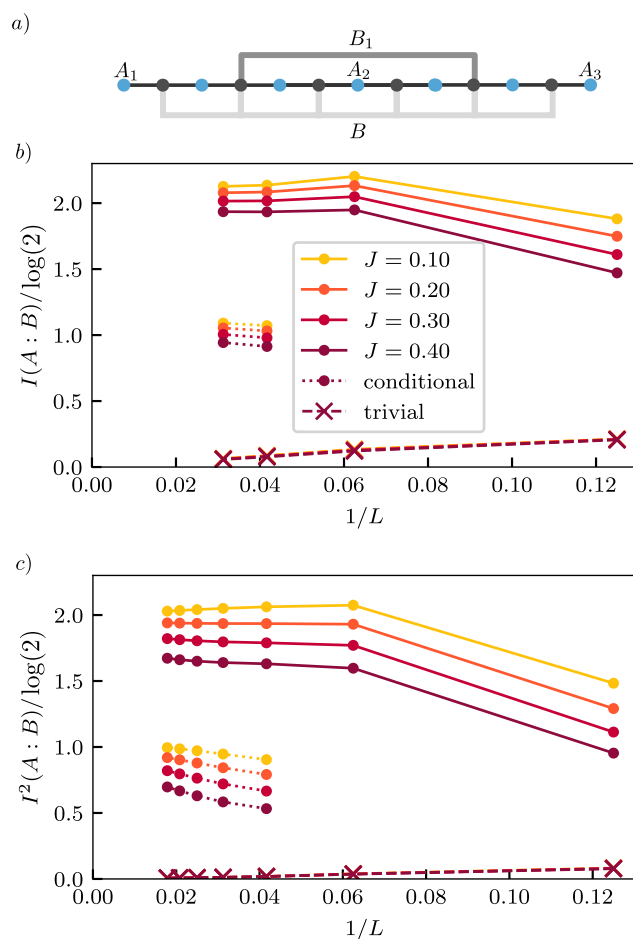


Figure 7.13 a) Sketch of the partitioning of the system; we take $A_1 = \frac{L}{4}$, $A_2 = \frac{L}{2}$ and $A_3 = \frac{3L}{4}$ and system sizes divisible by eight. b) The MI in the first excited state of the cluster model. The full lines corresponds to data in the topological phase at $K' = 1, K = 0.9$ and $h = 0$ for some J s shown in the legend, and the crosses corresponds to data in the trivial phase at $h = 2.5$. The dots connected by the dotted lines are data points for the conditional MI $I(A : B_1 | B_2)$, where the region B_1 only contains odd sites that are not directly neighboring the A region. c) The second order Rényi MI of the first excited state at the same points in the phase diagram.

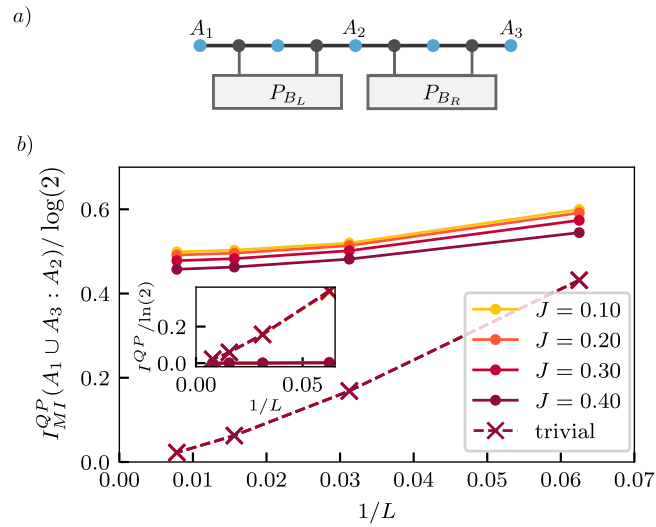


Figure 7.14 a) Sketch of the projection of the odd sites in between A_1, A_2 and A_3 to a sector with definite (e.g. even) parity. b) The measurement-induced MI in the first excited state of the cluster model $P_{B_L} P_{B_R} |QP\rangle$. The full line corresponds to data in the topological phase at $K' = 1, K = 0.9$ and $h = 0$ for some J shown in the legend, while the dotted lines corresponds to data in the trivial phase at $h = 2.5$. The inset shows the MI without the projection of the regions B_L and B_R to the even sector. Clearly the MI vanishes in both cases in the thermodynamic limit.

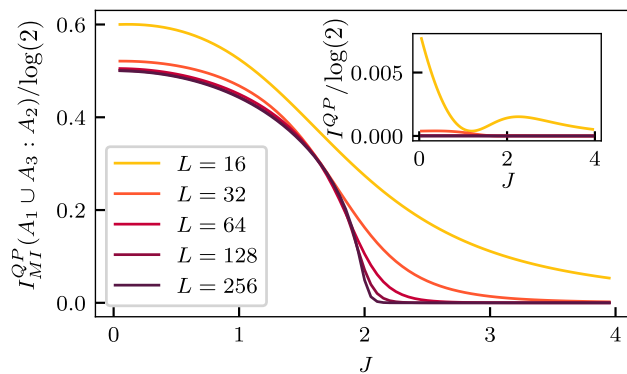


Figure 7.15 The measurement induced MI in the first excited state of the cluster model $P_{B_L} P_{B_R} |QP\rangle$ as a function of J with $K = K' = 1$ and $h = 0$. The inset shows the data without the projection of the regions B_L and B_R to the even sector.

7.5 Conclusion and outlook

In this work, we investigated entanglement features of different quasiparticles in various phases, and demonstrated how to identify distinct phases of matter via their low-energy excitations. The results obtained in this chapter might help the exploration of quantum phases from a quantum information perspective. In particular, we expect that the entanglement properties of quasiparticles can be adapted to examine quantum critical phenomena. We expect that some of our results, including the conditional mutual information diagnostic for **SPT** quasiparticles also apply to the cases where there are multiple quasiparticles present in the system [4]. However, in the presence of N quasiparticles, we need to evaluate the non-vanishing conditional mutual information between $N+2$ qubits and the region intersecting in between. When N becomes large, such multi-region mutual information gets overwhelmed with local entanglement patterns and can no longer be treated as an indicator for the hidden-orders of **SPT** phases. In addition, when the density of quasiparticles would become finite, the state has volume-law entanglement and we would not expect that our statements generalize.

As we have also extensively seen in the previous chapters, the evolution of entanglement in certain states can sometimes be related to many properties of the system, for instance the logarithmic entanglement growth in **MBL** systems [27]. In this respect, it would be interesting to see if the probes discussed in this chapter can still be useful in out-of-equilibrium scenarios.

8 Quantum sine-Gordon dynamics in coupled spin chains

Most of the content of this chapter can also be found in a previous publication of the author [5]. Text and figures have been adjusted to fit into the context of the thesis.

In recent years, highly controllable and tunable quantum simulators have been developed on different platforms, including ultracold atoms, trapped ions, and superconducting qubits. These settings enabled the experimental preparation and characterization of strongly-correlated non-equilibrium states of matter. In general, such states are extremely difficult to characterize by traditional analytical or numerical approaches, which defies a direct verification of the quantum simulation. To overcome this challenge, it is important to identify strongly correlated systems, whose dynamics can also be characterized with conventional theoretical means. In this respect, a prominent example is the sine-Gordon model [206–209]; a one-dimensional relativistic field theory which describes the low-energy physics of a multitude of experimental systems. The sine-Gordon model is a remarkable example of an integrable field theory [207, 210]. Its spectrum features topological excitations, akin to classical solitons, and their bound states, known as breathers. Out of equilibrium, integrability hinders thermalization and many efforts have been made to understand the exotic dynamics of this field theory [211–217].

The sine-Gordon model captures the low-energy sector of spin chains [218–223], spinful cold atom gases [208], specific quantum circuits [224, 225] and the interference of two one-dimensional quasi-condensates [226, 227]. The latter realization of the sine-Gordon model, proposed by Gritsev *et al.* [226], has been realized with coupled weakly-interacting quasi-condensates on atom chips [228], coupled by a potential barrier of adjustable height. The sine-Gordon Hamiltonian governs the relative phase between the two condensates, which is then probed through matter-wave interferometry [229, 230]. Importantly, the mass scale of the theory can be tuned by controlling the potential barrier. For weak interactions within the one-dimensional gases, as realized in these experiments, a semiclassical approximation of the sine-Gordon model accurately captures the equilibrium correlation functions of the relative phase [228, 231].

Out of equilibrium the situation is less clear, as high-energy excitations beyond the sine-Gordon description are inevitably created. Quench experiments in tunnel coupled quasi-condensates [232] are not described by a semiclassical analysis of the sine-Gordon model [233]. Attempts to include corrections beyond sine-Gordon arising from coupling to the symmetric-phase sector [234] and transverse mode excitations [235] seem not to be sufficient to quantitatively describe the experimental observations [232], which in contrast are well-captured by a semiclassical treatment of the full 3D geometry [236]. From a theoretical vantage point, both the massless and large mass limits (corresponding to large and weak barrier strengths respectively) become quadratic theories, and their dynamics are readily tractable [237–241]. Hence, they represent a good starting point for self-consistent Gaussian approximations [242]. Likewise, experiments focusing on

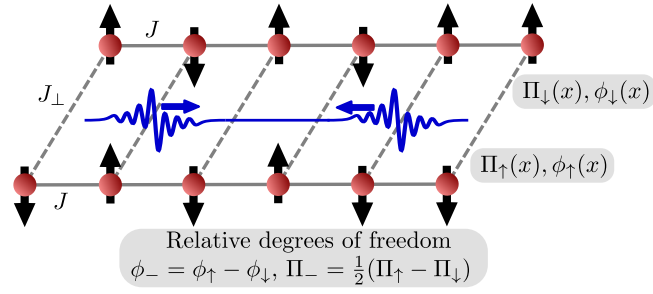


Figure 8.1 Sketch of the setup. Two XXZ spin chains, each realizing a Luttinger Liquid in the low-energy regime, are weakly tunnel coupled. The sine-Gordon model is realized in their relative degrees of freedom.

these regimes [243–247] are well captured by these approaches. Yet, fascinating physics arises precisely in the challenging regime of intermediate mass scales and far from the semiclassical limit, in which the rich dynamics of the field theory is unveiled. These considerations pose two questions. First, in order to probe strong quantum effects, it will be interesting to focus on the strong-coupling regime beyond the semiclassical limit. Second, assessing the validity regime of the emergent sine-Gordon descriptions in microscopic realizations will be pertinent.

These open questions motivate our work, in which we study the sine-Gordon dynamics emerging from the tunnel coupling between two one-dimensional XXZ spin chains, see Fig. 8.1, which realizes a lattice version of the original proposal of Ref. [226]. Our motivation to investigate lattice systems is twofold. On the one hand, MPS techniques [33, 34, 106] allow for a precise numerical characterization of the spectrum and the dynamics of the system. Therefore, well-defined boundaries to the effective sine-Gordon dynamics can be obtained. On the other hand, interactions in these settings are strong and tunable, and result in sine-Gordon realizations deep in the quantum regime. A realization of a model closely related to the spin ladder, that consists of coupled Bose-Hubbard chains is realizable with current experimental capabilities [248].

Our discussion is organized as follows. In Sec. 8.1 we introduce the coupled spin chains and review the emergence of the effective sine-Gordon dynamics. Sec. 8.2 provides a short summary of the integrability aspects of the sine-Gordon model, which are then compared in Sec. 8.3 with the numerical low-energy spectrum of the coupled chains. In Sec. 8.4 we analyze non-equilibrium scenarios and observe key signatures of integrable dynamics in scattering events of wave-packet excitations. The conclusions and outlook are contained in Sec. 8.5.

8.1 Model and setup

The sine-Gordon model is the central character of this chapter and is governed by the Hamiltonian

$$H_{\text{SG}} = \int dx \left(\frac{c^2 g^2}{2} \Pi^2 + \frac{1}{2g^2} (\partial_x \phi)^2 - \frac{c^2 m^2}{g^2} \cos(\phi) \right), \quad (8.1)$$

where the bosonic fields are canonical conjugates $[\phi(x), \Pi(y)] = i\delta(x-y)$ and ϕ has the meaning of a phase. The Hamiltonian is brought to the standard field theory notation

[209] by a simultaneous rescaling of the fields $\phi \rightarrow g\phi$ and $\Pi \rightarrow g^{-1}\Pi$, but in our context Eq. (8.1) is more convenient.

Above, c is the light-cone velocity of correlation spreading, m tunes the overall mass scale, and g is the interaction. The parameter g governs the scaling dimension [208] (in an RG sense) of $\cos\phi$: for $g^2c^2 > 8\pi$ the cosine term is irrelevant and the theory flows to the free boson conformal point. For $g^2c^2 < 8\pi$, interactions become relevant. As a consequence, the mass parameter m has an anomalous dimension scaling as $[m] = 1 - g^2c/(8\pi)$. We postpone a more detailed discussion of the field theory to Section 8.2. Here, we present its realization in tunnel-coupled spin chains (see Fig. 8.1) following the method of Ref. [226]. We thus consider two weakly tunnel-coupled XXZ spin chains

$$H = H_{\uparrow}^{\text{XXZ}} + H_{\downarrow}^{\text{XXZ}} + H_{\perp}, \quad (8.2)$$

where

$$H_{\alpha}^{\text{XXZ}} = J \sum_{i=0}^{L-2} \left(S_{i\alpha}^x S_{i+1\alpha}^x + S_{i\alpha}^y S_{i+1\alpha}^y + \Delta S_{i\alpha}^z S_{i+1\alpha}^z \right) \quad (8.3)$$

with $\alpha = \uparrow, \downarrow$ and $(S_{i\alpha}^x, S_{i\alpha}^y, S_{i\alpha}^z)$ the spin-1/2 operators. We choose the coupling between the two chains H_{\perp} in the form of a weak tunneling

$$H_{\perp} = \frac{J_{\perp}}{2} \sum_{i=0}^{L-1} \left(S_{i\uparrow}^+ S_{i\downarrow}^- + S_{i\uparrow}^- S_{i\downarrow}^+ \right) \quad (8.4)$$

with $S_{i\alpha}^{\pm} = S_{i\alpha}^x \pm iS_{i\alpha}^y$. Here, the coupling J_{\perp} is assumed to be small (specified below).

8.1.1 The sine-Gordon field theory on a spin ladder

To see the emergence of sine-Gordon physics, one first neglects the tunneling and focuses on the effective low-energy description of the two chains, assuming to be close to the ground state. To this end, one proceeds within the Luttinger Liquid approach [208, 249, 250] by introducing a phase field ϕ_{α} and its conjugate field Π_{α} for each of the two chains. It should be stressed that the Luttinger Liquid approach is of much wider applicability than the spin chain and only requires a $U(1)$ conserved charge (the z -magnetization in this case) and gapless excitations. In order to have linearly-dispersing gapless excitations over the ground state of Eq. (8.3), we focus on the XY-phase with $\Delta \in [-1, 1]$.

Each spin chain is thus described by the Luttinger Liquid Hamiltonian

$$H_{\alpha}^{\text{LL}} = \frac{1}{2\pi} \int dx v_s \left(\frac{1}{K} (\pi \Pi_{\alpha}(x))^2 + K (\partial_x \phi_{\alpha}(x))^2 \right), \quad (8.5)$$

where the Luttinger parameter K and sound velocity v_s fully characterize the many-body interactions. Within the bosonization language, the spin operators are represented as [251]

$$S_j^z \simeq \Pi(x) \quad S_j^+ \simeq \alpha e^{i\phi(x)}, \quad (8.6)$$

where only the most relevant terms (in an RG sense) are retained. The constant prefactor α in front of the phase is non-universal and depends on the microscopic properties of the model. We will treat it as a constant, that will however renormalize the bare mass of the sine-Gordon model, so it must be carefully taken into account.

As a second step, one now reintroduces the coupling between the two chains within the bosonization approach $H_{\perp} = |\alpha|^2 J_{\perp} \int dx \cos(\phi_{\uparrow} - \phi_{\downarrow})$. This strategy is only valid

in the weak tunnelling regime. The low-energy bosonized version of the whole Hamiltonian (8.2) then becomes

$$H \simeq \frac{v_s}{2\pi} \int dx \left(\frac{\pi^2}{2K} [(\Pi_\uparrow + \Pi_\downarrow)^2 + (\Pi_\uparrow - \Pi_\downarrow)^2] + \frac{K}{2} [(\partial_x \phi_\uparrow - \partial_x \phi_\downarrow)^2 + (\partial_x \phi_\uparrow + \partial_x \phi_\downarrow)^2] \right) + J_\perp \int dx |\alpha|^2 \cos(\phi_\uparrow - \phi_\downarrow) \quad (8.7)$$

Finally, one rotates the fields as $\phi_\pm = \phi_\uparrow \pm \phi_\downarrow$ and $\Pi_\pm = (\Pi_\uparrow \pm \Pi_\downarrow)/2$. Note here that the factor 2 that arises in the definition of Π_\pm is needed to enforce the standard commutation relations $[\phi_\pm(x), \Pi_\pm(y)] = i\delta(x-y)$.

In this new basis, the symmetric and anti-symmetric degrees of freedom are explicitly decoupled. While the former are still described by a non-interacting Luttinger liquid, the sine-Gordon Hamiltonian naturally emerges in the anti-symmetric sector

$$H_- = \int dx \frac{v_s}{2\pi} \left(\frac{2}{K} (\pi\Pi_-)^2 + \frac{K}{2} (\partial_x \phi_-)^2 \right) + J_\perp \int dx |\alpha|^2 \cos(\phi_-). \quad (8.8)$$

The equivalence with H_{SG} (8.1) is readily established with the identification $c = v_s$, $cg^2 = 2\pi/K$ and $J_\perp |\alpha|^2 = c^2 m^2 / g^2$. The sign of J_\perp is unimportant, since it can be changed by a global shift $\phi_- \rightarrow \phi_- + \pi$.

Various tunnel coupled one-dimensional discrete or continuous models would equally serve our purposes for realizing the sine-Gordon model. However, considering XXZ spin chains has the great advantage that the Luttinger parameters are analytically available. Indeed, the XXZ spin chain is a well known integrable model whose exact solution in the zero magnetization sector gives [252]

$$K = \frac{\pi}{2} \frac{1}{\pi - \arccos \Delta} \quad v_s = J \frac{\pi \sqrt{1 - \Delta^2}}{2 \arccos \Delta}. \quad (8.9)$$

In the next subsection 8.1.2, we will test the assumption of the decoupling between the symmetric and antisymmetric sectors by measuring correlation functions and numerically extracting the Luttinger parameter K of the symmetric sector. These estimates will indicate that K in the weak coupling regime $J_\perp/J < 0.3$, is very well compatible with the single-chain exact result, Eq. (8.9), showing that hybridization effects between the symmetric and antisymmetric sectors induced by beyond-sine-Gordon corrections are small. In the remainder of this chapter we will at most set $J_\perp/J = 0.2$ to be in the sine-Gordon regime and determine K and v_s from Eq. (8.9).

To conclude this subsection, we would like to briefly comment on the choice of the interchain coupling (8.4), and in particular on the absence of a zz interaction between the two chains $\propto \sum_j S_{j\uparrow}^z S_{j\downarrow}^z$. Indeed, in actual experimental realizations it is more natural to consider an interchain coupling with the same symmetries of the single chain dynamics. However, adding such a term does not harm the sine-Gordon description and only (weakly) renormalizes the Luttinger parameter and sound velocity [208]. In Sec. 8.3.4 we explicitly check that the effective sine-Gordon description remains unaltered despite of this additional contribution. Since adding the zz contribution makes numerical simulations slightly more expensive, we focus in the rest of the chapter on the simpler choice of Eq. (8.4). It is also worth noticing that an experimental setup can be realized

with the Bose-Hubbard model with on-site interactions and nearest-neighbor hopping terms [248]. In this case, a density-density interaction between the two ladders (analogue to the zz interaction in the coupled XXZ chains) is absent by construction. However, for our numerical studies the restricted local Hilbert space of the spin chain and the analytic solutions for its Luttinger parameters are advantageous over directly simulating the Bose-Hubbard model, which is why we focus on the former.

8.1.2 Luttinger parameter in the symmetric sector

As discussed before, the bosonization of the coupled chains predicts the emergence of the sine-Gordon field theory in the odd degrees of freedom, while the even sector remains a gapless Luttinger liquid. In this section, we provide a sanity check of this claim by numerically probing the static correlation functions of the ground state and comparing them with their analytic forms given in Refs. [253, 254]. Indeed, since the contribution of the gapless sector dominates the exponentially-decaying contribution of the massive antisymmetric part ϕ_- , the critical behavior is already clearly seen in single-chain correlation functions, furthermore giving access to K . The results are shown in Fig. 8.2. These fits are however hard to perform, particularly in the regime where $\Delta > 0$ due to the large oscillations in the correlation functions, which results in the large errorbars. We therefore show the results for both

$$\langle +- \rangle_r = \langle 0 | S_{\uparrow j}^+ S_{\uparrow k}^- | 0 \rangle - \langle 0 | S_{\uparrow j}^+ S_{\downarrow k}^- | 0 \rangle \quad (8.10)$$

and

$$\langle zz \rangle_r = \langle 0 | S_{\uparrow j}^z S_{\uparrow k}^z | 0 \rangle + \langle 0 | S_{\uparrow j}^z S_{\downarrow k}^z | 0 \rangle \quad (8.11)$$

with $r = |j - k|$. Notice that we include the interchain correlations as well, although we are considering the weak coupling limit. We have found that by including them the fits were improved, particularly for $\langle zz \rangle_r$. The errorbars shown in the figure are a combination of the uncertainty on the fit, and of the averaging over some different fitting domains $[r_{\min}, r_{\max}]$. We incorporate the latter because the fit of $\langle zz \rangle_r$ is quite sensitive to the choice of r_{\min} , due to non-universal short ranged corrections.

These estimates confirm that the Luttinger parameter of our model agrees with the single chain exact result (8.9) in the weak tunnelling regime. In particular, deviations are only found around $J_{\perp}/J \gtrsim 0.3$. For our analysis in the main text, we have considered $J_{\perp}/J = 0.1, 0.2$.

8.2 The quantum sine-Gordon model

We briefly review the main features of the sine-Gordon field theory and its exact solution, for an exhaustive discussion see Refs. [209, 210]. We mostly refer to the notation of Eq. (8.1), but occasionally relate g and K explicitly when convenient. As already mentioned in the introduction, the sine-Gordon field theory belongs to the class of exactly solvable models: its integrability is established both on the classical [255] and the quantum level [207]. The key characteristic of integrable systems is the presence of infinitely many local conservation laws [256]: this has deep consequences on the excitation spectrum and dynamics. First, conservation laws ensure the existence of asymptotic multiparticle states, in spite of the strong interactions. In the sine-Gordon

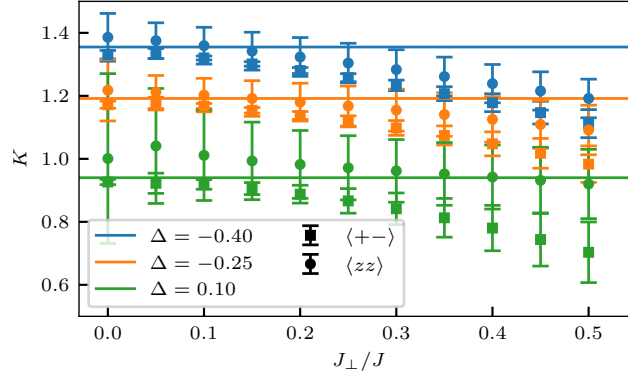


Figure 8.2 Luttinger parameter estimated from a fit to the static correlations in the ground state for a ladder system of size $L = 200$ rungs and for different values of the inter chain coupling J_{\perp}/J . The errorbars incorporate the uncertainty of the fit as well as the average over different spatial fitting ranges. The solid lines show the exact result for the single chain as given by Eq. (8.9).

case, the fundamental excitations are solitons and antisolitons connecting between the valleys of the cosine potential. These excitations have equal masses M_s and relativistic energy $E_s(\theta) = c^2 M_s \cosh \theta$ and momentum $P_s(\theta) = c M_s \sinh \theta$, with θ the relativistic rapidity. The soliton mass scale has a highly non-trivial dependence on the interaction and bare mass scale m [257]

$$c^2 M_s = \left(\frac{c^3 m^2 \pi \Gamma(1/(1+\xi))}{2g^2 \Gamma(\xi/(1+\xi))} \right)^{(1+\xi)/2} \frac{2\Gamma(\xi/2)}{\sqrt{\pi} \Gamma((1+\xi)/2)} \quad (8.12)$$

where $\xi = (8\pi/(g^2 c) - 1)^{-1} = (4K - 1)^{-1}$, and Γ is the Euler-Gamma function. In addition to solitons, the model also features non-topological excitations called breathers. Their masses are quantized according to

$$M_{B_n} = 2M_s \sin \left(n\xi \frac{\pi}{2} \right), \quad (8.13)$$

where $n = \{1, \dots, N\}$ with $N = \lfloor \xi^{-1} \rfloor = \lfloor 4K - 1 \rfloor$. Notice that the interaction g , or equivalently the Luttinger parameter K , tunes the quantumness of the model: for large values of K , the mass gaps between breathers diminish and ultimately merge in a continuum, which corresponds to the excitations of the classical theory. Hence, quantum effects are most prominent for small values of K (i.e. strong interactions in the one-dimensional channels).

The important task of connecting the asymptotic states with actual observables requires the knowledge of the matrix elements, also known as form factors. The form factor bootstrap [210] exploits the analytical properties of the scattering data to compute the sought-after matrix elements: this procedure is extremely challenging, but when possible leads to exact results. For our purposes, we are mostly interested in the vertex operator $e^{i\phi_-}$ [258–260]. Here we focus on the matrix elements between the ground state $|0\rangle$ and one-breather excitations $|B_n(\theta)\rangle$

$$\langle 0 | e^{i\phi_-} | B_n(\theta) \rangle = \mathcal{G}_g \frac{\sqrt{2} \cot(\xi\pi/2) \sin(n\pi\xi) \exp[I_n] e^{i\pi n/2}}{\sqrt{\cot(n\pi\xi/2) \prod_{s=1}^{n-1} \cot^2(s\pi\xi/2)}} \quad (8.14)$$

where

$$I_n = \int_0^\infty \frac{dt \sinh^2(tn\xi) \sinh[t(\xi - 1)]}{t \sinh(2t) \cosh(t) \sinh(t\xi)} \quad (8.15)$$

and the ground state expectation value $\mathcal{G}_g = \langle 0 | e^{i\phi} | 0 \rangle$ is exactly known [261]

$$\mathcal{G}_g = \left(\frac{c^3 m^2}{2g^2} \right)^\xi \frac{(1 + \xi) \tan \left[\frac{\pi\xi}{2} \right] \Gamma^2 \left[\frac{\xi}{2} \right]}{2\pi \Gamma^2 \left[\frac{1+\xi}{2} \right]} \left(\pi \frac{\Gamma \left[\frac{1}{1+\xi} \right]}{\Gamma \left[\frac{\xi}{1+\xi} \right]} \right)^{1+\xi}. \quad (8.16)$$

Interactions among sine-Gordon excitations are encoded in highly non-trivial scattering matrices. Importantly, the conservation of infinitely many charges allows only for elastic scattering. In this respect, two excitations with different masses (e.g. two breathers) can only be transmitted and never reflected: in this case, the logarithmic derivative of the scattering matrix is readily connected with the post-scattering space displacement experienced by two colliding wave packets. In Section 8.4 we will explicitly study such scattering events. The two-particle scattering matrix is the backbone of the integrability approach to the model and can be found in Ref. [207]. From that the breather-breather scattering matrix can be obtained by the form factor bootstrap. Since we are only interested in breather-breather scattering events, we focus on the latter for simplicity. Let $S^{(n,m)}(\theta)$ be the scattering matrix of a scattering between a breather of species n and m , with relative rapidity θ , which for $n \geq m$ reads [209]

$$S^{(n,m)}(\theta) = \frac{\sinh \theta - i \sin \left(\frac{n+m}{2\xi-1} \right) \sinh \theta - i \sin \left(\frac{n-m}{2\xi-1} \right)}{\sinh \theta + i \sin \left(\frac{n+m}{2\xi-1} \right) \sinh \theta + i \sin \left(\frac{n-m}{2\xi-1} \right)} \times \prod_{k=1}^{m-1} \frac{\sin^2 \left(\frac{m-n-2k}{4\xi-1} - i\theta/2 \right) \cos^2 \left(\frac{m+n-2k}{4\xi-1} - i\theta/2 \right)}{\sin^2 \left(\frac{m-n-2k}{4\xi-1} + i\theta/2 \right) \cos^2 \left(\frac{m+n-2k}{4\xi-1} + i\theta/2 \right)}, \quad (8.17)$$

where the renormalized interaction ξ has been defined below Eq. (8.12). The case $n < m$ can be recovered by using the unitary relation $S^{(n,m)}(\theta)S^{(m,n)}(-\theta) = 1$. The scattering matrix is a complex number with modulus 1, therefore one can define the scattering phase $\Theta^{(n,m)}(\theta) = -i \log S^{(n,m)}(\theta)$. The derivative of the scattering phase is connected with the spatial displacement after scattering, see e.g. Ref. [262]. In particular, let $\delta x_{B_n}^{(n,m)}(\theta_n, \theta_m)$ be the spatial displacement experienced by a breather of species n with rapidity θ_n colliding with a breather of species m and rapidity θ_m , then

$$\delta x_{B_n}^{(n,m)}(\theta_n, \theta_m) = \frac{1}{cM_{B_n} \cosh \theta_n} \partial_\theta \Theta^{(n,m)}(\theta) \Big|_{\theta=\theta_n-\theta_m}. \quad (8.18)$$

This is the analytical expression of the spatial displacement that we will use in Section 8.4. In the next section, we begin to explore the low-energy phase space of the spin ladder and quantitatively compare it with the sine-Gordon predictions.

8.3 Spectral analysis of the low energy sector

We systematically probe the low-energy sector of the spin ladder numerically and aim for a quantitative comparison with the sine-Gordon results. This allows us to provide

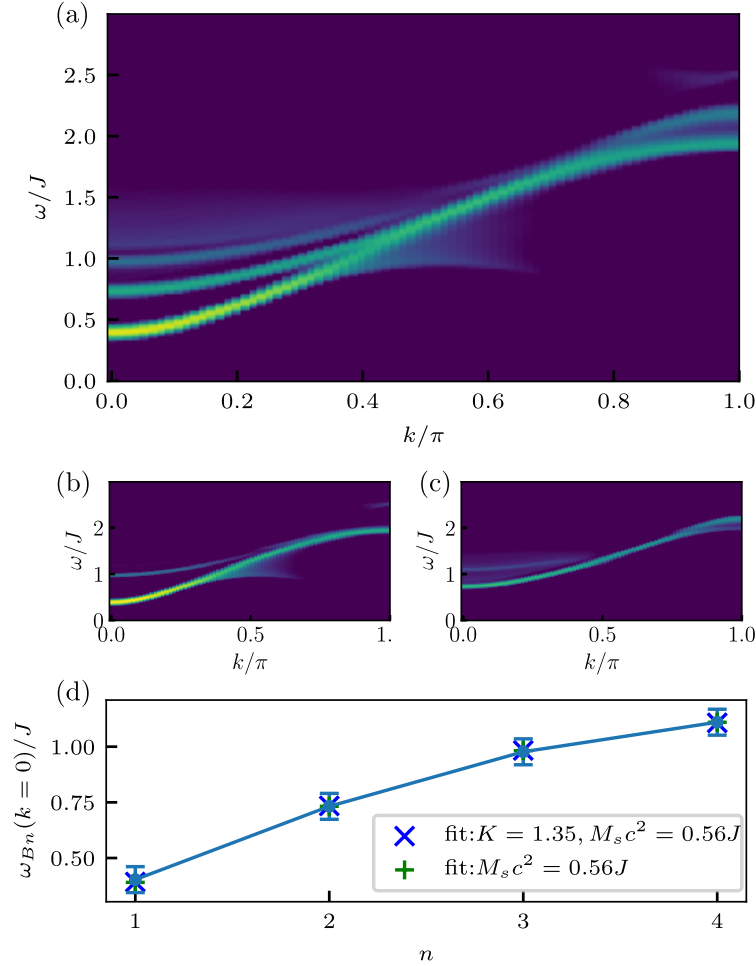


Figure 8.3 (a) The spectral function for a system of $L = 151$ rungs, with model parameters $\Delta = -0.4$ and $J_{\perp} = 0.2J$. We observe $N = 4$ sine-Gordon breathers as expected for $K = 1.35$ of the single chain. The color scale is logarithmic in the spectral weight. (b) Odd sector. (c) Even sector. (d) A fit of the breather energies $\omega(k=0) = c^2 M_{B_n}$ according to Eq. (8.13). The blue crosses are obtained by using both K and $c^2 M_s$ as fitting parameters, while the green pluses are obtained from $c^2 M_s$ as only fitting parameter, illustrating the validity of the single-chain analytic result.

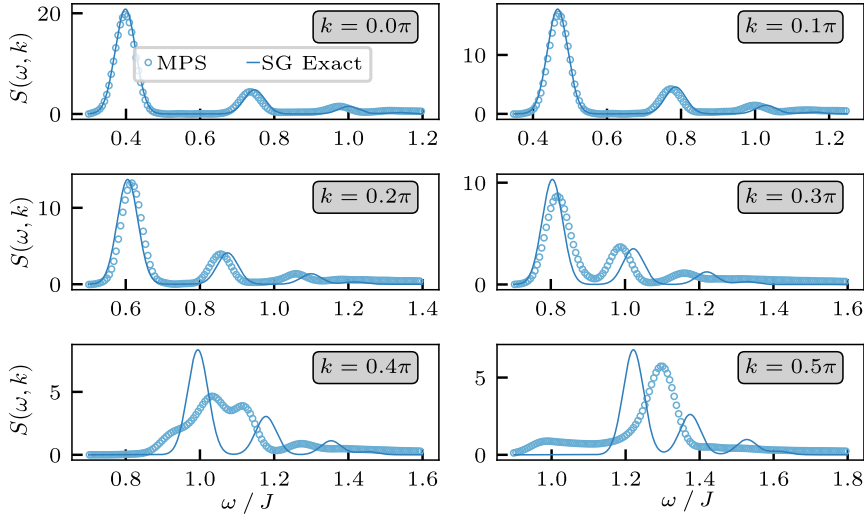


Figure 8.4 Momentum slices of the numerical spectral function shown in Fig. 8.3 compared to the analytical result Eq. (8.20), where only single breather contributions are included. At high momenta there are deviations from the analytic result.

bounds on the validity of the effective low-energy description. In 8.3.1, we show results for the full spectral function. In 8.3.2, we discuss an experimentally accessible protocol to extract the breather masses based on periodic modulations. In 8.3.3 we discuss a protocol to reduce the weight of the dominant breather contributions. In 8.3.4 we investigate the effect of an additional interchain interaction, and show that it does not alter the sine-Gordon description. We end this section in 8.3.5 by providing some numerical details about the calculation of the spectral function.

8.3.1 The spectral function

As the main probe of the excitation spectrum we consider the spectral function

$$S(\omega, k) = \int dt W_\sigma(t) e^{i\omega t} \sum_{j=-L/2}^{L/2} e^{ikj} \langle 0 | O_j^\dagger(t) O_0 | 0 \rangle_c, \quad (8.19)$$

where O_j is a local operator centered on site j , $|0\rangle$ is the ground state of the model (8.2). The Gaussian envelope $W_\sigma(t) = \exp\left(-\frac{1}{2}\frac{t^2}{\sigma^2}\right)$ smoothens out the Gibbs phenomenon in the Fourier transformation caused by the finite-time cutoff present in numerical simulations. To subtract the zero-frequency signal of the ground state, we consider the connected correlation function $\langle 0 | O_j^\dagger(t) O_0 | 0 \rangle_c = \langle 0 | O_j^\dagger(t) O_0 | 0 \rangle - \langle 0 | O_j^\dagger(t) | 0 \rangle \langle 0 | O_0 | 0 \rangle$.

In order to probe the particle content of the theory, we evaluate the spectral function for the single-rung operator $O_j = S_{j\uparrow}^+ S_{j\downarrow}^- \simeq |\alpha|^2 e^{i\phi_-}$, see Eq. (8.6). The non-universal prefactor α is the same governing the bare mass scale (8.8) and does not depend on the interchain coupling J_\perp . Note that we can also target specifically breathers with odd or even parity by respectively considering $O_j = (iS_{j\uparrow}^+ S_{j\downarrow}^- + \text{h.c.})$ or $O_j = (S_{j\uparrow}^+ S_{j\downarrow}^- + \text{h.c.})$.

The spectral function (8.19) can be computed by inserting a Lehmann decomposition of the identity in between the two observables and by expanding in the basis of the

asymptotic states of the field theory. By retaining only the one-particle contributions, one obtains

$$S(\omega, k) = \sum_n \int d\theta \delta(k - cM_{B_n} \sinh(\theta)) \sqrt{2\pi} |\alpha|^2 \sigma \times e^{-\frac{\sigma^2}{2}(\omega - c^2 M_{B_n} \cosh \theta)^2} |\langle 0 | e^{i\phi_-} | B_n(\theta) \rangle|^2. \quad (8.20)$$

As a first comparison, we track the relativistic dispersion law of the breathers and the mass ratios. To this end, we access the microscopic spectral function with MPS techniques to evaluate the real-time correlation function [263, 264]: first, we obtain the ground state $|0\rangle$ by the DMRG algorithm [34, 265], then we perform a real-time evolution of the state $O_0 |0\rangle$ with the TEBD algorithm [35, 263, 266]. For further details about the numerical evaluation of the spectral function, we refer to 8.3.5.

In Fig. 8.3(a) we show the spectral function of a ladder with $\Delta = -0.4$, corresponding to $K = 1.35$, and $J_\perp = 0.2J$. For this choice of parameters, we expect $N = 4$ breathers to appear in the spectral function as can be indeed observed. We also show the separate odd and even spectra respectively in Fig. 8.3(b) and 8.3(c). In Fig. 8.5 further spectral functions for a different number of breathers $N = 2, 3$ are shown and the coupling strength $J_\perp/J = 0.1, 0.2$ is varied. Notice that, at least for small momenta, the signal nicely follows the expected behavior of the relativistic dispersion law $E_{B_n}(k) = \sqrt{c^4 M_{B_n}^2 + c^2 k^2}$. The feature observed around $k \simeq \pi/2$ is a clear deviation from the sine-Gordon description and is a remnant of the single-chain spinon dispersion. In the single chain the lower edge of the spinon continuum at $k = \pi/2$ is perturbatively given by $(1 + 2\Delta/\pi)J$ [267, 268]. The weak tunnel coupling is only expected to strongly modify the low-energy regime $\omega \lesssim J$. In the higher energy regime our correlator perturbatively contains terms of the form $\langle 0_\uparrow | S_{j\uparrow}^-(t) S_{0\uparrow}^+ | 0_\uparrow \rangle$ with $|0_\uparrow\rangle$ the ground state restricted to the single chain, and unveils the lower edge of the spinon continuum at high momenta.

To test the validity of the mass prediction Eq. (8.13), we then extract the breather energies from the peaks of the spectral function at $k = 0$. In this case, we use the soliton energy and K as fitting parameters; see Fig. 8.3(d). As best fit parameters we obtain $K = 1.35 \pm 0.03$ and $c^2 M_s/J = 0.56 \pm 0.01$. The best-fit K is thus compatible with the single-chain exact result of $K = 1.35$ given by Eq. (8.9). The excellent agreement of numerical data with the mass law is already a clear signature of the sine-Gordon effective theory, but we now want to quantitatively compare the whole spectral functions Eqs. (8.19) and (8.20), thus confirming that breathers contribute through the form factor expression (8.14).

The sine-Gordon model determines the spectral function up to an overall constant α coming from the single-chain bosonization (8.6) which, in turn, sets the sine-Gordon bare mass scale and eventually the soliton mass through Eq. (8.12). Reversing the logic, we can look at the physical soliton mass as the free parameter to be determined, which unambiguously fixes the microscopic non-universal proportionality factor α . We first check the non-trivial dependence of the mass gap (mass of the lightest breather) with the coupling across the rungs J_\perp . Indeed, by feeding the microscopic value of the bare mass in Eq. (8.12), we obtain $\Delta E = c^2 M_{B_1} \propto J_\perp^{(1+\xi)/2}$, where the proportionality constants are J_\perp independent. In Fig. 8.7, we show the numerically computed energy gaps as a function of the rung coupling for several interaction strengths Δ , finding

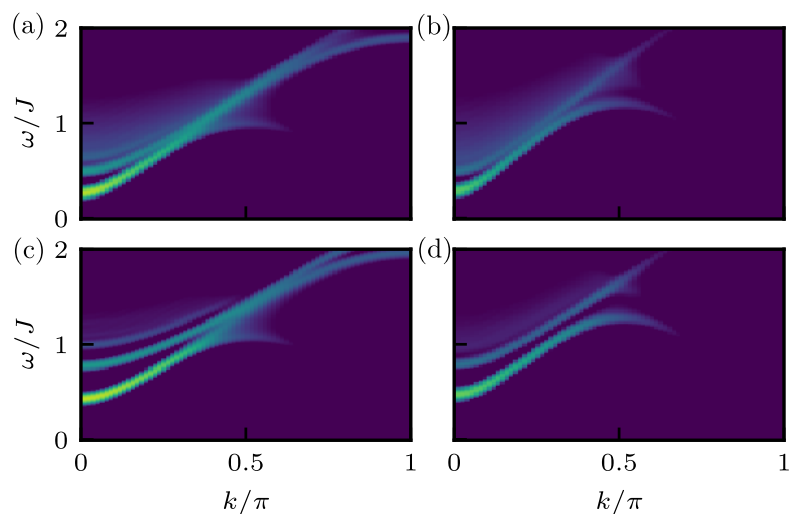


Figure 8.5 Spectral functions for a system of $L = 151$ rungs for two different values of Δ and two coupling strengths $J_{\perp}/J = 0.1, 0.2$. (a,b) Here $\Delta = -0.25$, corresponding to $K \simeq 1.18$ and $N = 3$ breathers. (c-d) Here $\Delta = 0.1$, corresponding to $K \simeq 0.94$ and $N = 2$ breathers. The color scale used in the spectral-density plots is logarithmic in order to make the higher lying breathers also visible compared to the lower ones.

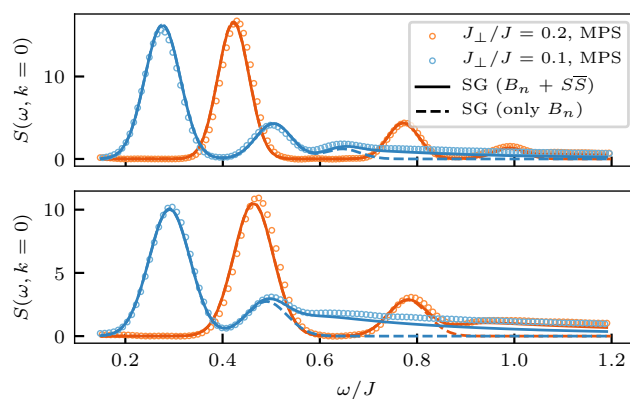


Figure 8.6 The profile of the spectral functions at $k = 0$ shown in Fig. 8.5 for both coupling strengths and their comparison to the exact result: the solid lines take into account the breathers and the soliton/anti-soliton continuum, while the dashed lines only takes into account single breather contributions.

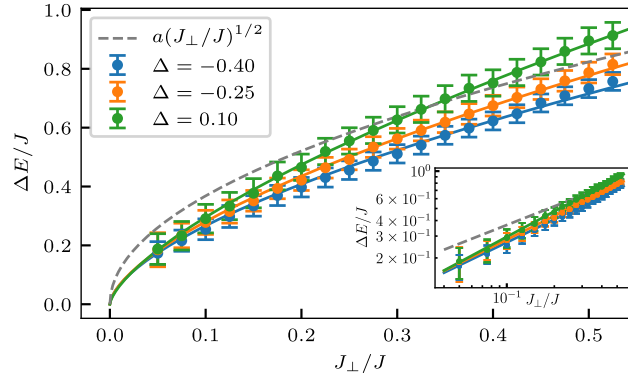


Figure 8.7 The energy gap in the anti-symmetric sector as obtained from the dynamic correlation functions of the ground state as a function of the interchain coupling. The solid lines show a fit of the data according to $a(J_{\perp}/J)^{\frac{1+\xi}{2}}$ with $\xi = (4K - 1)^{-1}$ fixed. The errorbars are set by the resolution in frequency space. The inset shows the same data in a logarithmic scale.

an excellent agreement with the non-trivial power law behavior in the whole range of explored parameters.

Equipped with this benchmark of Eq. (8.12), we can now pursue the program outlined above and extract the parameter α from the measurement of the energy gap. In Fig. 8.4 we quantitatively compare the energy dependence of the spectral function (8.19) shown in Fig. 8.3(a) with the sine-Gordon prediction (8.20) for different values of the momenta k : at small momenta, the agreement is excellent. We stress once again that α is the only fitting parameter. The Gaussian broadening of the peaks governed by σ in Eqs. (8.19) and (8.20) has been set equal in both cases. As one moves to higher momenta, small deviations from the field theory prediction become evident, but the peaks of the excitations are still clearly seen (see e.g. $k = 0.3\pi$). In this regime, we interpret the deviation as lattice corrections to the sine-Gordon relativistic dispersion relation, which is slightly bend towards smaller energies. As the momentum is further increased, the spinon contribution of a single chain starts to become dominant and the energy peaks of the sine-Gordon breathers disappear.

We further analyze the spectral function for different parameters, changing the number of breathers in the sine-Gordon spectrum, in Fig. 8.5. To quantitatively probe the field theory, we show the comparison between the numerical and analytic spectral function at zero momentum $k = 0$ in Fig. 8.6. Reducing the value of J_{\perp} , the energy scale of the excitations is lowered and the spectral function develops a continuous tail associated with multiparticle contributions, to be contrasted with the isolated peaks of single-breather terms. To capture this continuum, we add the soliton-antisoliton contribution to the spectral function (8.20). The solitonic form factors of the vertex operators have been computed in Ref. [258]. In Fig. 8.6 we compare the spectral function at $k = 0$ obtained by considering only the contribution of breathers (dashed line) with the extension to the soliton-antisoliton corrections (solid line) and the numerics (circles). The comparison shows that solitons capture the tails of the spectral function well. Depending on the value of K , the energy of the soliton-antisoliton pair can be comparable to the excitations of two breathers B_1 : we checked this correction to the spectral function, but the $B_1 - B_1$

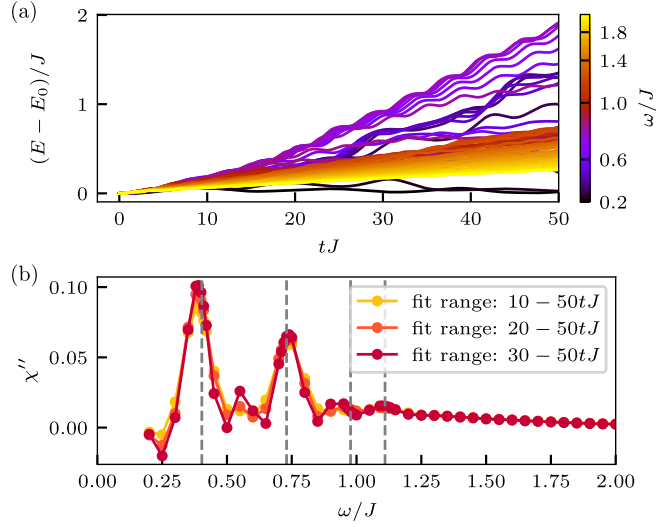


Figure 8.8 (a) Energy absorption for a small periodic drive. Here $\epsilon = J_{\perp}/4$. The system size is $L = 51$ and the model parameters are $\Delta = -0.4$ and $J_{\perp}/J = 0.2$. (b) Spectral functions extracted from the absorbed power from Eq. (8.22). The fit of the slope is performed in several time domains (legend). The dashed grey lines show the breather energies extracted from the spectral function at $k = 0$ (c.f. Fig. 8.3).

contribution turned out to be negligible. We thus attribute the small discrepancy with the numerical data to corrections beyond sine-Gordon.

From the spectral functions (shown in Figs. 8.3 and 8.5) it becomes apparent that the spectral weight of the higher lying breathers, with breather index $n > 2$ is strongly suppressed with respect to the lower lying ones. In the next section 8.3.3 we provide a form factor argument to increase the relative weight of the higher lying breather, that is based on computing the spectral function over a correlation function of a linear combination of single- and two-rung operators. However before that, we will first study a driving protocol to probe the masses of the breathers.

8.3.2 Breather spectroscopy from periodic modulations of the interchain coupling

While the spectral function (8.19) gives direct access to the low-energy spectrum of the coupled chains, measuring unequal-time correlation functions is challenging in realistic experimental scenarios. To this end, the fluctuation-dissipation theorem can be used to relate the spectral function to the energy absorption due to periodic drives. We consider a periodic modulation of the Hamiltonian $H(t) = H + V(t)$, where H is given by Eq. (8.2), and

$$V(t) = \epsilon \sin(\omega t) O \quad (8.21)$$

where we chose the perturbation as a linear combination of two terms $O = aO_1 + bO_2$, with $O_1 = \sum_{i=0}^{L-1} (S_{i\uparrow}^z - S_{i\downarrow}^z)$ and $O_2 = \sum_{i=0}^{L-1} (S_{i\uparrow}^+ S_{i\downarrow}^- + \text{h.c.})$.

The choice of the drive is motivated on physical grounds. O_1 is the z -magnetization difference between the two chains. Hence, driving O_1 can be achieved by applying a small magnetic field of opposite sign to the two chains. On the other hand, modulations

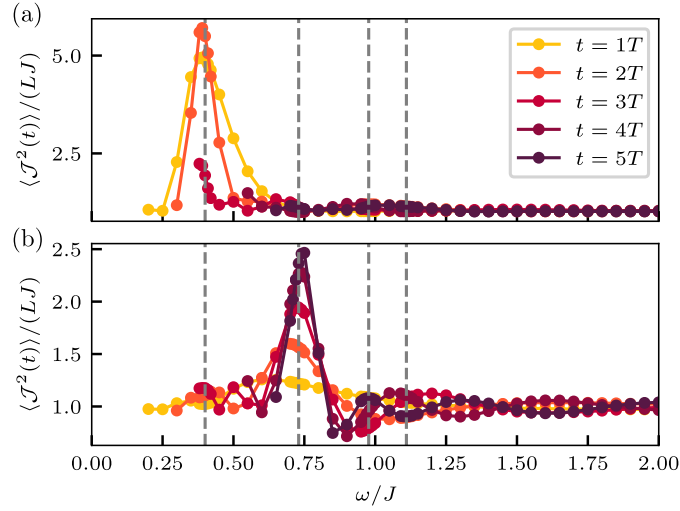


Figure 8.9 Current fluctuations measured at discrete times that are a multiples of the driving period $T = 2\pi/\omega$. The dashed grey lines show the breather energies extracted from the spectral function (see Fig. 8.3) at $k = 0$. The system size is $L = 51$ and the model parameters are $\Delta = -0.4$ and $J_{\perp}/J = 0.2$ (a) Here $\epsilon_1 = J_{\perp}/4$ and $\epsilon_2 = 0$, so we only target odd breathers and only B_1 strongly. (b) Here $\epsilon_1 = 0$ and $\epsilon_2 = J_{\perp}/4$, so here we only target even breathers and only B_2 strongly.

coupled to O_2 are obtained by manipulating the interchain coupling (8.4). Here, we focus on the linear response on the top of the ground state. Hence we limit ourselves to the case $\epsilon < J_{\perp}$. Within bosonization (8.6), $O_1 \sim \int dx \Pi_{-}(x)$ and $O_2 \sim \int dx \cos(\phi_{-})$. Therefore, the operators O_1 and O_2 respectively excite odd and even breathers from the ground state. In linear response theory, the fluctuation-dissipation theorem links the averaged absorbed energy to the spectral function at zero momentum. Defining $E(t) = \langle H(t) \rangle$, one has

$$\frac{\overline{dE}}{dt} = \frac{1}{T} \int_0^T dt \frac{dE(t)}{dt} = \frac{\epsilon^2 \omega}{4} S(\omega, 0), \quad (8.22)$$

where $T = 2\pi/\omega$ is the driving period. Hence the spectral function is directly probed by the slope of the on-average linear growth of the energy. Notice that the different parity of the operators $O_{1,2}$ leads to a splitting of the spectral function $S(\omega, k) = a^2 S_{O_1}(\omega, k) + b^2 S_{O_2}(\omega, k)$, where $S_{O_{\mu}}$ is the spectral function of the operator O_{μ} . Hence, the choice of the coefficients a, b does not have any physical meaning within the linear regime and we consider $a = b = 1$ to probe the even and odd sectors within a single measurement.

In Fig. 8.8(a) we show the energy growth for various driving frequencies, and in Fig. 8.8(b) we show the corresponding response function extracted from linear fits in several time windows. We compare the results to the breather energies extracted from the two-point correlation function, illustrating a very good agreement.

However, as the energy is probably hard to reconstruct from experimental data, we could alternatively aim to measure the current fluctuations

$$\langle \mathcal{J}^2 \rangle = \frac{1}{L} \sum_{ij} \langle \mathcal{J}_i \mathcal{J}_j \rangle \quad (8.23)$$

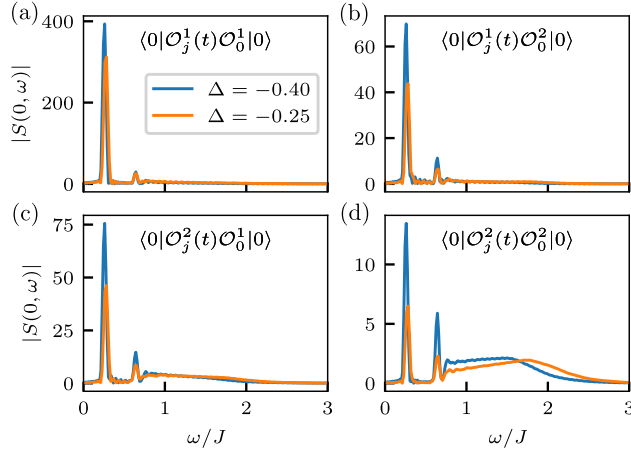


Figure 8.10 (a-d) Spectral functions at $k = 0$ evaluated from the correlation functions given in the panels for two different values of Δ . The interchain coupling is $J_{\perp}/J = 0.1$, and the system size $L = 151$. The peaks correspond to B_1 and B_3 and their relative strengths can be compared. For the two rung operators there is a continuum present, see panel (d).

with $\mathcal{J}_j = iS_{\uparrow j}^+ S_{\downarrow j}^- + \text{h.c.}$. Those can be readily accessed by rotating all spins with the local unitary

$$U = \prod_i e^{-i\frac{\pi}{4}(S_{i\uparrow}^+ S_{i\downarrow}^- + \text{h.c.})}, \quad (8.24)$$

and by measuring density $n_{i\uparrow}$, $n_{j\downarrow}$ correlations, in the new basis. Note that when $\epsilon_1 = 0$ the current expectation value $\langle \mathcal{J} \rangle = 0$ exactly, and that when $\epsilon_2 \neq 0$ the average over time of $\langle \mathcal{J} \rangle$ vanishes. However the current fluctuations are always finite and exhibit a strongly oscillating growth over time at resonant frequencies. Due to these strong oscillations it is sufficient (and the more practical) to only measure at discrete points in time that are multiples of the driving frequency $T = 2\pi/\omega$. These measurements are shown in Fig. 8.9, for respectively drives that target only odd and even breathers.

The spectral weight of B_3 and B_4 is probably too low to render these excitations observable in experiments, however the ratio between B_2 and B_1 is already sufficient to obtain the mass scaling.

8.3.3 Form factor suppression of B_1

The relative spectral weight of the breathers in the spectral function can be tuned by considering a linear combination of a single and a double rung operator, instead of just the single rung operator. This could be useful because the spectral weight of the breathers B_n with breather index $n > 2$ is strongly suppressed compared to the lower lying ones B_1, B_2 . Here we discuss a sine-Gordon form factor argument to reduce the weight of B_1 compared to B_3 (we will work in the odd breather sector). Introducing the single and two rung operators

$$\begin{aligned} O_j^1 &= S_{j\uparrow}^+ S_{j\downarrow}^- \\ O_j^2 &= S_{j\uparrow}^+ S_{j+1\uparrow}^+ S_{j\downarrow}^- S_{j+1\downarrow}^-, \end{aligned} \quad (8.25)$$

which according to bosonization are ($\alpha_{1,2} \in \mathbb{R}$)

$$O^1 = \alpha_1 e^{i\phi_-}, \quad O^2 = \alpha_2 e^{2i\phi_-}. \quad (8.26)$$

Our goal is to find a linear combination $\tilde{O} = O^1 + AO^2$ of these operators such that

$$\langle 0 | \tilde{O} | B_1 \rangle \simeq 0. \quad (8.27)$$

Within sine-Gordon, we have the following form factor for $B_1 - 0$

$$\langle 0 | e^{im\phi_-} | B_1 \rangle = 2i \langle 0 | e^{im\phi_-} | 0 \rangle \frac{\sin(m\pi\xi)}{\sin(\pi\xi)} \sqrt{\frac{\sin(\pi\xi)}{F_{\min}}} \quad (8.28)$$

with

$$F_{\min} = \frac{1}{\cos(\pi\xi/2)} \exp\left(\frac{1}{\pi} \int_0^{\pi\xi} dt \frac{t}{\sin t}\right). \quad (8.29)$$

We have that

$$\begin{aligned} \langle 0 | O^1 | 0 \rangle &= \alpha_1 \langle 0 | e^{i\phi_-} | 0 \rangle, \\ \langle 0 | O^2 | 0 \rangle &= \alpha_2 \langle 0 | e^{2i\phi_-} | 0 \rangle, \end{aligned} \quad (8.30)$$

and therefore to satisfy Eq. (8.27)

$$A \simeq -\frac{1}{2 \cos(\pi\xi)} \frac{\langle 0 | O^1 | 0 \rangle}{\langle 0 | O^2 | 0 \rangle}. \quad (8.31)$$

Due to the interchain symmetry $\langle 0 | O^{1,2} | 0 \rangle = \langle 0 | O^{1,2} | 0 \rangle^*$, we can simply translate the argument to the anti-symmetric combination of the operators

$$\begin{aligned} \mathcal{O}_j^{1,2} &= i\mathcal{O}_j^{1,2} + \text{h.c.} \\ \tilde{\mathcal{O}}_j &= \mathcal{O}_j^1 + A\mathcal{O}_j^2. \end{aligned} \quad (8.32)$$

Such that when we compute the spectral function Eq. (8.19) with $O_j(t) = \tilde{\mathcal{O}}_j(t)$, B_2 vanishes because of parity, and B_1 is significantly reduced by the above construction. We have numerically computed the four contributions to the correlation function separately

$$\begin{aligned} \langle 0 | \tilde{\mathcal{O}}_j(t) \tilde{\mathcal{O}}_0 | 0 \rangle &= \langle 0 | \mathcal{O}_j^1(t) \mathcal{O}_0^1 | 0 \rangle + A \langle 0 | \mathcal{O}_j^1(t) \mathcal{O}_0^2 | 0 \rangle \\ &\quad + A \langle 0 | \mathcal{O}_j^2(t) \mathcal{O}_0^1 | 0 \rangle + A^2 \langle 0 | \mathcal{O}_j^2(t) \mathcal{O}_0^2 | 0 \rangle. \end{aligned} \quad (8.33)$$

Their respective spectral functions at $k = 0$ are shown in Fig. 8.10 for different values of Δ . Each of the spectral functions detects B_1 and B_3 , however, with different relative weights. In the spectral function obtained from the two-rung operators, Fig. 8.10(d), there is also a continuum contribution present. When summing up the correlation functions according to Eq. (8.33) we can indeed reduce the contribution of the first peak significantly. The resulting spectral function at $k = 0$ are shown in Fig. 8.11a for different values of A , with $\Delta = -0.4$ and $J_{\perp}/J = 0.1$. Making A larger will always increase the spectral weight of the continuum, however the relative weight between B_1 and B_3 reaches a minimum at some intermediate A , that we have found numerically to be around $A = 5.3$. This can be compared to the value obtained from Eq. (8.31) by filling in the ground state expectation values (in the bulk) and the single-chain K , $A_{\text{Eq. (8.31)}} \approx 6.3$. The two values are in decent agreement.

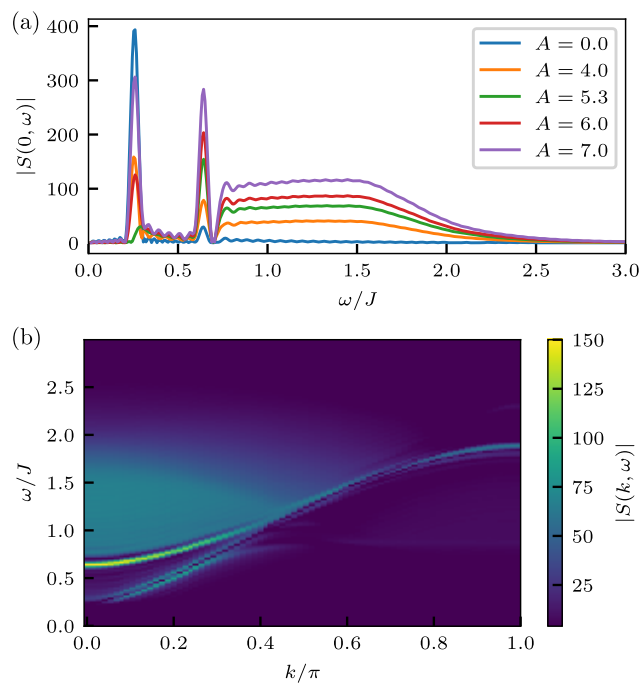


Figure 8.11 (a) Spectral functions from the combination of all contributions shown in Fig. 8.10 for $\Delta = -0.4$ according to Eq. (8.33) at $k = 0$ for some different values of A . The B_1 peak is reduced the most for $A = 5.3$. (b) Spectral function for $A = 5.3$. Here $\Delta = -0.4$, the interchain coupling is $J_{\perp}/J = 0.1$ and the system size is $L = 151$.

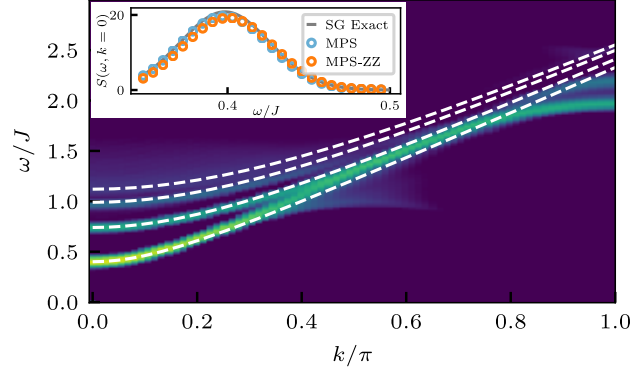


Figure 8.12 The same spectrum as shown in Fig. 8.3(a), but computed with an interchain interaction of strength $J_{\perp}^z = \Delta J_{\perp}$. The parameters of the system are $L = 151$, $\Delta = -0.4$ and $J_{\perp} = 0.2J$. The inset shows a close zoom on the profile of the first breather at $k = 0$. This data is compared to the same data with $J_{\perp}^z = 0$, and with the exact sine-Gordon prediction. The white dashed lines show the exact sine-Gordon dispersion for the four breathers as determined without the zz term, illustrating that the effect of the interchain zz interaction is negligible.

8.3.4 The contribution of the interchain zz coupling

In this section, we analyze the consequences of the interchain coupling $J_{\perp}^z \sum_j S_{j\uparrow}^z S_{j\downarrow}^z$ to the interaction (8.4). Within bosonization (8.6), such a modification amounts to adding a further term $J_{\perp}^z \int dx \Pi_{\uparrow}(x) \Pi_{\downarrow}(x)$ to the coupled Luttinger liquids. After some algebra, one obtains that the symmetric and antisymmetric sectors are still decoupled and are described by the sine-Gordon and the gapless boson Hamiltonian respectively. The only difference with the case where the zz coupling is absent consists in a weak renormalization of the Luttinger parameter and sound velocity in the two sectors, the renormalization being different in the symmetric and antisymmetric sectors. In particular, within the antisymmetric sector one finds

$$\begin{aligned} K &\rightarrow K_{\text{asym}} = K \left(1 - \frac{K J_{\perp}^z}{\pi v_s} \right)^{1/2} \\ v_s &\rightarrow v_{s,\text{asym}} = v_s \left(1 - \frac{K J_{\perp}^z}{\pi v_s} \right)^{-1/2}. \end{aligned} \quad (8.34)$$

Additional interactions coming from higher harmonic contributions of the S_j^z bosonization contribute as corrections beyond sine-Gordon [208], but these terms are irrelevant in a RG sense in the regime $4K > 1$. Therefore, these corrections can be neglected at low energies and do not harm the emergent sine-Gordon field theory description. To corroborate this result, in Fig. 8.12 we numerically computed the spectral function with the same parameters as the spectrum shown in Fig. 8.3(a), but with an additional interchain interaction of strength $J_{\perp}^z = \Delta J_{\perp}$. These spectra appear indeed identical. In the inset we show a zoom on the profile of the first breather peak at $k = 0$, and compare the two cases: the differences are minor. For the parameters shown, the renormalization according to Eq. (8.34) causes around $\sim 2\%$ of difference which indeed appears to be negligible.

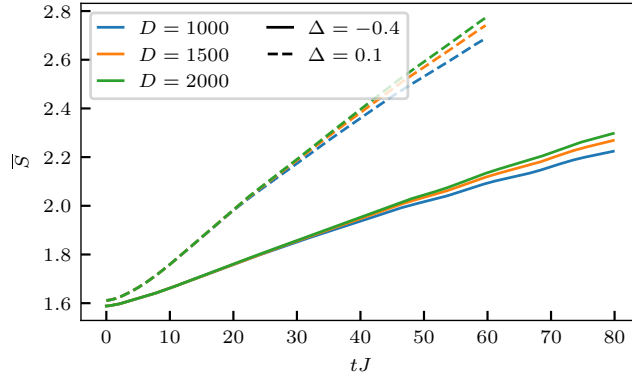


Figure 8.13 The growth of the average entanglement entropy per bond in the time-evolved state $e^{-iHt} S_{\uparrow j}^+ S_{\downarrow j}^- |0\rangle$ for different bond dimensions $D = 1000, 1500, 2000$ for a ladder system of size $L = 151$ and two different Δ . The tunnel coupling is $J_{\perp}/J = 0.1$

8.3.5 Technical details on the calculation of spectral functions

We provide some technical aspects on our MPS simulations for the spectral functions shown in Sec. 8.3. Our evaluation of the spectral function (8.19) relies on the computation of the unequal-time correlation function $C_j(t) = \langle 0 | O_j^\dagger(t) O_0 | 0 \rangle$. We explicitly perform the real-space time evolution and then the Fourier transformations to momentum and frequency space. To obtain the time evolution, we apply the TEBD algorithm [35, 263, 266] to the state $O_0 |0\rangle$, where $|0\rangle$ is the ground state of the ladder (8.2) obtained from DMRG [34, 265]. We group the sites connecting each rung of the ladder (labelled by \uparrow, \downarrow) to a single site, and map the ladder system to a chain with an increased local Hilbert space of dimension $d = 4$. Within this chain there are only two-site interactions. Hence, we can apply a fourth order TEBD scheme efficiently. As a next step, it suffices to compute the overlaps with $O_j |0\rangle$ at different time steps as

$$C_j(t) = e^{iE_0 t} \langle 0 | O_j^\dagger e^{-iHt} O_0 | 0 \rangle \quad (8.35)$$

with E_0 the ground-state energy. The operator O_0 acts in the middle of the system and ideally we want to exclude boundary reflections. Therefore, the maximal time of the simulation is chosen as $t_{\max} \lesssim L/(2v_s)$ with v_s the sound velocity. As the resolution in frequency space is directly related to t_{\max} , we simulate the largest system sizes possible. In practice, we simulated ladders up to $L = 151$ rungs for moderate $\Delta \in [-0.4, 0.1]$. The sound velocity is set by Δ (see Eq. (8.9) in the main text), so also t_{\max} and the frequency resolution will depend on Δ . As the sound velocity becomes larger with increasing Δ , the entanglement growth will be also more pronounced. In Fig. 8.13 we show the entanglement growth in a chain of $L = 151$ grouped sites, with $J_{\perp}/J = 0.1$, for two different values of Δ each at three different bond dimensions, where

$$\bar{S} = \frac{1}{L-1} \sum_b S_{\text{vN}}(b) \quad \text{with} \quad S_{\text{vN}}(b) = -\text{Tr}(\rho_b \log \rho_b). \quad (8.36)$$

with b running over all bonds, and ρ_b the bipartite reduced density matrix with respect to that bond. In the simulations shown in the main text, we typically use a bond dimensions of $D = 1500$. Before taking the Fourier transform to frequency space, we

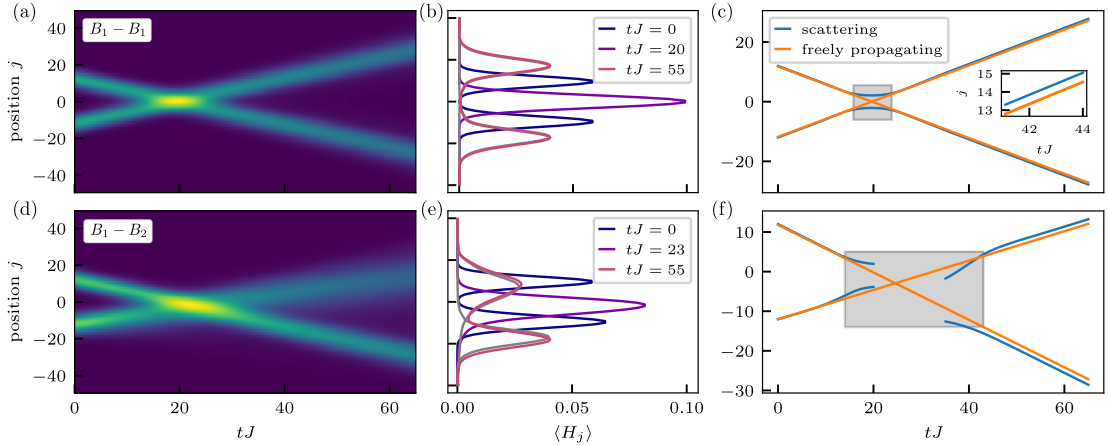


Figure 8.14 Wave packet scattering in the low-energy regime of the coupled chains with parameters $J_{\perp}/J = 0.1$, $\Delta = -0.4$ and $L = 101$. (a,d) The local energy as function of time for a scattering event between two B_1 quasiparticles with momentum $k = \pm 0.2\pi$, panel (a), and between B_1 and B_2 quasiparticles with respective momenta $k_1 = -0.2\pi$ and $k_2 = 0.15\pi$, panel (d). (b,e) The corresponding energy profiles at selected times, where the grey lines show the profile of the freely propagating wave packets at the latest time. (c,f) The associated average positions of the quasiparticles. The numerically obtained values for the scattering displacements are $\delta x_{B_1}^{(11)} \simeq 0.5$, see also the inset in panel (c), and $\delta x_{B_1}^{(12)} \simeq 1.4$, $\delta x_{B_2}^{(12)} \simeq 1.2$.

multiply the data with a Gaussian window with standard deviation σ [263], which we tune as function of the maximal time of the simulation t_{\max} . This sets the resolution in frequency space, and induces a broadening of the peaks.

8.4 Real-time scattering of sine-Gordon excitations

The excellent comparison between the ladder spectral function and the sine-Gordon field theory allowed us to identify the regime of validity of the latter. As a next step, we probe genuine non-equilibrium dynamics of the system. A clear signature of integrability can be found in scattering events: the existence of infinitely many conservation laws ensures complete elastic scatterings even if non-elastic scatterings are, in principle, energetically allowed. We thus create localized wave packets of the lighter breathers and observe their scattering dynamics. In this case, the sine-Gordon scattering matrix ensures complete transmission of breather-breather scatterings (to be contrasted with soliton-antisoliton scattering which, due to additional symmetries, can also be reflective). Complete transmissive scattering arises also in non-interacting theories, but in the sine-Gordon field theory interactions are strong and manifest as a spatial displacement after scattering. The displacement is completely determined by the exactly known scattering matrix [207], as we briefly reported in Sec. 8.2 (see also Refs. [269, 270] for numerical computation of scattering displacement in integrable spin chains).

The sine-Gordon excitations are collective low-energy modes that are not trivially connected to the spin configurations. To engineer a local breather excitation, we create

a Gaussian wave packet with momentum k , centered around site d with width $\bar{\sigma}$ by applying the operator

$$O_{d,k}^{(1)} = \frac{1}{\sqrt{2\pi\bar{\sigma}}} \sum_j e^{-\frac{(j-d)^2}{2\bar{\sigma}^2} + ikj} (S_{j\uparrow}^z - S_{j\downarrow}^z) \quad (8.37)$$

on the ground state $O_{d,k}^{(1)}|0\rangle$. Within bosonization $S_{j\uparrow}^z - S_{j\downarrow}^z \simeq \Pi_-$, hence the low-energy excitations are determined by the sine-Gordon form factors $\langle B_n(\theta)|\Pi_-|0\rangle$ which are exactly known [210], but their analytical expression is not needed for our purposes. The Π_- operator is odd under the \mathbb{Z}_2 symmetry of the sine-Gordon model $\phi_- \rightarrow -\phi_-$. Moreover, the matrix element is non vanishing only for breathers odd under parity, which correspond to odd integers n , and gets smaller as n is increased. Therefore, the operator (8.37) will with highest probability couple to the lightest breather. But this is not the only contribution: heavier breathers are expected to be excited as well and, most importantly, high-energy excitations beyond the sine-Gordon description are inevitably produced. To eliminate the unwanted contributions and target low-energy excitations within an energy interval ΔE , we perform a short imaginary-time evolution $e^{-\tau H}$, $\tau \sim 1/\Delta E$. After this, we indeed obtain clean wave packets that are moving with a speed compatible with the group velocity $v_1(k) = \partial_k E_{B_1}(k)$. In 8.4.3, we provide further technical details about the creation of the wave packets.

With the operator $O_{d,k}^{(1)}$ Eq. (8.37), we can target the first breather B_1 , but we also want to scatter wave packets of different species to highlight the sought-after transmission. To this end, we also create wave packets by using another operator $O_{d,k}^{(2)}$

$$O_{d,k}^{(2)} = \frac{1}{\sqrt{2\pi\bar{\sigma}}} \sum_j e^{-\frac{(j-d)^2}{2\bar{\sigma}^2} + ikj} (S_{j\uparrow}^+ S_{j\downarrow}^- + \text{h.c.} - \langle o_j \rangle). \quad (8.38)$$

In this case, we need to explicitly impose orthogonality with respect to the ground state $\langle 0|O_{d,k}^{(2)}|0\rangle = 0$ by subtracting the expectation value $\langle o_j \rangle = \langle 0|S_{j\uparrow}^+ S_{j\downarrow}^- + \text{h.c.}|0\rangle$. In bosonization, $[S_{j\uparrow}^+ S_{j\downarrow}^- + \text{h.c.}] \sim \cos \phi_-$, which is an even operator. Hence, in the low-energy sector $O_{d,k}^{(2)}|0\rangle$ couples only to wave packets of even breathers. Therefore, by cooling down the state $O_{d,k}^{(2)}|0\rangle$ with imaginary-time evolution, we can selectively excite wave packets of the second breather B_2 .

8.4.1 $B_1 - B_1$ scattering

We start by considering a symmetric $B_1 - B_1$ scattering event, where we initialize the state as

$$O_{-d,k_2}^{(1)} O_{d,k_1}^{(1)} |0\rangle, \quad (8.39)$$

with $d = 12$ and $k_2 = -k_1 = 0.2\pi$. We show the local energy profile as a function of time in Fig. 8.14(a), from this we indeed observe a very coherent motion of the wave packets. In Fig. 8.14(c) we plot the average position of the scattering wave packets in the upper-half ($x_{\text{u-h}}$) and in the lower-half ($x_{\text{l-h}}$) of the system as obtained by

$$\begin{aligned} x_{\text{u-h}} &= \frac{1}{\mathcal{N}} \sum_{j \in \text{u-h}} j \langle H_j \rangle^2 \quad \text{with} \quad \mathcal{N} = \sum_{j \in \text{u-h}} \langle H_j \rangle^2, \\ x_{\text{l-h}} &= \frac{1}{\mathcal{M}} \sum_{j \in \text{l-h}} j \langle H_j \rangle^2 \quad \text{with} \quad \mathcal{M} = \sum_{j \in \text{l-h}} \langle H_j \rangle^2. \end{aligned} \quad (8.40)$$

Note that these measures are only valid in the asymptotic regions before and after the scattering event, where the separation between the wave packets is much larger than their typical interaction length. Comparing the average position between the interacting and freely propagating case, we find a displacement of $\delta x_{B_1}^{(11)} \simeq 0.5$ (see inset in Fig. 8.14(c)). This value can be compared to the analytical result obtained from the S -matrix of the sine-Gordon theory. To obtain a concrete result, we have used the following: (i) the Luttinger parameter K and the sound velocity $v_s = c$ as obtained from the single chain by Eq. (8.9), for $\Delta = -0.4$, $K = 1.35$ and $c = 0.73J$, (ii) the soliton mass $M_s = \Delta E / (2c^2 \sin(\pi\xi/2))$ where we determined the energy gap $\Delta E/J = 0.26$ from the spectral function, (iii) the average speed of the wave packets $v = \pm 0.60J$ which we have obtained from a fit of the freely propagating wave packets and not from the original input momentum chosen in Eq. (8.37) as the imaginary time evolution could potentially slightly lower the initial momentum of the wave packet (see also 8.4.3). Finally, when the two wave packets collide, each excitation will scatter with all the breathers contained in the other wave packet and pile up the cumulative space displacement. Hence, we need to estimate the number of excited breathers. To this end, we consider the total energy carried by each wave packet and divide by the breather dispersion law computed at the rapidity extracted from the velocity measurement. From this analysis, we found that we excite approximately one breather in each wave packet. Using this last piece of information, we then obtain an analytic value of $\delta x_{B_1}^{(11)} = 0.44$ in good agreement with our numerical estimate. Notice that in the case of equal particles, one cannot distinguish between a transmission or reflection event. Hence, we now consider wavepackets of different breathers.

8.4.2 $B_1 - B_2$ scattering

Next, we consider a mixed $B_1 - B_2$ scattering event by initializing the state as

$$O_{-d,k_2}^{(2)} O_{d,k_1}^{(1)} |0\rangle, \quad (8.41)$$

with $k_1 = -0.2\pi$, $k_2 = 0.15\pi$ and $d = 12$. The wave packet associated with B_2 (the heavier quasiparticle) is expected to have a smaller velocity than the B_1 wave packet, and therefore also a larger broadening in time. The energy as a function of time for this process is shown in Fig. 8.14(d). In Fig. 8.14(f), we plot the average position of the wave packets. As the wave packet associated with B_2 is moving slower we extend (decrease) the upper-half (lower-half) of the system by 10 sites in the measurement of Eq. (8.40) (u-h/l-h = 60/40), but only after the scattering. Before the scattering we still divide the system in halves (u-h/l-h = 50/50). To check that is indeed a valid choice, we have also fitted a bi-modal Gaussian distribution to our data before and after scattering (no such fit is possible during the scattering event). The mean values of this distribution are in good agreement with the positions obtained from Eq. (8.40). From our data we extract the displacements $\delta x_{B_1}^{(12)} \simeq 1.4$ and $\delta x_{B_2}^{(12)} \simeq 1.2$. The analytical values obtained when plugging in the velocity of the quasiparticles $v_{B_1} = -0.60J$ and $v_{B_2} = 0.37J$, obtained from a fit to the freely propagating wave packets, are $\delta x_{B_1}^{(12)} = 1.49$ and $\delta x_{B_2}^{(12)} = 1.18$ again in very good agreement with our numerical estimates. In this case, we have also checked explicitly that the asymptotic velocities of the wave packets after scattering are not compatible with a reflection event, i.e. with the non-transmissive solution of the energy-momentum conservation $E_1(k_1) + E_2(k_2) = E_1(k'_1) + E_2(k'_2)$ and

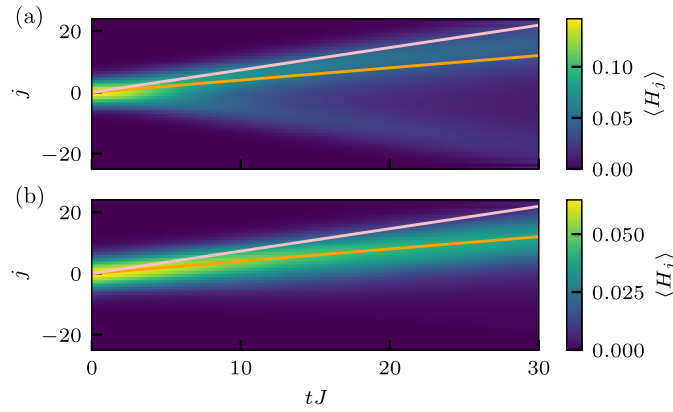


Figure 8.15 The real-time evolution of the state $e^{-\tau H} O_{0,k_2}^{(2)} |0\rangle$. (a) Without imaginary time evolution, $\tau = 0$. (b) With imaginary time evolution, $\tau = 4/J$. The wave packet is centred initially around momentum $k_2 = 0.15\pi$ and its width is $\bar{\sigma} = 4$. The system size is $L = 51$ and the model parameters are $\Delta = -0.4$ and $J_{\perp} = 0.1J$. In the case without imaginary time evolution, there is a two-particle contribution beyond sine-Gordon, that moves with a velocity close to the sound velocity v_s (pink line). A short imaginary time evolution eliminates this high-energy contribution, and we recover a single mode which moves with a velocity compatible with the group velocity as read off from the B_2 dispersion (orange line).

$k_1 + k_2 = k'_1 + k'_2$. Indeed, plugging in the above-mentioned velocities would give $v'_1 = 0.55J$ and $v'_2 = -0.45J$ as velocities after reflection. This is in contrast to the $B_1 - B_1$ event, for which reflection and transmission are degenerate.

8.4.3 Technical details on the creation of wave packets

The action of the operators given in Eqs. (8.37) and (8.38) on the ground state does not only excite the low-energy sine-Gordon part of the spectrum, but also higher-energy contributions. Indeed, in Fig. 8.15(a), we show the time evolution of the state $O_{0,k_2}^{(2)} |0\rangle$ with $k_2 = 0.15\pi$ and $|0\rangle$ the ground state. There is a highly-energetic two-particle contribution, as there is also an outgoing signal with negative momentum, that blurs the signal of the sine-Gordon breather. To eliminate this high-energy continuum contribution, we ‘cool down’ the system by performing a short imaginary-time evolution $e^{-\tau H}$, maximally up to imaginary times of around $\tau \approx 4/J$. After this, we indeed obtain a clear single mode that is moving with a speed lower than the sound velocity and compatible with the group velocity $v(k) = \partial_k E_{B_2}(k)$ according to the massive-relativistic dispersion of the second breather, as illustrated in Fig. 8.15(b).

We estimate the group velocities of our wave packets from fitting the massive-relativistic dispersion relation to the individual breather dispersions as obtained from the spectral functions. We restrict those fits to small momenta. We find that the fitted c of B_1 and B_2 slightly differs, as shown in Fig. 8.16(a). To enforce consistency, we fixed c to the single chain result of the sound velocity v_s , given by Eq. (8.9). For $\Delta = -0.4$, this corresponds to $v_s = 0.726J$. This value is also approximately the average of the fitted c 's shown in the legend of Fig. 8.16(a). We obtain the breather mass from the fitted value of the gap via $M_{B_n} = \omega_{B_n}(0)/c^2$, as indicated by the green lines.

There are no conserved quantities during the imaginary time evolution to cool down the state (this is always the case with **TEBD**-based algorithms). In addition, as imag-

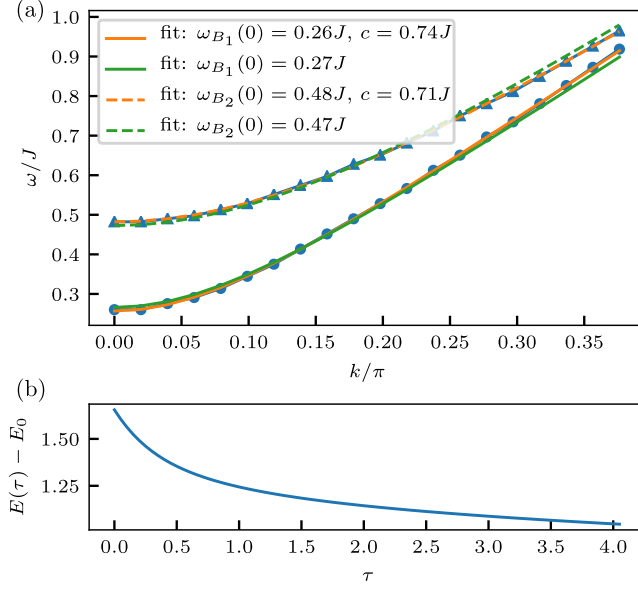


Figure 8.16 (a) Low momenta fits of the breather branches B_1 and B_2 . The data extracted from the spectral function is shown by the circles (B_1) and triangles (B_2). The lines are fits according to the massive relativistic dispersion $\omega_{B_n}(k) = \sqrt{k^2 c^2 + M_{B_n}^2 c^4}$ with either c and $\omega_{B_n}(0) = M_{B_n} c^2$ as a fitting parameters (orange lines) or with only the latter as free parameter with $c = v_s$ given by Eq. (8.9) (green lines). (b) The energy with respect to the ground state energy of the state $e^{-\tau H} O_{-d,k_2}^{(2)} O_{d,k_1}^{(1)} |0\rangle$ as a function of imaginary time. We stop the imaginary time evolution when $E(\tau) - E_0 \lesssim \omega_{B_1}(k_1) + \omega_{B_2}(k_2)$. The system size is $L = 101$ and the model parameters are $\Delta = -0.4$ and $J_{\perp} = 0.1J$.

inary time evolution is non-unitary the energy will not be conserved. In the long-time limit, imaginary time evolution acts as a projector on the ground state. However, we are not interested in the long time limit, and start from a state that is orthogonal to the ground state. By choosing the imaginary time-step small enough, we used $d\tau = 0.0025J$ in our simulations, the state stays orthogonal to the ground state (at least up to the relevant time scales). After the short imaginary time evolution, we checked that (i) the obtained state is still orthogonal to the ground state, and (ii) that the energy $E(\tau)$ of the obtained state is roughly compatible with $E(\tau) - E_0 \approx \omega_{B_1}(k_1) + \omega_{B_2}(k_2)$ with E_0 the ground state energy. The total energy difference as a function of imaginary time is shown in Fig. 8.16(b). The imaginary time evolution can in principle also lower the energy of the excitation along the single-particle breather dispersion, such that the group velocity of the wave packet could be overestimated when obtained from the initial momenta that are put in Eqs. (8.37),(8.38). We have checked this for our data, and this effect seems to be present but not very strong. When a higher precision is required, we directly fitted the velocity of our wave packets instead of determining it via the input momentum.

8.5 Conclusion and outlook

The sine-Gordon field theory is a ubiquitous low-energy description of one-dimensional quantum systems. Recent experiments focused on implementing it on highly-controllable quantum simulators based on coupled one-dimensional quasi-condensates [226, 228]. In this chapter, we considered two tunnel-coupled spin chains, realizing a lattice version of the sine-Gordon model proposed in Ref. [226]. The lattice realization has advantages for our purposes: First, the dynamics of coupled chains can be accurately determined numerically, which allows for a direct observation of the emergent sine-Gordon description and for a quantitative analysis of its validity regime. Second, the interactions in one-dimensional chains are strong and tunable, leading to sine-Gordon model field theory deep in the quantum regime.

By a numerical characterization of the spectral function, we have studied the sine-Gordon spectrum in the low-energy sector of the chain. Comparing the numerical data with exact predictions, we obtain precise regimes for the validity of the field theory. The observation of the rich sine-Gordon spectrum already supports the field theoretic approximation. Yet, a striking feature of the model is its integrability, resulting in unconventional non-equilibrium properties. As a probe of integrable dynamics, we studied scattering events of low-energy wave packets. Not only we observe fully transmissive scattering as expected from integrability, but we also indirectly observed the sine-Gordon scattering matrix by measuring the wave packet displacement after scattering.

Our work demonstrates that coupled ladder geometries are useful to realize a simulator of the sine-Gordon model in the quantum regime. Similar realizations as the one considered here based on coupled Bose-Hubbard models can be realized with current experimental techniques [248], leading to various interesting questions for future investigations. First, a characterization of experimentally-feasible protocols to selectively create and manipulate the sine-Gordon excitations will be of interest. To this end, numerical benchmarks will play an important role to assessing the validity of the quantum simulation and to keep unwanted effects under control. Second, the important question of characterizing the sine-Gordon dynamics beyond the few-excitation regime presents a formidable challenge. To this end, the theory of Generalized Hydrodynamics developed for integrable models [271–273] promises access to large scale dynamics. Numerical benchmarks will be helpful in testing the hydrodynamics predictions on small scales and in characterizing the short-time transients that are beyond the hydrodynamic approximation.

9 Conclusion

In this thesis we studied various phenomena in a selection of one-dimensional models ranging from MBL to emergent sine-Gordon integrability. In Chapter 2 we reviewed bipartite entanglement measures for *pure* states and introduced the concept of quantum thermalization [55, 63]. In Chapter 3 we introduced the Lindblad equation [38] and bipartite entanglement measures for *mixed* states [62]. The results presented in this thesis were mostly obtained numerically, by making extensive use of tensor-product state algorithms, based on MPS [33, 34]. We briefly reviewed those techniques in Chapter 4.

The results of this thesis indicate some promising new research directions, and can be summarized as follows. In Chapter 5, we investigated the dynamics of entanglement of MBL systems [23, 70] that are coupled to an environment. As entanglement proxy we used the third Rényi negativity [95, 97, 98]. This quantity is based on powers of the partially transposed density matrix. Hence to compute it, access to the full density matrix is required, but a full diagonalization is not needed. We assumed that the environment caused a dephasing process in the system. Therefore at late times, the system lost all the quantum coherences that were initially built up by the unitary time evolution, governed by the MBL Hamiltonian. The exact crossover point is set by the trade-off between the interaction strength ΔJ of the system which governs the entanglement growth, and the dephasing rate Γ which governs the entanglement loss. Indeed, if $\Delta J/\Gamma \gg 1$ we still observe the typical logarithmic growth of entanglement of MBL systems. At late-times the decay of entanglement is governed by dephasing, and we have illustrated that the entanglement decay happens according to a stretched exponential, which can be understood as a superposition of exponential decays over different decay rates [46]. These different decay rates are due to the strong disorder variations in the system.

In Chapter 6 we considered a similar setup for non-interacting and interacting Wannier-Stark localized systems [61, 79]. In the interacting and closed system, there is also a logarithmic growth of entanglement. However we have observed a faster initial growth, followed by a slower logarithmic growth. This faster initial growth can be reduced by making the potential less steep, by adding quadratic corrections [61, 79]. In the open system, we however did not observe a clear stretched exponential decay of the Rényi negativity. In case of disorder-induced MBL we attributed this type of decay to the presence of disorder, which is indeed absent in this setup. The competition of time scales remains intact, so we can still distinguish between interacting types of localization and non-interacting types on the condition that the dephasing is weak compared to the interactions.

For these setups an interesting new direction would be to investigate whether there is non-trivial physics remaining in the steady state when *non-hermitean* Lindblad operators govern the dissipation process. For such Lindblad operators, the steady state is not a trivial infinite temperature state any longer, but a NESS and could potentially contain interesting entanglement structure. As we have shown in this thesis, the Rényi negativity could be a very useful tool to investigate this structure. However, it is hard

to choose specific Lindblad operators for this task, and one must also be sure to have a faithful representation of the steady state. If real-time evolution is used, the complexity might become very large in the approach towards the steady state, and one must be sure to be able to overcome this barrier.

Our results also suggest that in experimental setups aiming to measure entanglement, it might be useful to measure Rényi negativities instead of Rényi entropies. While the Rényi entropies are sensitive to any type of heating and therefore always grow, the Rényi negativities decrease when heating effects become dominant. This comes however with the requirement that we need to be able to implement the partial transpose, and that the lowest order is the third instead of the second. Indeed, for a bipartite pure state the second Rényi entropy is sensitive to quantum correlations, while for a bipartite mixed state the second Rényi negativity is not. However both for pure and mixed states, the third Rényi negativity is sensitive to entanglement. In Ref. [99] Rényi negativities have been reconstructed from already existing measurements obtained by the application of random unitaries.

In Chapter 7 we investigated the entanglement of quasiparticles. Via the Z_2 symmetric Ising and trivial $U(1)$ -symmetric SSH chains, we illustrated that an odd $Z_2(\in U(1))$ charge of the quasiparticle in combination with reflection symmetry, leads to a double degenerate entanglement spectrum. On the other hand, the entanglement spectrum of the fundamental excitation of the topological SSH chain carries fragmentation patterns. For non-interacting models of this type, these features can also be understood in terms of the correlation matrix approach [164]. We also investigated MI probes suited for *strongly-interacting* SPT models that are characterized by a string order parameter, and applied these on the transverse-field cluster model. By performing large-scale DMRG simulations, and making use of these probes, we could locate the phase transition between the topological and trivial phase via the quasiparticle.

The obtained results might help in the understanding of quantum phases from the entanglement perspective. However, here we investigated purely static states, hence it would be useful to ask whether these MI protocols could potentially also be useful in more dynamical settings. In this respect, we note that in states with volume-law entanglement, which carry a finite density of quasiparticles, we do not expect these probes to work. However under a specific protocol that is not generating much entanglement, we might be able to still observe interesting dynamics of the MI.

Lastly in Chapter 8, we investigated a system of two tunnel-coupled XXZ spin chains. In the low-energy regime, this model can be described by an effective theory in decoupled symmetric and anti-symmetric sectors [226]. While the symmetric sector is described by the free Luttinger liquid, the anti-symmetric sector is described by the massive sine-Gordon model. We explicitly checked the emergence of this theory by finding good agreement with the exact results. We compared (i) the sine-Gordon spectrum with the spectrum of the ladder obtained by numerical simulation, and (ii) the sine-Gordon scattering displacements with the numerically determined displacements of our ladder model.

The ladder system based on Bose-Hubbard instead of XXZ chains, has high potential to form a realizable *quantum simulator* of the sine-Gordon model. Indeed, in currently existing quantum gas microscopes [248], the interactions within a single chain are highly tunable up to very strong interaction strengths $J/U \ll 1$. This in principle allows us to select a desired value for the Luttinger parameter. Also, the tunnel coupling which

set the mass scale of sine-Gordon, is potentially tunable, yet more challenging. While the fundamental breather masses of the first two breathers definitely seem measurable quantities when $T \lesssim J_{\perp}$, the real interesting and challenging question would be whether there is a feasible dynamical protocol that can probe sine-Gordon physics within the quantum regime where fundamental excitations can be resolved. In this context, it would be particularly nice to figure out a protocol that can create and detect a soliton, the topological excitation of the sine-Gordon theory that connects two minima of the cosine potential.

The results presented in this thesis show again that numerical simulations based on tensor-network techniques are extremely useful to understand the behavior of complex many-body quantum systems. We have seen that even when there is a large entanglement growth, like in the ladder system we discussed in Chapter 8, we are still able to push the simulation and to extract many physically relevant properties. However, in other cases, particularly in higher dimensions, performing such simulations remains an outstanding challenge [274,275]. Hence, a lot of territory in the field of out-of-equilibrium quantum systems remains unexplored. The major bottleneck is that classical machines are not the natural platform to simulate quantum dynamics. However, with the current progress in the development of quantum machines, we might hope to access some of these unexplored regimes in the future. Even in this respect, tensor-network methods will remain of particular importance, as they allow for a neat comparison with noisy data from analog quantum simulators [276], or from digital, universal, devices that are not yet error corrected [277–281].

Acknowledgments

First of all, I would like to thank my supervisor Michael Knap and my co-supervisor Frank Pollmann, for giving me the opportunity to join their groups in Munich, and for all their support and valuable feedback throughout these four years. I am especially grateful for Michael's expert advice, and his to-the-point attitude to turn problems into solutions. I am also grateful for his little hints about the social side of science, or on how to communicate results. Frank's positive mindset is very inspiring, and his enthusiasm during discussions forms a great thrive forward.

My special thanks also go to Alvis Bastianello for his guidance and availability over the last two years. It was a great pleasure working with him.

I also would like to thank Johannes Knolle for agreeing to be part of my thesis committee.

Both on the scientific and personal level, I have a lot of good memories from my time at the office in Garching: all thanks to the other group members. In particular, I would like to thank Johannes Hauschild who was extremely patient in answering all of my questions in the beginning of my PhD, and who was a tremendous help on the numerical side by his development of TeNPy. I also would like to thank my office mate Julian who was also helping me with all kind of matters in the beginning of my PhD. It has been a pleasure to meet Ruben, and I greatly benefited from the discussions we had about quasiparticles. I am also grateful to Laurens for the nice discussions we continued to have even after I finished my master project.

Of course, I also would like to thank all the members of the condensed-matter theory group for the nice atmosphere, the pleasant activities and the enjoyable lunches. I have many fond memories of the moments I spent with Pablo, ShengHsuan, Markus, Tibor, Johannes, Izabella, Alex, Clemens, Wilhelm, Philip and Stefan over the last years. I would also like to thank Karin for her help on the administrative side.

On the personal side, I am very grateful to my family for their unconditional love and encouragements. Especially my parents were always there to guide me through difficult moments. Finally, I am grateful to Kevin for all his love and support, and for all the beautiful memories we have built together over the years.

List of Figures

- 2.1 Wave-packet scattering in integrable models is subjected to strong constraints. On the left, we show a forbidden event where the particles are reflected, and hence change momentum. On the right, we show an allowed event. Here the momenta of the particles do not change. However, interactions between the particles result in spatial scattering displacements. 13
- 3.1 The eigenvalues of a random Lindbladian in the complex plane for various dissipation strengths. These plots illustrate the general properties of the eigenvalue spectrum of Lindbladians, i.e. that all eigenvalues come in complex pairs, have a negative real part and there is at least one eigenvalue that is exactly zero. For stronger dissipation strength, the spectrum becomes shaped like a lemon, a finding that stems from Refs. [84, 85]. 23
- 3.2 In the set of all states, separable states are a convex subset. These are embedded in the larger subset of states that are characterized by a PPT. States that are only contained in the red region do not have a PPT, and by the negation of (3.28), their entanglement can be detected. 26
- 3.3 The set of PPT states is contained in the set of states that satisfy the PPT-3 condition. The set of entangled states that violate the PPT-3 condition is smaller than the set of states that violate the PPT condition (3.28) (red part vs. red and purple part). 28
- 3.4 The logarithmic negativity \mathcal{E} and the third Rényi negativity R_3 for the two-qubit Werner state (3.43) defined by λ . R_3 is not an entanglement monotone as it takes a non-zero value in the separable regime $\lambda < 1/3$ 29
- 3.5 The ratio p_2^2/p_3 for the two-qubit Werner state defined by λ , see Eq. (3.43). For the Werner state the PPT-3 condition (3.42) is sufficient, so when $p_2^2/p_3 > 1$ the state is entangled. The inset shows a zoom for the smallest values of λ . The vertical grey line corresponds to $\lambda = 1/3$, and when $\lambda < 1/3$, the state is separable. 30
- 3.6 The set of all states in which the separable states are a subset. Entanglement witnesses divide the set in two parts: one in which they do not witness entanglement (here the left part), and one where they witness entanglement (here the right part). Therefore the witness $\mathcal{W}^{(1)}$ is better than $\mathcal{W}^{(2)}$ as it is able to detect more entangled states. 31

4.1	States that can be efficiently represented by an MPS form only a small subset of the Hilbert space. This subset is characterised by area-law scaling of the entanglement entropy. For instance, ground states of local gapped Hamiltonians fall into this class of area-law states. In the graph we plot the 25 largest singular values of the ground state of the paramagnetic TFI chain for a spin-1/2 system of $L = 10$ sites. These should be contrasted with the singular values of a state that is randomly drawn from the 2^{10} dimensional Hilbert space according to the Haar measure, which satisfies a volume law.	36
4.2	A sketch of the contraction of the three layer tensor network to compute $\text{Tr}[(\rho_{AB}^{T_B})^3]$. We take a bipartition of the system into two equal subsystems A and B , and take the transpose of the degrees of freedom of partition B , simultaneously with the trace of the system (green lines).	43
5.1	A sketch of our setup: a spin chain with disordered z -directed fields $h_i \in [-W, W]$, spin exchange Δ and coupling Γ to a bath.	46
5.2	A sketch of the R_3 entanglement probe, see Eq. (3.40), that we compute using tensor-network techniques. We make a bipartition of the system into two subsystems A and B , and partially transpose the degrees of freedom of subsystem B before taking the trace.	47
5.3	Quench dynamics of $R_3 = 2S_3$ in the closed quantum system at fixed system size $L = 14$ for various interaction strengths. In the inset we show the finite size scaling of R_3 at fixed interaction strength $\Delta = 1$, from bottom to top $L = 10, 12, 14, 16$. The errorbars show the standard error of the mean.	49
5.4	(a) Comparison of the average of R_3 obtained by the numerics over 2500 disorder realizations with system size $L = 16$ and $\Delta = 1$ and by the model described in the text with $\xi_1 = 0.40$ and $\xi_2 = 0.195$. The dashed grey line shows the curve of the model shifted by a constant. (b)-(d) Normalized histograms of the model and numerics at several times. The dotted vertical lines indicate the mean, while the dashed green line indicates the resonance at $2 \log 2$. The tails in the distributions of the model are more pronounced, as it does not take into account multi-spin couplings.	50
5.5	Dynamics of the Rényi negativity (top) and the imbalance (bottom) under a quench in the open or closed system ($L = 20$). The disorder is fixed to $W = 5J$ and the interaction strength is $\Delta = 1$ for the MBL system, and $\Delta = 0$ for the non-interacting Anderson localized system. The two darkest colors (red and blue) show the closed system for comparison. At intermediate time scales and for sufficiently weak dephasing strength, R_3 distinguishes MBL from single particle localization. A feature that is absent in the imbalance. In the insets we show the interquartile range (IQR) which forms a measure for the spread of the distribution.	51
5.6	Histograms at two different times (columns) corresponding to the averages shown in Fig. 5.5. (a)-(b) Interacting system with $\Delta = 1$. (c)-(d) Non-interacting system $\Delta = 0$. The green line indicates $R_3 = 2 \log 2$ which corresponds to the maximal entanglement between 2-spins.	52

- 5.7 Quench dynamics of the Rényi negativity R_3 in a system with disorder $W = 5J$ and coupling $\Gamma = 0.1J$. Top: MBL with interaction strength $\Delta = 1$. Bottom: Non-interacting system $\Delta = 0$. In the inset we show the best fitting parameter for the stretching exponent b with 3σ errorbars obtained by the least-square method. These exponents do not depend on the interactions up to leading order. The blue line shows one of the fitting functions with $b \approx 0.25$ 54
- 5.8 Relative error of the fourth order TEBD scheme for various simulation parameters for a small system of $L = 8$ spins. In the left column the coupling is $\Gamma = 0.01J$, in the right one $\Gamma = 1J$. In the top line we vary the maximal bond dimension. In the bottom line we vary the time step (in units of J^{-1}) at maximal bond dimension $\chi = 256$ 55
- 5.9 Relative error of the fourth order TEBD scheme for $L = 40$ spins with a coupling strength of $\Gamma = 0.01J$. On the left we show the relative difference between simulations with bond dimension χ and bond dimension $\chi_{\max} = 500$ with a time step of $dt = 0.05$. On the right we show the difference between simulation with time step is $dt = 0.1$ and $dt = 0.05$ at bond dimension χ 56
- 5.10 Comparison of the negativity (top) and the third Rényi negativity (bottom) in the Lindblad quench dynamics in the XXZ model at disorder $W = 5J$, interaction strength $\Delta = 1$ and small system size $L = 8$. The dashed blue line shows the stretched exponential fits $e^{-(\frac{\Gamma t}{\alpha})^b}$ for the decay. The stretching exponents are equal for both quantities. The insets show the same data in a different scale. The errorbars show the standard error of the mean and the averages are taken over 1000 disorder realizations. 56
- 5.11 Negativity dynamics in a small system of $L = 8$ spins. When spin-conservation is broken by adding a term $g \sum_i S_i^x$ to the Hamiltonian, the negativity dynamics stops abruptly at a finite time. In the left plot $g = 0.2J$, and in the right one $g = 0.4J$ 57
- 5.12 The quench dynamics of the Fisher information density $f_Q = F_Q/L$ at disorder $W = 5J$, interaction strength $\Delta = 1$ and system size $L = 8$. We show stretched exponential fits $e^{-(\frac{\Gamma t}{\alpha})^b}$ for the decay that start approximately at time $\sim \frac{1}{\Gamma}$. The inset shows the same data in a different scale. The errorbars show the standard error of the mean and the averages are taken over 1000 disorder realizations. 58
- 6.1 A sketch of our setup: A chain of spins (or, equivalently spinless fermions) is subjected to a linear potential with small quadratic corrections, and is uniformly coupled to an environment. 63
- 6.2 The evolution of the imbalance [(a)-(b)] and third Rényi negativity [(c)-(d)] in closed Wannier-Stark localized systems of $L = 24$ sites. The slope of the linear potential γ is given in the legend and the quadratic corrections have a strength of $\alpha = 2J$. The most striking difference between the non-interacting localized case (c) and the interacting localized case (d) is that entanglement can propagate through the system in the interacting case, most notably when the slope of the linear potential is not too strong. 64

- 6.3 The growth of entanglement quantified by the third Rényi negativity (entropy) R_3 in the isolated system. (a) When the system size is fixed, the interactions determine the onset of logarithmic growth. (b) When the potential parameter α is decreased the finite-time cross-over becomes more pronounced. (c) If only the system size is varied, t_{cross} is doubled with system sizes as indicated by the arrows. 65
- 6.4 The dynamics of R_3 in a Wannier-Stark system of length $L = 16$ with $\alpha = 2J$, $\gamma = 2J$ coupled to a dephasing environment. (a) Interacting case $\Delta = 0.5$, where we show the data for the closed non-interacting case for comparison (light grey line). R_3 reproduces the onset of entanglement growth for sufficiently weak dephasing. (b) Non-interacting case $\Delta = 0$. The coupling strengths are given in the legend. We averaged over about 100 initial states in the $M = 0$ sector for $\Gamma > 0$, and over about 300 states for $\Gamma = 0$ (exact diagonalization was used in this case). 66
- 6.5 The dynamics of R_3 in a Wannier-Stark system with $\alpha = 2J$, $\gamma = 2J$ coupled to a dephasing environment under a quench from the Néel state. The black dashed lines are stretched-exponential fits to intermediate-time regime of $L = 16$. (a) Interacting case $\Delta = 0.5$, the slope of the fit shown is $b \approx 0.37$. (b) Non-interacting case $\Delta = 0$, the slope of the fit shown is $b \approx 0.31$. In both cases the late-time dynamics deviates from stretched exponential decay. 67
- 6.6 The dynamics of the imbalance in a Wannier-Stark system with $\alpha = 2J$, $\gamma = 2J$ coupled to a dephasing environment under a quench from the Néel state. The black dashed lines are stretched-exponential fits for $L = 16$. (a) Interacting case $\Delta = 0.5$, the slope of the fit shown is $b \approx 0.59$. (b) Non-interacting case $\Delta = 0$, the slope of the fit shown is $b \approx 0.62$. Again, in both cases the late-time dynamics is incompatible with stretched exponential decay. 68
- 6.7 The dynamics of the negativity, R_3 , and the imbalance for a system of $L = 8$ sites under a quench starting from the Néel state. The tilted potential is characterized by $\alpha = \gamma = 2J$. The non-interacting ($\Delta = 0$) and interacting ($\Delta = 0.5$) cases are shown. The blue dashed lines show a stretched-exponential fit $\sim e^{-(\Gamma t/a)^b}$ for the intermediate-time regime and an exponential fit for the late-time regime. The stretching exponent b is written inside the panels with 3σ confidence level. 70
- 6.8 The dynamics of the negativity and R_3 for a system of $L = 8$ sites under a quench starting from a random initial state. Averages are taken over initial product states in the $M = 0$ sector. The tilted potential is characterized by $\alpha = \gamma = 2J$. The non-interacting ($\Delta = 0$) and interacting ($\Delta = 0.5$) cases are shown. The blue dashed lines show a stretched-exponential fit $\sim e^{-(\Gamma t/a)^b}$ for the intermediate-time regime and an exponential fit for the late-time regime. The stretching exponent b is written inside the panels with 3σ confidence level. 71
- 6.9 The same data as in Fig. 6.7 but in a different scale to make the exponential form of the tails visible. 72
- 6.10 The same data as Fig. 6.8 but in a different scale to make the exponential form of the tails visible. 73

- 7.1 A sketch of the SSH model in our setup: we consider chains of length $L = 4m$ (with m integer), such that we have an even number of unit cells in the trivial phase and an odd number in the topological phase. In the trivial phase the center bond is weak, while in the topological phase it is strong. 78
- 7.2 The correlation matrix spectra of the ground state and quasiparticle in the SSH chain. The simulations are performed on chains of $L = 400$ sites, but we rescaled the number of states with the system size as the results are universal. a) For the ground state in the trivial phase no in-gap states are present, half of the orbitals are filled and half are empty. b) There is an in-gap state for the quasiparticle in the trivial phase which is an extended bulk state reflecting the position uncertainty of the quasiparticle. c) There is also an in-gap state for the ground state in the topological phase but this one is due to the protected boundary modes. d) For the quasiparticle in the topological phase there are two in-gap states, one reflecting the bulk mode and one the boundary mode. Note that when δ approaches zero (from the negative side, as we are in the topological phase) the two in-gap states move further apart, which represents further mixing of the bulk/boundary modes. They can only disappear into the empty or filled orbitals by crossing the phase transition point at $\delta = 0$ 79
- 7.3 The entanglement spectrum of the first excited state in the trivial SSH model on a chain with $L = 20$ sites with $\delta = 0.5$. a) The non-interacting case with $U = 0$. b) The interacting case with $U = 0.2$. Both entanglement spectra exhibit two-fold degeneracy in all energy levels. 80
- 7.4 The entanglement spectrum of the first excited state in the PM Ising model (18 sites, $h_x = 1.5$). a) The non-interacting case with $J_x = 0$. b) The interacting case with $J_x = 0.2$. Both entanglement spectrum exhibit two-fold degeneracy in all energy levels. 81
- 7.5 Entanglement excess of the single magnon state with respect to the ground state in the paramagnetic phase of the TFI with $J_x/J_z = 0.1$ for a reflection symmetric bipartition. The red marker on the y-axis shows the expected $\log(2)$ excess. Inset: The two-fold degeneracy of the entanglement spectrum is protected by the reflection symmetry. 82
- 7.6 Entanglement excess of a single domain wall with respect to the symmetry-broken ground state in the ferromagnetic phase of the TFI model with $J_x/J_z = 0.1$. The red marker on the y-axis shows the expected $2 \log(2)$ excess. Inset: There are no symmetry-protected degeneracies in the entanglement spectrum. 83
- 7.7 The entanglement spectrum of the first excited state in the topological SSH model on a chain with $L = 20$ sites and $\delta = -0.5$. a) The non-interacting case with $U = 0$. The entanglement spectrum exhibit a clear fragmentation pattern with each fragment being particle-hole symmetric. The colors are added to make the fragmentation pattern clearly visible. b) The interacting case with $U = 0.2$. The fragmentation pattern is clear for the low-energy patterns but not for the higher ones. The particle-hole symmetry within each fragment is broken. 85

- 7.8 Sketch of the SSH model with periodic boundary conditions in our setup, we choose $L = 4m$ sites (with m integer) such that the trivial (topological) phase is characterized by the cutting of weak (strong) bonds. 86
- 7.9 The correlation matrix spectra for the topological SSH model with periodic boundary conditions. a) The spectrum of the ground state is characterized by two states $p_\alpha = 1/2$ because of the two boundary modes – one near each cut. b) For the quasiparticle in the topological phase, two in-gap edge states are hybridized via the zero energy bulk state in a particle-hole symmetric way. 87
- 7.10 Many-body entanglement spectra for the topological SSH model with periodic boundary conditions for a ring with $L = 20$ sites and $\delta = -0.5$. a) Non-interacting case $U = 0$. All quasienergy levels are two-fold degenerate due to one in-gap zero mode. The entire entanglement spectrum exhibits a clear fragmentation pattern with each fragment being particle-hole symmetric. b) Interacting case $U = 0.1$. The fragmentation pattern is destroyed for all but the lowest levels, but the two-fold degeneracy remains robust. 87
- 7.11 The MI in the ground state of the cluster model between the grey spins in the middle (B area) and the blue spins ($A = A_1 \cup A_2$) at the boundaries of the string. In the SPT phase $h_x < 1$ it is non-vanishing for the ground state. The dotted data points are the conditional MIs (7.23), where we subdivided the region B such that $B_2 = B \setminus B_1$ is the region the closest to the A spins. There is only a small difference between the MI and conditional MI near the transition as the correlations are still dominantly local. 90
- 7.12 a) Sketch of the projection of the odd sites in between A_1 and A_2 to a sector with definite (e.g. even) parity. b) The measurement induced MI in the ground state of the cluster model $P_B|GS\rangle$. The inset shows the data without the projection of the region B to the even sector. In this case the distant spins in the A region do not carry any mutual information in the thermodynamic limit, as expected. 91
- 7.13 a) Sketch of the partitioning of the system; we take $A_1 = \frac{L}{4}$, $A_2 = \frac{L}{2}$ and $A_3 = \frac{3L}{4}$ and system sizes divisible by eight. b) The MI in the first excited state of the cluster model. The full lines corresponds to data in the topological phase at $K' = 1, K = 0.9$ and $h = 0$ for some J s shown in the legend, and the crosses corresponds to data in the trivial phase at $h = 2.5$. The dots connected by the dotted lines are data points for the conditional MI $I(A : B_1|B_2)$, where the region B_1 only contains odd sites that are not directly neighboring the A region. c) The second order Rényi MI of the first excited state at the same points in the phase diagram. 93

- 7.14 a) Sketch of the projection of the odd sites in between A_1, A_2 and A_3 to a sector with definite (e.g. even) parity. b) The measurement-induced MI in the first excited state of the cluster model $P_{B_L}P_{B_R}|QP\rangle$. The full line corresponds to data in the topological phase at $K' = 1, K = 0.9$ and $h = 0$ for some J shown in the legend, while the dotted lines corresponds to data in the trivial phase at $h = 2.5$. The inset shows the MI without the projection of the regions B_L and B_R to the even sector. Clearly the MI vanishes in both cases in the thermodynamic limit. 94
- 7.15 The measurement induced MI in the first excited state of the cluster model $P_{B_L}P_{B_R}|QP\rangle$ as a function of J with $K = K' = 1$ and $h = 0$. The inset shows the data without the projection of the regions B_L and B_R to the even sector. 94
- 8.1 Sketch of the setup. Two XXZ spin chains, each realizing a Luttinger Liquid in the low-energy regime, are weakly tunnel coupled. The sine-Gordon model is realized in their relative degrees of freedom. 98
- 8.2 Luttinger parameter estimated from a fit to the static correlations in the ground state for a ladder system of size $L = 200$ rungs and for different values of the inter chain coupling J_{\perp}/J . The errorbars incorporate the uncertainty of the fit as well as the average over different spatial fitting ranges. The solid lines show the exact result for the single chain as given by Eq. (8.9). 102
- 8.3 (a) The spectral function for a system of $L = 151$ rungs, with model parameters $\Delta = -0.4$ and $J_{\perp} = 0.2J$. We observe $N = 4$ sine-Gordon breathers as expected for $K = 1.35$ of the single chain. The color scale is logarithmic in the spectral weight. (b) Odd sector. (c) Even sector. (d) A fit of the breather energies $\omega(k = 0) = c^2 M_{B_n}$ according to Eq. (8.13). The blue crosses are obtained by using both K and $c^2 M_s$ as fitting parameters, while the green pluses are obtained from $c^2 M_s$ as only fitting parameter, illustrating the validity of the single-chain analytic result. . . 104
- 8.4 Momentum slices of the numerical spectral function shown in Fig. 8.3 compared to the analytical result Eq. (8.20), where only single breather contributions are included. At high momenta there are deviations from the analytic result. 105
- 8.5 Spectral functions for a system of $L = 151$ rungs for two different values of Δ and two coupling strengths $J_{\perp}/J = 0.1, 0.2$. (a,b) Here $\Delta = -0.25$, corresponding to $K \simeq 1.18$ and $N = 3$ breathers. (c-d) Here $\Delta = 0.1$, corresponding to $K \simeq 0.94$ and $N = 2$ breathers. The color scale used in the spectral-density plots is logarithmic in order to make the higher lying breathers also visible compared to the lower ones. 107
- 8.6 The profile of the spectral functions at $k = 0$ shown in Fig. 8.5 for both coupling strengths and their comparison to the exact result: the solid lines take into account the breathers and the soliton/anti-soliton continuum, while the dashed lines only takes into account single breather contributions. 107

- 8.7 The energy gap in the anti-symmetric sector as obtained from the dynamic correlation functions of the ground state as a function of the interchain coupling. The solid lines show a fit of the data according to $a(J_{\perp}/J)^{\frac{1+\xi}{2}}$ with $\xi = (4K - 1)^{-1}$ fixed. The errorbars are set by the resolution in frequency space. The inset shows the same data in a logarithmic scale. 108
- 8.8 (a) Energy absorption for a small periodic drive. Here $\epsilon = J_{\perp}/4$. The system size is $L = 51$ and the model parameters are $\Delta = -0.4$ and $J_{\perp}/J = 0.2$. (b) Spectral functions extracted from the absorbed power from Eq. (8.22). The fit of the slope is performed in several time domains (legend). The dashed grey lines show the breather energies extracted from the spectral function at $k = 0$ (c.f. Fig. 8.3). 109
- 8.9 Current fluctuations measured at discrete times that are a multiples of the driving period $T = 2\pi/\omega$. The dashed grey lines show the breather energies extracted from the spectral function (see Fig. 8.3) at $k = 0$. The system size is $L = 51$ and the model parameters are $\Delta = -0.4$ and $J_{\perp}/J = 0.2$ (a) Here $\epsilon_1 = J_{\perp}/4$ and $\epsilon_2 = 0$, so we only target odd breathers and only B_1 strongly. (b) Here $\epsilon_1 = 0$ and $\epsilon_2 = J_{\perp}/4$, so here we only target even breathers and only B_2 strongly. 110
- 8.10 (a-d) Spectral functions at $k = 0$ evaluated from the correlation functions given in the panels for two different values of Δ . The interchain coupling is $J_{\perp}/J = 0.1$, and the system size $L = 151$. The peaks correspond to B_1 and B_3 and their relative strengths can be compared. For the two rung operators there is a continuum present, see panel (d). 111
- 8.11 (a) Spectral functions from the combination of all contributions shown in Fig. 8.10 for $\Delta = -0.4$ according to Eq. (8.33) at $k = 0$ for some different values of A . The B_1 peak is reduced the most for $A = 5.3$. (b) Spectral function for $A = 5.3$. Here $\Delta = -0.4$, the interchain coupling is $J_{\perp}/J = 0.1$ and the system size is $L = 151$ 113
- 8.12 The same spectrum as shown in Fig. 8.3(a), but computed with an interchain interaction of strength $J_{\perp}^z = \Delta J_{\perp}$. The parameters of the system are $L = 151$, $\Delta = -0.4$ and $J_{\perp} = 0.2J$. The inset shows a close zoom on the profile of the first breather at $k = 0$. This data is compared to the same data with $J_{\perp}^z = 0$, and with the exact sine-Gordon prediction. The white dashed lines show the exact sine-Gordon dispersion for the four breathers as determined without the zz term, illustrating that the effect of the interchain zz interaction is negligible. 114
- 8.13 The growth of the average entanglement entropy per bond in the time-evolved state $e^{-iHt} S_{\uparrow j}^+ S_{\downarrow j}^- |0\rangle$ for different bond dimensions $D = 1000, 1500, 2000$ for a ladder system of size $L = 151$ and two different Δ . The tunnel coupling is $J_{\perp}/J = 0.1$ 115

- 8.14 Wave packet scattering in the low-energy regime of the coupled chains with parameters $J_{\perp}/J = 0.1$, $\Delta = -0.4$ and $L = 101$. (a,d) The local energy as function of time for a scattering event between two B_1 quasiparticles with momentum $k = \pm 0.2\pi$, panel (a), and between B_1 and B_2 quasiparticles with respective momenta $k_1 = -0.2\pi$ and $k_2 = 0.15\pi$, panel (d). (b,e) The corresponding energy profiles at selected times, where the grey lines show the profile of the freely propagating wave packets at the latest time. (c,f) The associated average positions of the quasiparticles. The numerically obtained values for the scattering displacements are $\delta x_{B_1}^{(11)} \simeq 0.5$, see also the inset in panel (c), and $\delta x_{B_1}^{(12)} \simeq 1.4$, $\delta x_{B_2}^{(12)} \simeq 1.2$ 116
- 8.15 The real-time evolution of the state $e^{-\tau H} O_{0,k_2}^{(2)} |0\rangle$. (a) Without imaginary time evolution, $\tau = 0$. (b) With imaginary time evolution, $\tau = 4/J$. The wave packet is centred initially around momentum $k_2 = 0.15\pi$ and its width is $\bar{\sigma} = 4$. The system size is $L = 51$ and the model parameters are $\Delta = -0.4$ and $J_{\perp} = 0.1J$. In the case without imaginary time evolution, there is a two-particle contribution beyond sine-Gordon, that moves with a velocity close to the sound velocity v_s (pink line). A short imaginary time evolution eliminates this high-energy contribution, and we recover a single mode which moves with a velocity compatible with the group velocity as read off from the B_2 dispersion (orange line). 119
- 8.16 (a) Low momenta fits of the breather branches B_1 and B_2 . The data extracted from the spectral function is shown by the circles (B_1) and triangles (B_2). The lines are fits according to the massive relativistic dispersion $\omega_{B_n}(k) = \sqrt{k^2 c^2 + M_{B_n}^2 c^4}$ with either c and $\omega_{B_n}(0) = M_{B_n} c^2$ as a fitting parameters (orange lines) or with only the latter as free parameter with $c = v_s$ given by Eq. (8.9) (green lines). (b) The energy with respect to the ground state energy of the state $e^{-\tau H} O_{-d,k_2}^{(2)} O_{d,k_1}^{(1)} |0\rangle$ as a function of imaginary time. We stop the imaginary time evolution when $E(\tau) - E_0 \lesssim \omega_{B_1}(k_1) + \omega_{B_2}(k_2)$. The system size is $L = 101$ and the model parameters are $\Delta = -0.4$ and $J_{\perp} = 0.1J$ 120

Acronyms

DMRG density matrix renormalization group 3, 4, 33, 37, 38, 42, 89, 91, 106, 115, 124

ETH eigenstate-thermalization hypothesis 10, 11

GGE generalized Gibbs ensemble 12

LIOMs local integrals of motion 11, 14, 15, 45, 48, 61, 68

LOCC local operations and classical communication 8, 25, 30

MBL 95, 123 many-body localized 3, 4, 5, 6, 7, 11, 13, 14, 15, 16, 17, 27, 45, 46, 48, 49, 51, 53, 58, 59, 61, 62, 64, 69, 123, 130. many-body localization 6, 17, 45, 49, 51, 53, 54, 58, 61, 62, 66, 68, 69, 123, 130, 131.

MI mutual information 9, 75, 76, 89, 90, 91, 92, 93, 94, 124, 134, 135

MPO matrix-product operator 37, 38, 41, 42, 47, 54

MPS matrix-product state 3, 4, 5, 33, 34, 35, 36, 37, 38, 39, 40, 41, 46, 47, 62, 63, 84, 89, 98, 106, 115, 123, 130

NESS non-equilibrium steady state 24, 123

PPT positive partial transpose 25, 26, 27, 28, 29, 30, 31, 129

QFI quantum Fisher information 46, 57, 58

SPT symmetry-protected topological 3, 5, 6, 75, 76, 84, 86, 88, 90, 92, 95, 124, 134

SVD singular-value decomposition 8, 33, 34, 35, 38, 40

TEBD time-evolving block decimation 4, 33, 37, 39, 41, 46, 47, 54, 55, 106, 115, 119, 131

TFI transverse-field Ising 12, 36, 76, 80, 82, 83, 130, 133

Bibliography

Refs. [1–5] can be found in the [List of Publications](#).

- [6] S. Sachdev. *Quantum Phase Transitions*. Cambridge University Press, 2 edition, 2011.
- [7] J. Hubbard. “Electron correlations in narrow energy bands.” *Proceedings of the Royal Society of London. Series A, Mathematical and Physical Sciences* **276**, pp. 238, 1963.
- [8] J. Kanamori. “Electron correlation and ferromagnetism of transition metals.” *Progress of Theoretical Physics* **30**, pp. 275, 1963. doi:[10.1143/ptp.30.275](https://doi.org/10.1143/ptp.30.275).
- [9] M. C. Gutzwiller. “Effect of correlation on the ferromagnetism of transition metals.” *Phys. Rev. Lett.* **10**, pp. 159, 1963. doi:[10.1103/PhysRevLett.10.159](https://doi.org/10.1103/PhysRevLett.10.159).
- [10] D. P. Arovas, E. Berg, S. A. Kivelson, and S. Raghu. “The hubbard model.” *Annual Review of Condensed Matter Physics* **13**, pp. 239, 2022. doi:[10.1146/annurev-conmatphys-031620-102024](https://doi.org/10.1146/annurev-conmatphys-031620-102024).
- [11] M. Qin, T. Schäfer, S. Andergassen, P. Corboz, and E. Gull. “The hubbard model: A computational perspective.” *Annual Review of Condensed Matter Physics* **13**, pp. 275, 2022. doi:[10.1146/annurev-conmatphys-090921-033948](https://doi.org/10.1146/annurev-conmatphys-090921-033948).
- [12] T. D. Kühner and H. Monien. “Phases of the one-dimensional bose-hubbard model.” *Phys. Rev. B* **58**, pp. R14741, 1998. doi:[10.1103/PhysRevB.58.R14741](https://doi.org/10.1103/PhysRevB.58.R14741).
- [13] M. Greiner, O. Mandel, T. Esslinger, T. W. Hänsch, and I. Bloch. “Quantum phase transition from a superfluid to a mott insulator in a gas of ultracold atoms.” *Nature* **415**, pp. 39, 2002. doi:[10.1038/415039a](https://doi.org/10.1038/415039a).
- [14] X.-G. Wen. “Topological orders and edge excitations in fractional quantum hall states.” *Advances in Physics* **44**, pp. 405, 1995. doi:[10.1080/00018739500101566](https://doi.org/10.1080/00018739500101566).
- [15] L. D. Landau. “On the theory of phase transitions.” *Zh. Eksp. Teor. Fiz.* **7**, pp. 19, 1937.
- [16] F. D. M. Haldane. “Continuum dynamics of the 1-D heisenberg antiferromagnet: Identification with the o(3) nonlinear sigma model.” *Phys. Lett. A* **93**, pp. 464, 1983.
- [17] J. M. Kosterlitz and D. J. Thouless. “Ordering, metastability and phase transitions in two-dimensional systems.” *Journal of Physics C: Solid State Physics* **6**, pp. 1181, 1973. doi:[10.1088/0022-3719/6/7/010](https://doi.org/10.1088/0022-3719/6/7/010).

- [18] X. Chen, Z.-C. Gu, and X.-G. Wen. “Classification of gapped symmetric phases in one-dimensional spin systems.” *Phys. Rev. B Condens. Matter* **83**, pp. 035107, 2011.
- [19] N. Schuch, D. Pérez-García, and I. Cirac. “Classifying quantum phases using matrix product states and projected entangled pair states.” *Phys. Rev. B* **84**, p. 165139, 2011. doi:[10.1103/PhysRevB.84.165139](https://doi.org/10.1103/PhysRevB.84.165139).
- [20] D. Basko, I. Aleiner, and B. Altshuler. “Metal–insulator transition in a weakly interacting many-electron system with localized single-particle states.” *Annals of Physics* **321**, pp. 1126 , 2006. doi:<https://doi.org/10.1016/j.aop.2005.11.014>.
- [21] V. Oganesyan and D. A. Huse. “Localization of interacting fermions at high temperature.” *Phys. Rev. B* **75**, p. 155111, 2007. doi:[10.1103/PhysRevB.75.155111](https://doi.org/10.1103/PhysRevB.75.155111).
- [22] A. Pal and D. A. Huse. “Many-body localization phase transition.” *Phys. Rev. B* **82**, p. 174411, 2010. doi:[10.1103/PhysRevB.82.174411](https://doi.org/10.1103/PhysRevB.82.174411).
- [23] D. A. Abanin, E. Altman, I. Bloch, and M. Serbyn. “Colloquium: Many-body localization, thermalization, and entanglement.” *Rev. Mod. Phys.* **91**, p. 021001, 2019. doi:[10.1103/RevModPhys.91.021001](https://doi.org/10.1103/RevModPhys.91.021001).
- [24] F. Pollmann, A. M. Turner, E. Berg, and M. Oshikawa. “Entanglement spectrum of a topological phase in one dimension.” *Phys. Rev. B* **81**, p. 064439, 2010. doi:[10.1103/PhysRevB.81.064439](https://doi.org/10.1103/PhysRevB.81.064439).
- [25] F. Pollmann and A. M. Turner. “Detection of symmetry-protected topological phases in one dimension.” *Phys. Rev. B* **86**, p. 125441, 2012. doi:[10.1103/PhysRevB.86.125441](https://doi.org/10.1103/PhysRevB.86.125441).
- [26] M. Žnidarič, T. c. v. Prosen, and P. Prelovšek. “Many-body localization in the heisenberg xxz magnet in a random field.” *Phys. Rev. B* **77**, p. 064426, 2008. doi:[10.1103/PhysRevB.77.064426](https://doi.org/10.1103/PhysRevB.77.064426).
- [27] J. H. Bardarson, F. Pollmann, and J. E. Moore. “Unbounded growth of entanglement in models of many-body localization.” *Phys. Rev. Lett.* **109**, p. 017202, 2012. doi:[10.1103/PhysRevLett.109.017202](https://doi.org/10.1103/PhysRevLett.109.017202).
- [28] A. Lukin, M. Rispoli, R. Schittko, M. E. Tai, A. M. Kaufman, S. Choi, V. Khemani, J. Léonard, and M. Greiner. “Probing entanglement in a many-body–localized system.” *Science* **364**, pp. 256, 2019. doi:[10.1126/science.aau0818](https://doi.org/10.1126/science.aau0818).
- [29] A. Einstein, B. Podolsky, and N. Rosen. “Can quantum-mechanical description of physical reality be considered complete?” *Phys. Rev.* **47**, pp. 777, 1935. doi:[10.1103/PhysRev.47.777](https://doi.org/10.1103/PhysRev.47.777).
- [30] M. A. Nielsen and I. L. Chuang. *Quantum Computation and Quantum Information: 10th Anniversary Edition*. Cambridge University Press, 2010.
- [31] S. R. White. “Density matrix formulation for quantum renormalization groups.” *Phys. Rev. Lett.* **69**, pp. 2863, 1992. doi:[10.1103/PhysRevLett.69.2863](https://doi.org/10.1103/PhysRevLett.69.2863).

- [32] S. R. White. “Density-matrix algorithms for quantum renormalization groups.” *Phys. Rev. B* **48**, pp. 10345, 1993. doi:[10.1103/PhysRevB.48.10345](https://doi.org/10.1103/PhysRevB.48.10345).
- [33] F. Verstraete, V. Murg, and J. Cirac. “Matrix product states, projected entangled pair states, and variational renormalization group methods for quantum spin systems.” *Advances in Physics* **57**, pp. 143, 2008. doi:[10.1080/14789940801912366](https://doi.org/10.1080/14789940801912366).
- [34] U. Schollwöck. “The density-matrix renormalization group in the age of matrix product states.” *Ann. Phys.* **326**, pp. 96 , 2011. doi:[10.1016/j.aop.2010.09.012](https://doi.org/10.1016/j.aop.2010.09.012).
- [35] G. Vidal. “Efficient simulation of one-dimensional quantum many-body systems.” *Phys. Rev. Lett.* **93**, p. 040502, 2004. doi:[10.1103/PhysRevLett.93.040502](https://doi.org/10.1103/PhysRevLett.93.040502).
- [36] S. Paeckel, T. Köhler, A. Swoboda, S. R. Manmana, U. Schollwöck, and C. Hubig. “Time-evolution methods for matrix-product states.” *Annals of Physics* **411**, p. 167998, 2019. doi:<https://doi.org/10.1016/j.aop.2019.167998>.
- [37] J. Preskill. “Lecture notes for physics 219: Quantum computation.” *Caltech Lecture Notes* p. 7, 1999.
- [38] H.-P. Breuer and F. Petruccione. *The Theory of Open Quantum Systems*. Oxford University Press, 2007.
- [39] P. Calabrese and J. Cardy. “Time dependence of correlation functions following a quantum quench.” *Phys. Rev. Lett.* **96**, p. 136801, 2006. doi:[10.1103/PhysRevLett.96.136801](https://doi.org/10.1103/PhysRevLett.96.136801).
- [40] J. Eisert, M. Friesdorf, and C. Gogolin. “Quantum many-body systems out of equilibrium.” *Nature Physics* **11**, pp. 124, 2015. doi:[10.1038/nphys3215](https://doi.org/10.1038/nphys3215).
- [41] A. Mitra. “Quantum quench dynamics.” *Annual Review of Condensed Matter Physics* **9**, pp. 245, 2018. doi:[10.1146/annurev-conmatphys-031016-025451](https://doi.org/10.1146/annurev-conmatphys-031016-025451).
- [42] C. W. Gardiner and P. Zoller. *Quantum noise*. Springer Series in Synergetics. Springer, Berlin, Germany, 2010.
- [43] G. Lindblad. “On the generators of quantum dynamical semigroups.” *Communications in Mathematical Physics* **48**, pp. 119, 1976. doi:[10.1007/bf01608499](https://doi.org/10.1007/bf01608499).
- [44] T. c. v. Prosen. “Open xxz spin chain: Nonequilibrium steady state and a strict bound on ballistic transport.” *Phys. Rev. Lett.* **106**, p. 217206, 2011. doi:[10.1103/PhysRevLett.106.217206](https://doi.org/10.1103/PhysRevLett.106.217206).
- [45] A. Carmele, M. Heyl, C. Kraus, and M. Dalmonte. “Stretched exponential decay of majorana edge modes in many-body localized kitaev chains under dissipation.” *Phys. Rev. B* **92**, p. 195107, 2015. doi:[10.1103/PhysRevB.92.195107](https://doi.org/10.1103/PhysRevB.92.195107).
- [46] M. H. Fischer, M. Maksymenko, and E. Altman. “Dynamics of a many-body-localized system coupled to a bath.” *Phys. Rev. Lett.* **116**, p. 160401, 2016. doi:[10.1103/PhysRevLett.116.160401](https://doi.org/10.1103/PhysRevLett.116.160401).
- [47] E. Levi, M. Heyl, I. Lesanovsky, and J. P. Garrahan. “Robustness of many-body localization in the presence of dissipation.” *Phys. Rev. Lett.* **116**, p. 237203, 2016. doi:[10.1103/PhysRevLett.116.237203](https://doi.org/10.1103/PhysRevLett.116.237203).

- [48] M. V. Medvedyeva, T. c. v. Prosen, and M. Žnidarič. “Influence of dephasing on many-body localization.” *Phys. Rev. B* **93**, p. 094205, 2016. doi:[10.1103/PhysRevB.93.094205](https://doi.org/10.1103/PhysRevB.93.094205).
- [49] B. Everest, I. Lesanovsky, J. P. Garrahan, and E. Levi. “Role of interactions in a dissipative many-body localized system.” *Phys. Rev. B* **95**, p. 024310, 2017. doi:[10.1103/PhysRevB.95.024310](https://doi.org/10.1103/PhysRevB.95.024310).
- [50] I. Vakulchyk, I. Yusipov, M. Ivanchenko, S. Flach, and S. Denisov. “Signatures of many-body localization in steady states of open quantum systems.” *Phys. Rev. B* **98**, p. 020202, 2018. doi:[10.1103/PhysRevB.98.020202](https://doi.org/10.1103/PhysRevB.98.020202).
- [51] L.-N. Wu and A. Eckardt. “Bath-induced decay of stark many-body localization.” *Phys. Rev. Lett.* **123**, p. 030602, 2019. doi:[10.1103/PhysRevLett.123.030602](https://doi.org/10.1103/PhysRevLett.123.030602).
- [52] H. Kim and D. A. Huse. “Ballistic spreading of entanglement in a diffusive nonintegrable system.” *Phys. Rev. Lett.* **111**, p. 127205, 2013. doi:[10.1103/PhysRevLett.111.127205](https://doi.org/10.1103/PhysRevLett.111.127205).
- [53] J. M. Deutsch. “Quantum statistical mechanics in a closed system.” *Phys. Rev. A* **43**, pp. 2046, 1991. doi:[10.1103/PhysRevA.43.2046](https://doi.org/10.1103/PhysRevA.43.2046).
- [54] M. Srednicki. “Chaos and quantum thermalization.” *Phys. Rev. E* **50**, pp. 888, 1994. doi:[10.1103/PhysRevE.50.888](https://doi.org/10.1103/PhysRevE.50.888).
- [55] L. D’Alessio, Y. Kafri, A. Polkovnikov, and M. Rigol. “From quantum chaos and eigenstate thermalization to statistical mechanics and thermodynamics.” *Adv. Phys.* **65**, 239 (2016) 2015. doi:[10.1080/00018732.2016.1198134](https://doi.org/10.1080/00018732.2016.1198134).
- [56] F. H. L. Essler and M. Fagotti. “Quench dynamics and relaxation in isolated integrable quantum spin chains.” *J. Stat. Mech. (2016) 064002* 2016. doi:[10.1088/1742-5468/2016/06/064002](https://doi.org/10.1088/1742-5468/2016/06/064002).
- [57] M. Schreiber, S. S. Hodgman, P. Bordia, H. P. Lüschen, M. H. Fischer, R. Vosk, E. Altman, U. Schneider, and I. Bloch. “Observation of many-body localization of interacting fermions in a quasirandom optical lattice.” *Science* **349**, pp. 842, 2015. doi:[10.1126/science.aaa7432](https://doi.org/10.1126/science.aaa7432).
- [58] V. Alba and P. Calabrese. “Entanglement and thermodynamics after a quantum quench in integrable systems.” *Proceedings of the National Academy of Sciences* **114**, pp. 7947, 2017. doi:[10.1073/pnas.1703516114](https://doi.org/10.1073/pnas.1703516114).
- [59] T. Kinoshita, T. Wenger, and D. S. Weiss. “A quantum newton's cradle.” *Nature* **440**, pp. 900, 2006. doi:[10.1038/nature04693](https://doi.org/10.1038/nature04693).
- [60] E. van Nieuwenburg, Y. Baum, and G. Refael. “From bloch oscillations to many-body localization in clean interacting systems.” *Proc. Natl. Acad. Sci. U.S.A.* **116**, pp. 9269, 2019. doi:[10.1073/pnas.1819316116](https://doi.org/10.1073/pnas.1819316116).
- [61] M. Schulz, C. A. Hooley, R. Moessner, and F. Pollmann. “Stark many-body localization.” *Phys. Rev. Lett.* **122**, p. 040606, 2019. doi:[10.1103/PhysRevLett.122.040606](https://doi.org/10.1103/PhysRevLett.122.040606).

- [62] O. Gühne and G. Tóth. “Entanglement detection.” *Physics Reports* **474**, pp. 1, 2009. doi:[10.1016/j.physrep.2009.02.004](https://doi.org/10.1016/j.physrep.2009.02.004).
- [63] M. Rigol, V. Dunjko, and M. Olshanii. “Thermalization and its mechanism for generic isolated quantum systems.” *Nature* **452**, pp. 854, 2008. doi:[10.1038/nature06838](https://doi.org/10.1038/nature06838).
- [64] M. Srednicki. “The approach to thermal equilibrium in quantized chaotic systems.” *Journal of Physics A: Mathematical and General* **32**, pp. 1163, 1999. doi:[10.1088/0305-4470/32/7/007](https://doi.org/10.1088/0305-4470/32/7/007).
- [65] E. H. Lieb and F. Y. Wu. “Absence of mott transition in an exact solution of the short-range, one-band model in one dimension.” *Phys. Rev. Lett.* **20**, pp. 1445, 1968. doi:[10.1103/PhysRevLett.20.1445](https://doi.org/10.1103/PhysRevLett.20.1445).
- [66] E. H. Lieb and F. Wu. “The one-dimensional hubbard model: a reminiscence.” *Physica A: Statistical Mechanics and its Applications* **321**, pp. 1, 2003. doi:[10.1016/s0378-4371\(02\)01785-5](https://doi.org/10.1016/s0378-4371(02)01785-5).
- [67] E. T. Jaynes. “Information theory and statistical mechanics.” *Phys. Rev.* **106**, pp. 620, 1957. doi:[10.1103/PhysRev.106.620](https://doi.org/10.1103/PhysRev.106.620).
- [68] M. Rigol, V. Dunjko, V. Yurovsky, and M. Olshanii. “Relaxation in a completely integrable many-body quantum system: An ab initio study of the dynamics of the highly excited states of 1d lattice hard-core bosons.” *Phys. Rev. Lett.* **98**, p. 050405, 2007. doi:[10.1103/PhysRevLett.98.050405](https://doi.org/10.1103/PhysRevLett.98.050405).
- [69] R. Nandkishore and D. A. Huse. “Many-body localization and thermalization in quantum statistical mechanics.” *Annual Review of Condensed Matter Physics* **6**, pp. 15, 2015. doi:[10.1146/annurev-conmatphys-031214-014726](https://doi.org/10.1146/annurev-conmatphys-031214-014726).
- [70] F. Alet and N. Laflorencie. “Many-body localization: An introduction and selected topics.” *Comptes Rendus Physique* **19**, pp. 498, 2018. doi:<https://doi.org/10.1016/j.crhy.2018.03.003>. Quantum simulation / Simulation quantique.
- [71] P. W. Anderson. “Absence of diffusion in certain random lattices.” *Phys. Rev.* **109**, pp. 1492, 1958. doi:[10.1103/PhysRev.109.1492](https://doi.org/10.1103/PhysRev.109.1492).
- [72] D. J. Thouless. “A relation between the density of states and range of localization for one dimensional random systems.” *Journal of Physics C: Solid State Physics* **5**, pp. 77, 1972. doi:[10.1088/0022-3719/5/1/010](https://doi.org/10.1088/0022-3719/5/1/010).
- [73] B. Bauer and C. Nayak. “Area laws in a many-body localized state and its implications for topological order.” *Journal of Statistical Mechanics: Theory and Experiment* **2013**, p. P09005, 2013. doi:[10.1088/1742-5468/2013/09/p09005](https://doi.org/10.1088/1742-5468/2013/09/p09005).
- [74] M. Serbyn, Z. Papic, and D. Abanin. “Local conservation laws and the structure of the many-body localized states.” *Phys. Rev. Lett.* **111**, p. 127201, 2013. doi:[10.1103/PhysRevLett.111.127201](https://doi.org/10.1103/PhysRevLett.111.127201).

- [75] D. A. Huse, R. Nandkishore, and V. Oganesyan. “Phenomenology of fully many-body-localized systems.” *Phys. Rev. B* **90**, p. 174202, 2014. doi:[10.1103/PhysRevB.90.174202](https://doi.org/10.1103/PhysRevB.90.174202).
- [76] V. Ros, M. Müller, and A. Scardicchio. “Integrals of motion in the many-body localized phase.” *Nuclear Physics B* **891**, pp. 420, 2015. doi:<https://doi.org/10.1016/j.nuclphysb.2014.12.014>.
- [77] J. Z. Imbrie, V. Ros, and A. Scardicchio. “Local integrals of motion in many-body localized systems.” *Annalen der Physik* **529**, p. 1600278, 2017. doi:[10.1002/andp.201600278](https://doi.org/10.1002/andp.201600278).
- [78] M. Serbyn, Z. Papić, and D. A. Abanin. “Universal slow growth of entanglement in interacting strongly disordered systems.” *Phys. Rev. Lett.* **110**, p. 260601, 2013. doi:[10.1103/PhysRevLett.110.260601](https://doi.org/10.1103/PhysRevLett.110.260601).
- [79] S. R. Taylor, M. Schulz, F. Pollmann, and R. Moessner. “Experimental probes of stark many-body localization.” *Phys. Rev. B* **102**, p. 054206, 2020. doi:[10.1103/PhysRevB.102.054206](https://doi.org/10.1103/PhysRevB.102.054206).
- [80] R. Yao, T. Chanda, and J. Zakrzewski. “Many-body localization in tilted and harmonic potentials.” *Phys. Rev. B* **104**, 2021. doi:[10.1103/physrevb.104.014201](https://doi.org/10.1103/physrevb.104.014201).
- [81] G. H. Wannier. “Dynamics of band electrons in electric and magnetic fields.” *Rev. Mod. Phys.* **34**, pp. 645, 1962. doi:[10.1103/RevModPhys.34.645](https://doi.org/10.1103/RevModPhys.34.645).
- [82] M. M. Wilde. *Preface to the Second Edition*, pp. xi–xii. Cambridge University Press, 2 edition, 2017. doi:[10.1017/9781316809976.001](https://doi.org/10.1017/9781316809976.001).
- [83] R. Kubo. “The fluctuation-dissipation theorem.” *Reports on Progress in Physics* **29**, pp. 255, 1966. doi:[10.1088/0034-4885/29/1/306](https://doi.org/10.1088/0034-4885/29/1/306).
- [84] S. Denisov, T. Laptjeva, W. Tarnowski, D. Chruściński, and K. Życzkowski. “Universal spectra of random lindblad operators.” *Phys. Rev. Lett.* **123**, p. 140403, 2019. doi:[10.1103/PhysRevLett.123.140403](https://doi.org/10.1103/PhysRevLett.123.140403).
- [85] L. Sá, P. Ribeiro, T. Can, and T. c. v. Prosen. “Spectral transitions and universal steady states in random kraus maps and circuits.” *Phys. Rev. B* **102**, p. 134310, 2020. doi:[10.1103/PhysRevB.102.134310](https://doi.org/10.1103/PhysRevB.102.134310).
- [86] T. Can, V. Oganesyan, D. Orgad, and S. Gopalakrishnan. “Spectral gaps and midgap states in random quantum master equations.” *Phys. Rev. Lett.* **123**, p. 234103, 2019. doi:[10.1103/PhysRevLett.123.234103](https://doi.org/10.1103/PhysRevLett.123.234103).
- [87] L. Gurvits. “Classical deterministic complexity of edmonds’ problem and quantum entanglement.” 2003. arXiv:[quant-ph/0303055v1](https://arxiv.org/abs/quant-ph/0303055v1).
- [88] A. Peres. “Separability criterion for density matrices.” *Phys. Rev. Lett.* **77**, pp. 1413, 1996. doi:[10.1103/PhysRevLett.77.1413](https://doi.org/10.1103/PhysRevLett.77.1413).
- [89] G. Vidal and R. F. Werner. “Computable measure of entanglement.” *Phys. Rev. A* **65**, p. 032314, 2002. doi:[10.1103/PhysRevA.65.032314](https://doi.org/10.1103/PhysRevA.65.032314).

- [90] M. Horodecki, P. Horodecki, and R. Horodecki. “Separability of mixed states: necessary and sufficient conditions.” *Physics Letters A* **223**, pp. 1, 1996. doi:[https://doi.org/10.1016/S0375-9601\(96\)00706-2](https://doi.org/10.1016/S0375-9601(96)00706-2).
- [91] J. Gray, A. Bayat, A. Pal, and S. Bose. “Scale invariant entanglement negativity at the many-body localization transition.” 2019. arXiv:[1908.02761v1](https://arxiv.org/abs/1908.02761).
- [92] C. G. West and T.-C. Wei. “Global and short-range entanglement properties in excited, many-body localized spin chains.” 2018. arXiv:[1809.04689v1](https://arxiv.org/abs/1809.04689).
- [93] B. Chiaro, C. Neill, A. Bohrdt, M. Filippone, F. Arute, K. Arya, R. Babbush, D. Bacon, J. Bardin, R. Barends, S. Boixo, D. Buell, B. Burkett, Y. Chen, Z. Chen, R. Collins, A. Dunsworth, E. Farhi, A. Fowler, B. Foxen, C. Gidney, M. Giustina, M. Harrigan, T. Huang, S. Isakov, E. Jeffrey, Z. Jiang, D. Kafri, K. Kechedzhi, J. Kelly, P. Klimov, A. Korotkov, F. Kostritsa, D. Landhuis, E. Lucero, J. McClean, X. Mi, A. Megrant, M. Mohseni, J. Mutus, M. McEwen, O. Naaman, M. Neeley, M. Niu, A. Petukhov, C. Quintana, N. Rubin, D. Sank, K. Satzinger, A. Vainsencher, T. White, Z. Yao, P. Yeh, A. Zalcman, V. Smelyanskiy, H. Neven, S. Gopalakrishnan, D. Abanin, M. Knap, J. Martinis, and P. Roushan. “Direct measurement of non-local interactions in the many-body localized phase.” 2019. arXiv:[1910.06024](https://arxiv.org/abs/1910.06024).
- [94] P. Calabrese, J. Cardy, and E. Tonni. “Entanglement negativity in quantum field theory.” *Phys. Rev. Lett.* **109**, p. 130502, 2012. doi:[10.1103/PhysRevLett.109.130502](https://doi.org/10.1103/PhysRevLett.109.130502).
- [95] P. Calabrese, J. Cardy, and E. Tonni. “Entanglement negativity in extended systems: a field theoretical approach.” *Journal of Statistical Mechanics: Theory and Experiment* **2013**, p. P02008, 2013. doi:[10.1088/1742-5468/2013/02/p02008](https://doi.org/10.1088/1742-5468/2013/02/p02008).
- [96] M. Rangamani and M. Rota. “Comments on entanglement negativity in holographic field theories.” doi:[10.1007/JHEP10\(2014\)060](https://doi.org/10.1007/JHEP10(2014)060).
- [97] J. Gray, L. Bianchi, A. Bayat, and S. Bose. “Machine-learning-assisted many-body entanglement measurement.” *Phys. Rev. Lett.* **121**, p. 150503, 2018. doi:[10.1103/PhysRevLett.121.150503](https://doi.org/10.1103/PhysRevLett.121.150503).
- [98] K.-H. Wu, T.-C. Lu, C.-M. Chung, Y.-J. Kao, and T. Grover. “Entanglement renyi negativity across a finite temperature transition: A monte carlo study.” *Phys. Rev. Lett.* **125**, p. 140603, 2020. doi:[10.1103/PhysRevLett.125.140603](https://doi.org/10.1103/PhysRevLett.125.140603).
- [99] A. Elben, R. Kueng, H.-Y. R. Huang, R. van Bijnen, C. Kokail, M. Dalmonte, P. Calabrese, B. Kraus, J. Preskill, P. Zoller, and B. Vermersch. “Mixed-state entanglement from local randomized measurements.” *Phys. Rev. Lett.* **125**, p. 200501, 2020. doi:[10.1103/PhysRevLett.125.200501](https://doi.org/10.1103/PhysRevLett.125.200501).
- [100] A. Neven, J. Carrasco, V. Vitale, C. Kokail, A. Elben, M. Dalmonte, P. Calabrese, P. Zoller, B. Vermersch, R. Kueng, and B. Kraus. “Symmetry-resolved entanglement detection using partial transpose moments.” *npj Quantum Information* **7**, 2021. doi:[10.1038/s41534-021-00487-y](https://doi.org/10.1038/s41534-021-00487-y).

- [101] V. Vitale, A. Elben, R. Kueng, A. Neven, J. Carrasco, B. Kraus, P. Zoller, P. Calabrese, B. Vermersch, and M. Dalmonte. “Symmetry-resolved dynamical purification in synthetic quantum matter.” *SciPost Phys.* **12**, p. 106, 2022. doi:[10.21468/SciPostPhys.12.3.106](https://doi.org/10.21468/SciPostPhys.12.3.106).
- [102] S. L. Braunstein and C. M. Caves. “Statistical distance and the geometry of quantum states.” *Phys. Rev. Lett.* **72**, pp. 3439, 1994. doi:[10.1103/PhysRevLett.72.3439](https://doi.org/10.1103/PhysRevLett.72.3439).
- [103] P. Hyllus, W. Laskowski, R. Krischek, C. Schwemmer, W. Wieczorek, H. Weinfurter, L. Pezzé, and A. Smerzi. “Fisher information and multiparticle entanglement.” *Phys. Rev. A* **85**, p. 022321, 2012. doi:[10.1103/PhysRevA.85.022321](https://doi.org/10.1103/PhysRevA.85.022321).
- [104] G. Tóth. “Multipartite entanglement and high-precision metrology.” *Phys. Rev. A* **85**, p. 022322, 2012. doi:[10.1103/PhysRevA.85.022322](https://doi.org/10.1103/PhysRevA.85.022322).
- [105] J. Smith, A. Lee, P. Richerme, B. Neyenhuis, P. Hess, P. Hauke, M. Heyl, D. Huse, and C. Monroe. “Many-body localization in a quantum simulator with programmable random disorder.” *Nature Physics* **12**, 2015. doi:[10.1038/nphys3783](https://doi.org/10.1038/nphys3783).
- [106] J. Hauschild and F. Pollmann. “Efficient numerical simulations with Tensor Networks: Tensor Network Python (TeNPy).” *SciPost Phys. Lect. Notes* p. 5, 2018. doi:[10.21468/SciPostPhysLectNotes.5](https://doi.org/10.21468/SciPostPhysLectNotes.5). Code available from <https://github.com/tenpy/tenpy>.
- [107] J. Eisert, M. Cramer, and M. B. Plenio. “Area laws for the entanglement entropy.” *Reviews of Modern Physics* **82**, pp. 277, 2010. doi:[10.1103/revmodphys.82.277](https://doi.org/10.1103/revmodphys.82.277).
- [108] D. N. Page. “Average entropy of a subsystem.” *Phys. Rev. Lett.* **71**, pp. 1291, 1993. doi:[10.1103/PhysRevLett.71.1291](https://doi.org/10.1103/PhysRevLett.71.1291).
- [109] E. Bianchi, L. Hackl, M. Kieburg, M. Rigol, and L. Vidmar. “Volume-law entanglement entropy of typical pure quantum states.” 2021. doi:[10.48550/ARXIV.2112.06959](https://doi.org/10.48550/ARXIV.2112.06959).
- [110] S. Östlund and S. Rommer. “Thermodynamic limit of density matrix renormalization.” *Phys. Rev. Lett.* **75**, pp. 3537, 1995. doi:[10.1103/PhysRevLett.75.3537](https://doi.org/10.1103/PhysRevLett.75.3537).
- [111] C. Lanczos. “An iteration method for the solution of the eigenvalue problem of linear differential and integral operators.” *Journal of research of the National Bureau of Standards* **45**, pp. 255, 1950.
- [112] F. Verstraete, J. J. García-Ripoll, and J. I. Cirac. “Matrix product density operators: Simulation of finite-temperature and dissipative systems.” *Phys. Rev. Lett.* **93**, p. 207204, 2004. doi:[10.1103/PhysRevLett.93.207204](https://doi.org/10.1103/PhysRevLett.93.207204).
- [113] M. Zwolak and G. Vidal. “Mixed-state dynamics in one-dimensional quantum lattice systems: A time-dependent superoperator renormalization algorithm.” *Phys. Rev. Lett.* **93**, p. 207205, 2004. doi:[10.1103/PhysRevLett.93.207205](https://doi.org/10.1103/PhysRevLett.93.207205).
- [114] F. Verstraete, J. I. Cirac, and V. Murg. “Matrix product states, projected entangled pair states, and variational renormalization group methods for quantum spin systems.” doi:[10.1080/14789940801912366](https://doi.org/10.1080/14789940801912366).

- [115] T. Prosen and I. Pižorn. “Operator space entanglement entropy in a transverse ising chain.” *Phys. Rev. A* **76**, p. 032316, 2007. doi:[10.1103/PhysRevA.76.032316](https://doi.org/10.1103/PhysRevA.76.032316).
- [116] R. Vosk and E. Altman. “Many-body localization in one dimension as a dynamical renormalization group fixed point.” *Phys. Rev. Lett.* **110**, p. 067204, 2013. doi:[10.1103/PhysRevLett.110.067204](https://doi.org/10.1103/PhysRevLett.110.067204).
- [117] S. Gopalakrishnan, M. Müller, V. Khemani, M. Knap, E. Demler, and D. A. Huse. “Low-frequency conductivity in many-body localized systems.” *Phys. Rev. B* **92**, p. 104202, 2015. doi:[10.1103/PhysRevB.92.104202](https://doi.org/10.1103/PhysRevB.92.104202).
- [118] K. Agarwal, E. Altman, E. Demler, S. Gopalakrishnan, D. A. Huse, and M. Knap. “Rare-region effects and dynamics near the many-body localization transition.” *Annalen der Physik* **529**, p. 1600326, 2017. doi:[10.1002/andp.201600326](https://doi.org/10.1002/andp.201600326).
- [119] H. P. Lüschen, P. Bordia, S. S. Hodgman, M. Schreiber, S. Sarkar, A. J. Daley, M. H. Fischer, E. Altman, I. Bloch, and U. Schneider. “Signatures of many-body localization in a controlled open quantum system.” *Phys. Rev. X* **7**, p. 011034, 2017. doi:[10.1103/PhysRevX.7.011034](https://doi.org/10.1103/PhysRevX.7.011034).
- [120] P. Bordia, H. Lüschen, S. Scherg, S. Gopalakrishnan, M. Knap, U. Schneider, and I. Bloch. “Probing slow relaxation and many-body localization in two-dimensional quasiperiodic systems.” *Phys. Rev. X* **7**, p. 041047, 2017. doi:[10.1103/PhysRevX.7.041047](https://doi.org/10.1103/PhysRevX.7.041047).
- [121] T. Brydges, A. Elben, P. Jurcevic, B. Vermersch, C. Maier, B. P. Lanyon, P. Zoller, R. Blatt, and C. F. Roos. “Probing rényi entanglement entropy via randomized measurements.” *Science* **364**, pp. 260, 2019. doi:[10.1126/science.aau4963](https://doi.org/10.1126/science.aau4963).
- [122] M. Rispoli, A. Lukin, R. Schittko, S. Kim, M. E. Tai, J. Léonard, and M. Greiner. “Quantum critical behaviour at the many-body localization transition.” *Nature* **573**, pp. 385, 2019. doi:[10.1038/s41586-019-1527-2](https://doi.org/10.1038/s41586-019-1527-2).
- [123] Z. Lenarčič, E. Altman, and A. Rosch. “Activating many-body localization in solids by driving with light.” *Phys. Rev. Lett.* **121**, p. 267603, 2018. doi:[10.1103/PhysRevLett.121.267603](https://doi.org/10.1103/PhysRevLett.121.267603).
- [124] Z. Lenarčič, O. Alberton, A. Rosch, and E. Altman. “Critical behavior near the many-body localization transition in driven open systems.” *Phys. Rev. Lett.* **125**, p. 116601, 2020. doi:[10.1103/PhysRevLett.125.116601](https://doi.org/10.1103/PhysRevLett.125.116601).
- [125] V. K. Varma, A. Raj, S. Gopalakrishnan, V. Oganesyan, and D. Pekker. “Length scales in the many-body localized phase and their spectral signatures.” *Phys. Rev. B* **100**, p. 115136, 2019. doi:[10.1103/PhysRevB.100.115136](https://doi.org/10.1103/PhysRevB.100.115136).
- [126] R. Singh, J. H. Bardarson, and F. Pollmann. “Signatures of the many-body localization transition in the dynamics of entanglement and bipartite fluctuations.” *New Journal of Physics* **18**, p. 023046, 2016. doi:[10.1088/1367-2630/18/2/023046](https://doi.org/10.1088/1367-2630/18/2/023046).
- [127] M. P. Almeida, F. de Melo, M. Hor-Meyll, A. Salles, S. P. Walborn, P. H. S. Ribeiro, and L. Davidovich. “Environment-induced sudden death of entanglement.” *Science* **316**, pp. 579, 2007. doi:[10.1126/science.1139892](https://doi.org/10.1126/science.1139892).

- [128] T. Yu and J. H. Eberly. “Sudden death of entanglement.” *Science* **323**, pp. 598, 2009. doi:[10.1126/science.1167343](https://doi.org/10.1126/science.1167343).
- [129] G. Tóth and I. Apellaniz. “Quantum metrology from a quantum information science perspective.” *Journal of Physics A: Mathematical and Theoretical* **47**, p. 424006, 2014. doi:[10.1088/1751-8113/47/42/424006](https://doi.org/10.1088/1751-8113/47/42/424006).
- [130] P. Hauke, M. Heyl, L. Tagliacozzo, and P. Zoller. “Measuring multipartite entanglement through dynamic susceptibilities.” *Nature Physics* **12**, p. 778, 2016.
- [131] J. Cai and W. Song. “Novel schemes for directly measuring entanglement of general states.” *Phys. Rev. Lett.* **101**, p. 190503, 2008. doi:[10.1103/PhysRevLett.101.190503](https://doi.org/10.1103/PhysRevLett.101.190503).
- [132] H. A. Carteret. “Noiseless quantum circuits for the peres separability criterion.” *Phys. Rev. Lett.* **94**, p. 040502, 2005. doi:[10.1103/PhysRevLett.94.040502](https://doi.org/10.1103/PhysRevLett.94.040502).
- [133] F. Mintert, M. Kuś, and A. Buchleitner. “Concurrence of mixed multipartite quantum states.” *Phys. Rev. Lett.* **95**, p. 260502, 2005. doi:[10.1103/PhysRevLett.95.260502](https://doi.org/10.1103/PhysRevLett.95.260502).
- [134] A. J. Daley, H. Pichler, J. Schachenmayer, and P. Zoller. “Measuring entanglement growth in quench dynamics of bosons in an optical lattice.” *Phys. Rev. Lett.* **109**, p. 020505, 2012. doi:[10.1103/PhysRevLett.109.020505](https://doi.org/10.1103/PhysRevLett.109.020505).
- [135] Y. Zhou, P. Zeng, and Z. Liu. “Single-copies estimation of entanglement negativity.” *Phys. Rev. Lett.* **125**, p. 200502, 2020. doi:[10.1103/PhysRevLett.125.200502](https://doi.org/10.1103/PhysRevLett.125.200502).
- [136] S. J. van Enk and C. W. J. Beenakker. “Measuring $\text{Tr}\rho^n$ on single copies of ρ using random measurements.” *Phys. Rev. Lett.* **108**, p. 110503, 2012. doi:[10.1103/PhysRevLett.108.110503](https://doi.org/10.1103/PhysRevLett.108.110503).
- [137] Y. Nakata, C. Hirche, M. Koashi, and A. Winter. “Efficient quantum pseudorandomness with nearly time-independent hamiltonian dynamics.” *Phys. Rev. X* **7**, p. 021006, 2017. doi:[10.1103/PhysRevX.7.021006](https://doi.org/10.1103/PhysRevX.7.021006).
- [138] A. Elben, B. Vermersch, M. Dalmonte, J. I. Cirac, and P. Zoller. “Rényi entropies from random quenches in atomic hubbard and spin models.” *Phys. Rev. Lett.* **120**, p. 050406, 2018. doi:[10.1103/PhysRevLett.120.050406](https://doi.org/10.1103/PhysRevLett.120.050406).
- [139] B. Vermersch, A. Elben, M. Dalmonte, J. I. Cirac, and P. Zoller. “Unitary n -designs via random quenches in atomic hubbard and spin models: Application to the measurement of rényi entropies.” *Phys. Rev. A* **97**, p. 023604, 2018. doi:[10.1103/PhysRevA.97.023604](https://doi.org/10.1103/PhysRevA.97.023604).
- [140] A. Elben, B. Vermersch, C. F. Roos, and P. Zoller. “Statistical correlations between locally randomized measurements: A toolbox for probing entanglement in many-body quantum states.” *Phys. Rev. A* **99**, p. 052323, 2019. doi:[10.1103/PhysRevA.99.052323](https://doi.org/10.1103/PhysRevA.99.052323).
- [141] G. Carleo, F. Becca, M. Schiró, and M. Fabrizio. “Localization and glassy dynamics of many-body quantum systems.” *Scientific Reports* **2**, 2012. doi:[10.1038/srep00243](https://doi.org/10.1038/srep00243).

- [142] W. D. Roeck and F. Huveneers. “Asymptotic quantum many-body localization from thermal disorder.” *Communications in Mathematical Physics* **332**, pp. 1017, 2014. doi:[10.1007/s00220-014-2116-8](https://doi.org/10.1007/s00220-014-2116-8).
- [143] T. Grover and M. P. A. Fisher. “Quantum disentangled liquids.” *J. Stat. Mech.: Theory Exp.* **2014**, p. P10010, 2014. doi:[10.1088/1742-5468/2014/10/p10010](https://doi.org/10.1088/1742-5468/2014/10/p10010).
- [144] M. Schiulaz, A. Silva, and M. Müller. “Dynamics in many-body localized quantum systems without disorder.” *Phys. Rev. B* **91**, p. 184202, 2015. doi:[10.1103/PhysRevB.91.184202](https://doi.org/10.1103/PhysRevB.91.184202).
- [145] N. Y. Yao, C. R. Laumann, J. I. Cirac, M. D. Lukin, and J. E. Moore. “Quasi-many-body localization in translation-invariant systems.” *Phys. Rev. Lett.* **117**, p. 240601, 2016. doi:[10.1103/PhysRevLett.117.240601](https://doi.org/10.1103/PhysRevLett.117.240601).
- [146] J. M. Hickey, S. Genway, and J. P. Garrahan. “Signatures of many-body localisation in a system without disorder and the relation to a glass transition.” *J. Stat. Mech.: Theory Exp.* **2016**, p. 054047, 2016. doi:[10.1088/1742-5468/2016/05/054047](https://doi.org/10.1088/1742-5468/2016/05/054047).
- [147] M. van Horssen, E. Levi, and J. P. Garrahan. “Dynamics of many-body localization in a translation-invariant quantum glass model.” *Phys. Rev. B* **92**, p. 100305, 2015. doi:[10.1103/PhysRevB.92.100305](https://doi.org/10.1103/PhysRevB.92.100305).
- [148] M. Brenes, M. Dalmonte, M. Heyl, and A. Scardicchio. “Many-body localization dynamics from gauge invariance.” *Phys. Rev. Lett.* **120**, p. 030601, 2018. doi:[10.1103/PhysRevLett.120.030601](https://doi.org/10.1103/PhysRevLett.120.030601).
- [149] A. Smith, J. Knolle, R. Moessner, and D. L. Kovrizhin. “Absence of ergodicity without quenched disorder: From quantum disentangled liquids to many-body localization.” *Phys. Rev. Lett.* **119**, p. 176601, 2017. doi:[10.1103/PhysRevLett.119.176601](https://doi.org/10.1103/PhysRevLett.119.176601).
- [150] N. D. Oppong, G. Pasqualetti, O. Bettermann, P. Zechmann, M. Knap, I. Bloch, and S. Fölling. “Probing transport and slow relaxation in the mass-imbalanced fermi-hubbard model.” 2020. arXiv:[2011.12411v1](https://arxiv.org/abs/2011.12411v1).
- [151] B. Gadway, D. Pertot, J. Reeves, M. Vogt, and D. Schneble. “Glassy behavior in a binary atomic mixture.” *Phys. Rev. Lett.* **107**, p. 145306, 2011. doi:[10.1103/PhysRevLett.107.145306](https://doi.org/10.1103/PhysRevLett.107.145306).
- [152] A. Tomadin, R. Mannella, and S. Wimberger. “Many-body interband tunneling as a witness of complex dynamics in the bose-hubbard model.” *Phys. Rev. Lett.* **98**, p. 130402, 2007. doi:[10.1103/PhysRevLett.98.130402](https://doi.org/10.1103/PhysRevLett.98.130402).
- [153] R. Yao and J. Zakrzewski. “Many-body localization of bosons in an optical lattice: Dynamics in disorder-free potentials.” *Phys. Rev. B* **102**, p. 104203, 2020. doi:[10.1103/PhysRevB.102.104203](https://doi.org/10.1103/PhysRevB.102.104203).
- [154] V. Khemani, M. Hermele, and R. Nandkishore. “Localization from hilbert space shattering: From theory to physical realizations.” *Phys. Rev. B* **101**, p. 174204, 2020. doi:[10.1103/PhysRevB.101.174204](https://doi.org/10.1103/PhysRevB.101.174204).

- [155] E. V. H. Doggen, I. V. Gornyi, and D. G. Polyakov. “Stark many-body localization: Evidence for hilbert-space shattering.” *Phys. Rev. B* **103**, p. L100202, 2021. doi:[10.1103/PhysRevB.103.L100202](https://doi.org/10.1103/PhysRevB.103.L100202).
- [156] G. H. Wannier. “Wave functions and effective hamiltonian for bloch electrons in an electric field.” *Phys. Rev.* **117**, pp. 432, 1960. doi:[10.1103/PhysRev.117.432](https://doi.org/10.1103/PhysRev.117.432).
- [157] S. Scherg, T. Kohlert, P. Sala, F. Pollmann, B. H. Madhusudhana, I. Bloch, and M. Aidelsburger. “Observing non-ergodicity due to kinetic constraints in tilted fermi-hubbard chains.” *Nature Communications* **12**, 2021. doi:[10.1038/s41467-021-24726-0](https://doi.org/10.1038/s41467-021-24726-0).
- [158] Q. Guo, C. Cheng, H. Li, S. Xu, P. Zhang, Z. Wang, C. Song, W. Liu, W. Ren, H. Dong, R. Mondaini, and H. Wang. “Stark many-body localization on a superconducting quantum processor.” *Phys. Rev. Lett.* **127**, p. 240502, 2021. doi:[10.1103/PhysRevLett.127.240502](https://doi.org/10.1103/PhysRevLett.127.240502).
- [159] W. Morong, F. Liu, P. Becker, K. S. Collins, L. Feng, A. Kyprianidis, G. Pagano, T. You, A. V. Gorshkov, and C. Monroe. “Observation of stark many-body localization without disorder.” *Nature* **599**, pp. 393, 2021. doi:[10.1038/s41586-021-03988-0](https://doi.org/10.1038/s41586-021-03988-0).
- [160] E. Guardado-Sanchez, A. Morningstar, B. M. Spar, P. T. Brown, D. A. Huse, and W. S. Bakr. “Subdiffusion and heat transport in a tilted two-dimensional fermi-hubbard system.” *Phys. Rev. X* **10**, p. 011042, 2020. doi:[10.1103/PhysRevX.10.011042](https://doi.org/10.1103/PhysRevX.10.011042).
- [161] L. Amico, R. Fazio, A. Osterloh, and V. Vedral. “Entanglement in many-body systems.” *Rev. Mod. Phys.* **80**, pp. 517, 2008. doi:[10.1103/RevModPhys.80.517](https://doi.org/10.1103/RevModPhys.80.517).
- [162] P. Calabrese and A. Lefevre. “Entanglement spectrum in one-dimensional systems.” *Phys. Rev. A* **78**, p. 032329, 2008. doi:[10.1103/PhysRevA.78.032329](https://doi.org/10.1103/PhysRevA.78.032329).
- [163] P. Calabrese and J. Cardy. “Entanglement entropy and conformal field theory.” *Journal of Physics A: Mathematical and Theoretical* **42**, p. 504005, 2009. doi:[10.1088/1751-8113/42/50/504005](https://doi.org/10.1088/1751-8113/42/50/504005).
- [164] I. Peschel and V. Eisler. “Reduced density matrices and entanglement entropy in free lattice models.” *Journal of Physics A: Mathematical and Theoretical* **42**, p. 504003, 2009. doi:[10.1088/1751-8113/42/50/504003](https://doi.org/10.1088/1751-8113/42/50/504003).
- [165] F. Pollmann, E. Berg, A. M. Turner, and M. Oshikawa. “Symmetry protection of topological phases in one-dimensional quantum spin systems.” *Phys. Rev. B* **85**, p. 075125, 2012. doi:[10.1103/PhysRevB.85.075125](https://doi.org/10.1103/PhysRevB.85.075125).
- [166] M. Fannes, B. Nachtergaele, and R. W. Werner. “Finitely correlated states on quantum spin chains.” *Commun. Math. Phys.* **144**, p. 443, 1992. doi:[10.1007/BF02099178](https://doi.org/10.1007/BF02099178).
- [167] A. Alexandradinata, T. L. Hughes, and B. A. Bernevig. “Trace index and spectral flow in the entanglement spectrum of topological insulators.” *Phys. Rev. B* **84**, p. 195103, 2011. doi:[10.1103/PhysRevB.84.195103](https://doi.org/10.1103/PhysRevB.84.195103).

- [168] E. Prodan, T. L. Hughes, and B. A. Bernevig. “Entanglement spectrum of a disordered topological chern insulator.” *Phys. Rev. Lett.* **105**, p. 115501, 2010. doi:[10.1103/PhysRevLett.105.115501](https://doi.org/10.1103/PhysRevLett.105.115501).
- [169] L. Fidkowski. “Entanglement spectrum of topological insulators and superconductors.” *Phys. Rev. Lett.* **104**, p. 130502, 2010. doi:[10.1103/PhysRevLett.104.130502](https://doi.org/10.1103/PhysRevLett.104.130502).
- [170] A. Chandran, V. Khemani, and S. L. Sondhi. “How universal is the entanglement spectrum?” *Phys. Rev. Lett.* **113**, p. 060501, 2014. doi:[10.1103/PhysRevLett.113.060501](https://doi.org/10.1103/PhysRevLett.113.060501).
- [171] M. P. Zaletel, R. S. K. Mong, and F. Pollmann. “Topological characterization of fractional quantum hall ground states from microscopic hamiltonians.” *Phys. Rev. Lett.* **110**, p. 236801, 2013. doi:[10.1103/PhysRevLett.110.236801](https://doi.org/10.1103/PhysRevLett.110.236801).
- [172] Y. Zhang, T. Grover, A. Turner, M. Oshikawa, and A. Vishwanath. “Quasiparticle statistics and braiding from ground-state entanglement.” *Phys. Rev. B* **85**, p. 235151, 2012. doi:[10.1103/PhysRevB.85.235151](https://doi.org/10.1103/PhysRevB.85.235151).
- [173] A. Kitaev and J. Preskill. “Topological entanglement entropy.” *Phys. Rev. Lett.* **96**, 110404, 2006. doi:[10.1103/PhysRevLett.96.110404](https://doi.org/10.1103/PhysRevLett.96.110404).
- [174] M. Levin and X.-G. Wen. “Detecting topological order in a ground state wave function.” *Phys. Rev. Lett.* **96**, 110405, 2006. doi:[10.1103/PhysRevLett.96.110405](https://doi.org/10.1103/PhysRevLett.96.110405).
- [175] X. Chen, Z.-C. Gu, and X.-G. Wen. “Local unitary transformation, long-range quantum entanglement, wave function renormalization, and topological order.” *Phys. Rev. B* **82**, p. 155138, 2010. doi:[10.1103/PhysRevB.82.155138](https://doi.org/10.1103/PhysRevB.82.155138).
- [176] X. Chen, Z.-C. Gu, Z.-X. Liu, and X.-G. Wen. “Symmetry-protected topological orders in interacting bosonic systems.” *Science* **338**, pp. 1604, 2012. doi:[10.1126/science.1227224](https://doi.org/10.1126/science.1227224).
- [177] X. Chen, Z.-X. Liu, and X.-G. Wen. “Two-dimensional symmetry-protected topological orders and their protected gapless edge excitations.” *Phys. Rev. B* **84**, p. 235141, 2011. doi:[10.1103/PhysRevB.84.235141](https://doi.org/10.1103/PhysRevB.84.235141).
- [178] A. M. Turner, F. Pollmann, and E. Berg. “Topological phases of one-dimensional fermions: An entanglement point of view.” *Phys. Rev. B* **83**, p. 075102, 2011. doi:[10.1103/PhysRevB.83.075102](https://doi.org/10.1103/PhysRevB.83.075102).
- [179] H. Li and F. D. M. Haldane. “Entanglement spectrum as a generalization of entanglement entropy: Identification of topological order in non-abelian fractional quantum hall effect states.” *Phys. Rev. Lett.* **101**, p. 010504, 2008. doi:[10.1103/PhysRevLett.101.010504](https://doi.org/10.1103/PhysRevLett.101.010504).
- [180] H.-H. Tu, Y. Zhang, and X.-L. Qi. “Momentum polarization: An entanglement measure of topological spin and chiral central charge.” *Phys. Rev. B* **88**, p. 195412, 2013. doi:[10.1103/PhysRevB.88.195412](https://doi.org/10.1103/PhysRevB.88.195412).
- [181] S. Matsuura, X. Wen, L.-Y. Hung, and S. Ryu. “Charged topological entanglement entropy.” *Phys. Rev. B* **93**, p. 195113, 2016. doi:[10.1103/PhysRevB.93.195113](https://doi.org/10.1103/PhysRevB.93.195113).

- [182] I. Marvian. “Symmetry-protected topological entanglement.” *Phys. Rev. B* **95**, p. 045111, 2017. doi:[10.1103/PhysRevB.95.045111](https://doi.org/10.1103/PhysRevB.95.045111).
- [183] W. Ding and K. Yang. “Entanglement entropy and mutual information in bose-einstein condensates.” *Phys. Rev. A* **80**, p. 012329, 2009. doi:[10.1103/PhysRevA.80.012329](https://doi.org/10.1103/PhysRevA.80.012329).
- [184] M. A. Metlitski and T. Grover. “Entanglement entropy of systems with spontaneously broken continuous symmetry.” *arXiv preprint arXiv:1112.5166* 2011.
- [185] O. A. Castro-Alvaredo, C. De Fazio, B. Doyon, and I. M. Szécsényi. “Entanglement content of quasiparticle excitations.” *Physical review letters* **121**, p. 170602, 2018.
- [186] V. Eisler and F. Maislinger. “Front dynamics in the xy chain after local excitations.” *arXiv preprint arXiv:1909.02841* 2019.
- [187] O. A. Castro-Alvaredo, C. De Fazio, B. Doyon, and I. M. Szécsényi. “Entanglement content of quantum particle excitations. part ii. disconnected regions and logarithmic negativity.” *Journal of High Energy Physics* **2019**, p. 58, 2019.
- [188] A. Jafarizadeh and M. Rajabpour. “Bipartite entanglement entropy of the excited states of free fermions and harmonic oscillators.” *Physical Review B* **100**, p. 165135, 2019.
- [189] O. A. Castro-Alvaredo, C. De Fazio, B. Doyon, and I. M. Szécsényi. “Entanglement content of quantum particle excitations. part i. free field theory.” *Journal of High Energy Physics* **2018**, p. 39, 2018.
- [190] J. Zhang and M. A. Rajabpour. “Universal rényi entanglement entropy of quasiparticle excitations.” *EPL (Europhysics Letters)* **135**, p. 60001, 2021. doi:[10.1209/0295-5075/ac130e](https://doi.org/10.1209/0295-5075/ac130e).
- [191] J. Zhang and M. A. Rajabpour. “Corrections to universal rényi entropy in quasiparticle excited states of quantum chains.” *Journal of Statistical Mechanics: Theory and Experiment* **2021**, p. 093101, 2021. doi:[10.1088/1742-5468/ac1f28](https://doi.org/10.1088/1742-5468/ac1f28).
- [192] D. A. Abanin and E. Demler. “Measuring entanglement entropy of a generic many-body system with a quantum switch.” *Phys. Rev. Lett.* **109**, p. 020504, 2012. doi:[10.1103/PhysRevLett.109.020504](https://doi.org/10.1103/PhysRevLett.109.020504).
- [193] A. M. Kaufman, M. E. Tai, A. Lukin, M. Rispoli, R. Schittko, P. M. Preiss, and M. Greiner. “Quantum thermalization through entanglement in an isolated many-body system.” *Science* **353**, pp. 794, 2016. doi:[10.1126/science.aaf6725](https://doi.org/10.1126/science.aaf6725).
- [194] K. Choo, C. W. Von Keyserlingk, N. Regnault, and T. Neupert. “Measurement of the entanglement spectrum of a symmetry-protected topological state using the ibm quantum computer.” *Physical review letters* **121**, p. 086808, 2018.
- [195] A. M. Turner, Y. Zhang, and A. Vishwanath. “Band topology of insulators via the entanglement spectrum.” *arXiv preprint arXiv:0909.3119* 2009.
- [196] W. P. Su, J. R. Schrieffer, and A. J. Heeger. “Solitons in polyacetylene.” *Phys. Rev. Lett.* **42**, pp. 1698, 1979. doi:[10.1103/PhysRevLett.42.1698](https://doi.org/10.1103/PhysRevLett.42.1698).

- [197] P. Fromholz, G. Magnifico, V. Vitale, T. Mendes-Santos, and M. Dalmonte. “Entanglement topological invariants for one-dimensional topological superconductors.” *Phys. Rev. B* **101**, p. 085136, 2020. doi:[10.1103/PhysRevB.101.085136](https://doi.org/10.1103/PhysRevB.101.085136).
- [198] Y. You, J. Bibo, and F. Pollmann. “Higher-order entanglement and many-body invariants for higher-order topological phases.” *Phys. Rev. Research* **2**, p. 033192, 2020. doi:[10.1103/PhysRevResearch.2.033192](https://doi.org/10.1103/PhysRevResearch.2.033192).
- [199] J. Haegeman, D. Pérez-García, I. Cirac, and N. Schuch. “Order parameter for symmetry-protected phases in one dimension.” *Phys. Rev. Lett.* **109**, p. 050402, 2012. doi:[10.1103/PhysRevLett.109.050402](https://doi.org/10.1103/PhysRevLett.109.050402).
- [200] C.-M. Jian, I. H. Kim, and X.-L. Qi. “Long-range mutual information and topological uncertainty principle.” 2015. arXiv:[1508.07006](https://arxiv.org/abs/1508.07006).
- [201] M. Suzuki. “Relationship among Exactly Soluble Models of Critical Phenomena. I*): 2D Ising Model, Dimer Problem and the Generalized XY-Model.” *Progress of Theoretical Physics* **46**, pp. 1337, 1971. doi:[10.1143/PTP.46.1337](https://doi.org/10.1143/PTP.46.1337).
- [202] R. Raussendorf and H. J. Briegel. “A one-way quantum computer.” *Phys. Rev. Lett.* **86**, pp. 5188, 2001. doi:[10.1103/PhysRevLett.86.5188](https://doi.org/10.1103/PhysRevLett.86.5188).
- [203] B. Zeng, X. Chen, D.-L. Zhou, and X.-G. Wen. *Quantum Information Meets Quantum Matter*. Springer New York, 2019.
- [204] M. den Nijs and K. Rommelse. “Preroughening transitions in crystal surfaces and valence-bond phases in quantum spin chains.” *Phys. Rev. B* **40**, pp. 4709, 1989. doi:[10.1103/PhysRevB.40.4709](https://doi.org/10.1103/PhysRevB.40.4709).
- [205] D. Ben-Zion, J. McGreevy, and T. Grover. “Disentangling quantum matter with measurements.” *Phys. Rev. B* **101**, p. 115131, 2020. doi:[10.1103/PhysRevB.101.115131](https://doi.org/10.1103/PhysRevB.101.115131).
- [206] S. Coleman. “Quantum sine-gordon equation as the massive thirring model.” *Phys. Rev. D* **11**, pp. 2088, 1975. doi:[10.1103/PhysRevD.11.2088](https://doi.org/10.1103/PhysRevD.11.2088).
- [207] A. B. Zamolodchikov and A. B. Zamolodchikov. “Factorized s-matrices in two dimensions as the exact solutions of certain relativistic quantum field theory models.” *Annals of Physics* **120**, pp. 253, 1979. doi:[https://doi.org/10.1016/0003-4916\(79\)90391-9](https://doi.org/10.1016/0003-4916(79)90391-9).
- [208] T. Giamarchi. *Quantum physics in one dimension*, volume 121. Clarendon press, 2003.
- [209] G. Mussardo. *Statistical field theory: an introduction to exactly solved models in statistical physics*. Oxford University Press, 2010.
- [210] F. A. Smirnov. *Form Factors in Completely Integrable Models of Quantum Field Theory*. World Scientific, 1992.
- [211] B. Bertini, D. Schuricht, and F. H. L. Essler. “Quantum quench in the sine-gordon model.” *Journal of Statistical Mechanics: Theory and Experiment* **2014**, p. P10035, 2014. doi:[10.1088/1742-5468/2014/10/p10035](https://doi.org/10.1088/1742-5468/2014/10/p10035).

- [212] M. Kormos and G. Zaránd. “Quantum quenches in the sine-gordon model: A semiclassical approach.” *Phys. Rev. E* **93**, p. 062101, 2016. doi:[10.1103/PhysRevE.93.062101](https://doi.org/10.1103/PhysRevE.93.062101).
- [213] A. C. Cubero and D. Schuricht. “Quantum quench in the attractive regime of the sine-gordon model.” *Journal of Statistical Mechanics: Theory and Experiment* **2017**, p. 103106, 2017. doi:[10.1088/1742-5468/aa8c2e](https://doi.org/10.1088/1742-5468/aa8c2e).
- [214] I. Kukuljan, S. Sotiriadis, and G. Takacs. “Correlation functions of the quantum sine-gordon model in and out of equilibrium.” *Phys. Rev. Lett.* **121**, 2018. doi:[10.1103/physrevlett.121.110402](https://doi.org/10.1103/physrevlett.121.110402).
- [215] C. Rylands and N. Andrei. “Loschmidt amplitude and work distribution in quenches of the sine-gordon model.” *Phys. Rev. B* **99**, p. 085133, 2019. doi:[10.1103/PhysRevB.99.085133](https://doi.org/10.1103/PhysRevB.99.085133).
- [216] I. Kukuljan, S. Sotiriadis, and G. Takács. “Out-of-horizon correlations following a quench in a relativistic quantum field theory.” *Journal of High Energy Physics* **2020**, p. 224, 2020. doi:[10.1007/JHEP07\(2020\)224](https://doi.org/10.1007/JHEP07(2020)224).
- [217] B. Bertini, L. Piroli, and M. Kormos. “Transport in the sine-gordon field theory: From generalized hydrodynamics to semiclassics.” *Phys. Rev. B* **100**, p. 035108, 2019. doi:[10.1103/PhysRevB.100.035108](https://doi.org/10.1103/PhysRevB.100.035108).
- [218] I. Affleck and M. Oshikawa. “Field-induced gap in cu benzoate and other $s = \frac{1}{2}$ antiferromagnetic chains.” *Phys. Rev. B* **60**, pp. 1038, 1999. doi:[10.1103/PhysRevB.60.1038](https://doi.org/10.1103/PhysRevB.60.1038).
- [219] S. A. Zvyagin, A. K. Kolezhuk, J. Krzystek, and R. Feyerherm. “Excitation hierarchy of the quantum sine-gordon spin chain in a strong magnetic field.” *Phys. Rev. Lett.* **93**, p. 027201, 2004. doi:[10.1103/PhysRevLett.93.027201](https://doi.org/10.1103/PhysRevLett.93.027201).
- [220] I. Umegaki, H. Tanaka, T. Ono, H. Uekusa, and H. Nojiri. “Elementary excitations of the $s = \frac{1}{2}$ one-dimensional antiferromagnet KCuF_6 in a magnetic field and quantum sine-gordon model.” *Phys. Rev. B* **79**, p. 184401, 2009. doi:[10.1103/PhysRevB.79.184401](https://doi.org/10.1103/PhysRevB.79.184401).
- [221] A. C. Tiegel, A. Honecker, T. Pruschke, A. Ponomaryov, S. A. Zvyagin, R. Feyerherm, and S. R. Manmana. “Dynamical properties of the sine-gordon quantum spin magnet CuPM at zero and finite temperature.” *Phys. Rev. B* **93**, p. 104411, 2016. doi:[10.1103/PhysRevB.93.104411](https://doi.org/10.1103/PhysRevB.93.104411).
- [222] A. K. Bera, B. Lake, F. H. L. Essler, L. Vanderstraeten, C. Hubig, U. Schollwöck, A. T. M. N. Islam, A. Schneidewind, and D. L. Quintero-Castro. “Spinon confinement in a quasi-one-dimensional anisotropic heisenberg magnet.” *Phys. Rev. B* **96**, p. 054423, 2017. doi:[10.1103/PhysRevB.96.054423](https://doi.org/10.1103/PhysRevB.96.054423).
- [223] P. Bouillot, C. Kollath, A. M. Läuchli, M. Zvonarev, B. Thielemann, C. Rüegg, E. Orignac, R. Citro, M. Klanjšek, C. Berthier, M. Horvatić, and T. Gimarchi. “Statics and dynamics of weakly coupled antiferromagnetic spin- $\frac{1}{2}$ ladders in a magnetic field.” *Phys. Rev. B* **83**, p. 054407, 2011. doi:[10.1103/PhysRevB.83.054407](https://doi.org/10.1103/PhysRevB.83.054407).

- [224] A. Roy and H. Saleur. “Quantum electronic circuit simulation of generalized sine-gordon models.” *Phys. Rev. B* **100**, p. 155425, 2019. doi:[10.1103/PhysRevB.100.155425](https://doi.org/10.1103/PhysRevB.100.155425).
- [225] A. Roy, D. Schuricht, J. Hauschild, F. Pollmann, and H. Saleur. “The quantum sine-gordon model with quantum circuits.” *Nuclear Physics B* **968**, p. 115445, 2021. doi:<https://doi.org/10.1016/j.nuclphysb.2021.115445>.
- [226] V. Gritsev, A. Polkovnikov, and E. Demler. “Linear response theory for a pair of coupled one-dimensional condensates of interacting atoms.” *Phys. Rev. B* **75**, p. 174511, 2007. doi:[10.1103/PhysRevB.75.174511](https://doi.org/10.1103/PhysRevB.75.174511).
- [227] V. Gritsev, E. Demler, M. Lukin, and A. Polkovnikov. “Spectroscopy of collective excitations in interacting low-dimensional many-body systems using quench dynamics.” *Phys. Rev. Lett.* **99**, p. 200404, 2007. doi:[10.1103/PhysRevLett.99.200404](https://doi.org/10.1103/PhysRevLett.99.200404).
- [228] T. Schweigler, V. Kasper, S. Erne, I. Mazets, B. Rauer, F. Cataldini, T. Langen, T. Gasenzer, J. Berges, and J. Schmiedmayer. “Experimental characterization of a quantum many-body system via higher-order correlations.” *Nature* **545**, pp. 323, 2017. doi:[10.1038/nature22310](https://doi.org/10.1038/nature22310).
- [229] T. Schumm, S. Hofferberth, L. M. Andersson, S. Wildermuth, S. Groth, I. Bar-Joseph, J. Schmiedmayer, and P. Krüger. “Matter-wave interferometry in a double well on an atom chip.” *Nature Physics* **1**, pp. 57, 2005. doi:[10.1038/nphys125](https://doi.org/10.1038/nphys125).
- [230] S. Hofferberth, I. Lesanovsky, B. Fischer, T. Schumm, and J. Schmiedmayer. “Nonequilibrium coherence dynamics in one-dimensional bose gases.” *Nature* **449**, pp. 324, 2007. doi:[10.1038/nature06149](https://doi.org/10.1038/nature06149).
- [231] T. V. Zache, T. Schweigler, S. Erne, J. Schmiedmayer, and J. Berges. “Extracting the field theory description of a quantum many-body system from experimental data.” *Phys. Rev. X* **10**, p. 011020, 2020. doi:[10.1103/PhysRevX.10.011020](https://doi.org/10.1103/PhysRevX.10.011020).
- [232] M. Pigneur, T. Berrada, M. Bonneau, T. Schumm, E. Demler, and J. Schmiedmayer. “Relaxation to a phase-locked equilibrium state in a one-dimensional bosonic josephson junction.” *Phys. Rev. Lett.* **120**, p. 173601, 2018. doi:[10.1103/PhysRevLett.120.173601](https://doi.org/10.1103/PhysRevLett.120.173601).
- [233] D. X. Horváth, I. Lovas, M. Kormos, G. Takács, and G. Zaránd. “Nonequilibrium time evolution and rephasing in the quantum sine-gordon model.” *Phys. Rev. A* **100**, p. 013613, 2019. doi:[10.1103/PhysRevA.100.013613](https://doi.org/10.1103/PhysRevA.100.013613).
- [234] Y. D. van Nieuwkerk and F. H. L. Essler. “On the low-energy description for tunnel-coupled one-dimensional Bose gases.” *SciPost Phys.* **9**, p. 25, 2020. doi:[10.21468/SciPostPhys.9.2.025](https://doi.org/10.21468/SciPostPhys.9.2.025).
- [235] Y. D. van Nieuwkerk, J. Schmiedmayer, and F. H. Essler. “Josephson oscillations in split one-dimensional Bose gases.” *SciPost Phys.* **10**, p. 90, 2021. doi:[10.21468/SciPostPhys.10.4.090](https://doi.org/10.21468/SciPostPhys.10.4.090).

- [236] J.-F. Mennemann, I. E. Mazets, M. Pigneur, H. P. Stimming, N. J. Mauser, J. Schmiedmayer, and S. Erne. “Relaxation in an extended bosonic josephson junction.” *Phys. Rev. Research* **3**, p. 023197, 2021. doi:[10.1103/PhysRevResearch.3.023197](https://doi.org/10.1103/PhysRevResearch.3.023197).
- [237] L. Foini and T. Giamarchi. “Nonequilibrium dynamics of coupled luttinger liquids.” *Phys. Rev. A* **91**, p. 023627, 2015. doi:[10.1103/PhysRevA.91.023627](https://doi.org/10.1103/PhysRevA.91.023627).
- [238] L. Foini and T. Giamarchi. “Relaxation dynamics of two coherently coupled one-dimensional bosonic gases.” *The European Physical Journal Special Topics* **226**, pp. 2763, 2017. doi:[10.1140/epjst/e2016-60383-x](https://doi.org/10.1140/epjst/e2016-60383-x).
- [239] P. Ruggiero, L. Foini, and T. Giamarchi. “Large-scale thermalization, prethermalization, and impact of temperature in the quench dynamics of two unequal luttinger liquids.” *Phys. Rev. Research* **3**, p. 013048, 2021. doi:[10.1103/PhysRevResearch.3.013048](https://doi.org/10.1103/PhysRevResearch.3.013048).
- [240] Y. D. van Nieuwkerk, J. Schmiedmayer, and F. H. L. Essler. “Projective phase measurements in one-dimensional Bose gases.” *SciPost Phys.* **5**, p. 46, 2018. doi:[10.21468/SciPostPhys.5.5.046](https://doi.org/10.21468/SciPostPhys.5.5.046).
- [241] P. Ruggiero, P. Calabrese, L. Foini, and T. Giamarchi. “Quenches in initially coupled tomonaga-luttinger liquids: a conformal field theory approach.” *SciPost Phys.* **11**, p. 55, 2021. doi:[10.21468/SciPostPhys.11.3.055](https://doi.org/10.21468/SciPostPhys.11.3.055).
- [242] Y. D. van Nieuwkerk and F. H. L. Essler. “Self-consistent time-dependent harmonic approximation for the sine-gordon model out of equilibrium.” *Journal of Statistical Mechanics: Theory and Experiment* **2019**, p. 084012, 2019. doi:[10.1088/1742-5468/ab3579](https://doi.org/10.1088/1742-5468/ab3579).
- [243] B. Rauer, S. Erne, T. Schweigler, F. Cataldini, M. Tajik, and J. Schmiedmayer. “Recurrences in an isolated quantum many-body system.” *Science* **360**, pp. 307, 2018. doi:[10.1126/science.aan7938](https://doi.org/10.1126/science.aan7938).
- [244] T. Langen, R. Geiger, M. Kuhnert, B. Rauer, and J. Schmiedmayer. “Local emergence of thermal correlations in an isolated quantum many-body system.” *Nature Physics* **9**, pp. 640, 2013. doi:[10.1038/nphys2739](https://doi.org/10.1038/nphys2739).
- [245] M. Kuhnert, R. Geiger, T. Langen, M. Gring, B. Rauer, T. Kitagawa, E. Demler, D. Adu Smith, and J. Schmiedmayer. “Multimode dynamics and emergence of a characteristic length scale in a one-dimensional quantum system.” *Phys. Rev. Lett.* **110**, p. 090405, 2013. doi:[10.1103/PhysRevLett.110.090405](https://doi.org/10.1103/PhysRevLett.110.090405).
- [246] M. Gring, M. Kuhnert, T. Langen, T. Kitagawa, B. Rauer, M. Schreitl, I. Mazets, D. A. Smith, E. Demler, and J. Schmiedmayer. “Relaxation and prethermalization in an isolated quantum system.” *Science* **337**, pp. 1318, 2012. doi:[10.1126/science.1224953](https://doi.org/10.1126/science.1224953).
- [247] T. Langen, S. Erne, R. Geiger, B. Rauer, T. Schweigler, M. Kuhnert, W. Rohringer, I. E. Mazets, T. Gasenzer, and J. Schmiedmayer. “Experimental observation of a generalized gibbs ensemble.” *Science* **348**, pp. 207, 2015. doi:[10.1126/science.1257026](https://doi.org/10.1126/science.1257026).

- [248] I. Bloch, J. Dalibard, and W. Zwerger. “Many-body physics with ultracold gases.” *Rev. Mod. Phys.* **80**, pp. 885, 2008. doi:[10.1103/RevModPhys.80.885](https://doi.org/10.1103/RevModPhys.80.885).
- [249] F. D. M. Haldane. “Effective harmonic-fluid approach to low-energy properties of one-dimensional quantum fluids.” *Phys. Rev. Lett.* **47**, pp. 1840, 1981. doi:[10.1103/PhysRevLett.47.1840](https://doi.org/10.1103/PhysRevLett.47.1840).
- [250] M. A. Cazalilla. “Bosonizing one-dimensional cold atomic gases.” *Journal of Physics B: Atomic, Molecular and Optical Physics* **37**, pp. S1, 2004. doi:[10.1088/0953-4075/37/7/051](https://doi.org/10.1088/0953-4075/37/7/051).
- [251] S. Lukyanov. “Low energy effective hamiltonian for the xxz spin chain.” *Nuclear Physics B* **522**, pp. 533, 1998. doi:[https://doi.org/10.1016/S0550-3213\(98\)00249-1](https://doi.org/10.1016/S0550-3213(98)00249-1).
- [252] J. Sirker and M. Bortz. “The openXXZ-chain: bosonization, the bethe ansatz and logarithmic corrections.” *Journal of Statistical Mechanics: Theory and Experiment* **2006**, pp. P01007, 2006. doi:[10.1088/1742-5468/2006/01/p01007](https://doi.org/10.1088/1742-5468/2006/01/p01007).
- [253] T. Hikihara and A. Furusaki. “Correlation amplitude for the $s = \frac{1}{2}$ XXZ spin chain in the critical region: Numerical renormalization-group study of an open chain.” *Phys. Rev. B* **58**, pp. R583, 1998. doi:[10.1103/PhysRevB.58.R583](https://doi.org/10.1103/PhysRevB.58.R583).
- [254] T. Hikihara and A. Furusaki. “Spin correlations in the two-leg antiferromagnetic ladder in a magnetic field.” *Phys. Rev. B* **63**, p. 134438, 2001. doi:[10.1103/PhysRevB.63.134438](https://doi.org/10.1103/PhysRevB.63.134438).
- [255] S. Novikov, S. V. Manakov, L. Pitaevskii, and V. E. Zakharov. *Theory of solitons: the inverse scattering method*. Springer Science & Business Media, 1984.
- [256] V. E. Korepin, N. M. Bogoliubov, and A. G. Izergin. *Quantum inverse scattering method and correlation functions*, volume 3. Cambridge university press, 1997.
- [257] A. B. Zamolodchikov. “Mass scale in the sine-gordon model and its reductions.” *International Journal of Modern Physics A* **10**, pp. 1125, 1995. doi:[10.1142/s0217751x9500053x](https://doi.org/10.1142/s0217751x9500053x).
- [258] S. Lukyanov. “Form factors of exponential fields in the sine-gordon model.” *Modern Physics Letters A* **12**, pp. 2543, 1997. doi:[10.1142/S0217732397002673](https://doi.org/10.1142/S0217732397002673).
- [259] G. Takács. “Form factor perturbation theory from finite volume.” *Nuclear Physics B* **825**, pp. 466, 2010. doi:<https://doi.org/10.1016/j.nuclphysb.2009.10.001>.
- [260] A. Koubek and G. Mussardo. “On the operator content of the sinh-gordon model.” *Physics Letters B* **311**, pp. 193, 1993. doi:[https://doi.org/10.1016/0370-2693\(93\)90554-U](https://doi.org/10.1016/0370-2693(93)90554-U).
- [261] S. Lukyanov and A. Zamolodchikov. “Exact expectation values of local fields in the quantum sine-gordon model.” *Nuclear Physics B* **493**, pp. 571, 1997. doi:[https://doi.org/10.1016/S0550-3213\(97\)00123-5](https://doi.org/10.1016/S0550-3213(97)00123-5).

- [262] B. Doyon, T. Yoshimura, and J.-S. Caux. “Soliton gases and generalized hydrodynamics.” *Phys. Rev. Lett.* **120**, p. 045301, 2018. doi:[10.1103/PhysRevLett.120.045301](https://doi.org/10.1103/PhysRevLett.120.045301).
- [263] S. R. White and A. E. Feiguin. “Real-time evolution using the density matrix renormalization group.” *Phys. Rev. Lett.* **93**, p. 076401, 2004. doi:[10.1103/PhysRevLett.93.076401](https://doi.org/10.1103/PhysRevLett.93.076401).
- [264] S. R. White and I. Affleck. “Spectral function for the $s = 1$ heisenberg antiferromagnetic chain.” *Phys. Rev. B* **77**, p. 134437, 2008. doi:[10.1103/PhysRevB.77.134437](https://doi.org/10.1103/PhysRevB.77.134437).
- [265] S. R. White. “Density matrix formulation for quantum renormalization groups.” *Phys. Rev. Lett.* **69**, pp. 2863, 1992. doi:[10.1103/PhysRevLett.69.2863](https://doi.org/10.1103/PhysRevLett.69.2863).
- [266] A. J. Daley, C. Kollath, U. Schollwöck, and G. Vidal. “Time-dependent density-matrix renormalization-group using adaptive effective hilbert spaces.” *Journal of Statistical Mechanics: Theory and Experiment* **2004**, p. P04005, 2004. doi:[10.1088/1742-5468/2004/04/p04005](https://doi.org/10.1088/1742-5468/2004/04/p04005).
- [267] A. K. Kolezhuk, H.-J. Mikeska, K. Maisinger, and U. Schollwöck. “Spinon signatures in the critical phase of the $(1, \frac{1}{2})$ ferrimagnet in a magnetic field.” *Phys. Rev. B* **59**, pp. 13565, 1999. doi:[10.1103/PhysRevB.59.13565](https://doi.org/10.1103/PhysRevB.59.13565).
- [268] U. Schollwöck, J. Richter, D. J. J. Farnell, and R. F. Bishop (editors). *Quantum Magnetism*. Springer Berlin Heidelberg, 2004.
- [269] R. Vlijm, M. Ganahl, D. Fioretto, M. Brockmann, M. Haque, H. G. Evertz, and J.-S. Caux. “Quasi-soliton scattering in quantum spin chains.” *Phys. Rev. B* **92**, p. 214427, 2015. doi:[10.1103/PhysRevB.92.214427](https://doi.org/10.1103/PhysRevB.92.214427).
- [270] M. Van Damme, L. Vanderstraeten, J. De Nardis, J. Haegeman, and F. Verstraete. “Real-time scattering of interacting quasiparticles in quantum spin chains.” *Phys. Rev. Research* **3**, p. 013078, 2021. doi:[10.1103/PhysRevResearch.3.013078](https://doi.org/10.1103/PhysRevResearch.3.013078).
- [271] O. A. Castro-Alvaredo, B. Doyon, and T. Yoshimura. “Emergent hydrodynamics in integrable quantum systems out of equilibrium.” *Phys. Rev. X* **6**, p. 041065, 2016. doi:[10.1103/PhysRevX.6.041065](https://doi.org/10.1103/PhysRevX.6.041065).
- [272] B. Bertini, M. Collura, J. De Nardis, and M. Fagotti. “Transport in out-of-equilibrium xxz chains: Exact profiles of charges and currents.” *Phys. Rev. Lett.* **117**, p. 207201, 2016. doi:[10.1103/PhysRevLett.117.207201](https://doi.org/10.1103/PhysRevLett.117.207201).
- [273] A. Bastianello, B. Bertini, B. Doyon, and R. Vasseur. “Introduction to the special issue on emergent hydrodynamics in integrable many-body systems.” *Journal of Statistical Mechanics: Theory and Experiment* **2022**, p. 014001, 2022. doi:[10.1088/1742-5468/ac3e6a](https://doi.org/10.1088/1742-5468/ac3e6a).
- [274] P. Corboz. “Variational optimization with infinite projected entangled-pair states.” *Phys. Rev. B* **94**, p. 035133, 2016. doi:[10.1103/PhysRevB.94.035133](https://doi.org/10.1103/PhysRevB.94.035133).

- [275] L. Vanderstraeten, J. Haegeman, P. Corboz, and F. Verstraete. “Gradient methods for variational optimization of projected entangled-pair states.” *Phys. Rev. B* **94**, p. 155123, 2016. doi:[10.1103/PhysRevB.94.155123](https://doi.org/10.1103/PhysRevB.94.155123).
- [276] I. Bloch, J. Dalibard, and S. Nascimbène. “Quantum simulations with ultracold quantum gases.” *Nature Physics* **8**, pp. 267, 2012. doi:[10.1038/nphys2259](https://doi.org/10.1038/nphys2259).
- [277] J. I. Cirac and P. Zoller. “Quantum computations with cold trapped ions.” *Phys. Rev. Lett.* **74**, pp. 4091, 1995. doi:[10.1103/PhysRevLett.74.4091](https://doi.org/10.1103/PhysRevLett.74.4091).
- [278] J. I. Cirac and P. Zoller. “Goals and opportunities in quantum simulation.” *Nature Physics* **8**, pp. 264, 2012. doi:[10.1038/nphys2275](https://doi.org/10.1038/nphys2275).
- [279] C. D. Bruzewicz, J. Chiaverini, R. McConnell, and J. M. Sage. “Trapped-ion quantum computing: Progress and challenges.” *Applied Physics Reviews* **6**, p. 021314, 2019. doi:[10.1063/1.5088164](https://doi.org/10.1063/1.5088164).
- [280] H.-L. Huang, D. Wu, D. Fan, and X. Zhu. “Superconducting quantum computing: A review.” 2020. arXiv:[2006.10433](https://arxiv.org/abs/2006.10433).
- [281] J. Preskill. “Quantum computing in the NISQ era and beyond.” *Quantum* **2**, p. 79, 2018. doi:[10.22331/q-2018-08-06-79](https://doi.org/10.22331/q-2018-08-06-79).